Efficient Designs for LiFi System

Janis Sperga

Department of Electronic and Electrical Engineering

University of Strathclyde, Glasgow

December 17, 2024

This thesis is the result of the author's original research. It has been composed by the author and has not been previously submitted for examination which has led to the award of a degree.

Signed: Janis Sperga

Date: 26th of July 2024

Acknowledgments

Firstly, I would like to offer my deepest gratitude to my primary supervisor, Professor Harald Haas, for introducing me to and guiding me through the exciting world of LiFi. I would also like to thank Professor Ivan Andonovic and Professor Craig Michie for supervising the final stages of this project.

Furthermore, I would like to express my gratitude to my host company during this project, pureLiFi Ltd. In particular, my deepest gratitude goes to my colleagues at the company, Dr. Rui Bian and Dr. Mohammed Sufyan Islim, whose supervision and assistance were of paramount importance to this project.

I want to thank the ENLIGHT'EM project (H2020-MSCA ITN-2018 No. 814215) for the financial support and training provided. I would also like to thank the main coordinators of the project, Dr. Borja Genovés Guzmán and Dr. Domenico Giustiniano.

I also want to thank my peers within the project and company with whom I have had many engaging and exciting discussions on theoretical and practical questions. In particular, I would like to thank Gianluca Martena, Dr. Eoin Murphy, Dr. John Kosman, and Andy Aitken, from whom I have learned a lot.

Finally, I want to express my heartfelt gratitude to my most supportive wife, Elina, and my lovely son, Eduards, to whom I dedicate this work. I also want to thank my parents, Aivars and Tereze, for supporting me throughout this long and exciting journey.

Abstract

LiFi (short for light fidelity) is emerging as a complementary technology to the existing radio frequency (RF) telecommunication ecosystem. With the increasing data throughput and power consumption demands of new wireless RF standards, developing a LiFi physical layer that supports high data throughput (at least 10 Gbit/s) and energy-efficient transmission (less than 1 nJ/bit) is paramount.

Designing a high-speed and power-efficient LiFi system necessitates considering both the transmission protocol and the optoelectronic front-end. The first part of the thesis addresses this by exploring the use of the Generalised Space Shift Keying (GSSK) technique for digital baseband modulation. However, to maintain stable communication under changing channel conditions, an adaptive GSSK algorithm is required, which includes beam selection and codebook adjustment based on instantaneous channel conditions. The thesis explores such algorithm and demonstrates that, depending on the use case, a transmission protocol based on adaptive GSSK can be used for high-speed and energy-efficient LiFi transceiver design, even in mobile scenarios.

To demonstrate the viability of adaptive GSSK for real system deployment, the thesis introduces a practical DSP implementation of an HDL-synthesizable adaptive GSSK algorithm for field-programmable gate arrays (FPGAs).

Beyond modulation techniques, optoelectronic front-end elements can limit system performance. Custom receiver optics for high-speed photodiodes (PD) or PD arrays can enhance the LiFi transceiver's performance. The thesis adopts freeform optics design methodology, typically used for far-field irradiance pattern generation, for receiver optics design, which can be tailored for specific scenarios such as an adaptive GSSK link.

In summary, the thesis demonstrates how a high-speed, power-efficient LiFi system can be implemented using the proposed adaptive GSSK algorithm. The efficiency of such a system can be further enhanced by a freeform optical concentrator, which can be customised to suit the transmission technique. These contributions lay the foundation for a high-speed, power-efficient LiFi transceiver prototype.

Contents

List of Figures

List of Tables

Acronyms and abbreviations

3GPP NR 3rd Generation Partnership Project New Radio

4G LTE 4th Generation Long-term Evolution

5G 5th Generation

AC Alternating Current

ACO-OFDM Asymmetric Clipping Optical OFDM

ADC Analogue-to-Digital Converter

AM Amplitude Modulation

AP Access Point

APD Avalanche Photodiode

AR Augmented Reality

AWGN Additive White Gaussian Noise

BER Bit Error Ratio

BJT Bipolar Junction Transistor

CMOS Complementary Metal-oxide Semiconductor

CP Cyclic Prefix

CPC Compound Parabolic Concentrator

DAC	Digital-to-Analogue Converter
DC	Direct Current
DCO-OFDM	DC-Biased Optical OFDM
DD	Direction Detection
DOE	Diffractive Optical Element
DSP	Digital Signal Processing
DTIRC	Dielectric Totally Internally Reflecting Concentrator
EB	Exabyte
EI	Edge Intelligence
eU-OFDM	Enhanced Unipolar OFDM
FEC	Forward Error Coder
FFT	Fast Fourier Transform
FLIP-OFDM	Flip Orthogonal Frequency Division Multiplexing
FLO	Floating Point Operations
FM	Frequency Modulation
FoV	Field-of-View
FPGA	Field Programmable Gate Array
GaAs	Gallium Arsenide
GaN	Gallium Nitride
Gbit/s	Gigabits Per Second
Ge	Germanium

GHz Gigahertz

GSM Generalised Spatial Modulation

GSPS Giga-Samples Per Second

GSSK Generalised Space Shift Keying

HDL Hardware Description Language

ICI Inter-Channel Interference

ICT Information and Communication Technology

ID Identification

IEEE Institute of Electrical and Electronics Engineers

IM Intensity Modulation

InGaAs Indium Gallium Arsenide

InP Indium Phosphide

IoT Internet of Things

LAP Linear Assignment Problem

LD Laser Diode

LDPC Low Density Parity-Check

LED Light Emitting Diode

LiDAR Light Detection and Ranging

LiFi Light Fidelity

LIS Large Intelligent Surfaces

LoS Line-of-Sight

LUT	Look-Up Table
MA	Monge-Ampère
MCM	Multi-Carrier Modulation
MHP	Most Hazardous Position
MHz	MegaHertz
MIMO	Multiple Input and Multiple Output
MISO	Multiple-Input and Single-Output
ML	Maximum Likelihood
mmWave	Millimetre Wave
MOSC	Modulation Order Selection Criterion
MPE	Maximum Permissible Exposure
MTP	Mass Transportation Problem
NLoS	Non-Line-of-Sight
NOMA	Non-orthogonal Multiple Access
NRZ-OOK	Non-Return-to-Zero On-Off-Keying
OH-SM	Optimal Hybrid-SM
OOK	On-Off Keying
OP-AMP	Operational Amplifier
OWC	Optical Wireless Communication
PAM	Pulse Amplitude Modulation
PAM-DMT	Pulse-Amplitude Modulation Discrete Multitone Modulation

PAPR Peak-to-Average Power Ratio

PCSEL Photonic Crystal Surface-Emitting Laser

PD Photodiode

PEP Pairwise Error Probability

PMMA Polymethyl Methacrylate

POL Primary Optical Lenslet

PPM Pulse Position Modulation

PWM Pulse Width Modulation

QAM Quadrature Amplitude Modulation

QPSK Quadrature Phase Shift Keying

RC Repetition Coding

RF Radio-Frequency

RX Receiver

Sag Sagitta

SCM Single Carrier Modulation

SER Symbol Error Ratio

Si Silicon

SiPM Silicon Photomultiplier

SLM Spatial Light Modulator

SM Spatial Modulation

SMP Spatial Multiplexing

SMS	Simultaneous Multiple Surface
SNR	Signal-to-Noise Ratio
SOL	Secondary Optical Lenslet
SPAD	Single Photon Avalanche Diode
SSK	Space Shift Keying
SSL	Solid State Lighting
SSN	Self-Sustaining Network
TGR	Probe Trigger Signal
THz	Terahertz
TIA	Transimpedance Amplifier
TIR	Total Internal Reflection
TX	Transmitter
UE	User Equipment
U-OFDM	Unipolar OFDM
URLLC	Ultra-Reliable Low-Latency Communications
VCSEL	Vertical Cavity Surface Emitting Laser
VLC	Visible Light Communication
VR	Virtual Reality
WDM	Wavelength Division Multiplexing

List of Mathematical Symbols

$\mathrm{d}_{(\mathbf{x}_k,\mathbf{x}'_k)}$	Mutual Euclidean distance between symbols $\mathbf{x}_k$ and $\mathbf{x}_{k'}$
α	Yaw
α_{e}	Electron ionisation coefficient
α_{h}	Hole ionisation coefficient
α_{PD}	Relative fraction of light incident at the photodiode
$\bar{\psi}_{\mathrm{r}}$	Mean incidence angle
β	Pitch
$\delta()$	Dirac delta function
ϵ_0	Permitivity of vacuum
ϵ_{r}	Relative permitivity of the semiconductor
η	Spectral efficiency
Γ	Correction factor for non-linearity
γ	Roll
γ^{elec}	Electrical SNR
$\hat{\mathbf{x}}_k$	Estimated transmission vector
κ_{ion}	Ionisation ratio

l_{PD}	Photodiode avalanche layer thickness
λ	Wavelength of light
$\mathbb{A}_{\mathrm{r}}$	Set of locally and temporally available receivers
$\mathbb{A}_{\mathrm{t}}$	Set of locally and temporally available transmitter beams
$\mathbb{B}$	Locally and temporally chosen binary permutation vector set
$\mathbb{E}_{\mathrm{r,t}}$	Set of locally and temporally engaged receivers and transmitter beams
$\mathbb{E}_{\mathrm{r}}$	Set of locally and temporally engaged receivers
$\mathbb{E}_{\mathrm{t}}$	Set of locally and temporally engaged transmitter beams
$\mathbb{R}^3$	Real co-ordiante space
$\mathbb{S}$	Source domain
$\mathbb{T}$	Target domain
$\mathbb{X}$	Symbol alphabet
$\mathbf{b}$	Binary permutation vector
$\mathbf{e}$	Unit vector of global axis
$\mathbf{H}_0$	DC channel gain matrix
$\mathbf{I}_{N_{\mathrm{r}}^{\mathrm{e}}}$	$N_{\mathrm{t}}^{\mathrm{e}} \times N_{\mathrm{r}}^{\mathrm{e}}$ dimension identity matrix
$\mathbf{n}$	AWGN vector
$\mathbf{n}$	Normal vector
$\mathbf{P}$	MTP solution mapping
$\mathbf{R}$	Rotation matrix
$\mathbf{r}$	Receiver relative position to the transmitter beam

$\mathbf{u}$	Vector describing points on the freeform surface
$\mathbf{v}$	Vector describing points on the target surface
$\mathbf{X}$	Random X variable
$\mathbf{x}_k$	Symbol vector
$\mathbf{Y}$	Random Y variable
$\mathbf{y}$	Received signal vector
$\mathcal{E}_\mathrm{r}$	Local and temporal power set of all possible combinations of receivers
$\mathcal{E}_\mathrm{t}$	Local and temporal power set of all possible combinations of engaged transmitter beams
$\mathcal{N}(0, \sigma^2)$	Normal distribution with 0 mean and σ^2 variance
EE	Energy efficiency
$\mathrm{E}(\cdot)$	Expectation operator
FF	Fill factor
FLO	Floating point operations
$\max(\cdot)$	Maximum value operator
rec	Rectangular function
SNR	Signal-to-Noise Ratio
μ	Mean value
∇	Del operator
ν	Frequency of light
Ω	Receiver/transmitter beam orientation vector
Φ	Light flux

$\Phi(\mathbf{u}_i)$	Eikonal function of ith lenslet
$\Phi_{1/2}^{\mathrm{lens}}$	Half intensity angle of the condenser lens
ψ	Incidence angle of the light beam at the receiver
Ψ_{c}	Acceptance angle of the optical concentrator
ρ	Cost function
$\sigma(\cdot)$	Standard deviation operator
σ_{APD}^2	APD total noise variance
$\sigma_{\mathrm{bcg,APD}}^2$	Background shot noise variance of an APD
$\sigma_{\mathrm{bcg,PIN}}^2$	Background shot noise variance of a p-i-n photodiode
σ_{PIN}^2	P-i-n photodiode total noise variance
$\sigma_{\mathrm{shot,APD}}^2$	Shot noise variance of an APD
$\sigma_{\mathrm{shot,PIN}}^2$	Shot noise variance of p-i-n photodiode
σ_{TIA}^2	TIA input noise variance
σ_{T}^2	Thermal Johnson Nyquist noise variance
τ	Coherence time
τ_{sel}	Selection time of algorithm
Θ	Parameter matrix describing multiple receiver, transmitter orientation, location and time
θ	Parameter describing receiver, transmitter orientation, location and time for a single channel
Θ_{VCSEL}	Divergence angle of VCSEL
$\varnothing$	Empty set

φ	Emission angle
$\varphi_{1/2}$	Half-power half angle
A_t	Target area
A_{in}	Input aperture area of concentrator
A_{out}	Output aperture area of concentrator
A_{PD}	Photoactive area of the PD
B	Bandwidth
C	Channel capacity
c	Speed of light
$C_{\mathrm{data}}^{\mathrm{peak}}$	Maximum data throughput
C_{data}	Data throughput
$C_{\mathrm{MIMO}}^{N_{\mathrm{t}}^{\mathrm{e}} \times N_{\mathrm{r}}^{\mathrm{e}}}$	MIMO channel capacity
C_{opt}	Optical concentration
d	Distance from transmitter to receiver
$d_{\mathrm{H}(\mathbf{x}_k, \mathbf{x}_{k'})}$	Hamming distance or the number of erroneous bits between symbols $\mathbf{x}_k$ and $\mathbf{x}_{k'}$
D_{LED}	diameter of the LED array
D_{lens}	Condenser lens diameter
d_{PD}	Photodiode diameter
$E(\mathbf{v})$	Irradiance generated at the target surface
E_0	Input irradiance
E_t	Target irradiance

List of Mathematical Symbols

$E_{\hbar\omega}$	Photon energy
E_{amp}	Amplification energy
F	GSSK codebook
f	Signal frequency
$f_{\mathbb{X}(\boldsymbol{\Theta}(t))}$	Symbol mapping function
F_{APD}	Excess noise factor
f_{lens}	Focal length of lens
G_{Array}	Array gain
G_{con}	Non-imaging concentrator gain
G_{filter}	Optical filter gain
G_{lens}	Lens gain
G_{TIA}	TIA Gain
h	Planck's constant
$h(0)$	DC channel gain
$H(B)$	Photodiode frequency response
$H(C_{\mathrm{data}}^{\mathrm{peak}})$	Entropy of data throughput distribution
$h(t)$	Channel gain
I	Generated photocurrent
I_{array}	Array photocurrent
I_{bias}	Bias current
I_{RMS}	RMS drive current

$J_{\mathbf{P}}$	Jacobian of the co-ordinate transformation
k_{b}	Boltzmann constant
l_i	Engaged receiver
M	Number of constellation points
m_j	Available transmitter
M_{APD}	Avalanche multiplication gain
m_{LED}	Lambertian emission order
$n(t)$	AWGN noise sample with zero mean
N_{TIA}^2	Input referred current noise density
$N^{\mathrm{ops,sel}}$	Number of floating point operations for beam selection
n_j	Engaged transmitter
N_{bit}	Number of binary operations
n_{con}	Concetrator material refractive index
$N_{\mathrm{r}}^{\mathrm{a}}$	Number of available receivers. Superscript denotes the receivers that are "available"
$N_{\mathrm{r}}^{\mathrm{e}}$	Number of engaged receivers. Superscript denotes the receivers that are "engaged"
N_{t}	Number of transmitters
$N_{\mathrm{t}}^{\mathrm{a}}$	Number of available transmitter beams. Superscript denotes the transmitter beams that are "available"
$N_{\mathrm{t}}^{\mathrm{e}}$	Number of engaged transmitter beams. Superscript denotes the transmitter beams that are "engaged"
O	Landau's symbol

P^{elec}	Received electrical power
$P_{\mathrm{opt}}^{\mathrm{lens}}$	Optical power after condenser lens
$P_{\mathbf{x}_k \to \mathbf{x}_{k'}}$	Pairwise error probability
$P_{\mathbf{x}_k}$	A priori probability to select a transmission vector $\mathbf{x}_k$
P_{ADC}	ADC power consumption
P_{a}	Analogue front-end power consumption
P_{bit}	Bit error ratio
P_{DAC}	DAC power consumption
P_{d}	Digital power consumption
P_{emit}	Emitter power consumption
P_{link}	Total power consumption of the link
P_{opt}	Emitted beam optical power
$P_{\mathrm{r,bcg}}$	Optical power at the receiver from the background radiation
$P_{\mathrm{r,opt}}$	Received optical power
P_{RX}	Receiver power consumption
P_{s}	Symbol error ratio
P_{TIA}	TIA power consumption
$P_{\mathrm{TX,driver}}$	TX driver power consumption
P_{TX}	Transmitter power consumption
P_{VCSEL}	Optical output power of VCSEL
Q	Q-function

q	Elementary charge
R_s	Series resitance of photodiode
R_{cov}	Coverage
R_{load}	Load resistance
$R_{\text{PD,rel}}$	Relative responsivity of the photodiode
R_{PD}	Photodiode's responsivity
S	Freeform surface
s_0	Lattice spacing
s_{array}	Spacing between chips
S_{LED}	Radiant intensity of the LED
T	Ambient or circuit temperature
T_{count}	Counter period
T_{filter}	Filter transmissivity
T_{optic}	Transmissivity of the optical element
T_{PD}	Photodetector target surface
T_{samp}	Sample time
V	Peak-to-peak voltage
V_{array}	Array voltage
V_{bias}	Bias voltage
$V_{\text{min,act}}$	Minimal activation voltage for the receiver
$V_{\text{noise,rms}}$	Noise rms voltage

$V_{\mathrm{signal,rms}}$	Received signal rms voltage
V_{TGR}	Trigger voltage
V_{TX}	Transmitted signal voltage generated at the receiver
v_s	Carrier saturation velocity
W	Performance metric
w	Beam radius
w_0	Beam waist
W_{phot}	Beam irradiance
x	X co-ordinate
$x_{\mathrm{s}}(t)$	Transmitted signal
y	Y co-ordinate
$y_{\mathrm{s}}(t)$	Received signal
z	Z co-ordinate

List of Mathematical Symbols

Chapter 1

Introduction

1.1 Motivation

Mobile data serves as both a primary impetus for and a significant challenge within modern society. Our reliance on wireless communication has intensified in both daily life and industrial sectors. According to estimations by Ericsson, monthly mobile data traffic reached 93 exabytes (EB) by the end of 2022 and is expected to expand by a factor of 3.5 to 329 EB per month by 2028 [1]. The COVID-19 pandemic had further intensified the increase in demand for data traffic, which witnessed a 40% increase from February to mid-April of 2020 [2].

The escalating data traffic corresponds to an increase in energy consumption. Estimates suggest that Information and Communication Technology (ICT) [3] contributes to between $5-9\%$ of the worldwide energy usage and approximately 2% of global CO2 emissions, which is comparable to the fuel emissions from the entire aviation industry [4]. Although the rise in energy consumption attributed to ICT has been more gradual than previously projected[1] [5], the burgeoning proliferation of the Internet of Things (IoT), exhibiting an annual market expansion of 20% [6], along with the emergence of Virtual Reality (VR) technologies [7,8], is poised to significantly elevate energy usage at the consumer level.

The telecommunications sector has duly acknowledged this challenge, establishing

[1]A principal factor in the slower-than-anticipated growth of energy consumption has been the markedly enhanced energy efficiency of data servers [5].

stringent energy criteria and a strategic roadmap for energy efficiency and consumption within their networks [9]. The capabilities of 5G and WiFi 5 significantly surpass those of the previous generation's 4G and WiFi 4 connections, in terms of both data rate and energy efficiency. The 3GPP NR (5G) standard has realised a 90% enhancement in energy efficiency compared to 4G LTE [10], while the IEEE 802.11ac (WiFi 5) standard has achieved a tenfold improvement over the IEEE 802.11n (WiFi 4), achieving an energy efficiency of 1 nJ/bit [11].

Nevertheless, the advent of more energy-efficient 5G networks comes with the trade-off of a considerable increase in data consumption, particularly due to the rise of Industry 4.0 [12]. Studies forecast that the quantity of connected devices will surge to 100 billion by 2030 [13] and that the data traffic managed by 5G networks will exceed that of 4G by a factor of one thousand [14]. Despite current advances in energy efficiency, it is projected that a 5G network could utilise 140% more energy than its 4G predecessor [15, 16]. Consequently, next-generation wireless networks necessitate further substantial enhancements in energy efficiency to combat rise in energy consumption due to the increasing connectivity.

Presently, there is an extensive array of research underway pertaining to the energy efficiency of both existing wireless networks (5G and WiFi 6) and forthcoming generations (6G and WiFi 7). Research efforts are exploring a variety of solutions: the deployment of massive Multiple Input and Multiple Output (MIMO) systems [17–19], lean carrier design [20, 21], the integration of advanced sleep modes [21, 22], and the application of machine learning techniques [23]. Additional research is focused on Edge Intelligence (EI) [24], extending frequency bands beyond sub-6 GHz to the teraHertz (THz) range [25, 26], employing Non-orthogonal Multiple Access (NOMA) approach [27, 28], utilising Large Intelligent Surfaces (LIS) [29, 30], swarm intelligence network algorithms [31], and Self-Sustaining Networks (SSN) [32].

While these technological solutions hold promise for enhanced data throughput and energy efficiency, the escalating demand for bandwidth presents an increasingly intricate challenge. A seemingly straightforward remedy involves expanding the baseband by integrating new segments of the spectrum; for the 3GPP an extension up to 71

GHz is considered [33], for 6G teraHertz bands are being proposed [34]. However, such expansions are counterbalanced by the propagation characteristics of these environments, which include high path loss — inversely related to wavelength — pronounced molecular absorption within specific bands [35], and the manufacturing complexities associated with teraHertz devices [36].

In deployment scenarios considering extremely high data rates (on the order of several gigabits per second), the efficacy of these solutions in enhancing the energy efficiency of next-generation wireless technology—amid increasingly stringent energy efficiency requirements—remains a considerable challenge.

An alternative to the prevailing Radio-Frequency (RF) solutions lies in Optical Wireless Communication (OWC) [37, 38] and its sub-type, Visible Light Communication (VLC) [39, 40]. Over the past decade, VLC and OWC have surfaced as tenable complementary to contemporary RF wireless technologies. Analogous to the proposed next-generation sub-millimetre wave (mmWave) technologies, they present access to a vast and unregulated light spectrum of 300 teraHertz [41], which they utilise for data transmission and reception. The spectrum is expandable into the infrared region with wavelengths of as much as 1550 nm in consideration [42]. Contrary to mmWave technologies, OWC and VLC boast a well-established baseline technology, with a plethora of commercially available suppliers and off-the-shelf components capable of achieving data transmission rates of several gigabits per second—rates [43–45] that are ambitious targets for the more complex forthcoming RF wireless systems.

LiFi, short for 'light fidelity' (coined by Professor Harald Haas in 2011 [46]), presents an alternative to WiFi and 5G based on OWC or VLC, forming a fully networked, bi-directional, multi-user communications system [47]. Recently, companies such as pureLiFi, Signify, ZERO1, Oledcomm, Velmenni, Lucibel, and Lightbee have advanced and showcased a variety of innovative LiFi, VLC, and OWC products [48]. Additionally, the IEEE 802.11bb task group has enacted necessary modifications to the IEEE 802.11 standard to facilitate interoperability between LiFi and WiFi, with LiFi systems operating within the optical infrared spectrum ranging from 800 to 1000 nanometres [49].

However, for LiFi-based technology to fully emerge as a viable market complementary to next-generation RF wireless technologies, which are subject to increasingly stringent energy-saving mandates, it must align with green design principles [50]. This necessitates the development of energy-efficient system designs that are at minimum on par with their RF-based counterparts in terms of energy efficiency, i.e $< 1\,\mathrm{nJ/bit}$ [11]. Furthermore, for LiFi networks to integrate seamlessly and complement next-generation RF wireless networks, they must meet high data throughput demands. As the forthcoming 5G and WiFi-6 networks are poised to offer connectivity with data throughput of 10 Gbit/s [51, 52] the development of highly energy-efficient LiFi devices should be contextualized within this 10 Gbit/s benchmark framework.

Attaining high energy efficiency and data throughput in a LiFi network necessitates primary focus on the physical layer design, which includes the OWC or VLC transmitter and receiver—integral components of the system [47]. Such physical layer analysis and design development should cover holistically a range of aspects, from modulation techniques to opto-electronic front-end design and channel state adaptive algorithms.

1.1.1 Main Contributions

The thesis investigates physical layer designs and techniques to achieve high data throughput (up to 10 Gbit/s) and high energy efficiency (less than 1 nJ/bit) for VLC or OWC wireless links. The thesis addresses this challenge from two perspectives: modulation techniques and optoelectronic front-end. The main contributions of this work can be summarized as follows:

- **Adaptive generalised space shift keying (GSSK) algorithms**.
  We analyse a transmission protocol based on GSSK for both mobile VLC and fixed OWC scenarios. The performance of this transmission protocol is heavily dependent on instantaneous channel conditions. Therefore, adaptive beam selection and encoding algorithms are required to ensure stable connectivity.
  We present various adaptive GSSK algorithms based on different beam selection criteria. Specifically, we analyse beam selection algorithms based on the maximal minimum Euclidean distance criterion, the maximal signal-to-noise ratio (SNR) criterion, as well as our proposed optimal GSSK channel ratio selection criterion.

Each algorithm possesses its own trade-offs in terms of computational complexity, achievable data throughput, and data throughput spatial uniformity, with the optimal GSSK channel ratio selection criterion providing intermediary results in all categories.

We embed these algorithms in VLC and OWC link models with an optoelectronic front-end selected to achieve the required data throughput. Our modeling shows that for high-speed VLC link implementation, adaptive GSSK can be used in mobile scenarios. However, the energy efficiency is very low, primarily due to the high power consumption of the high bandwidth transmitter. This is due to the high voltage required to drive in-series connected micro-LEDs in order to minimise their capacitance for the required bandwidth enhancement. In contrast, in a device-to-device OWC scenario, adaptive GSSK is well-suited for high data throughput and energy-efficient data transmission, with comparable performance in data throughput and energy efficiency to direct current biased optical orthogonal frequency division multiplexing (DCO-OFDM).

This contribution demonstrates that, depending on the use case scenario, a transmission protocol based on adaptive GSSK is a considerable alternative to existing common data transmission algorithms such as DCO-OFDM when high speed and high energy efficiency are required. The presented beam selection algorithms and computational complexity analysis demonstrate the viability of a LiFi transceiver system utilising such a communication protocol, even in mobile scenarios where channel conditions can change significantly over short time periods.

- **Adaptive GSSK Algorithm Simulink Implementations**.

  While the first contribution focused on the theoretical modeling of the different adaptive GSSK algorithm performance, the second contribution deals with a practical digital signal processing (DSP) implementation of hardware description language (HDL) synthesizable adaptive GSSK algorithm utilising maximal minimum Euclidean distance beam selection criterion.

  The results of this contribution show how, using basic DSP building blocks, an adaptive GSSK system can be designed for field-programmable gate array

(FPGA) implementation. The adaptive properties of the algorithm are demonstrated on a per data packet basis with appropriate training preambles, which are used to identify number of available transmitter beams for the selection, the number of beams to be selected and the training GSSK symbols.
This contribution builds on the previous work by demonstrating a practically viable implementation of the adaptive GSSK, which can be used towards developing a functioning prototype utilising the transmission protocol.

- **Freeform Receiver Concentrator**.
While the previous two contributions primarily deal with communication protocols and algorithms, the third contribution is centered on optical front-end design. Here, we adapt the freeform optics design methodology, which is primarily used to generate an irradiance pattern in the far-field, for receiver optics. To validate the method, we design a simple thin on-axis lens consisting of multiple freeform lenslets to provide light focusing, yielding similar performance to convex and Fresnel lenses.
More beneficial for LiFi applications, however, is a 10-degree field-of-view (FoV) concentrator, which has comparable performance to a compound parabolic concentrator (CPC) in terms of achievable optical concentration while retaining a more uniform concentrated beam pattern.
The importance of uniformity becomes more apparent when we expand our analysis to an array of photodiodes. CPCs struggle to provide uniform concentration gain across multiple angular directions, whereas the performance of our freeform concentrator remains consistent. This makes a freeform concentrator a strong design candidate for high-speed optical communication systems that utilise photodiode arrays.
The better control of the beam profile at the receiver plane, can also benefit a GSSK based system, where a freeform optical concentrator could be designed to redirect different incidence angle transmitter beams onto different photodetectors, which can be leveraged to enhance distinguishability between different beams and spectral efficiency of the link.

> The contribution demonstrates that by leveraging existing freeform optics design methodology for far-field beam shaping, receiver concentrating optics can be effectively designed. This expands our knowledge beyond commonly known imaging and non-imaging solutions. Furthermore, the good performance of the freeform optics receiver concentrator when paired with photodiode arrays presents a novel approach to designing optical front-ends for high data throughput VLC or OWC links in LiFi. Furthermore, a custom design of freeform optics could be designed to ehnance the performance of LiFi system utilising GSSK as a transmission protocol.

1.1.2 Thesis Layout

The rest of the thesis is organised as follows:
Chapter 2 provides an introduction to the relevant background of the thesis, focusing on key aspects of data transmission and reception in optical wireless communication and visible light communication for LiFi. This chapter includes an overview of opto-electronic front-end components, channel modeling, photodetection noise, modulation schemes, and power consumption models.
Chapters 3 and 4 present the first main contribution of the thesis. In Chapter 3 we introduce the adaptive GSSK algorithm utilising various beam selection algorithms and derive for each beam selection algorithm computational complexity. We present the channel models for both indoor VLC and OWC scenarios with the aim to achieve high data throughput (up to 10 Gbit/s). Chapter 4 focuses on MATLAB Monte Carlo computer simulations. The analysis of the results in the chapter focuses on achieved data throughput, computational complexity of beam selection algorithms, spatial uniformity of data throughput, power consumption, and energy efficiency.
Chapter 5 focuses on the second main contribution of the thesis. Here, we present an HDL-synthesizable DSP implementation of adaptive GSSK using the maximal Euclidean distance criterion beam selection algorithm in MathWorks Simulink.
Chapter 6 addresses the third main contribution of the thesis. It introduces a novel method for designing freeform receiver optics. A proof of concept for an on-axis narrow

field-of-view (FoV) lens and a 10-degree FoV concentrator are presented based on this method. The performance, in terms of concentration gain, is analysed for both single photodiodes and arrays of photodiodes.

Chapter 7 summarizes and concludes the thesis. It discusses the study's limitations and provides recommendations for future research.

Chapter 2

Background

2.1 Introduction

Optical communication generally refers to the transmission of information through light. Information is encoded optically at the transmitter, then conveyed across an optical channel, and subsequently received, decoded, and reproduced by a receiver [53]. Although recent years have seen the development of innovative optical communication technologies, such as LiFi [47], the initial instances of optical communication can be traced back to antiquity, where rudimentary methods like smoke signals and fire beacons were employed for signalling [54].

Presently, the most pervasive form of optical communication is fibre optic communication, employed globally by numerous telecommunication companies. This technology facilitates the transmission of telephone and cable television signals and provides internet communication [55]. The current world record holder is National institute of information and communications technology (NICT) in Japan, with a record data throughput of 1.53 Pbit/s per channel over 25.9 km [56].

Since the 1970s, the advancement of optical fibre communication has spurred the technological development of transmitter and receiver semiconductor devices, such as Laser Diodes (LDs), Light Emitting Diodes (LEDs) and Photodiodes (PDs), which originally predominantly operated in the Infrared (IR) spectrum [57]. However, lately with the advancements coloured and white LEDs [58], and microLEDs [59], the availability of visible light spectrum for optical communication technology has grown significantly.

OWC is a form of optical communication that facilitates the transmission and reception of information via a wireless free-space optical channel, eliminating the need for fibre or wire [38]. The optical channel may be indoor, atmospheric, or underwater, and can operate on a Line-of-Sight (LoS) or Non-Line-of-Sight (NLoS) basis [53].

The initial proof-of-concept for IR OWC links emerged alongside semiconductor lighting technology in the early 1960s [60], with the first OWC television transmission demonstrated by MIT Lincoln Laboratory in early 1962 [53]. This demonstration achieved a distance of over 30 miles using a Gallium Arsenide (GaAs) LED. The first long-distance laser free-space atmospheric communication link was demonstrated later in 1962, spanning a range of 18 miles with a Helium-Neon (He:Ne) laser [61].

One of the primary limitations of early OWC technology was the absence of compact and cost-effective transmitters [62]. Initially, laser technology was confined to gas lasers, such as helium-neon (He:Ne) lasers, or solid-state lasers like the Neodymium-doped Yttrium Aluminum Garnet (Nd:YAG) laser, which were typically too large and costly for use in small devices [62]. Consequently, in its early years, OWC technology was considered impractical and superfluous when juxtaposed with the more economical and accessible RF technology, thus relegating its use primarily to niche applications such as satellite and military communications [60].

In recent decades, significant advancements in semiconductor lighting device technology and manufacturing have substantially reduced the size and cost of semiconductor lasers, LDs, LEDs, Vertical Cavity Surface-Emitting Lasers (VCSELs) and PDs [62]. This progression has facilitated their widespread integration into a variety of devices, such as smartphones, cameras, laser printers, televisions, and other smart devices [62]. The resulting ubiquity of semiconductor devices has catalysed a resurgence of interest in OWC [60].

The development of Solid-State Lighting (SSL) has significantly propelled advancements in VLC technology [39]. VLC, a subset of OWC, exploits the visible light spectrum ranging from 380 nm to 750 nm, corresponding to a 370 THz wide unlicensed spectrum, for wireless data transmission [40]. This technology can be seamlessly integrated with lighting applications and their existing infrastructure [40].

In VLC systems, the communication signal is created by superimposing a modulated signal onto the DC (Direct Current) bias of an solid state optical device. VLC predominantly employs SSL devices such as LEDs [40], but can also employ LDs [63], and micro-LEDs [64] for signal transmission, with PDs serving as receivers [39]. The commercial prevalence of these devices and the established SSL infrastructure pave the way for the broad commercial deployment of wireless links based on VLC technology [40].

Although, as previously mentioned, the origins of VLC can be traced back to ancient times, the contemporary concept of using light for simultaneous illumination and information transmission was proposed in 2003 at Nakagawa Laboratory, Keio University, Japan [53]. This proposition marked the establishment of VLC as a distinct and standalone technology.

2.2 Light as an Information Carrier

Information within light can generally be encoded and decoded using either Intensity Modulation with Direct Detection (IM-DD) or coherent modulation schemes [53]. In the case of IM-DD, the information is encoded in a single degree of freedom, namely, the emitted light intensity at the transmitting end. The receiver directly detects the signal strength as the photocurrent induced by the photoelectric effect within the photodetector [53]. To achieve this objective, the transmitted signal must be positive and real-valued. By contrast, in an RF-based system, the data carrier can be complex and bipolar when emitted from an antenna. IM-DD is the simplest and most widely used method for information detection [53].

Coherent detection, while more complex than IM-DD, offers the advantage of enabling the complete restoration of information from the optical signal carrier wave [53]. This includes the amplitude or in-phase (I) component, the phase or quadrature (Q) component, and the polarisation of the complex optical electric field [53]. Coherent detection employs heterodyne or homodyne detection techniques and necessitates adaptive control for the phase and polarisation of the signal carrier wave in the received signal [53].

2.3 Opto-electronic Front-End Elements

IM/DD is the method most commonly employed in VLC and OWC systems [53]. In such systems, the transmitter processes digital data, which is modulated, scaled and transformed into an analogue electrical signal via a Digital-to-Analogue Converter (DAC) [65]. This electrical signal is subsequently converted into a light signal by an optical source, such as an LED [40, 65], microLED [64], LD [63], VCSEL [44], or Photonic Crystal Surface-Emitting Laser (PCSEL) [66]. The transmitter can use existing RF basebands such as WiFi baseband in the IEEE 802.11bb standard [49] or operate with a custom baseband. Optionally, depending on the use case, the transmitter may utilise an optical element to shape the transmitted beam's irradiance pattern to suit the target coverage area [67].

The light beam, carrying the signal, propagates through the optical channel until the receiver detects it using direct detection (DD) [53]. At this point, the light is transduced back into an electrical signal with additionally acquired Additive White Gaussian Noise (AWGN) [53]. This conversion is achieved using either a single PD or an array of PDs [68]. Various types of PDs can be employed for light detection in OWC and VLC, including p-i-n photodiodes [69], Avalanche Photodiodes (APDs) [70], Single-Photon Avalanche Diodes (SPADs) [70], Schottky photodiodes [71], and p-n photodiodes [72]. Optionally, the receiver may also utilise optical filters and concentrating optics to enhance the Signal-to-Noise Ratio (SNR) [73].

The electrical signal is then filtered and reconverted into a digital signal via an Analogue-to-Digital Converter (ADC), and subsequently demodulated into data bits [65]. The block diagram of a typical IM/DD OWC or VLC system is depicted in Figure 2.1.

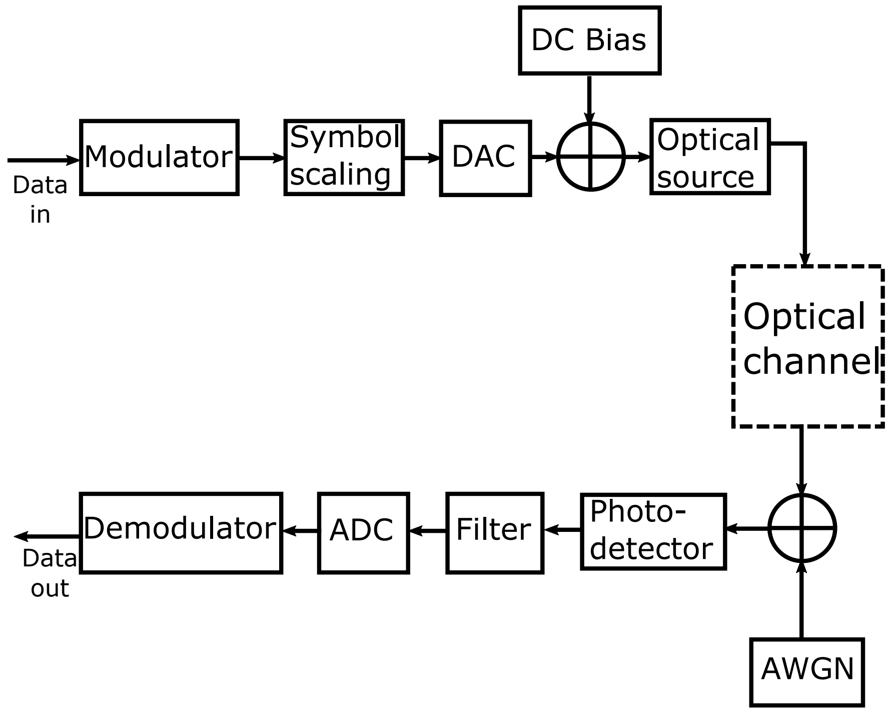

Figure 2.1: IM/DD OWC or VLC system block diagram.

2.3.1 Transmitter Front-End

Typically, for an IR OWC link, the choice of optical sources falls on such devices as VCSELs [74], LDs [75], or the more recently emerging PCSELs [66] depending on the application and the wavelength requirements. These devices commonly operate at the range emission wavelengths from 750 nm to 1550 nm [66,76–81]. They are characterised by their narrow emission wavelengths, Gaussian beam distribution in the single mode operation [82], high achievable bandwidth [83] (on the order of multiple GHz, with potentials reaching tens of GHz), and relatively high electrical-to-optical conversion efficiency (approximately up to 50% for VCSELs [82] and up to 70% for laser diodes [84]). These are however the higher reported achievable efficiencies, which can be achieved by carefully optimised design, for example, by utilising waveguides [85] or intracavity gratings as waveguides [86]. Commercially cheaper VCSELs and laser diodes report lower efficiency values typically around $20-25\%$ [87]. Additionally, all IR sources are subject to stringent laser eye safety requirements [88].

In contrast, for the majority of VLC applications, LEDs are preferred due to their widespread presence in existing SSL infrastructure [40] and more relaxed eye safety requirements for the visible light sources [65, 88].

Nevertheless, the pursuit of achieving widespread commercial implementation of high data throughput VLC based on LEDs remains challenging due to the limited -3 dB bandwidth of commercially available off-the-shelf LEDs, which is typically around $10-20$ MHz [65]. Although high data throughput can be attained through the use of suitable multiplexing techniques, such as OFDM and Wavelength Division Multiplexing (WDM) [45], this is offset by the drawback of increased power consumption in the LED driver circuitry [89] and from the additional Digital Signal Processing (DSP) components [90].

An alternative approach to addressing the bandwidth deficiency and link power consumption issues associated with LEDs is to consider miniaturising them, that is, utilising micro-LEDs [91, 92]. This approach is motivated by the fact that the responsivity of an LED, specifically its rise and fall time, is dependent on its internal capacitance. This capacitance, in turn, is proportional to the area of the LED's active region; thus, reducing the size of the LED can lead to improved performance [93].

2.3.2 Vertical Cavity Surface-Emitting Laser

In OWC systems, VCSELs are prospective optical sources due to their high bandwidth properties, making them ideally suited for applications requiring high data throughput [44, 94, 95]. A VCSEL, is a type of laser diode [82]. The main difference between them is that standard LDs are edge-emitting, while VCSELs emit light vertically from the surface of the semiconductor chip [82]. This vertical emission can facilitate straightforward integration of VCSELs onto a chip [96–98].

The resonator within a VCSEL is created using an active layer, a few micrometres thick, consisting of multiple quantum wells, which is surrounded by multiple layers of Bragg reflectors [82]. The advantage of this design is the ease of chip integration due to the vertical emission. However, a drawback is the limited emission area size, beyond which the beam quality significantly deteriorates [82]. Consequently, for multiple high-performance, high-bandwidth VCSELs, the diameter of a VCSEL mesa is typically only a few micrometres [82].

Similar to LEDs, VCSELs operate on the principle of electroluminescence [82]. Typically, current is applied to the active layer through a ring electrode [99] and is confined to the region supporting the resonator mode [82]. Within this region, injected charges recombine with quantum dots, emitting light through electroluminescence [82]. This light is then further amplified by stimulated emission, a process that is facilitated by the Bragg reflector layers [82].

Typical VCSEL emission wavelengths range from 750 to 980 nm, with 850 nm being the most prevalent [82]. These wavelengths are characteristic of the GaAs/AlGaAs material system [82]. However, longer wavelengths, such as 1310 and 1550 nm, can be achieved using GaInNAs quantum wells on GaAs substrates [82] or InAlGaAs quantum wells on InP substrates [100, 101].

If the emission area of a VCSEL is maintained at a few micrometres in diameter, it can achieve single-mode transverse emission, ensuring a high-quality, single-mode Gaussian beam output profile [82]. A Gaussian beam irradiance at distance z from the beam source and radial distance r away from the beam optical axis can be modelled using [93]:

$$W_{\text{phot}}(r, z) = P_{\text{opt}} \frac{1}{\pi w(z)^2/2} \exp\left(-2\frac{r^2}{w(z)^2}\right), \tag{2.1}$$

where P_{opt} is beam's optical power, $w(z)$ is the beam radius defined as the distance from the beam axis where irradiance drops to $1/e^2$ of the maximum value [93].

Furthermore, VCSELs are capable of producing a low beam divergence [82], which describes the rate at which the laser beam expands from its beam waist (the location where the beam radius is at its minimum) [93]. This characteristic facilitates straightforward VCSEL collimation, achievable with simple optical lenses. In comparison, laser diodes exhibit significantly larger beam divergence [102], which is highly assymetric making collimation difficult [93]. The beam divergence half-angle θ is given by [93]:

$$\theta = \frac{\lambda}{\pi w_0}, \tag{2.2}$$

where λ is wavelength and w_0 represents beam waist.

Owing to the aforementioned advantages, VCSELs have seen widespread implementation in high-speed OWC applications. Proposed applications include up to Tbit/s backhaul connection [74], 250 Gbit/s over 5000 km inter satellite links [103], and 250 Gbit/s long haul OWC channels over 500 km distance [104].

2.3.3 Light Emitting Diode

For VLC links, LEDs are the optical sources most frequently considered for communication [65]. An LED is a semiconductor device comprising p-doped and n-doped semiconductor crystals. The p-doped semiconductor possesses excess holes, whereas the n-doped semiconductor contains excess electrons. A p-n junction separates the two types of crystals [93].

When no voltage is applied, the depletion region at the junction inhibits electrons in the n-doped semiconductor from recombining with holes in the p-doped semiconductor [93]. However, applying a forward voltage across the junction enables the current to overcome the intrinsic electric field of the depletion layer, allowing electrons to recombine with holes, which results in light emission through electroluminescence [93].

The emission wavelength of LEDs is dependent on the bandgap of the semiconductor material. To produce a specific colour [93], different LEDs can be combined on a single chip, or alternatively, a layer of light-emitting phosphor may be used in conjunction with the LEDs [105].

The radiant intensity of an LED can be modelled using Lambertian model [53]:

$$S_{\mathrm{LED}} = P_{\mathrm{LED}} \frac{(m_{\mathrm{LED}} + 1)}{2\pi} \cos^{m_{\mathrm{LED}}}(\varphi), \tag{2.3}$$

where P_{LED} is the optical output power of the LED, φ is the radiant angle and m_{LED} is the Lambertian emission order of the LED, which is related to the half-power half-angle $\varphi_{1/2}$, which is given as [53]:

$$m_{\mathrm{LED}} = -\frac{\ln 2}{\ln \cos(\varphi_{1/2})}. \tag{2.4}$$

As previously mentioned, the typical bandwidth of a commercial LED suitable for VLC communication ranges between $10 - 20\,\mathrm{MHz}$ [65]. One of the primary reasons for this limited bandwidth is the capacitance of the p-n junction, which affects the charge carrier lifetime in the active region [93]. This large capacitance arises in most commercial LEDs from the illumination requirements, wherein high output optical power is typically expected [106]. Such power necessitates a large active region area, which, in turn, results in an increased capacitance of the junction [106].

The miniaturisation of LEDs to enhance bandwidth has garnered significant research interest over the past decade. Active research has been undertaken in the field of micro GaN (Gallium Nitride) [91, 107] and InGaN LEDs [108]. In the paper by Xie et al., over 10 Gbit/s was achieved using a GaN series-biased micro-LED array with a -3 dB bandwidth of 980 MHz [109]. Most recently, a -3 dB bandwidth of up to 3.6 GHz has been achieved using InGaN quantum dot microLEDs [110].

Apart from GaN, alternative semiconductor junctions are also being explored; for instance, Carreira et al. have demonstrated a 1 Gbit/s VLC link utilising an AlGaInP red micro-LED [111].

While the miniaturisation of LEDs offers the advantage of significant bandwidth improvement, it also presents a drawback: a marked reduction in illumination from the transmitter, which can lead to a severe decrease in the SNR, thus severely limiting the operational range of the VLC link. Nonetheless, considerable progress has been made in the development of small, ultrabright micro-LEDs. Notably, Bai et al. have demonstrated InGaN micro-LEDs with a luminance exceeding 10^7 cd/m^2 [112].

2.3.4 Non Linearity of Optical Sources

A characteristic shared by semiconductor optical sources is their nonlinear response to increasing current [113]. This response is illustrated in Figure 2.2a and Figure 2.2b. It is evident that at low current densities, the electrical-to-optical conversion efficiency remains consistent, with optical power rising linearly alongside an increase in current.

However, with further increases in current, there is a notable decrease in conversion efficiency, a phenomenon referred to as 'current droop' [115]. Analogously, a marked decline in electrical-to-optical conversion efficiency is also observed with rising temperatures, an effect termed 'thermal droop' [116]. Several quantum mechanisms have been proposed to account for both phenomena [115].

The nonlinearity displayed by the optical sources can considerably impact the performance of OWC or VLC links, resulting in distortions, especially when multi-level modulation schemes are employed. A significant body of research has been dedicated

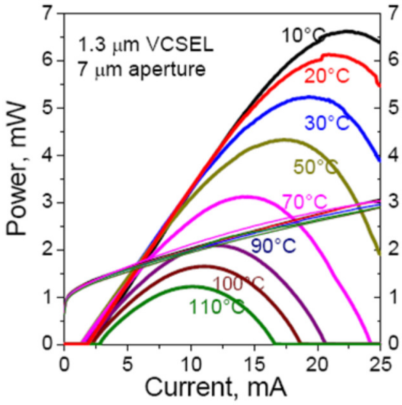

(a)

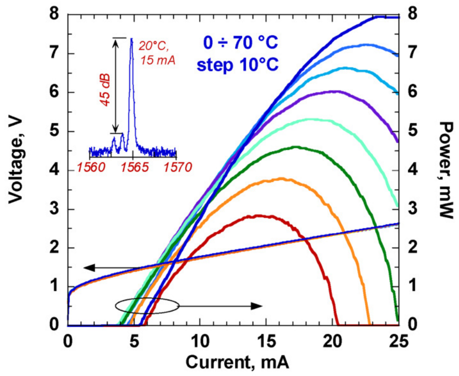

(b)

Figure 2.2: VCSEL light-current curves from [114] demonstrating the effect of current and temperature droop. At a) 1.3 μm and b) 1.55 μm.

to the development of equalizers and pre-distortion techniques aimed at reducing the effect of nonlinear distortions on the SNR [117–119].

2.3.5 Transmitter Driver

A transmitter driver refers to the circuitry that modulates the optical source. Typically, digital binary information is processed through a modulator or encoder, which maps digital bits to transmission symbols [53]. Each symbol can correspond to a particular amplitude, phase, quadrature [53], colour [120], polarisation [121], or a combination of parameters, depending on the modulation scheme employed [53].

For the majority of modulation schemes, the digital data characterising the symbol is converted into an analogue electrical signal by the use of a DAC [65]. Commercially available DACs can achieve sampling rates of up to 20.48 Giga-Samples per Second (GSPS) on a single channel (Texas instruments DAC39RF10) [122]. While there are multi-channel options, the sampling rate typically decreases when multiple channels are used [123]. A significant drawback of DACs in high data throughput communication is their relatively high power consumption at such elevated frequencies. For instance, a 20.48 GSPS DAC's power consumption can reach up to 3.8 W, which markedly affects the energy efficiency of the communication link [122].

DAC is a critical component in the transmitter circuit for signals with multiple amplitude levels [65]. However, in principle, binary modulation schemes like On-Off Keying (OOK) do not necessarily require the use of a DAC. This is because the modulated signal, superimposed on the DC bias, can be applied by simply switching the optical source on or off [89]. Circuits for this purpose can be straightforwardly realised through the use of transistors, such as Bipolar Junction Transistors (BJTs) [124]. The primary drawback of this approach is the limited spectral efficiency of binary modulation schemes, where at most, a single bit can be encoded per symbol [89].

Once the digital signal is converted into an analogue one, it may require amplification by a direct current (DC) amplifier if the output analogue signal is too weak relative to the dynamic range of the optical source [89]. Subsequently, the modulated signal is combined with the DC bias of the optical source. Typically, a bias tee is utilised to merge the signal and the bias [53].

In both OWC and VLC, the signal received at the receiver end is characterised by intensity, a property of the electrical field that is inherently real and non-negative. Consequently, the transmitted signal in OWC and VLC must also be real and positive [53]. This requirement can significantly influence energy efficiency, especially when high data throughput links are in consideration. In such cases, commonly DC-Biased Optical OFDM (DCO-OFDM) is employed to achieve high data throughput with limited available bandwidth [125]. In DCO-OFDM, a substantial DC bias is applied to the modulated signal to prevent clipping that would occur due to the negative parts of the signal [125]. This biasing can adversely impact the energy efficiency of the link [126].

In recent years, there has been substantial research aimed at optimising such driver circuits. For instance, Rodriguez et al. [89] and Sebastián et al. [127] have demonstrated that by using two DC-DC power converters connected in output-series, it is possible to efficiently split the AC (Alternating Current) and DC components of the signal. This results in an overall driver circuit efficiency of around 90%. Further enhancements in circuitry efficiency can be achieved by developing an efficient amplitude modulator in conjunction with a ripple canceller [128], as well as by employing the out-phasing technique, which is characteristic of existing RF solutions [129].

2.3.6 Transmitter Optics

Transmitter optics are as critical to link design as the optoelectronic components themselves. Collimating optics play a vital role in point-to-point communication links, where they ensure that the light beam travels long distances with minimal energy loss [53]. Typically, simple convex or plano-convex lenses are employed for this purpose [53]. Nevertheless, in indoor OWC or VLC settings, beam shaping can also be advantageous to enhance the beam's energy density at the intended target area to boost SNR.

Although light collimation represents one of the simplest approaches to beam shaping, there exists a much larger variety of more specialized optics designed to tailor radiant intensity. These include diffusers [130], beam homogenisers (biprism, fly's eye lenslet arrays) [131], Diffractive Optical Elements (DOEs) [132], aspheric lenses [133], Spatial Light Modulators (SLMs) equipped with micromirror arrays or liquid crystals [131, 134], cylindrical lenses [135], metalenses [136] and metasurfaces [137], and freeform lenses [138]. These optical components may be utilised to attain a specific irradiance distribution at the receiver plane, enhance the Maximum Permissible Exposure (MPE) [88, 139], or reduce the mutual interference of multiple beams [140].

Alongside beam shaping optics, optical beam steering elements can also be employed. The beam steering has the capacity to adapt and redirect the transmitter beam in response to feedback from the link. Contemporary methods for beam steering typically employ mechanical means, either macroscopic or microscopic [141]. Devices used for this purpose encompass a range of technologies, including Risley prisms [142], mirrors mounted on motorised rotation stages [143], arrays of micromirrors actuated electrostatically [144], SLMs that utilise liquid crystals [145], and the more recently proposed tunable metasurfaces [137].

2.3.7 Receiver Front-End

In the framework of OWC and VLC transceivers, the design of the optical receiver is as crucial as that of the transmitter in determining the attainable data throughput and energy efficiency. An effective receiver design requires a comprehensive approach that integrates both the optoelectronic and optical elements to meet the desired performance objectives.

After the transmitted beam has propagated over the optical channel to reach the receiver, the photodetector converts the optical energy of the beam into the electrical energy [53]. This conversion occurs as the energy from incident photons is transduced via the photoelectric effect into generating the electrical charge of the resulting photocurrent [93]. The typically small photocurrent, on the order of tens-to-hundreds of microamperes, is then transformed into a voltage and amplified by a Transimpedance Amplifier (TIA) [146]. Subsequently, the received signal voltage may be optionally passed through electrical filters and further amplified by an RF amplifier. The final analogue signal voltage is converted into a digital signal by an ADC, which is then decoded to extract the data bits [65].

2.3.8 Photodiode

In OWC and VLC, PDs are commonly utilised for optical detection and the conversion of light into photocurrent [53].

Generally, a PD employs a p-i-n or p-n junction to generate photoinduced charges. Analogous to LEDs, a photodiode typically comprises two semiconductor crystals that are doped p-type and n-type [93]. In a p-i-n photodiode, the depletion layer is expanded by incorporating an intrinsic or lightly doped semiconductor layer, for example, pure Silicon (Si), situated between the p and n doped semiconductor layers. The photon absorption, which contributes to the photocurrent can only happen within the depletion layer or in its vicinity, because of the absence of the accelerating electrical field outside the depletion layer.

In contrast to LEDs, which operate primarily under forward bias voltage, a PD utilises reverse bias to enhance its depletion layer [93]. This reverse bias serves several crucial functions: first, it increases the width of the depletion layer, thereby enlarging the area where photons can induce charge generation through the internal photoelectric effect. Second, it increases the electric field within the depletion layer, which accelerates the separation of charge carriers and lowers the likelihood of their recombination within this region.

Additionally, the expansion of the depletion layer reduces the junction's capacitance, which in turn influences the RC constant of the photodiode and its bandwidth [93]. It is worth noting that due to the inherently increased depletion layer width, p-i-n PDs are much more common than p-n PDs because they offer better responsivity and bandwidth, which is a vital requirement for OWC and VLC links.

Consequently, the bandwidth and the photodiode's responsivity can be tuned [93]. However, there is a limit to how much the reverse bias voltage can be increased, constrained by the maximum value known as the breakdown voltage. Beyond this point, there is an exponential increase in the dark current, even with minimal incident photon flux, which can lead to a rapid rise in temperature and potential damage to the photodiode if not properly managed.

The responsivity of a photodiode, denoted as R_{PD}, quantifies the photocurrent generated per unit of incident optical power by photons [93]. Responsivity typically varies with wavelength and is a characteristic parameter of the PD. Photons impinging on the PD are converted to the photocurrent solely within the depletion layer, provided that the photon's energy exceeds the semiconductor material's bandgap. The photodiode's responsivity is related to the quantum efficiency of PD η_{PD} ($0 \leq \eta_{\mathrm{PD}} \leq 1$), which is the probability that an incident photon will generate a charge carrier pair contributing to the photocurrent. This relation is given as [93]:

$$R_{\mathrm{PD}} = \eta_{\mathrm{PD}} \frac{q}{h\nu}, \tag{2.5}$$

here q is elementary charge, h is Planck's constant, ν is free space frequency of light. The generated photocurrent can be expressed as [53]:

$$I = P_{\mathrm{r,opt}} R_{\mathrm{PD}}, \tag{2.6}$$

where $P_{\mathrm{r,opt}}$ represents the optical power absorbed by the photodiode (PD) in the depletion layer and its vicinity, an area commonly referred to as the photoactive area.

While it might seem that improving the responsivity and photocurrent of a PD could be easily achieved by enlarging the depletion layer, this approach has a significant drawback [93]. Specifically, it considerably increases the charge transit time, adversely impacting the PD's response time and consequently reducing its bandwidth.

The aforementioned trade-off, coupled with the reality that p-i-n PDs operating in reverse bias mode can generate only a single electron-hole pair per photon (responsivity is less than 1 A/W) [93], poses significant challenges for their deployment in high-data-throughput free-space links due to the SNR constraints.

This limitation can be addressed through the development of APDs. An APD operates under a high reverse bias (up to 400 V in silicon-based devices [147]), utilising a strong electric field within the junction to accelerate the charge carriers [70, 93].

The fundamental operating principle of APDs lies in exploiting the avalanche gain resulting from impact ionisation [93]. This phenomenon occurs when photoinduced charged particles within the multiplication layer are accelerated to kinetic energies surpassing the semiconductor material's bandgap energy. Consequently, a charge carrier, either an electron or a hole, can generate an additional electron-hole pair upon colliding with another carrier. Given a sufficiently strong electric field, this can lead to an exponential increase in charge carriers, a process known as avalanche multiplication.

Ideally, an APD should be designed for single-carrier type multiplication, meaning that either electrons or holes alone are responsible for the avalanche process [93]. Mixed ionisation can lead to increased noise levels in the multiplication process, diminish the APD's bandwidth, and make the device more prone to unstable and damaging avalanche breakdowns. The parameter that characterises the type of ionisation occurring within an APD is known as the ionisation ratio, denoted by κ_{ion} and is defined as follows [93]:

$$\kappa_{\mathrm{ion}} = \frac{\alpha_{\mathrm{h}}}{\alpha_{\mathrm{e}}}, \tag{2.7}$$

where α_{h}, α_{e} are ionisation coefficients of holes and electrons respectively. The ionisation coefficient represents the average distances between consecutive ionisations.

In comparison to p-i-n and p-n diodes, APDs have non-unity gain M_{APD} due to the avalanche multiplication. For electron injection majority APDs the gain is given as [93]:

$$M_{\mathrm{APD}} = \frac{1-\kappa_{\mathrm{ion}}}{\exp\left(-(1-\kappa_{\mathrm{ion}})\alpha_{\mathrm{e}} l_{\mathrm{PD}}\right)-\kappa_{\mathrm{ion}}}. \tag{2.8}$$

Here l_{PD} is the thickness of multiplication layer of photodiode. For Si APDs the multiplication gain can reach up to 250, resulting in a high responsivity of up to 130 A/W for Si APDs [53]. The photocurrent of APDs is given by the following equation [53]:

$$I = P_{\mathrm{r,opt}} R_{\mathrm{APD,0}} M_{\mathrm{APD}}, \tag{2.9}$$

where $R_{\mathrm{APD,0}}$ is the responsivity of the APD at a unit multiplication gain.

One of the primary challenges associated with APDs arises from the presence of an additional time constant known as the avalanche buildup time [93]. This constant represents the time required for the avalanche process to occur and subsequently to settle down. Despite this challenge, recent literature and a variety of commercial products demonstrate the development of APDs with multiple GHz bandwidth, suitable for high-speed OWC or VLC systems.

APDs that are operated in Geiger mode, where a single incident photon is sufficient to initiate avalanche multiplication, are known as SPADs. [70, 93]. These devices and their required circuitry are extensively researched for use in Light Detection and Ranging (LiDAR) applications [148]. However, there has also been considerable recent research interest in exploring the potential use of SPADs in VLC and OWC applications [149].

VLC receivers primarily require the use of silicon-based photodiodes, such as p-i-n PDs, APDs, and SPADs, owing to their spectral sensitivity aligning better with the visible light spectrum range of $380-700$ nm [53]. For OWC receivers, silicon-based PDs are appropriate for wavelengths below 1100 nm [53]. However, for longer wavelengths—beyond 1100 nm-PDs made from materials like Indium Phosphide (InP), Indium Gallium Arsenide (InGaAs), or Germanium (Ge) are recommended [93].

2.3.9 Receiver Circuitry

For digital read-out, it is necessary to convert typically small photocurrent current into a readable amplified voltage [65]. While a simple solution involves connecting the PD to a load resistor to facilitate this conversion, this configuration, in practice, tends to suffer from reduced bandwidth and linearity. To overcome these limitations, a TIA is employed to convert the current into voltage [150].

A TIA typically comprises an Operational Amplifier (OP-AMP) and a feedback circuit. This feedback circuit includes a feedback resistor, which sets the TIA's gain, and a feedback (or compensation) capacitor, which governs the circuit's bandwidth and stability [150]. The OP-AMP, feedback resistor, and capacitor are connected in parallel, forming a low-pass filter that is essential for the stabilization of the TIA.

The output voltage signal from the TIA may then be further filtered using low-pass filters to eliminate high-frequency noise components [53]. Subsequently, the signal voltage can be additionally amplified by an RF amplifier.

The analogue voltage can ultimately be converted into a digital signal using an ADC [65]. The fastest commercially available ADCs can achieve a 12-bit resolution with a sampling rate of up to 10.4 GSPS in single-channel mode, or 5.2 GSPS in dual-channel mode [151]. Similar to DACs, high-speed ADCs exhibit high power consumption, which can reach up to 4 W [151]. ADCs are a crucial component in systems employing non-binary (multiple-symbol) modulation schemes.

2.3.10 Receiver Optics

In addition to optoelectronic elements, other optical front-end components are typically necessary. These may include concentration optics and optical bandpass filters, the latter of which serve to block out significant portions of background illumination [73].

Bandpass filters are commonly constructed from multiple thin dielectric layers, with the filtering effect resulting from optical interference, which depends on the incidence angle and wavelength of light [152]. The dependence on the incidence angle can shift the passband of the oblique incident light, a phenomenon known as passband shift [153].

A photoreceiver detects incident optical power, which is proportional to the effective light collection area of the PD. However, increasing the PD area is generally undesirable, which, as discussed, can result in a substantial decrease in the receiver's bandwidth [93].

Concentrating optics are often utilised to enhance the SNR for this very reason. These optics can be categorised as either imaging [53] or non-imaging [73]; imaging optics preserve the image of the incident radiance, whereas non-imaging optics do not.

Imaging optics, which commonly encompass types of convex, plano-convex, or aspheric lenses, are generally most appropriate for precisely aligned point-to-point links [53]. They characteristically exhibit a low Field-of-View (FoV), resulting in a narrow reception coverage area and a low tolerance for misalignment. However, high optical concentration can be achieved with a narrow FoV [154]. The smaller the photoactive area of the receiver, the lower its tolerance to misalignment becomes.

Increasing the tolerance to misalignment can be achieved by positioning the PD closer to the lens's exit aperture, at a point where the concentrated rays have not yet converged to a single (focal) point [67]. However, this adjustment leads to a trade-off where the photon energy density reaching the PD's photoactive area is reduced, resulting in a diminished optical concentration gain [155].

Alternatively, non-imaging concentrators have been frequently considered for OWC and VLC links [73]. Various types of non-imaging concentrators suitable for communication links include hemispherical lenses [73], Compound Parabolic Concentrators (CPC) [156], Dielectric Totally Internally Reflecting Concentrators (DTIRC) [157], Total Internal Reflection (TIR) lenses [158], and Köhler concentrators [159]. Generally, non-imaging optics offer a better trade-off between optical concentration and FoV, which is limited by their acceptance half-angle Ψ_{c} [53].

Additionally, one can increase the received optical signal power while maintaining the required bandwidth by arranging PDs in $N \times N$ arrays [146]. Such an arrangement can significantly relax the FoV constraints for the required SNR, which is crucial for high data throughput links in free space.

However, as we will show later, this approach introduces new challenges in the design of concentrating optics. The limitations of these, particularly CPCs, are discussed more in detail in Chapter 6, which also explores how novel receiver optical concentrating elements designed based on freeform optics, can offer advantages for high data throughput in OWC and VLC receivers.

2.4 Channel Modelling

So far, we have discussed the opto-electronic front-end elements; however, another crucial component of an OWC or VLC link is the optical channel itself, through which the modulated light signal propagates. Generally, as previously mentioned, an optical channel can be wired or wireless, LoS or NLoS, and it may operate in various environments such as indoor, atmospheric, underwater, or even extraterrestrial settings [53].

An optical channel is characterised by its channel impulse response, denoted as $h(t)$ [53]. In LoS links, which are the primary focus of this work, an optical channel acts as an attenuator of the light signal. Furthermore, in IM/DD OWC or VLC links, the high-frequency nature of the optical carrier itself (i.e., the wavelength of light) can be disregarded. The relationship between the received and transmitted signals, y and x, are characterised by the following equations [53]:

$$\begin{aligned} y_{\mathrm{s}}(t) &= R_{\mathrm{PD}} x_{\mathrm{s}}(t) \circledast h(t) + n(t) \\ &= \int_{-\infty}^{+\infty} R_{\mathrm{PD}} x_{\mathrm{s}}(\tau) h(t-\tau) d\tau + n(t), \end{aligned} \tag{2.10}$$

here $n(t)$ is AWGN and $\circledast$ symbolises convolution operation. The DC channel gain $h(0)$ is given by [53]:

$$h(0) = \int_{-\infty}^{+\infty} h(t) dt. \tag{2.11}$$

In short-distance scenarios characteristic of most indoor LoS environments, multipath dispersion can be ignored and the channel gain can be considered as a frequency-independent linear attenuation coefficient. In such cases, $h(0) = h$, and the impulse response simplifies to the following [53]:

$$h(t) = h\delta(t - \frac{d}{c}), \tag{2.12}$$

here d represents the distance from the transmitter to the receiver, δ is the Dirac delta function and c is the speed of light.

VLC channels are often modelled based on the principle of Lambertian emission.

In addition, non-imaging concentrators equipped with optical filters are used to block unnecessary background radiation. This model assumes the use of a single PD for signal reception [53]:

$$h = \begin{cases} \frac{(m_{\mathrm{LED}}+1)}{2\pi d^2} \cos^{m_{\mathrm{LED}}}(\varphi) A_{\mathrm{PD}} \cos(\psi) G_{\mathrm{filter}}(\psi, \lambda) G_{\mathrm{con}}(\psi) & \psi \leq \Psi_{\mathrm{c}} \\ 0 & \psi > \Psi_{\mathrm{c}} \end{cases}, \tag{2.13}$$

here $G_{\mathrm{filter}}(\psi, \lambda)$ characterises the transmissivity of the optical filter, $G_{\mathrm{con}}(\psi)$ is the non-imaging concentrator gain, ψ is the incidence angle of the light beam relative to the surface normal vector of receiver.

This model, however, is limited to Lambertian emitters (primarily LEDs), thus its applicability to OWC where Gaussian sources (laser diodes and VCSELs) are prevalent is constrained. In cases of OWC, Gaussian beam models [93] or ray tracing [67] simulations can be employed to determine the channel gain. In our work, we opt for the latter. Furthermore, this model overlooks the irradiance and radiance characteristics at the PD and optical concentrator interface. Additionally, the model is restricted to a single PD; the introduction of an array of PDs necessitates an irradiance analysis at the concentrator array interface. This is discussed in more detail in Chapter 6.

2.5 Photodetection Noise

Every optical channel is inherently noisy. It is a well-known fact that the channel capacity is fundamentally limited by noise, as stated by the Shannon-Hartley theorem [160]. Therefore, it is critical to identify and model the noise sources in the telecommunication link.

In OWC and VLC, one of the main sources of noise originates from the statistical nature of incident photons at the PD [53]. This is known as shot noise. As we already understand, a PD utilises the photoelectric effect to generate photocurrent, through the absorption of photons and the excitation of electron-hole pairs. However, while the mean arrival rate of photons per unit area and time at the depletion layer is constant, the instantaneous flux of photons is fundamentally nondeterministic. This is a consequence of the Heisenberg uncertainty principle, particularly the energy-time uncertainty [161]. Consequently, the photon arrival rate is described by Poisson statistics [53].

Another source of shot noise arises from background radiation, which can also contribute to charge carrier generation but carries no useful information [53]. For this reason, particularly in VLC links, optical bandpass filters are employed to reduce the total flux of incident background radiation at the PD.

Owing to Poisson statistics, the variance of the number of photons arriving at a time instant t is equal to the mean photon arrival rate. When this is converted to photocurrent without avalanche multiplication, as in the case of p-i-n PDs, this leads to a shot noise variance of [53]:

$$\sigma^2_{\text{shot,PIN}} = 2q\langle I\rangle B, \tag{2.14}$$

where $\langle I\rangle$ denotes the mean generated photocurrent and B represents the bandwidth. For ADPs the noise arising from the random nature of avalanche multiplication should also be considered. In such cases, the shot noise variance is [53]:

$$\sigma^2_{\text{shot,APD}} = 2q\langle I\rangle M^2_{\text{APD}} F_{\text{APD}} B, \tag{2.15}$$

here F_{APD} is the excess noise factor. Excess noise is defined as the ratio of the mean square avalanche multiplication gain $\langle M^2 \rangle$ to the mean gain. The excess noise factor is related to the ionisation ratio κ_{ion} and the multiplication gain M through the following equation [53]:

$$F_{\text{APD}} = M_{\text{APD}}\kappa_{\text{ion}} + (2 - \frac{1}{M_{\text{APD}}})(1 - \kappa_{\text{ion}}). \tag{2.16}$$

Different semiconductor materials exhibit varying excess noise factors due to different ionisation ratios. For instance, silicon has a very low ionisation ratio (about 0.02), indicating that avalanche multiplication is mediated almost exclusively by electrons [93]. This results in typical excess noise factors ranging from 3 to 4.9 for gains of 150 to 500. In contrast, germanium has an ionisation ratio close to unity (about 0.9), meaning that both electrons and holes contribute nearly evenly to the avalanche multiplication. This leads to a much larger excess noise factor of about 9.2 for a typical gain of 10. Consequently, Si APDs have found widespread application, while Ge APDs have not.

The background illumination shot noise can be expressed as for p-i-n PDs as [53]:

$$\sigma^2_{\text{bcg,PIN}} = 2qP_{\text{r,bcg}}R_{\text{PD}}B, \tag{2.17}$$

where $P_{\text{r,bcg}}$ optical power from the background radiation. For the APDs the background shot noise is [53]:

$$\sigma^2_{\text{bcg,APD}} = 2qP_{\text{r,bcg}}R_{\text{PD}}M^2_{\text{APD}}F_{\text{APD}}B. \tag{2.18}$$

Another source of noise in the receiver circuit is thermal Johnson–Nyquist noise, attributable to the thermal fluctuations of electrons [53]. The current variance due to thermal noise is given by the following equation [53]:

$$\sigma^2_{\text{T}} = \frac{4k_{\text{B}}TB}{R_{\text{load}}}, \tag{2.19}$$

here T is the receiver circuit temperature, k_{B} is the Boltzmann constant and R_{load} is the load resistance of the receiver circuit.

The last major noise source in OWC and VLC receiver circuits is the input-referred current noise, σ^2_{TIA} of a TIA [162]. The primary contributor to noise at low frequencies is flicker noise (also known as $1/f$ noise), which is inversely dependent on the signal frequency f. At high frequencies, the thermal noise of the TIA circuit, proportional to f^2, becomes dominant. The input referred current noise density N_{TIA} is usually specified in TIA datasheets in terms of pA/$\sqrt{\mathrm{Hz}}$. The TIA input noise variance then can be calculated as:

$$\sigma^2_{\mathrm{TIA}} = N^2_{\mathrm{TIA}} B. \tag{2.20}$$

Due to the additive properties of Gaussian distributions, we can sum all the noise contributions to estimate the total noise variance [53]. For p-i-n PDs, the total noise variance is calculated as follows:

$$\sigma^2_{\mathrm{PIN}} = N_0 B = 2q\langle I\rangle B + 2qP_{\mathrm{r,bcg}} R_{\mathrm{PD}} B + \frac{4k_{\mathrm{B}}TB}{R_{\mathrm{load}}} + N^2_{\mathrm{TIA}} B, \tag{2.21}$$

where N_0 is the power spectral density of the total noise. For the APDs we get:

$$\sigma^2_{\mathrm{APD}} = N_0 B = 2q\langle I\rangle M^2_{\mathrm{APD}} F_{\mathrm{APD}} B + 2qP_{\mathrm{r,bcg}} R_{\mathrm{PD}} M^2_{\mathrm{APD}} F_{\mathrm{APD}} B + \frac{4k_{\mathrm{B}}TB}{R_{\mathrm{load}}} + N^2_{\mathrm{TIA}} B. \tag{2.22}$$

2.6 Modulation Schemes

In OWC and VLC, modulation schemes are primarily based on IM-DD [53]. These schemes can be either single-carrier or multi-carrier, consisting of only one carrier or multiple subcarriers within a data frame, respectively. Furthermore, while data in OWC and VLC can be modulated using analogue intensity modulation techniques, such as frequency modulation (FM) and amplitude modulation (AM), digital baseband techniques are more prevalent in VLC and OWC [2] [53]. The preference for digital baseband techniques stems from the previously discussed non-linearity of LEDs and VCSELs at high biasing currents, which leads to harmonic and intermodulation distortions. These distortions are more pronounced with continuous analogue modulation signals compared to discrete digital ones [53, 65].

Single Carrier Modulation Schemes

In a Single Carrier Modulation scheme (SCM), transmitted information bits are modulated onto a single frequency carrier [53]. Various well-known digital SCMs can be applied to VLC and OWC links. For example, in IM/DD, information can be encoded in multiple intensity levels of optical source emission, as seen in Pulse Amplitude Modulation (PAM) [164]. Other methods include Pulse Width Modulation (PWM) [165] and Pulse Position Modulation (PPM) [166], where pulses are typically rectangular in shape. If alternative waveforms, such as sine waves, are used, other symbol parameters can be employed. These include phase and quadrature, which form the basis for Quadrature Phase Shift Keying (QPSK) [167] and, when combined with multiple amplitude levels, Quadrature Amplitude Modulation (QAM) [168].

The simplest modulation scheme within this category is On-Off Keying (OOK) [169], where the information directly modulates the intensity of the LED or VCSEL by switching between two states – 'on' and 'off' or 'high' and 'low'. This modulation scheme is binary, represented by two states. As previously discussed, such modulation

[2]The namesake of digital baseband techniques comes from the fact that the data in this schemes is not translated to a much higher frequency before intensity modulation and the spectrum of the modulated data is within the vicinity of DC (direct current) [163].

schemes can drive optical sources without requiring a DAC. Furthermore, a simple Class-D amplifier can be employed for the transmitter driver circuitry [170].

When considering a high data throughput link, high bandwidth and high spectral efficiency are generally desirable. Often, this leads to a trade-off between the two, as demonstrated in the following well known Hartley's law [171]:

$$C_{\text{data}} \leq 2\log_2(M)B = 2\eta B, \tag{2.23}$$

where C_{data} is the data throughput, η represents the spectral efficiency represented by bit/s/Hz while B is the single sided modulation bandwidth and M is the number of constellation points.

Depending on the targeted data throughput and link parameters, the bandwidth or energy budget of the link may be limited. In such scenarios, a high spectral efficiency and an advantageous SNR versus Bit Error Ratio (BER) trade-off for a given spectral efficiency are crucial in selecting a modulation scheme. However, many Single Carrier Modulation schemes (SCMs) may fail to meet these requirements due to either low achievable spectral efficiency or a poor SNR versus BER trade-off [53]. A prime example of the first case is OOK, where the spectral efficiency is limited to just $\eta = 1\,\text{bit/s/Hz}$, leading to very high bandwidth requirements to achieve high data throughput [53].

The latter case is exemplified by PAM. While PAM allows for arbitrarily high spectral efficiency, a significant drawback emerges: within the limited linear region of the optical source, the density of the symbols rapidly increases with increasing spectral efficiency due to the nearest number of neighbouring symbols being limited to 2 [65]. This leads to diminished mutual Euclidean distances between symbols, resulting in a rapid increase in BER for a given SNR as the spectral efficiency increases making the modulation scheme being best suited for high SNR links.

One way to address this challenge is to exploit different parameters of the symbols, instead of relying solely on amplitude. For instance, significantly improved BER versus SNR performance for a given spectral efficiency can be achieved using QAM [53]. In QAM, various quadrature phase shifts are used to enhance spectral efficiency without increasing the symbol density within the amplitude domain [172]. However, this approach has a drawback: it is sensitive to timing jitter [173] and Intersymbol Interference (ISI) [174], issues that become more pronounced at higher bandwidths.

Multi Carrier Modulation Schemes

As mentioned in the previous chapter, most SCM schemes either suffer from low achievable spectral efficiency, poor BER versus SNR performance, or are limited by jitter and ISI, thus hindering their capability to support very high data throughput solutions. A commonly employed method to address these challenges is the use of Multi-Carrier Modulation (MCM) techniques, which, as the name suggests, involve the use of multiple carriers within a data frame [65]. In MCM, multiple modulated RF sub-carriers are combined into a single waveform, which then modulates the optical source. The most frequently used schemes in MCM are based on OFDM [65].

OFDM, a group of MCM schemes, is the most utilised solution for high data throughput and Intersymbol Interference ISI robust applications in both RF (IEEE 802.11 standard) [175] and OWC/VLC [176]. The fundamental concept of OFDM most frequently involves transmitting data in parallel using QAM modulated sub-carriers through frequency division multiplexing [177]. In essence, OFDM divides the available spectrum into N sub-carriers. Since each sub-carrier is narrowband (occupying $1/NT$ bandwidth, where T is the length of the OFDM frame) and experiences nearly flat fading, OFDM systems facilitate simple equalisation. The orthogonality and robustness against ISI of the sub-carriers are achieved through the use of Fast Fourier Transform (FFT) and a Cyclic Prefix (CP) [177]. Furthermore, the performance of OFDM links can be enhanced by employing adaptive bit loading techniques, such as the Levin-Campello algorithm [178].

The implementation of OFDM in OWC and VLC communication systems imposes an additional constraint that the time-domain signal must be both real-valued and unipolar [176]. To ensure the signal is real-valued, Hermitian symmetry must be imposed on an OFDM frame [176]. Two methods commonly used to achieve a unipolar signal in OWC and VLC are Direct Current Biased Optical OFDM (DCO-OFDM) and Asymmetric Clipping Optical OFDM (ACO-OFDM) [179].

In the former method, DCO-OFDM, a DC bias is applied to ensure that all information carrying sub-carriers are positive valued [179]. In contrast, ACO-OFDM enables only the odd sub-carriers while setting the even sub-carriers to zero [179]. The use of DC bias in DCO-OFDM increases the Peak-to-Average Power Ratio (PAPR) of the link, significantly reducing its energy efficiency [125]. ACO-OFDM, although avoiding DC bias and having a lower PAPR, comes with the trade-off of reduced spectral efficiency, as only the odd sub-carriers are used to carry data, effectively halving it [125, 179].

Furthermore, due to the high PAPR in OFDM, selecting the appropriate biasing point becomes particularly important, as the linear range of most optical sources is limited either by their inherent linear range or by laser eye safety constraints [125]. To avoid distortions, the OFDM signal should be clipped at certain power levels. However, the clipping process itself can introduce additional distortions; therefore, a careful selection of both biasing and clipping points is required [125].

While recent advancements in OFDM have significantly contributed to achieving high data throughput links in free-space optical OWC/VLC systems, the main drawback is achieving high energy efficiency. OFDM systems heavily rely on power amplifiers, which are known to struggle with energy efficiency [129], exacerbated by the typically high PAPR of DCO-OFDM or the reduced spectral efficiency of ACO-OFDM [125]. Although other OFDM schemes exist that circumvent these limitations [180–183], they suffer from high computational and implementation complexity.

Multiple-input-multiple-output (MIMO) Schemes

An alternative approach to improving energy efficiency while maintaining high data throughput is to exploit channel diversity and multiplexing gains using MIMO transmission techniques, which involve the use of multiple transmitters and receivers within the link [184].

The most basic MIMO technique, applicable to both RF and OWC/VLC systems, is Repetition Coding (RC) [185, 186]. In this technique, the same signal waveform is simultaneously transmitted by multiple synchronised transmitters, resulting in amplified signal strength at the receivers. The spectral efficiency of the RC technique is determined by the spectral efficiency of the individual signal, which is $\eta = \log_2(M)$.

Alternatively, to increase data throughput different independent signal streams can be transmitted over a MIMO channel, a technique known as Spatial Multiplexing (SMP) [187]. Here N_t transmitters are used for N_t independent data transmission streams. In comparison to RC, SMP achieves a spectral efficiency of $\eta = N_\mathrm{t} \log_2(M)$.

Spatial Modulation (SM) is another MIMO technique that, in addition to the signal domain, utilises the spatial domain to encode information [188]. It leverages varying channel gains across different pairs of transmitters and receivers. This capability enables SM to achieve a spectral efficiency of $\eta = \log_2(N_\mathrm{t}) + \log_2(M)$. During SM transmission, only a single transmitter out of N_t is active. For instance, a 4-transmitter SM link employing 4-Pulse Amplitude Modulation (4-PAM) can achieve a spectral efficiency of $\eta = 4\,\mathrm{bit/s/Hz}$, where 2 bits represent the activated transmitter, and the other 2 bits represent the PAM level transmitted by the active transmitter.

SM can be further extended to Generalised Spatial Modulation (GSM), where multiple transmitters can be simultaneously active during symbol transmission [189]. In this modulation scheme, the number of possible activation combinations of transmitters is $2^{\mathrm{N_t}}$. Therefore, Generalised Spatial Modulation (GSM) can achieve a maximum spectral efficiency of $\eta = N_\mathrm{t} + \log_2(M)$.This means that, as per the previous example, GSM can achieve the same spectral efficiency as Spatial Modulation (SM) with only half the number of transmitters. However, the drawback is that GSM is more prone to Inter-Channel Interference (ICI) and produces a higher decoding complexity compared to SM.

A specific case of GSM, where the signal domain is represented by a binary modulation (such as OOK), is known as Generalised Space Shift Keying (GSSK) [190]. This MIMO modulation technique will be discussed in more detail in Chapter 3.

2.7 Power Consumption Modelling

The power consumption of an OWC or VLC link is a paramount benchmark parameter in the context of next-generation green communication [50]. Generally, the power consumption is proportional to the bandwidth of the link [191]. Consequently, links with very high data throughput are expected to have higher power consumption, whereas those with low data throughput will experience significantly lower power consumption. Therefore, to effectively compare the performance of these links against other communication systems, such as RF based ones, it is more practical to use energy efficiency as a metric [192].

The energy efficiency, denoted as EE characterises the amount of energy required to transmit a unit of data (bit) for a given data throughput (or channel capacity) C in the link can be expressed as follows [192]:

$$\mathrm{EE}(B) = \frac{\mathrm{P}_{\mathrm{link}}(B)}{C(B)}, \tag{2.24}$$

where P_{link} is the total power consumption of the link, which includes receiver, transmitter optoelectronic front-end, DSP and networking layer power consumption.

The link power consumption can be divided into two analogue and digital part [191]:

$$P_{\mathrm{link}}(B) = P_{\mathrm{a}}(B) + P_{\mathrm{d}}(B), \tag{2.25}$$

where P_{a} represents the power consumption of analogue or optoelectronic front-end devices in the link, and P_{d} denotes the digital power consumption arising from DSP and networking layer processing.

Generally, modelling the digital power consumption is quite challenging, as it can depend on various factors, such as the implementation and optimisation of DSP, the energy efficiency of the signal processing device (for example, on a Field Programmable Gate Array or FPGA for short), which can vary significantly from device to device, and the networking layer protocols and algorithms, among others.

For the evaluation of physical layer performance, the analogue component is as important, if not more so, than the digital one. By assessing the power consumption of the analogue component, one can determine the lower limit of power consumption (or the upper limit of energy efficiency). Such an assessment can be instrumental in determining whether the optoelectronic design under investigation is feasible for the targeted energy efficiency and data throughput. This approach offers significant merit, as while one can optimise the algorithms and implementation of DSP and the networking layer to enhance energy efficiency, the overall improvement will be constrained by the energy efficiency of the physical layer.

The analogue power consumption for a typical OWC and VLC system can be straightforwardly decomposed as follows [193]:

$$P_{\mathrm{a}}(B) = P_{\mathrm{TX}}(B) + P_{\mathrm{RX}}(B) = P_{\mathrm{ADC}}(B) + P_{\mathrm{DAC}}(B) + P_{\mathrm{emit}} + P_{\mathrm{TX,driver}} + P_{\mathrm{TIA}}, \quad (2.26)$$

here $P_{\mathrm{ADC(DAC)}}(B)$ is the power consumption of ADC (DAC), $P_{\mathrm{emit}}(B)$ is the power consumption of optical source, $P_{\mathrm{TX,driver}}(B)$ is the power consumption of TX driver and P_{TIA} is the power consumption of TIA.

2.8 Summary

In this chapter, the concepts of OWC and VLC are introduced. We provide a detailed description of the essential optoelectronic front-end elements and principles behind their operational modes for both the transmitter and receiver ends. Furthermore, we analyse the channel modeling and identify sources of photodetection noise. We also delve into a discussion of both single-carrier and multi-carrier digital modulation techniques employed in OWC and VLC. Additionally, we present various MIMO techniques. Finally, we examine power consumption modeling.

Chapter 3

Adaptive Generalised Space Shift Keying (GSSK) Algorithms

3.1 Introduction

An VLC or OWC system can employ incoherent light sources such as LEDs [53, 194], micro-LEDs [64,109,195,196] or VCSELs [44,53,197] in IM/DD techniques. One of the main requirements for these wireless communication systems is high data throughput (in multiple Gbit/s). Experimental VLC demonstration of up to 15.73 Gbit/s aggregate data rate using WDM has been presented in [45] using off-shelf components. More recent research has achieved a remarkable aggregate data rate of 28.93 Gbit/s in WDM link by utilising a single-chip silicon substrate LED array within a free-space communication link [198].

In OWC data transmission rates of up to 37.4 Gbit/s per channel and an aggregate capacity of 224 Gbit/s have been achieved over a distance of 3 m using WDM and a holographic beam steerer as shown in [199]. Additionally, data throughput of up to 400 Gbit/s has been reported in [200] a fibre-wireless-fibre link where both transmitter and receiver are steered. The highest up to date aggregate data rate surpassing 1 Tbit/s over 3.5 m distance is demonstrated utilising a ten-channel WDM OWC link [201].

Another crucial benchmark parameter for OWC and VLC links, especially in the framework of green communication technology, is energy efficiency [50, 202–204].The concept of energy efficiency concerns the capacity of a modulation scheme utilised in the physical layer of choice to transmit data at a specified throughput level in relation to the amount of energy it consumes [192]. A wide array of research topics encompass the endeavour of the energy efficiency enhancement of VLC and OWC links.

At the physical layer the energy efficiency can be advanced through various means. Firstly, one such avenue involves the design of transmitter optical sources in the chip and optics level to attain higher electrical-to-optical conversion efficiency [50, 205, 206]. This entails maximizing the amount of optical power generated for a given amount of electrical power input with related concept of external quantum efficiency [205]. Secondly, developing photodetectors and their associated optics and circuitry to optimise responsivity and signal amplification while constraining the power consumption [50, 67, 207–210]. Furthermore, modulation techniques and modulation bandwidth plays pivotal role in determining the overall energy efficiency of the communication link [50, 211, 212]. The factors collectively influence how effectively data can be transmitted while minimizing power consumption [50].

A comprehensive scope of research has been applied on the concurrent enhancement of the spectral and energy efficiency within the domain of VLC and OWC systems [213]. Of notable interest is the exploration of multi-carrier modulation techniques such as optical orthogonal frequency division multiplexing (O-OFDM) [214]. Modulation techniques such as DCO-OFDM [215], ACO-OFDM [216], Unipolar OFDM (U-OFDM) [181], Flip Orthogonal Frequency Division Multiplexing (FLIP-OFDM) [217], enhanced Unipolar OFDM (eU-OFDM) [182] and Pulse-Amplitude Modulation Discrete Multitone Modulation (PAM-DMT) [218], as well as hybrid OFDM techniques combining multiple basic OFDM schemes [214].

However, it is essential to consider that the implementation of multi-carrier modulation techniques necessitates the incorporation of comparatively advanced transmitter driver circuitry, encompassing voltage amplifiers and DAC, along with sophisticated DSP circuitry. The complexity of the transmitter opto-electronic front-end and DSP can exhibit a notable increase in power consumption within the communication link, especially when dealing with higher modulation bandwidths [89, 194].

One effective strategy, which can enhance the spectral efficiency while maintaining a constant modulation order (potentially decreasing it) within the electrical domain of the transmitter signal involves utilisation of MIMO based transmission techniques. The techniques leverage the spatial diversity and array gain by employing multiple transmitters and receivers [184]. MIMO techniques, whether in the RF or in the optical domain can exploit differences in DC optical channel gains of various transmitter and receiver pairs. The channel differences are characterised by the channel correlation [219].

A classic example of such a MIMO modulation scheme, which exploits differences in DC channel gains is SM [188]. Within the SM framework the encoding of transmitted bits involves a distinct mapping to a active a specific beam pattern. A beam activation pattern is described by a set of transmitter beams in either "on" or "off" state. Each pattern can transmit a waveform of an electrical domain signal associated with a constellation point derived from the selected modulation, such as PAM or QAM. In the context of SM it is important to note that within the beam activation pattern only a single transmitter beam can be in "high" state while all others remain in the "low" state. In such transmission, the binary digits are encoded in the particular beam activation pattern of the singular activated beams and in the signal transmitted by them.

GSM [189] is a type of SM, where multiple transmitter beams within the beam activation pattern can be simultaneously active in "high" state. While in "high" state they all simultaneously transmit the same signal waveform. In such case the binary bits are encoded both in the particular activation pattern of multiple active beams and in the signal waveform transmitted by them.

A distinct variant of SM, which exclusively maps transmitted bits to a unique beam activation pattern while restricting the electrical domain signal constellation points to binary levels ("high" and "low") is called Space Shift Keying (SSK) [220]. In essence, SSK entails a single transmitter transmitting an OOK signal in the electrical domain. However, due to the different DC channel gains between different receiver pairs, multi-level signal levels emerge at the receivers in the electrical domain. SSK possesses a significant advantage over SM, characterized by reduced computational complexity and resilience to non-linearity effects exhibited by transmitters such as LEDs [113]. However, SSK's spectral efficiency is constrained by the logarithm of the number of beams, rendering it primarily suitable for applications with moderate target data rates [220].

Enhanced spectral efficiency compared to SSK can be achieved through the utilisation of combinations involving multiple concurrently active beams in high state, resulting in what is referred to as GSSK [190]. Notably, an experimental demonstration has showcased a spectral efficiency of up to 16 bits per symbol in GSSK link [221]. SSK and GSSK, in general, do not necessitate the use of a DAC for the data transmission as the transmitter circuitry can be directly driven by a digital voltage source output pin such as FPGA [222]. This, in turn, substantially reduces complexity of the driver circuitry and can be utilised to boost energy efficiency of the communication link.

Numerous theoretical and empirical investigations have been conducted on the incorporation of GSSK in VLC and OWC systems [45, 221, 223, 224]. The studies encompass a range of aspects, such as the selection of transmitter beam sets [225] and adaptive GSSK modulation to accommodate dynamic channel conditions [226]. However, a comprehensive evaluation of the performance of an adaptive GSSK link in the context of indoor VLC and OWC scenarios, with a focus on high data throughput (multiple Gbit/s) and high energy efficiency ($\approx 1\,\mathrm{nJ/bit}$) implementation is lacking. Furthermore, such an evaluation has yet to be conducted utilising off-the-shelf component models to determine the feasibility of adaptive GSSK for next generation high data throughput applications within the green communications framework.

An adaptive GSSK algorithm is tested with various transmitter beam selection criteria such as maximal minimal Euclidean distance and maximal SNR. Additionally, we introduce a method for transmitter beam selection based on an optimal GSSK channel ratio condition, which we elaborate on in this study. We compare the performance of adaptive GSSK using different transmitter beam set selection criteria within a VLC angle diversity hemispherical transceiver model. This model is designed to represent a free space indoor mobile use case. The transmitter and receiver front-end are selected to maximise the data throughput with the set target of 10 Gbit/s. We evaluate and compare the 3 adaptive GSSK transmitter beam set selectors in terms of the mean data throughput achieved in the indoor scenario. The evaluation and comparative analysis of the computational complexity is conducted to offer estimates for the approximate lower latency bound linked to each transmitter beam set selector.

Furthermore, we present an OWC directional device-to-device communication scenario set at 1 m transmitter-receiver distance and $20 \times 20\,\mathrm{cm}^2$ target area at the receive plane. Here transmitter beams are arranged in symmetrical square lattices. Within this framework we explore two distinct scenarios concerning the arrangement of transmitter beams: namely, close spacing and sparse spacing.

In the first configuration we seek to replicate the conditions of a small form factor device as a transmitter such as a smartphone, where transmitter beam sources, for example, VCSELs are densely clustered. We make the assumption that a passive beam shaping devices, such as optical wedge prisms, are applied to modify the irradiance patterns of these beams at the receive plane. No active beam shaping or steering is assumed.

On the other hand, the second configuration concerns a larger form factor device for the transmitter end, such as a display. Here the transmitter beam sources are positioned at greater distances from each other, and no beam shaping or steering mechanisms are employed.

In both scenarios, we carefully select the transmitter and receiver off-the-self front-end components for OWC-type communication. The target minimum data throughput is set to be same as in the VLC scenario. We subsequently compare the performance of these scenarios in terms of mean data throughput within the defined coverage radius of the target area in the receive plane. Our investigation encompasses the testing of various numbers of transmitter beams within the grid and different spacing intervals between them, providing a comprehensive analysis of their impact on performance.

Lastly, our study evaluates the energy efficiency for both OWC and VLC scenarios based on the off-shelf opto-electronic components. Furthermore, a comparative analysis of energy efficiency is provided for the OWC device-to-device link scenario. Here, the energy efficiency of adaptive GSSK link is compared to QAM and DCO-OFDM links designed to operate with the same opto-electronic front-end components.

3.2 Generalised Space Shift Keying

In the existing body of literature there are two primary definitions of GSSK. The first interpretation involves binary encoding of the symbols within the beam activation pattern wherein a fixed number of beams are concurrently active [190]. Conversely, the second interpretation diverges by considering the number of active beams in the beam activation pattern as variable, encompassing both indices of active and inactive beams [223]. In the latter technique the spectral efficiency of the link exhibits proportionality to the overall count of beams engaged in the link.

In GSSK the data transmission exclusively leverages symbols within the spatial domain. The data encoding is achieved by utilisation of various beam activation patterns, wherein each unique pattern corresponds to a symbol within the constellation space. Each of these beam patterns encompasses a multitude of active and inactive transmitter beams. In the depicted activation pattern, every transmitter beam is associated with a designated index. This index is directly mapped to the respective bit position within the data transmission symbol as illustrated in Figure 3.1. Contingent upon whether the i^{th} bit b_i assumes a binary state of “1” or “0”, the i^{th} transmitter beam emits optical power P_i that corresponds to either a ”high” or ”low” magnitude such that:

$$P(b_i) = \begin{cases} P_{\text{H}} & b_i = 1 \\ P_{\text{L}} & b_i = 0. \end{cases}$$

In this work we are adopting the GSSK definition as outlined in [223] where the number of active and inactive transmitter beams within the beam activation pattern varies. Within this definition the total count of existing beam activation patterns equals to 2^{N_t}, where N_t denotes the count of transmitters participating in the communication link. Each of these activation patterns effectively serves as a constellation point, which

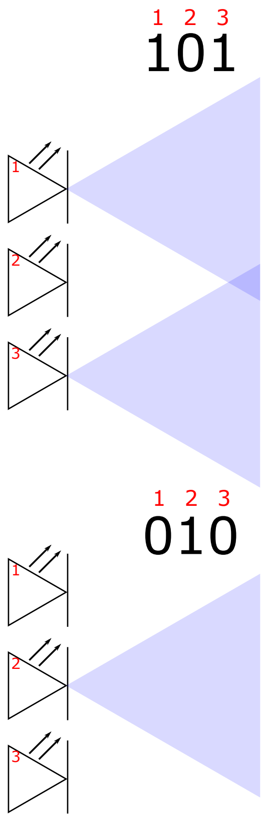

Figure 3.1: GSSK Encoding: In this representation, transmitters are identified by red indices, which correspond to specific bit positions within the data symbol. Depending on whether the associated bit holds a logical "1" or "0" value, the transmitter emits "high" or "low" optical power.

subsequently maps to a corresponding electrical domain constellation point as reconstructed at the receiver. This mapping results in a linear relationship between spectral efficiency and the number of engaged beams.

The bit error performance of GSSK is contingent on the Euclidean distance between mutually distinct activation patterns observed at the receivers [225]. This dependence is subject to the optical DC channel gain difference between different transmitter-receiver pairs in a MIMO channel, which determines their distinguishability.

The imposition of a minimum Euclidean distance poses constraints on the density, range and coverage of optical link deployment, particularly when dealing with compact devices of limited form factor. Consequently, it proves advantageous in the deployment of GSSK-based communication systems to incorporate angle or spatial diversity techniques [227, 228]. An approach to address these limitations can involve distribution of transmitter beams and receivers uniformly across the hemispherical surfaces [229]. Additionally, further improvements can be realized by incorporating optical bandpass filters into the system [73].

Another crucial factor influencing error performance in GSSK systems is the choice of the plurality of engaged beams for beam activation patterns [229]. A major part of up-to-date theoretical research and experimental investigations concerning SSK and related modulation schemes have predominantly employed a complete set of a predetermined transmitter beams and receivers.

However, there exist instances and situations that frequently arise where the set of accessible transmitter beams and receivers can undergo substantial alterations. Such changes might manifest when, for instance, a sudden obstruction partially blocks the communication path. Alternatively, receivers positions or orientations with respect to the transmitters may evolve over time. In such situations, it is conceivable that a portion or even the entirety of the initially available transmitters could shift out of the receivers' FoV. This dynamic mobility scenario typifies use cases where receiving User Equipment (UE) such as smartphone, is in motion relative to the transmitter Access Point (AP) or other user devices.

Furthermore, contingent upon the prevailing channel conditions, it may be advantageous to activate only a subset of the available transmitter beams to enhance the mutual Euclidean distance between distinct beam activation patterns. Conversely, there may also be cases where the opposite holds true and the channel supports engagement of an expanded set of available transmitter beams.

Hence, to ensure reliable communication with GSSK in non-stationary settings, the adoption of a location and channel condition adaptive method for selecting engaged beam sets becomes a critical necessity. The method should construct an adaptive codebook of beam activation patterns. Such adaptability is required to ensures the system's robustness when confronted with dynamic changes in the transmission environment and receiver mobility.

The exploration of adaptive codebooks in MIMO transmission has been extensively investigated within the realm of RF communication, as evidenced by previous studies such as [230] and [231]. This area of research can be also categorised under the domain of link adaptation [232]. Adaptive MIMO RF codebook schemes have been devised to address the challenges posed by time-varying channel distributions. For instance, within the 802.16m standard, adaptive codebook methods are considered to tackle dynamic channel conditions. These codebooks dynamically adjust the distribution of codewords in accordance with channel statistics, which are characterized by the transmit covariance matrix that describes spatial correlations across antennas [233].

In the domain of MIMO SM, the pursuit of link adaptation can be approached from various angles. One avenue involves the utilisation of antenna selection techniques, as proposed in [234], where antennas are chosen based on either optimized Euclidean distance or optimized channel capacity criteria.

Another strategy involves the implementation of adaptive modulation, as presented by Yang in [235], which employs a Modulation Order Selection Criterion (MOSC) algorithm based on maximizing the minimum Euclidean distance. Antenna selection and adaptive modulation, can be combined, as exemplified in Yang's subsequent work detailed in [236]. There adaptive modulation, transmit mode switching techniques are integrated into Optimal Hybrid-SM (OH-SM).

Further investigations in the field of adaptive SM are endeavors encompassing constellation optimization [237], randomization [238], power allocation [239], and transmit precoding algorithms [232]. These efforts primarily aim at achieving BER minimization and complexity reduction.

In the realm of adaptive SSK techniques, Chung and Hung approached multi-antenna selection in their 2012 work [240]. They proposed three distinct selection criteria, each tailored to address different properties of the channel gain matrix. The first criterion prioritised the maximisation of the column vector within the channel matrix, akin to the classical SNR maximisation [241]. The second criterion centred on the similarity between column channel matrix vectors, effectively analogous to the maximisation of minimal Euclidean distances [234]. Finally, combined both approaches in the 3rd - hybrid criterion.

Conversely, in the domain of MIMO communication adaptive GSSK was introduced by Ntotin and Di Renzo in 2013 [226]. Their method adopted a closed-loop precoding strategy. This approach allowed for enhanced transmit-diversity gains surpassing the capabilities of traditional GSSK with static antenna configurations.

Within the realm of VLC, the pursuit of adaptive SM techniques for massive MIMO systems has also garnered significant attention. Xu in [242] proposed a method for the adaptive selection of LED sets, centered on the minimisation of ICI as a key criterion.

Another noteworthy avenue in the realm of adaptive SM for VLC is the channel adaptive bit mapping scheme introduced in [243]. This scheme offers a versatile solution capable of adapting SM to an arbitrary number of transmitters. By dynamically adjusting the bit mapping based on channel conditions without transmitter number constraint, it provides a flexible framework for optimising data transmission using SM.

For indoor VLC scenarios with energy efficiency as a target benchmark, [244] introduces an adaptive MIMO method. This method selects between SM, RC, and spatial multiplexing depending on the prevailing channel conditions. By making dynamic choices between transmission techniques based on real-time channel assessments, it optimises energy consumption.

For GSSK the optimal symbol set selection based on the maximal minimum Euclidean distance maximisation between different LED beams is presented in [225]. To achieve optimisation, the authors adopt LED beam set selection search space reduction using clustering and local tree search. Recently, there is a substantial interest in employing GSSK VLC links in NOMA [245], in that framework a naive Bayesian beam selection algorithm is proposed in [246]. Another recent approach is to utilise machine learning for the LED set selection with reconfigurable intelligent surfaces proposed in [247].

3.3 Adaptive GSSK Algorithm

In this study, the concept of adaptive GSSK incorporates transmitter beam selection, receiver selection, and spectral efficiency adjustment - the number of engaged beams in the communication link. These adaptations are made in response to the local (DC) channel conditions within the communication link.

An optical single user GSSK link is characterised by a MIMO or Multiple-Input and Single-Output (MISO) optical DC channel. In this setup, one or multiple receivers receive a composite signal from multiple transmitter beams. The received signal depends on various transmitter optical beam activation patterns, each associated with a specific signal amplitude at the receiver. The signal amplitude from a particular beam activation pattern may vary between multiple receivers. The study considers mobile use case type scenarios. In this case the receivers are assumed to be integrated into user-operated devices such as smartphones, tablets, laptops, or other similar gadgets.

The channel state between i^{th} receiver and j^{th} transmitter optical beam is characterised by an optical DC channel gain h_{ij}. The channel gain is contingent on several time-dependent conditions. One crucial factor is the relative positioning of the receiver with respect to the source of the transmitter optical beam, which is given as:

$$\mathbf{r}_{ij}(t) = \mathbf{r}_i(t) - \mathbf{r}_j(t) = [(x_i(t) - x_j(t))\mathbf{e}_1, (y_i(t) - y_j(t))\mathbf{e}_2, (z_i(t) - z_j(t))\mathbf{e}_3],$$

here $\mathbf{e}_1, \mathbf{e}_2, \mathbf{e}_3$ are unit length vectors of global x, y and z axes given in m, and t is time (s).

Another factor to consider is the receiver's relative orientation to the transmitter beam, which determines the angle of light incidence $\psi_{ij}(t)$ at the receiver. The orientation of an object with respect to the global axes within $\mathbb{R}^3$ space can be characterised through three elementary rotations. The elementary rotations are described by Euler angles - α, β, γ given in rad [248]. A vector describing an i^{th} receiver orientation to the global axes can be then written as $\mathbf{\Omega_i}(t) = [\alpha_i(t), \beta_i(t), \gamma_i(t)]$ and j^{th} transmitter beam's as $\mathbf{\Omega_j}(t) = [\alpha_j(t), \beta_j(t), \gamma_j(t)]$ respectively.

The optical DC channel characteristics may exhibit temporal variations over time

t, even when the relative positions and orientations of transmitter beams and receivers remain constant. This temporal variability can arise in scenarios involving obstructions, fog as well as channel scintillation resulting from atmospheric or underwater turbulence [53].

The optical DC channel gain is then a function dependent on all of these parameters such that $h_{ij} = f(\theta_{ij}(t))$, with:

$$\theta_{ij}(t) = [\mathbf{r}_{ij}(t), \mathbf{\Omega_i}(t), \mathbf{\Omega_j}(t), t],$$

the optical DC channel gain matrix is then:

$$\mathbf{H}_0(\mathbf{\Theta}(t)) = \begin{bmatrix} h_{11}(\theta_{11}(t)) & ... & h_{1N_\mathrm{t}}(\theta_{1,N_\mathrm{t}}(t)) \\ \vdots & \ddots & \vdots \\ h_{N_\mathrm{r},1}(\theta_{N_\mathrm{r},1}(t)) & ... & h_{N_\mathrm{r},N_\mathrm{t}}(\theta_{N_\mathrm{r},N_\mathrm{t}}(t)) \end{bmatrix}, \tag{3.1}$$

where N_t is number of transmitter beams and N_r is number of receivers present in the channel. Generally, the number of transmitter beams and receivers that can support data transmission can vary locally and temporally and is not necessarily equal to their total number present in the channel.

In optical GSSK, any data sequence s is represented by an n-tuple consisting of a single or multiple binary permutation vectors $\mathbf{b}_k$, where $\mathbf{b}_k = [b_0, b_1, ...b_{N_\mathrm{t}^\mathrm{e}(\mathbf{\Theta}(t))-1}]^\mathrm{T} \in \mathbb{B}(\mathbf{\Theta}(t))$ and $b_{j,k} \in \{0,1\}$ is mapped one-to-one to a symbol vector given as $\mathbf{x}_k = [x_0, x_1, ...x_{N_\mathrm{t}^\mathrm{e}(\mathbf{\Theta}(t))-1}]^\mathrm{T} \in \mathbb{X}(\mathbf{\Theta}(t))$, $x_{j,k} \in \{P_\mathrm{L}, P_\mathrm{H}\}$ using a mapping function $f_{\mathbb{X}(\mathbf{\Theta}(t))}$: $\mathbf{b}_k \in \mathbb{B}(\mathbf{\Theta}(t)) \mapsto \mathbf{x}_k \in \mathbb{X}(\mathbf{\Theta}(t))$. Here $\mathbb{B}(\mathbf{\Theta}(t))$ and $\mathbb{X}(\mathbf{\Theta}(t))$ are the locally and temporally chosen binary permutation vector set and symbol alphabet.

The selection of sets and mapping functions is determined based on the chosen receiver and transmitter beams. In the context of this study for the GSSK encoded data transmission, the receiver and transmitter beams that are selected for participation within the beam activation patterns are referred to as "engaged." The indices within a symbol vector correspond to the indices of these engaged transmitter beams. The variable $N_\mathrm{t}^\mathrm{e}(\mathbf{\Theta}(t))$ represents the count of engaged transmitter beams selected from the total available beams. Each engaged transmitter beam emits optical power at a level of P_{H} when active and P_{L} when inactive.

In this study, we define a codebook for GSSK data transmission as:

$$F(\boldsymbol{\Theta}(t)) = \{\mathbb{B}(\boldsymbol{\Theta}(t)), \mathbb{X}(\boldsymbol{\Theta}(t)), f_{\mathbb{X}(\boldsymbol{\Theta}(t))}, \mathbf{H}_0(\boldsymbol{\Theta}(t))\}. \tag{3.2}$$

The codebook encompasses a binary permutation vector set, a symbol alphabet, and a one-to-one mapping function. It operates by taking binary serial data as input, representing it through binary permutation vectors, and subsequently mapping these binary vectors into symbol vectors selected from the symbol alphabet. Now, the size of the GSSK symbol alphabet, which is locally and temporally assembled based on the codebook is:

$$|\mathbb{X}(\boldsymbol{\Theta}(t))| = |\mathbb{B}(\boldsymbol{\Theta}(t))| = 2^{N_{\mathrm{t}}^{\mathrm{e}}(\boldsymbol{\Theta}(t))}.$$

The number of engaged transmitter beams $N_{\mathrm{t}}^{\mathrm{e}}(\boldsymbol{\Theta}(t)) = |\mathbb{E}_{\mathrm{t}}(\boldsymbol{\Theta}(t))|$ can be smaller than the number of transmitter beams locally and temporally available for the selection $N_{\mathrm{t}}^{\mathrm{a}}(\boldsymbol{\Theta}(t)) = |\mathbb{A}_{\mathrm{t}}(\boldsymbol{\Theta}(t))|$, such that $N_{\mathrm{t}}^{\mathrm{e}}(\boldsymbol{\Theta}(t)) \leq N_{\mathrm{t}}^{\mathrm{a}}(\boldsymbol{\Theta}(t))$. Here $\mathbb{E}_{\mathrm{t}}(\boldsymbol{\Theta}(t)) = \{n_0, n_1, ..., n_{N_{\mathrm{t}}^{\mathrm{e}}(\boldsymbol{\Theta}(t))-1}\}$ is the set of locally and temporally engaged transmitter beams n_j and $\mathbb{A}_{\mathrm{t}}(\boldsymbol{\Theta}(t)) = \{m_0, m_1, ..., m_{N_{\mathrm{t}}^{\mathrm{a}}(\boldsymbol{\Theta}(t))-1}\}$ is the set of all locally and temporally available transmitter beams m_j with properties $\mathbb{E}_{\mathrm{t}}(\boldsymbol{\Theta}(t)) \subseteq \mathbb{A}_{\mathrm{t}}(\boldsymbol{\Theta}(t))$ and $\mathbb{E}_{\mathrm{t}}(\boldsymbol{\Theta}(t)) \in \mathcal{E}_{\mathrm{t}}(\boldsymbol{\Theta}(t))$, where $\mathcal{E}_{\mathrm{t}}(\boldsymbol{\Theta}(t))$ is:

$$\mathcal{E}_{\mathrm{t}}(\boldsymbol{\Theta}(t)) = \{\varnothing, \mathbb{E}_{\mathrm{t},0}(\boldsymbol{\Theta}(t)), \mathbb{E}_{\mathrm{t},1}(\boldsymbol{\Theta}(t)), ..., \mathbb{E}_{\mathrm{t},2^{|\mathbb{E}_{\mathrm{t}}(\boldsymbol{\Theta}(t))|}-1}(\boldsymbol{\Theta}(t))\},$$

the local and temporal power set of all possible $\mathbb{E}_{\mathrm{t},\kappa}(\boldsymbol{\Theta}(t))$ sets of combinations of engaged transmitter beams. The empty set $\varnothing$ is included for the completeness, and represents the case where no transmitters are available.

Similarly one can define the set $\mathbb{E}_{\mathrm{r}}(\boldsymbol{\Theta}(t)) = \{l_0, l_1, ..., l_{N_{\mathrm{r}}^{\mathrm{e}}(\boldsymbol{\Theta}(t))-1}\} \subseteq \mathbb{A}_{\mathrm{r}}(\boldsymbol{\Theta}(t))$ of locally and temporally engaged receivers l_i and $\mathbb{E}_{\mathrm{r}}(\boldsymbol{\Theta}(t)) \in \mathcal{E}_{\mathrm{r}}(\boldsymbol{\Theta}(t))$ where $\mathcal{E}_{\mathrm{r}}(\boldsymbol{\Theta}(t))$ is given as:

$$\mathcal{E}_{\mathrm{r}}(\boldsymbol{\Theta}(t)) = \{\varnothing, \mathbb{E}_{\mathrm{r},0}(\boldsymbol{\Theta}(t)), E_{\mathrm{r},1}(\boldsymbol{\Theta}(t))...\mathbb{E}_{2^{|E_{\mathrm{r}}(\boldsymbol{\Theta}(t))|}-1}(\boldsymbol{\Theta}(t))\},$$

with the number of locally and temporally engaged receivers given as $N_{\mathrm{r}}^{\mathrm{e}}(\boldsymbol{\Theta}(t)) = |\mathbb{E}_{\mathrm{r}}(\boldsymbol{\Theta}(t))|$.

An engaged set of transmitter beams and receivers can be written as their union: $\mathbb{E}_{\mathrm{t,r}}(\boldsymbol{\Theta}(t)) = \mathbb{E}_{\mathrm{t}}(\boldsymbol{\Theta}(t)) \cup \mathbb{E}_{\mathrm{r}}(\boldsymbol{\Theta}(t))$. $\mathbb{E}_{\mathrm{t,r}}(\boldsymbol{\Theta}(t))$ determines the content of the codebook through some internal mapping function such that:

$$F(\boldsymbol{\Theta}(t)) = f(\mathbb{E}_{\mathrm{t,r}}(\boldsymbol{\Theta}(t))) = F(\mathbb{E}_{\mathrm{t,r}}(\boldsymbol{\Theta}(t))). \tag{3.3}$$

Therefore, the selection of $\mathbb{E}_{\mathrm{t,r}}(\boldsymbol{\Theta}(t))$ determines codebook selection. For the selection an input optical DC channel gain matrix of all available transmitters and receivers is required:

$$\mathbf{H}_{0,\mathrm{a}}(\boldsymbol{\Theta}(t)) = \begin{bmatrix} h_{11}(\theta_{11}(t)) & \cdots & h_{1N_{\mathrm{t}}^{\mathrm{a}}(\boldsymbol{\Theta}(t))}(\theta_{1,N_{\mathrm{t}}^{\mathrm{a}}(\boldsymbol{\Theta}(t))}(t)) \\ \vdots & \ddots & \vdots \\ h_{N_{\mathrm{r}}^{\mathrm{a}}(\boldsymbol{\Theta}(t)),1}(\theta_{N_{\mathrm{r}},1}(t)) & \cdots & h_{N_{\mathrm{r}}^{\mathrm{a}}(\boldsymbol{\Theta}(t)),N_{\mathrm{t}}^{\mathrm{a}}(\boldsymbol{\Theta}(t))}(\theta_{N_{\mathrm{r}}^{\mathrm{a}}(\boldsymbol{\Theta}(t)),N_{\mathrm{t}}^{\mathrm{a}}(\boldsymbol{\Theta}(t))}(t)) \end{bmatrix}. \tag{3.4}$$

In order for a specific combination of transmitter beams and receivers to be engaged, it must locally and temporally maximise some performance metric denoted as W. The metric is closely associated with the quality of the user experience in LiFi, OWC or VLC.

Before we proceed to define the engaged transmitter beam and receiver set as a function that maximises the metric W, it is necessary to first define the metric itself. In this context, a metric is defined as a function that takes all the elements of the set as its input and maps them to a single real scalar value. This scalar value serves to characterize the metric, and it is used to assess and quantify the performance or quality as follows:

$$W(\mathbb{E}) = f : \mathbb{E} \mapsto \mathbb{R}^1.$$

We can then define $\mathbb{E}_{\mathrm{t,r}}(\boldsymbol{\Theta}(t))$ as a solution to a maximisation problem as follows:

$$\mathbb{E}_{\mathrm{t,r}}(\boldsymbol{\Theta}(t)) = \underset{\substack{\mathbb{E}_{\mathrm{t},\kappa}(\boldsymbol{\Theta}(t)) \subseteq \mathcal{E}_{\mathrm{t}}(\boldsymbol{\Theta}(t)) \\ \mathbb{E}_{\mathrm{r},\chi}(\boldsymbol{\Theta}(t)) \subseteq \mathcal{E}_{\mathrm{r}}(\boldsymbol{\Theta}(t))}}{\operatorname{argmax}} W(\mathbb{E}_{\mathrm{t},\kappa}(\boldsymbol{\Theta}(t)) \cup \mathbb{E}_{\mathrm{r},\chi}(\boldsymbol{\Theta}(t))). \tag{3.5}$$

In the realm of optical GSSK, this performance metric can take various forms depending on the specific objectives. It might involve minimizing connectivity loss, maximizing channel capacity, optimizing SNR, enhancing energy efficiency, and so on.

The particular choice of metric can vary according to the specific use case scenarios being addressed. However, in the context of a LiFi deployment, a primary goal would be to ensure that the quality of user experience is maintained at a high level by minimizing the occurrence of connectivity loss (outages) to the greatest extent possible. Another two important metrics are channel capacity C (or data throughput) and energy efficiency EE, which are related to each other through [192]:

$$\mathrm{EE} = \frac{P_\mathrm{c}}{C}, \tag{3.6}$$

where P_c - power consumption of the link.

In general, it is typically desirable to maximise both of these metrics while taking into account power consumption constraints and safety considerations related to laser eye safety. To enhance the GSSK channel capacity, it becomes necessary to increase the number of transmitters and/or receivers in the communication link. To illustrate this, we consider the channel capacity of a $N_\mathrm{t}^\mathrm{e} \times N_\mathrm{r}^\mathrm{e}$ GSSK link.

In the case of GSSK, the closed-form solutions of the channel capacity are considerably difficult to obtain when optimal Maximum-Likelihood (ML) detection is considered [227, 228], which we assume in this work. Instead, it is more useful is the fact that upper bound of the channel capacity for GSM and GSSK is know and is less or equal to the $N_\mathrm{t}^\mathrm{e} \times N_\mathrm{r}^\mathrm{e}$ spatially multiplexed MIMO channel capacity [249, 250]:

$$C_\mathrm{GSSK} \leq C_\mathrm{MIMO}^{N_\mathrm{t}^\mathrm{e} \times N_\mathrm{r}^\mathrm{e}}, \tag{3.7}$$

here C_GSSK - channel capacity of GSSK link, $C_\mathrm{MIMO}^{N_\mathrm{t}^\mathrm{e} \times N_\mathrm{r}^\mathrm{e}}$ - MIMO channel capacity, which for a constant MIMO channel with total optical emission power constraint P is given as [184, 249, 250]:

$$C_\mathrm{MIMO}^{N_\mathrm{t}^\mathrm{e} \times N_\mathrm{r}^\mathrm{e}} = \mathrm{E}_\mathbf{H}(\log_2(\det(\mathbf{I}_{N_\mathrm{r}^\mathrm{e}} + \frac{1}{N_\mathrm{t}^\mathrm{e}}\mathrm{SNR} \times \mathbf{H}\mathbf{H}^T))), \tag{3.8}$$

here $\mathbf{I}_{N_\mathrm{r}^\mathrm{e}}$ - $N_\mathrm{t}^\mathrm{e} \times N_\mathrm{r}^\mathrm{e}$ dimension identity matrix, $\mathrm{E}(\cdot)$ - expectation operator. We employ the transpose operation rather than the conjugate transpose, as LiFi channel gain matrices are constrained to possess solely real values. In the case of GSSK, the total transmitted optical power denoted as P is evenly distributed among the N_t^e active transmitter beams. The task is then to search for $\mathbb{E}_{\mathrm{t,r}}(\mathbf{\Theta}(t))$ that maximises channel capacity as given by Equations (3.7) and (3.8).

In a real-world LiFi scenario, the GSSK link's SNR is constrained by factors such as maximum permissible exposure (MPE) or power consumption limits. When symbols with higher optical power are subject to MPE constraints, the incorporation of additional engaged beams necessitates an increase in symbol density within the Euclidean space and decrease in the mutual Euclidean distance between the symbols. This intuitive observation implies the existence of an optimal number of engaged transmitter beams and receivers that maximise channel capacity. As a result, it suggests that the set selection problem described in Equation (3.8) takes on a convex nature when either channel capacity or energy efficiency through (3.6) is the focus of consideration:

$$\mathbb{E}_{\mathrm{t,r}}(\mathbf{\Theta}(t)) = \underset{\substack{\mathbb{E}_{\mathrm{t},\kappa}(\mathbf{\Theta}(t)) \subseteq \mathcal{E}_\mathrm{t}(\mathbf{\Theta}(t)) \\ \mathbb{E}_{\mathrm{r},\chi}(\mathbf{\Theta}(t)) \subseteq \mathcal{E}_\mathrm{r}(\mathbf{\Theta}(t))}}{\operatorname{argmax}} C_{\mathrm{GSSK}}(\mathbb{E}_{\mathrm{t},\kappa}(\mathbf{\Theta}(t)) \cup \mathbb{E}_{\mathrm{r},\chi}(\mathbf{\Theta}(t))), \tag{3.9}$$

or

$$\mathbb{E}_{\mathrm{t,r}}(\mathbf{\Theta}(t)) = \underset{\substack{\mathbb{E}_{\mathrm{t},\kappa}(\mathbf{\Theta}(t)) \subseteq \mathcal{E}_\mathrm{t}(\mathbf{\Theta}(t)) \\ \mathbb{E}_{\mathrm{r},\chi}(\mathbf{\Theta}(t)) \subseteq \mathcal{E}_\mathrm{r}(\mathbf{\Theta}(t))}}{\operatorname{argmax}} EE_{\mathrm{GSSK}}(\mathbb{E}_{\mathrm{t},\kappa}(\mathbf{\Theta}(t)) \cup \mathbb{E}_{\mathrm{r},\chi}(\mathbf{\Theta}(t))), \tag{3.10}$$

both with the search space of size $2^{(N_\mathrm{t}^\mathrm{a}(\mathbf{\Theta}(t)) + N_\mathrm{r}^\mathrm{a}(\mathbf{\Theta}(t)))}$.

After selecting $\mathbb{E}_{\mathrm{t,r}}(\mathbf{\Theta}(t))$ and defining the codebook as $F(\mathbf{\Theta}(t)) = F(\mathbb{E}_{\mathrm{t,r}}(\mathbf{\Theta}(t)))$, the transmission of symbols over the MIMO channel by the engaged transmitter beams and received by the engaged receivers is characterised by a $N_\mathrm{r}^\mathrm{e}(\mathbf{\Theta}(t)) \times N_\mathrm{t}^\mathrm{e}(\mathbf{\Theta}(t))$ dimension optical DC channel gain matrix:

$$\mathbf{H}_{0,\mathrm{e}}(\mathbf{\Theta}(t)) = \begin{bmatrix} h_{11}(\theta_{11}(t)) & \dots & h_{1N_\mathrm{t}^\mathrm{e}(\mathbf{\Theta}(t))}(\theta_{1,N_\mathrm{t}^\mathrm{e}(\mathbf{\Theta}(t))}(t)) \\ \vdots & \ddots & \vdots \\ h_{N_\mathrm{r}^\mathrm{e}(\mathbf{\Theta}(t)),1}(\theta_{N_\mathrm{r},1}(t)) & \dots & h_{N_\mathrm{r}^\mathrm{e}(\mathbf{\Theta}(t)),N_\mathrm{t}^\mathrm{e}(\mathbf{\Theta}(t))}(\theta_{N_\mathrm{r}^\mathrm{e}(\mathbf{\Theta}(t)),N_\mathrm{t}^\mathrm{e}(\mathbf{\Theta}(t))}(t)) \end{bmatrix}. \tag{3.11}$$

Each matrix element $h_{ij}(\theta_{ij}(t))$ corresponds to an optical DC channel gain between the engaged pair of $l_i \in \mathbb{E}_\mathrm{r}(\mathbf{\Theta}(t))$ (i^th) receiver and $n_j \in \mathbb{E}_\mathrm{t}(\mathbf{\Theta}(t))$ (j^th) transmitter. The received over the optical DC channel signal is given by the vector $\mathbf{y}(\mathbf{\Theta}(t)) = [y_0, y_1, ...y_{N_\mathrm{r}^\mathrm{e}(\mathbf{\Theta}(t))-1}]^\mathrm{T} \in \mathbb{R}_{N_\mathrm{r}^\mathrm{e}(\mathbf{\Theta}(t))\times 1}$, where $\mathbf{y}(\mathbf{\Theta}(t))$ is given as:

$$\mathbf{y}(\mathbf{\Theta}(t)) = \mathbf{H}_{0,\mathrm{e}}(\mathbf{\Theta}(t))\mathbf{x}_k + \mathbf{n}(\mathbf{\Theta}(t)), \tag{3.12}$$

where $\mathbf{x}_k \in \mathbb{X}(\mathbf{\Theta}(t)) \subseteq F(\mathbb{E}_{\mathrm{t,r}}(\mathbf{\Theta}(t)))$ and $\mathbb{R}_{N_\mathrm{r}^\mathrm{e}(\mathbf{\Theta}(t))\times 1}$ dimension vector $\mathbf{n}(\mathbf{\Theta}(t))$ denotes the AWGN vector, the elements of which are distributed by $\mathcal{N}(0, \sigma_i^2(\mathbf{\Theta}(t)))$, where $\sigma_i^2(\mathbf{\Theta}(t))$ is variance of effective noise process at the i^th receiver. Assuming that the noise contribution from each j^th transmitter beam to the i^th receiver is a random and independent process, we can express $\sigma_i^2(\mathbf{\Theta}(t))$ using the variance sum law as follows:

$$\sigma_i^2(\mathbf{\Theta}(t)) = \sum_{j=0}^{N_\mathrm{t}^\mathrm{e}(\mathbf{\Theta}(t))-1} \sigma_{ij}^2(\mathbf{\Theta}(t)) + \sigma_{\mathrm{R},i}^2(\mathbf{\Theta}(t)),$$

here, the first term describes the noise component dependent on the transmitted signal at the i^th receiver (e.g., shot noise). The second term describes the noise component independent of the transmitted signal (e.g., thermal noise and TIA voltage noise). The noise variance is calculated as:

$$\sigma_{ij}^2(\mathbf{\Theta}(t)) = N_{0,ij}(\mathbf{\Theta}(t))B,$$

where $N_{0,ij}(\mathbf{\Theta}(t))$ is the transmitted signal dependent single-sided noise power spectral density at the i^th receiver and B - the effective noise process bandwidth. Same expression can be applied for the independent component:

$$\sigma_{\mathrm{R},i}^2(\mathbf{\Theta}(t)) = N_{0,\mathrm{R},i}(\mathbf{\Theta}(t))B,$$

here $N_{0,\mathrm{R},i}(\mathbf{\Theta}(t))$ describes single-sided noise power spectral density of the independent transmitted signal effective noise process.

In this study, the detection at the receiver end is based on the ML detection principle where the estimated transmission vector $\hat{\mathbf{x}}_k$ is given from:

$$\begin{aligned}\hat{\mathbf{x}}_k &= \underset{\mathbf{x}_k \in \mathbb{X}(\boldsymbol{\Theta}(t))}{\operatorname{argmax}} \ p_{\mathbf{y}}(\mathbf{y}(\boldsymbol{\Theta}(t))|\mathbf{H}_{\mathrm{e}}(\boldsymbol{\Theta}(t))\mathbf{x}_k) \\ &= \underset{\mathbf{x}_k \in \mathbb{X}(\boldsymbol{\Theta}(t))}{\operatorname{argmin}} \ |\mathbf{y}(\boldsymbol{\Theta}(t)) - \mathbf{H}_{\mathrm{e}}(\boldsymbol{\Theta}(t))\mathbf{x}_k|_{\mathrm{F}}^2.\end{aligned} \tag{3.13}$$

Alternative decoding methods, such as the least squares error decoding approach, can be employed. The estimated transmission vector is then linked to the corresponding binary permutation vector denoted as $\hat{\mathbf{b}}_k$. This vector can either be directly used to generate the decoded data sequence $\hat{s}$ or be input into a channel coding scheme, such as a Forward Error Coder (FEC) or a Reed-Solomon coder.

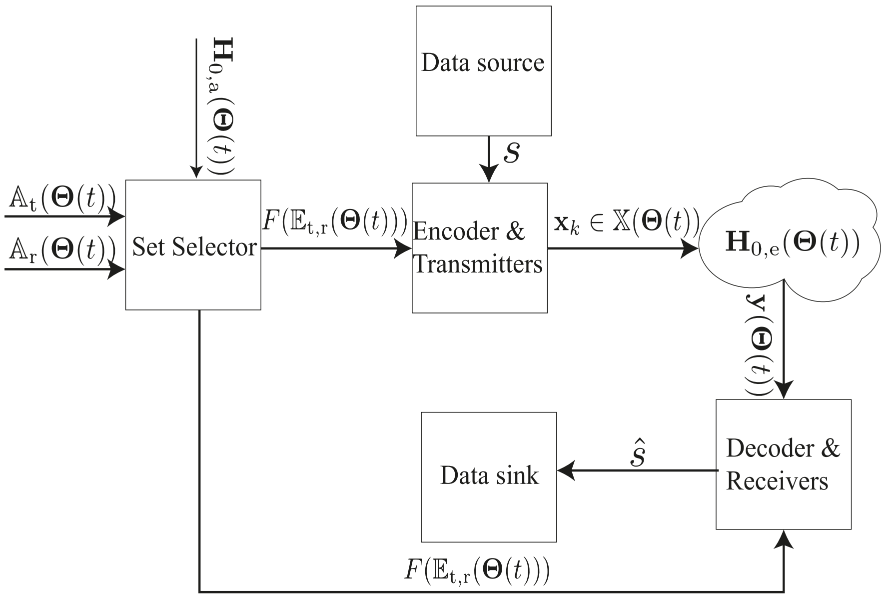

Figure 3.2: Adaptive GSSK block-diagram.

Following our discussion, we can now define the adaptive GSSK algorithm as one that engages in transmitter beam and receiver selection based on a metric, solving (3.5) while considering a user experience quality-related metric denoted as W. Subsequently, the algorithm constructs a codebook, as detailed in (3.2), using (3.3), and proceeds to transmit data through the channel, represented by (3.1). The received signal, described by (3.12), is then decoded using the maximum likelihood principle, as outlined in (3.13), or employing alternative decoding techniques. For algorithm codebook compilation channel estimation can be performed during the set selection using some known pilot signal.

The adaptive GSSK algorithm can be conceptually divided into three distinct parts: transmitter beam and receiver set selection (set selector), encoding, and decoding. A visual representation of the adaptive GSSK algorithm's is provided in Figure 3.2.

3.3.1 GSSK Link Bit Error Ratio

A useful parameter to analyse GSSK link performance, is BER. We employ the widely recognized union bounding technique [251]. Our approach commences with a general expression for the Symbol Error Ratio (SER):

$$P_{\mathrm{s}}(\boldsymbol{\Theta}(t)) \leq \sum_{k=1}^{|\mathbb{X}(\boldsymbol{\Theta}(t))|} \sum_{k'=1}^{|\mathbb{X}(\boldsymbol{\Theta}(t))|} P_{\mathbf{x}_k}(\boldsymbol{\Theta}(t)) d_{\mathrm{H}(\mathbf{x}_k,\mathbf{x}_{k'})} P_{\mathbf{x}_k \rightarrow \mathbf{x}_{k'}}(\boldsymbol{\Theta}(t)), \tag{3.14}$$

here $d_{\mathrm{H}(\mathbf{X}_k,\mathbf{X}_{k'})}$ - Hamming distance or the number of erroneous bits between symbols $\mathbf{x}_k$ and $\mathbf{x}_{k'}$. $P_{\mathbf{x}_k}(\boldsymbol{\Theta}(t))$ - a priori probability to select a transmission vector $\mathbf{x}_k$. The Pairwise Error Probability (PEP) for a binary modulation [252] is given as:

$$\begin{aligned} P_{\mathbf{x}_k \rightarrow \mathbf{x}_{k'}}(\boldsymbol{\Theta}(t)) &= Q\left(\frac{1}{2}\sqrt{\frac{d^2_{(\mathbf{x}_k,\mathbf{x}_{k'})}(\boldsymbol{\Theta}(t))}{\sigma^2_{(\mathbf{x}_k,\mathbf{x}_{k'})}(\boldsymbol{\Theta}(t))}}\right) \\ &= Q\left(\frac{1}{2}\frac{|\mathbf{H}(\boldsymbol{\Theta}(t))\Delta_{\mathbf{X}_k,\mathbf{X}_{k'}}|_{\mathrm{F}}}{\sigma_{(\mathbf{x}_k,\mathbf{x}_{k'})}(\boldsymbol{\Theta}(t))}\right), \end{aligned} \tag{3.15}$$

here $d_{(\mathbf{x}_k,\mathbf{x}'_k)}$ - mutual Euclidean distance between symbols $\mathbf{x}_k$ and $\mathbf{x}_{k'}$, and $\Delta_{\mathbf{x}_k,\mathbf{x}_{k'}}$ is defined as:

$$\Delta_{\mathbf{x}_k,\mathbf{x}_{k'}} = \mathbf{x}_k - \mathbf{x}_{k'}.$$

For the a priori probability $P_{\mathbf{X}_k}(\boldsymbol{\Theta}(t))$ we assume that all symbols within the alphabet have an equal likelihood, thus:

$$P_{\mathbf{x}_k}(\boldsymbol{\Theta}(t)) = \frac{1}{|\mathbb{X}(\boldsymbol{\Theta}(t))|}. \tag{3.16}$$

Inserting (3.15) and (3.16) into SER union bound expression (3.14) we get:

$$P_{\mathrm{s}}(\boldsymbol{\Theta}(t)) \leq \frac{1}{|\mathbb{X}(\boldsymbol{\Theta}(t))|} \sum_{k=1}^{|\mathbb{X}(\boldsymbol{\Theta}(t))|} \sum_{k'=1}^{|\mathbb{X}(\boldsymbol{\Theta}(t))|} d_{\mathrm{H}(\mathbf{x}_k,\mathbf{x}_{k'})} Q\left(\frac{1}{2}\frac{|\mathbf{H}(\boldsymbol{\Theta}(t))\Delta_{\mathbf{x}_k,\mathbf{x}_{k'}}|_{\mathrm{F}}}{\sigma_{(\mathbf{x}_k,\mathbf{x}_{k'})}(\boldsymbol{\Theta}(t))}\right). \tag{3.17}$$

Ultimately, to obtain the BER union bound, we consider the contribution of only the nearest neighbours, resulting in a single erroneous bit. Consequently, we can approximate the BER from the SER, as detailed in [252], in the following manner:

$$P_{\mathrm{bit}}(\boldsymbol{\Theta}(t)) \approx \frac{P_{\mathrm{s}}(\boldsymbol{\Theta}(t))}{\log_2 |\mathbb{X}(\boldsymbol{\Theta}(t))|} = \frac{P_{\mathrm{s}}(\boldsymbol{\Theta}(t))}{N_{\mathrm{t}}^{\mathrm{e}}(\boldsymbol{\Theta}(t))}. \tag{3.18}$$

We get the final BER union bound expression by inserting (3.17) into (3.18):

$$\begin{aligned} P_{\mathrm{bit}}(\boldsymbol{\Theta}(t)) \leq \frac{1}{|\mathbb{X}(\boldsymbol{\Theta}(t))| N_{\mathrm{t}}^{\mathrm{e}}(\boldsymbol{\Theta}(t))} & \sum_{k=1}^{|\mathbb{X}(\boldsymbol{\Theta}(t))|} \sum_{k'=1}^{|\mathbb{X}(\boldsymbol{\Theta}(t))|} d_{\mathrm{H}(\mathbf{X}_k,\mathbf{X}_{k'})} \\ \times Q\left(\frac{1}{2}\frac{|\mathbf{H}(\boldsymbol{\Theta}(t))\Delta_{\mathbf{x}_k,\mathbf{x}_{k'}}|_{\mathrm{F}}}{\sigma_{(\mathbf{x}_k,\mathbf{x}_{k'})}(\boldsymbol{\Theta}(t))}\right)&. \end{aligned} \tag{3.19}$$

3.3.2 Adaptive GSSK Algorithm Set Selector

We will now focus on the set selector part of the adaptive GSSK algorithm. As described in the preceding section, $\mathbf{H}_{0,\mathrm{a}}(\boldsymbol{\Theta}(t))$, $\mathbb{A}_{\mathrm{t}}(\boldsymbol{\Theta}(t))$ and $\mathbb{A}_{\mathrm{r}}(\boldsymbol{\Theta}(t))$, it is essential to recognize that these parameters generally rely on a multitude of factors. These factors include but are not limited to: relative positions of the receivers with respect to the transmitter beams, the opto-electronic front-end of both the receivers and the transmitter beam sources, the orientation of both the receiver and transmitter beams and on the time dependent channel conditions.

The variability associated with the aforementioned factors give rise to the possibility of selecting a multitude of different sets of $\mathbb{E}_{\mathrm{t},\kappa}(\boldsymbol{\Theta}(t)) \in \mathcal{E}_{\mathrm{t}}(\boldsymbol{\Theta}(t))$ and $\mathbb{E}_{\mathrm{r},\chi}(\boldsymbol{\Theta}(t)) \in \mathcal{E}_{\mathrm{r}}(\boldsymbol{\Theta}(t))$. Given the input values of $\mathbf{H}_{0,\mathrm{a}}(\boldsymbol{\Theta}(t))$, $\mathbb{A}_{\mathrm{t}}(\boldsymbol{\Theta}(t))$ and $\mathbb{A}_{\mathrm{r}}(\boldsymbol{\Theta}(t))$ the set selector solves (3.5) and using (3.2) outputs $F(\mathbb{E}_{\mathrm{t,r}}(\boldsymbol{\Theta}(t)))$ to the encoder and the decoder.

In the context of LiFi deployment, where users have the freedom of movement, it is paramount to recognize that the channel conditions can undergo rapid fluctuations as a function of $\boldsymbol{\Theta}(t)$. However, there are time intervals, denoted as $\Delta t = t_2 - t_1$, where the channel gains and transmitter beam and receiver sets can be reasonably considered as constant and time correlated, specifically when Δt is less than the channel coherence time, denoted as τ.

For mobile indoor LiFi scenarios, this coherence time is typically around few hundreds of ms [253]. Consequently, during the time periods of channel coherence the set selection of $\mathbb{E}_{\mathrm{t,r}}(\boldsymbol{\Theta}(t))$ is time constrained to $t_{\mathrm{sel}} << \tau$, where t_{sel} denotes the time required to make selection of $\mathbb{E}_{\mathrm{t,r}}(\boldsymbol{\Theta}(t))$.

Latency constitutes another important aspect of the user experience metric requiring substantial consideration in the design of an adaptive GSSK-based LiFi system. In the realm of 5G NR (new radio) [254], one of its fundamental tenets is Ultra-Reliable Low-Latency Communications (URLLC), necessitating over the interface latency levels as low as, or even lower than 1 ms [255, 256]. As emerging services with stringent latency requirements like streaming, video conferencing [257], Augmented Reality (AR) and VR [258] continue to gain prominence in consumer applications, a LiFi-based system must align with these latency prerequisites within the context of mobile usage scenarios. Therefore, to select $\mathbb{E}_{\mathrm{t,r}}(\boldsymbol{\Theta}(t))$ condition $t_{\mathrm{sel}} \leq 1\,\mathrm{ms}$ must be satisfied.

Consider the scenario where the set selector is employed to solve the optimization problem (3.9), aimed to maximise channel capacity. In order to assess the latency impact resulting from the selection of transmitter beams and receiver sets, we derive the number of Floating-point Operations (FLO) associated with solving (3.9).
The detailed derivation of this computation is provided in Appendix A.

$$N^{\mathrm{ops,sel}}_{C_{\mathrm{GSSK}}} = \sum_{\substack{\mathbb{E}_{\mathrm{r},\kappa}\in \\ \mathcal{E}_{\mathrm{r}}(\boldsymbol{\Theta}(t))}}^{|\mathcal{E}_{\mathrm{r}}(\boldsymbol{\Theta}(t))|} \sum_{\substack{\mathbb{E}_{\mathrm{t},\kappa}\in \\ \mathcal{E}_{\mathrm{t}}(\boldsymbol{\Theta}(t))}}^{|\mathcal{E}_{\mathrm{t}}(\boldsymbol{\Theta}(t))|} ((N^2_{\mathrm{bit}}|\mathbb{E}_{\mathrm{r}}(\boldsymbol{\Theta}(t))|^2(|\mathbb{E}_{\mathrm{r}}(\boldsymbol{\Theta}(t))| + |\mathbb{E}_{\mathrm{t}}(\boldsymbol{\Theta}(t))| + 1)$$
$$+ N_{\mathrm{bit}}|\mathbb{E}_{\mathrm{r}}(\boldsymbol{\Theta}(t))|(|\mathbb{E}_{\mathrm{r}}(\boldsymbol{\Theta}(t))| + 1) + \frac{|\mathbb{E}_{\mathrm{r}}(\boldsymbol{\Theta}(t))|(|\mathbb{E}_{\mathrm{t}}(\boldsymbol{\Theta}(t))| - 1)}{2}) + 2^{2(N^{\mathrm{a}}_{\mathrm{t}}(\boldsymbol{\Theta}(t)) + N^{\mathrm{a}}_{\mathrm{r}}(\boldsymbol{\Theta}(t)))}. \tag{3.20}$$

If we assume energy efficiency as the performance metric under test denoted as W, it can be straightforwardly demonstrated that the number of operations for solving (3.10) is equal to (3.9) with an additional $2^{(|\mathcal{E}_{\mathrm{r}}(\boldsymbol{\Theta}(t))|+|\mathcal{E}_{\mathrm{t}}(\boldsymbol{\Theta}(t))|)}$ divisions:

$$N^{\mathrm{ops,sel}}_{EE_{\mathrm{GSSK}}} = N^{\mathrm{ops,sel}}_{C_{\mathrm{GSSK}}} + 2^{(N^{\mathrm{a}}_{\mathrm{t}}(\boldsymbol{\Theta}(t))+N^{\mathrm{a}}_{\mathrm{r}}(\boldsymbol{\Theta}(t)))} N^{2}_{\mathrm{bit}}. \tag{3.21}$$

In this work, we assume that matrix channel gain elements are represented by 16-bit numbers denoted as N_{bit} for performing arithmetic operations. As can be seen from (3.20) and (3.21), the number of operations exponentially grows with the last term, which depends on the search space of all combinations of available transmitters and receivers. The time complexity upper bound of (3.20) and (3.21) asymptotically tends to:

$$\lim_{|\mathbb{E}_{\mathrm{t},\kappa}(\boldsymbol{\Theta}(t))|\to\infty} N^{\mathrm{ops,sel}}_{C_{\mathrm{GSSK}}} = O(2^{2(N^{\mathrm{a}}_{\mathrm{t}}(\boldsymbol{\Theta}(t))+N^{\mathrm{a}}_{\mathrm{r}}(\boldsymbol{\Theta}(t)))}) \tag{3.22}$$

Figures 3.3 and 3.4 illustrate the relation between the number of operations, the selection time required to solve (3.9) with respect to the available transmitter beams and receivers in the channel. In the figures, the dashed lines represent the maximum permissible latency, which is set at 1 ms. To evaluate t_{sel} we assume processing power of 3681.3×10^{9} FLO/s (floating point operations per second) based on commercially available state-of-art smartphone processors such as Qualcomm SM8550-AC Snapdragon 8 Gen 2 [259]. The selection time t_{sel} can be then calculated as:

$$t_{\mathrm{sel}} = \frac{N^{\mathrm{ops,sel}}_{C_{\mathrm{GSSK}}}}{\mathrm{FLO/s}}. \tag{3.23}$$

Comparing Figures 3.3 and 3.4, we observe a more substantial increase in $N^{\mathrm{ops,sel}}_{C_{\mathrm{GSSK}}}$ against $N^{\mathrm{a}}_{\mathrm{r}}$ compared to $N^{\mathrm{a}}_{\mathrm{t}}$. This difference arises due to the complexity with evaluating determinant, which is proportional to $|\mathbb{E}_{\mathrm{r},\kappa}|^{3}$ in (3.20). This dependency can be inverted by reordering the channel gain terms in the channel matrix (transposing h_{ij} to h_{ji}). In that case the increase of $N^{\mathrm{ops,sel}}_{C_{\mathrm{GSSK}}}$ would exhibit stronger contingency on $N^{\mathrm{a}}_{\mathrm{t}}$ compared to $N^{\mathrm{a}}_{\mathrm{r}}$. The choice on matrix indexing can be based on the particular use case scenario.

From both Figures, the number of operations computed in (3.20) demonstrates the challenges of solving (3.9) directly for the receiver and transmitter beam selection. The

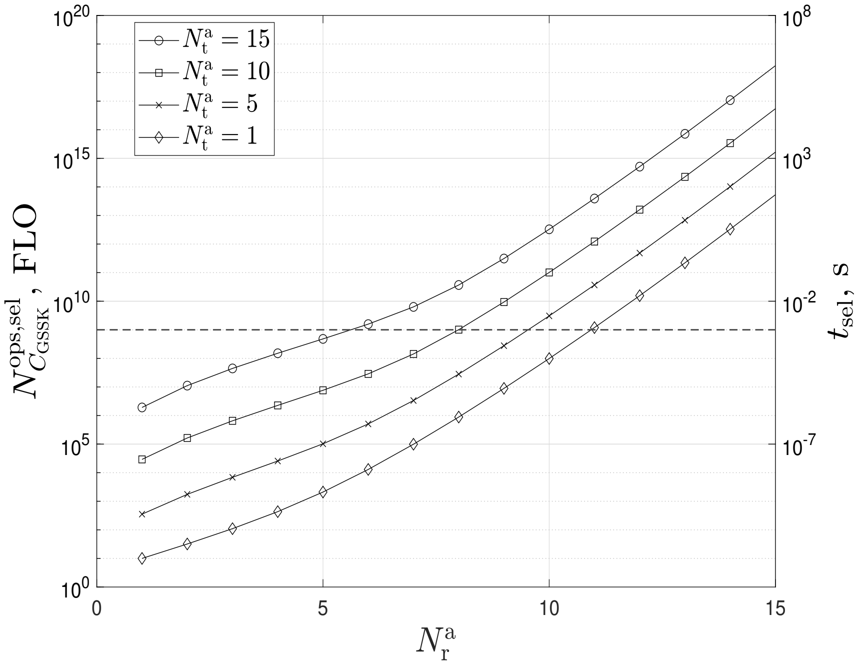

Figure 3.3: Number of floating point operations (FLO) and selection time required to select $\mathbb{E}_{\mathrm{t,r}}(\mathbf{\Theta}(t))$, which maximises C_{GSSK} for various fixed $N_{\mathrm{r}}^{\mathrm{a}}$ dependent on $N_{\mathrm{t}}^{\mathrm{a}}$. The dashed line represents maximal latency.

cardinalities of $\mathbb{A}_{\mathrm{t}}(\mathbf{\Theta}(t))$ and $\mathbb{A}_{\mathrm{r}}(\mathbf{\Theta}(t))$, which define the search space for $\mathbb{E}_{\mathrm{t,r}}(\mathbf{\Theta}(t))$, that can be used for the beam selection, are constrained to low values to retain the permissible latency.

Generally, we want the search space to be as extensive as possible to accommodate a wide range of use-case scenarios involving varying number of available transmitter beam sources and receivers are considered. However, Figure 3.4 shows the largest achievable search space occurs when $N_{\mathrm{r}}^{\mathrm{a}} = 5$ and $N_{\mathrm{t}}^{\mathrm{a}} = 10$. An increase in the number of available receivers results in a reduced transmitter beam search space within acceptable latency limits. For example, when $N_{\mathrm{r}}^{\mathrm{a}} = 10$, the number of available transmitters for the selection decreases to $N_{\mathrm{t}}^{\mathrm{a}} = 4$, whereas for $N_{\mathrm{r}}^{\mathrm{a}} = 15$ transmitter selection cannot be performed within the latency constraints.

From (3.20) and Figures 3.4 and 3.3 we can conclude that directly solving (3.9) within latency constraints is only feasible when a small number of receivers is employed in the link. This limitation hinders the practical utility of this type of engaged

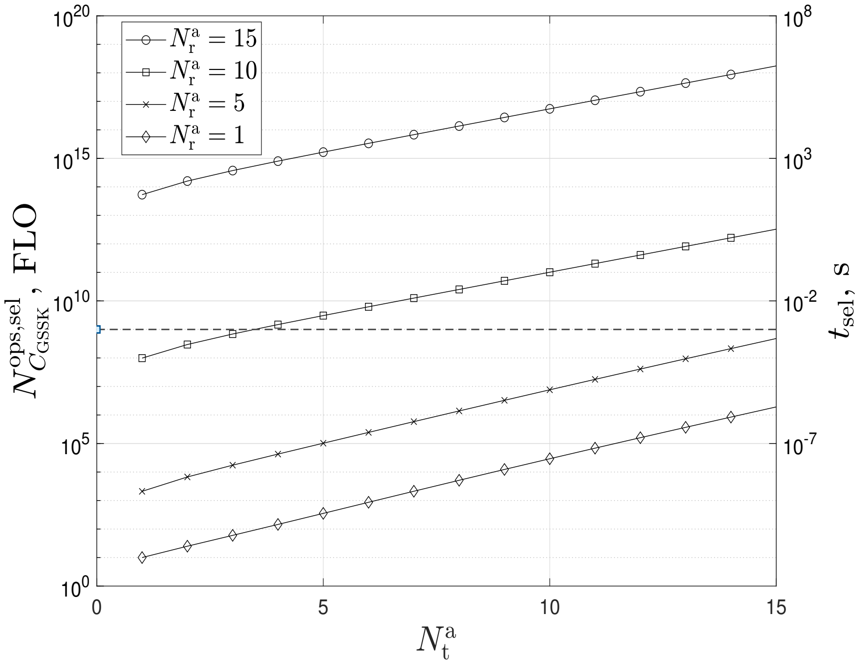

Figure 3.4: Number of floating point operations (FLO) and selection time required to select $\mathbb{E}_{\mathrm{t,r}}(\boldsymbol{\Theta}(t))$, which maximises C_{GSSK} for various fixed $N_{\mathrm{t}}^{\mathrm{a}}$ dependent on $N_{\mathrm{r}}^{\mathrm{a}}$. The dashed line represents maximal latency.

transmitter beam and receiver set selector.

A further challenge in implementing this set selector arise from the necessity of evaluating the SNR term in (3.8) would require measuring SNR for each i^{th} receiver and j^{th} transmitter beam pair. Furthermore, the noise variance for each pair can vary significantly due to shot noise, which depends on the incident optical power at each receiver. Additionally, while (3.8) assumes equal SNR for all symbols during transmission, in practice, due to shot noise each symbol will have a distinct noise variance.

Maximal Minimum Euclidean Distance Based Set Selector

Alternatively, instead of attempting to directly solve (3.9) or (3.10), we can set the target metric W to be the maximum number of engaged transmitter beams that minimises BER $P_{\mathrm{bit}}(\boldsymbol{\Theta}(t))$ subject to the constraint that $P_{\mathrm{bit}}(\boldsymbol{\Theta}(t)) < P_{\mathrm{bit,0}}$, where $P_{\mathrm{bit,0}}$ represents the maximum BER threshold. Such threshold can be set, for example, 1×10^{-9}

when no channel coding is assumed [260] or 3.8×10^{-3} when FEC is applied [261]. With this approach we select transmitter beam and receiver set that maximises spectral efficiency while keeping BER within permissible threshold. For a given bandwidth B and spectral efficiency, this can be conceptualised as attempting to increase mutual information $I(\mathbf{X}|\mathbf{Y})$ between transmitted symbol (represented by random variable $\mathbf{X}$ and received symbol, (represented by a random variable $\mathbf{Y}$) tending towards the channel capacity.

However, analytically estimating BER can be computationally complex, as can be inferred from (3.19). Specifically, calculation of Q-function repeated over the entire search space significantly increases the computational demands. Instead, we can observe that from (3.15) and (3.19) that BER strongly depends on the mutual Euclidean distances between different symbols. When the SNR is sufficiently high, we can assume that only the nearest neighbours contribute to BER with the highest error probability contribution originating from symbols with the minimal mutual Euclidean distance.

Therefore, the task of minimising BER can be approximated by finding $\mathbb{E}_{\mathrm{t,r}}(\mathbf{\Theta}(t))$ that maximises the minimal mutual Euclidean distance $d_{\mathbf{x}_k,\mathbf{x}_{k'}} > 0$ between symbols $\mathbf{x}_k$ and $\mathbf{x}_{k'}$ of $\mathbb{X}(\mathbf{\Theta}(t))$ constructed from $(\mathbb{E}_{\mathrm{t},\kappa}(\mathbf{\Theta}(t)) \cup \mathbb{E}_{\mathrm{r},\chi}(\mathbf{\Theta}(t)))$ similar to work in [234]. The constraints of this optimisation problem include maximisation of engaged number of transmitter beams, and ensuring that $P_{\mathrm{bit}}(\mathbf{\Theta}(t)) < P_{\mathrm{bit},0}$.

Set selection Algorithm 1 is designed to address the given task. This algorithm takes as the input the sets of all available transmitter beams and receivers. For the sake of simplicity, it engages all available receivers in the selection. This assumption is justified since one can adjust the availability condition based on the signal strength at the i^{th} receiver relative to a predetermined threshold (trigger), thereby eliminating receivers with a detrimental contribution to BER, for instance, those exhibiting considerably smaller SNR compared to other receivers. Receiver availability can be based using a front-end dependent signal input threshold levels or triggers, for example, such as signal amplitude or SNR.

The algorithm searches in $\mathcal{E}_{\mathrm{t}}^{g}(\mathbf{\Theta}(t)) = \{\forall\, \mathbb{E}_{\mathrm{t},\kappa}(\mathbf{\Theta}(t)) \in \mathcal{E}_{\mathrm{t}}(\mathbf{\Theta}(t)) \,:\, \forall\, |\mathbb{E}_{\mathrm{t},\kappa}(\mathbf{\Theta}(t))| = g\}$, where $g \in \{1, 2, 3, ..., N_{\mathrm{t}}^{\mathrm{a}}(\mathbf{\Theta}(t))\}$ for $\mathbb{E}_{\mathrm{t,r}}(\mathbf{\Theta}(t))$ in the ascending cardinality or-

Algorithm 1: Maximal Minimum Euclidean Distance Criterion Based Set Selector

Input: $\mathbb{A}_{\mathrm{t}}(\mathbf{\Theta}(t))$,$\mathbb{A}_{\mathrm{r}}(\mathbf{\Theta}(t)), \mathbf{H}_{0,\mathrm{A}}(\mathbf{\Theta}(t))$,
Define: $P_{\mathrm{bit},0}$ as the upper BER threshold,
Set: $\tilde{\mathbb{E}}_{\mathrm{t,r}}(\mathbf{\Theta}(t)) = \{\mathbb{A}_{\mathrm{r}}(\mathbf{\Theta}(t)) \cup \varnothing\}$, $P_{\mathrm{bit}} = 0$, $l = 1$,
while $P_{\mathrm{bit}} < P_{\mathrm{bit},0}$ **do**
  Set $\tilde{\mathbb{E}}'_{\mathrm{t,r}}(\mathbf{\Theta}(t)) = \tilde{\mathbb{E}}_{\mathrm{t,r}}(\mathbf{\Theta}(t))$,
  Select $\tilde{\mathbb{E}}_{\mathrm{t,r}}(\mathbf{\Theta}(t))$ that:

$$\begin{aligned}
\underset{\substack{\mathbb{E}_{\mathrm{t},\kappa}(\mathbf{\Theta}(t)) \subseteq \mathbb{A}_{\mathrm{t}}(\mathbf{\Theta}(t)),\\ \mathbb{E}_{\mathrm{t},\kappa}(\mathbf{\Theta}(t)) \in \mathcal{E}_{\mathrm{t}}(\mathbf{\Theta}(t))}}{\text{maximize}} \quad & \min d_{(\mathbf{x}_k, \mathbf{x}'_k)} \\
\text{subject to} \quad & d_{(\mathbf{x}_k, \mathbf{x}'_k)} > 0, \\
& \{\mathbf{x}_k, \mathbf{x}'_k \in \mathbb{X}_\kappa(\mathbf{\Theta}(t))\}, \\
& \mathbb{X}_\kappa(\mathbf{\Theta}(t)) = f(\mathbb{E}_{\mathrm{t},\kappa}(\mathbf{\Theta}(t))), \\
& |\mathbb{X}(\mathbf{\Theta}(t))| = 2^{|\mathbb{E}_{\mathrm{t},\kappa}(\mathbf{\Theta}(t))|}, \\
& |\mathbb{E}_{\mathrm{t},\kappa}(\mathbf{\Theta}(t))| = l, \\
& \mathbb{E}_{\mathrm{r},\kappa}(\mathbf{\Theta}(t)) = \mathbb{A}_{\mathrm{r}}(\mathbf{\Theta}(t))
\end{aligned}$$

  Estimate P_{bit} for the selected set $\tilde{\mathbb{E}}_{\mathrm{t}}(\mathbf{\Theta}(t))$
  if $P_{\mathrm{bit}} > P_{\mathrm{bit},0} \wedge l == 1$ **then**
    return $\mathbb{E}_{\mathrm{t,r}}(\mathbf{\Theta}(t)) = \varnothing$
    break
  else if $P_{\mathrm{bit}} > P_{\mathrm{bit},0} \wedge l > 1$ **then**
    return $\mathbb{E}_{\mathrm{t,r}}(\mathbf{\Theta}(t)) = \tilde{\mathbb{E}}'_{\mathrm{t}}(\mathbf{\Theta}(t))$
    break
  else
    continue
  end
  return $\mathbb{E}_{\mathrm{t,r}}(\mathbf{\Theta}(t)) = \tilde{\mathbb{E}}_{\mathrm{t,r}}(\mathbf{\Theta}(t)), F(\mathbf{\Theta}(t)) = F(\mathbb{E}_{\mathrm{t,r}}(\mathbf{\Theta}(t)))$
end

der of the engagable transmitter beam sets starting with $g = 1$ until either subsets $\mathcal{E}_{\mathrm{t}}^{g}(\mathbf{\Theta}(t))(b = N_{\mathrm{t}}^{\mathrm{a}}(\mathbf{\Theta}(t)))$ are searched through or $\mathcal{E}_{\mathrm{t}}^{g}(\mathbf{\Theta}(t))$ is reached that satisfies following:

$$\begin{aligned}
\mathcal{E}_{\mathrm{t}}^{g}(\mathbf{\Theta}(t)) = \{\forall\, \mathbb{E}_{\mathrm{t},\kappa}(\mathbf{\Theta}(t)) \in \mathcal{E}_{\mathrm{t}}(\mathbf{\Theta}(t)) \,:\, \forall\, |\mathbb{E}_{\mathrm{t},\kappa}(\mathbf{\Theta}(t))| = g \\
\wedge\, \forall\, \mathbb{E}_{\mathrm{t},\kappa}(\mathbf{\Theta}(t)) : P_{\mathrm{bit}}(\mathbb{E}_{\mathrm{t},\kappa}(\mathbf{\Theta}(t))) > P_{\mathrm{bit},0}\},
\end{aligned}$$

where last part signifies, that each engaged beam subset $\mathbb{E}_{\mathrm{t},\kappa}(\mathbf{\Theta}(t))$ in the set $\mathcal{E}_{\mathrm{t}}^{g}(\mathbf{\Theta}(t))$

satisfies the BER requirements. To evaluate the computational complexity of this algorithm we first note the Euclidean distance expression for two symbols:

$$d_{\mathbf{x}_k,\mathbf{x}_{k'}}(\mathbf{\Theta}(t)) = |\mathbf{H}(\mathbf{\Theta}(t))\Delta_{\mathbf{X}_k,\mathbf{X}_{k'}}|_{\mathrm{F}}. \tag{3.24}$$

It is shown in Appendix B that the number of operations for evaluating (3.24) is:

$$N^{\mathrm{ops}}_{d_{\mathbf{x}_k,\mathbf{x}_{k'}}}(\mathbb{E}_{\mathrm{t},\kappa}(\mathbf{\Theta}(t))) = N^{\mathrm{a}}_{\mathrm{r}}(\mathbf{\Theta}(t))N_{\mathrm{bit}}(|\mathbb{E}_{\mathrm{t},\kappa}(\mathbf{\Theta}(t))|N_{\mathrm{bit}} + 1 + N_{\mathrm{bit}}) + |\mathbb{E}_{\mathrm{t},\kappa}(\mathbf{\Theta}(t))|N_{\mathrm{bit}}. \tag{3.25}$$

For each set $\mathbb{E}_{\mathrm{t},\kappa}(\mathbf{\Theta}(t))$, there are $\binom{2^{|\mathbb{E}_{\mathrm{t},\kappa}(\mathbf{\Theta}(t))|}}{2}$ distinct Euclidean distances between unique symbols to be evaluated. Therefore,the number of operations required to evaluate all the unique Euclidean distances in the set $\mathbb{E}_{\mathrm{t},\kappa}(\mathbf{\Theta}(t))$ and select the minimum is:

$$N^{\mathrm{ops}}_{\mathbb{E}_{\mathrm{t},\kappa}(\mathbf{\Theta}(t))} = N^{\mathrm{ops}}_{d_{\mathbf{x}_k,\mathbf{x}_{k'}}}(\mathbb{E}_{\mathrm{t},\kappa}(\mathbf{\Theta}(t)))\binom{2^{|\mathbb{E}_{\mathrm{t},\kappa}(\mathbf{\Theta}(t))|}}{2} + (\binom{2^{|\mathbb{E}_{\mathrm{t},\kappa}(\mathbf{\Theta}(t))|}}{2})^2, \tag{3.26}$$

the second term accounts the sorting algorithm complexity used to select minimum Euclidean distance. The time complexity upper bound of (3.26) asymptotically tends to:

$$\lim_{|\mathbb{E}_{\mathrm{t},\kappa}(\mathbf{\Theta}(t))|\to\infty} N^{\mathrm{ops}}_{\mathbb{E}_{\mathrm{t},\kappa}(\mathbf{\Theta}(t))} = O((\binom{2^{|\mathbb{E}_{\mathrm{t},\kappa}(\mathbf{\Theta}(t))|}}{2})^2). \tag{3.27}$$

The total number of operations to select $\mathbb{E}_{\mathrm{t,r}}(\mathbf{\Theta}(t))$ up to the number of engaged transmitter beams $|\mathbb{E}_{\mathrm{t}}(\mathbf{\Theta}(t))| = G$ can be calculated as follows:

$$N^{\mathrm{ops}}_{\mathrm{tot}}(|\mathbb{E}_{\mathrm{t}}(\mathbf{\Theta}(t))| = G) = \sum_{g=1}^{g=G} \sum_{\substack{\mathbb{E}_{\mathrm{t},\kappa}(\mathbf{\Theta}(t)) \\ \in\mathcal{E}^g_{\mathrm{t}}(\mathbf{\Theta}(t))}} (N^{\mathrm{ops}}_{\mathbb{E}_{\mathrm{t},\kappa}(\mathbf{\Theta}(t))} + |\mathcal{E}^g_{\mathrm{t}}(\mathbf{\Theta}(t))|^2), \tag{3.28}$$

the second term in the sum represents the number of operations required to select the set that maximises the minimum Euclidean distance in the set $\mathcal{E}^g_{\mathrm{t}}(\mathbf{\Theta}(t))$. The number of summations for $g = G$ is $\binom{N^{\mathrm{a}}_{\mathrm{t}}(\mathbf{\Theta}(t))}{G}$.

The number of operations and selection time required for Algorithm 1 as a function of engaged receivers and transmitter beams are represented in Figure 3.5 and Figure 3.6 respectively. Similar to Figures 3.3 and 3.4, the dashed line indicates the maximum

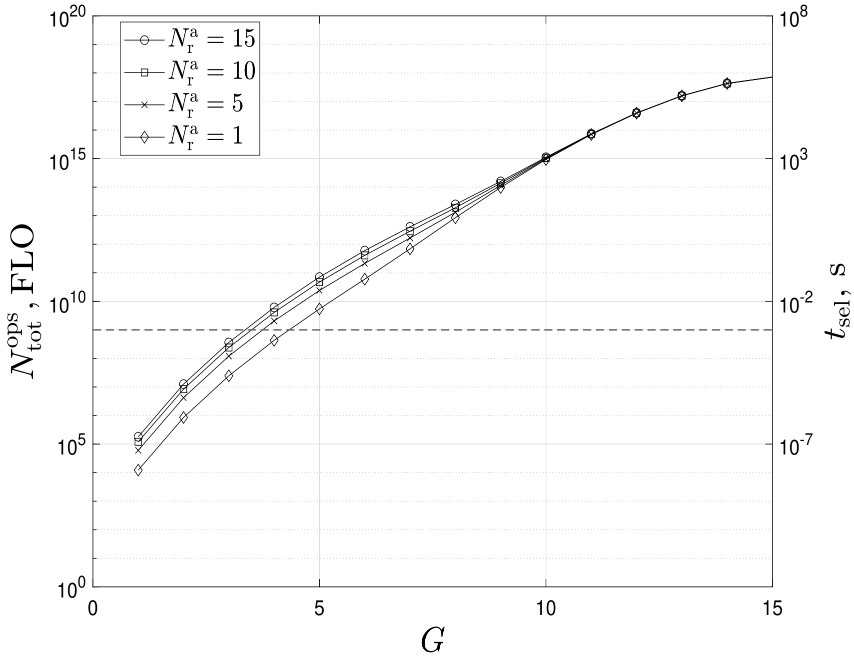

Figure 3.5: Number of floating point operations (FLO) and selection time required to perform maximal minimal Euclidean distance based set selection for various fixed $N_{\mathrm{r}}^{\mathrm{a}}$ dependent on G. Dashed line indicates maximal latency.

permissible latency. The number of available transmitter beams in both Figures is set to 15.

In Figure 3.5 there is a strong exponential growth in number of operations as the number of engaged beams increases. The complexity for various number of receivers converges towards the same asymptotic curve at $G = 10$ as expected from (3.27).

In Figure 3.6, we observe a comparatively smaller increase in the complexity as the number of available receivers grows. The primary source of computational complexity arises from the need to compute a large number of unique pairwise Euclidean distances together with the increasing size of the search space. For instance, when $G = 2$ we need to evaluate only 6 distances but for $G = 6$ this number grows to 2016.

Figure 3.7 illustrates the impact on the number of available transmitters on the computational complexity of Algorithm 1. In this evaluation, we maintain the number of available receivers at 15. We observe that depending on the number of available transmitter beams, the number of maximum engaged transmitter beams within the

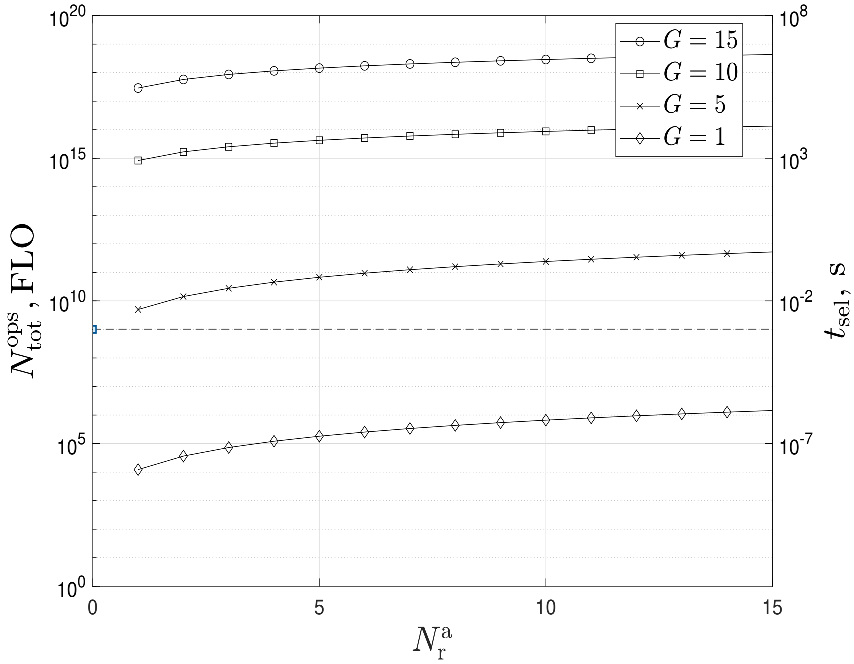

Figure 3.6: Number of floating point operations (FLO) and selection time required to perform maximal minimal Euclidean distance based set selection for various fixed G dependent on $N_{\mathrm{r}}^{\mathrm{a}}$. Dashed line indicates maximal latency.

latency constraints transmitters can vary from $G = 5$ for $N_{\mathrm{t}}^{\mathrm{a}} = 5$ to $G = 3$ for $N_{\mathrm{t}}^{\mathrm{a}} = 15$.

From results above we can conclude that the computational complexity of the maximal minimum Euclidean distance selection is comparable to that of channel capacity maximisation. However, unlike the channel capacity maximisation the primary limitation here arises from the number of available and engaged transmitter beams (target spectral efficiency). The limitation arises from the large search space of all the possible combinations of engaged beams. This implies that the adaptive GSSK algorithm using Euclidean distance as a beam selection criterion can support a large number of receivers but it is constrained to a low number of available transmitter beams in the link that it can process within the latency requirements.

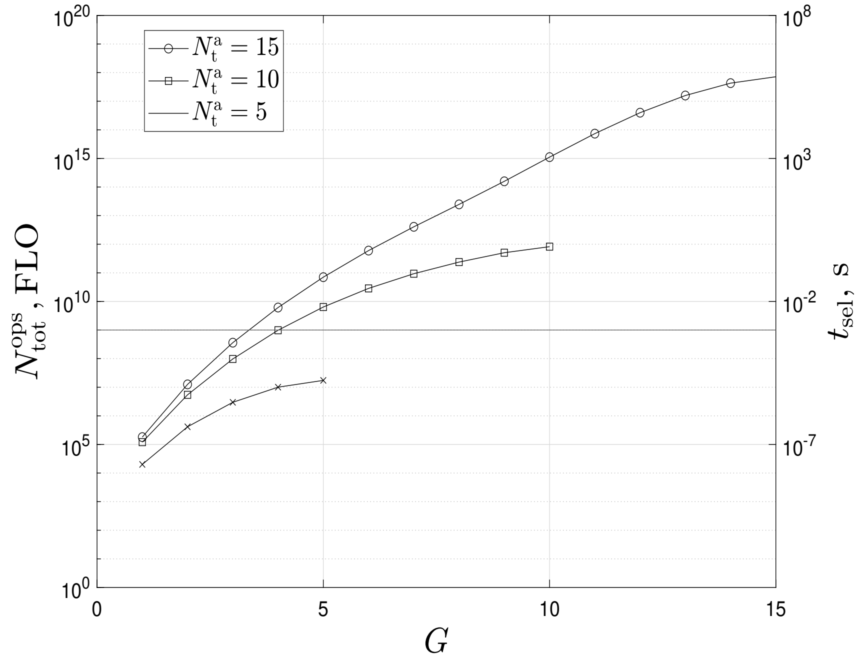

Figure 3.7: Number of floating point operations (FLO) and selection time required to perform maximal minimal Euclidean distance based set selection for various fixed N_t^a dependent on G. Dashed line indicates maximal latency.

Maximal SNR Based Set Selector

As we have seen, the selections based on the previous two metrics are computationally costly. Another parameter that can be used for the codebook selection is SNR. In this case, the algorithm selects a transmitter beam set that maximises the total channel gain:

$$\Delta_{h_k} = \sum_{i=1}^{|\mathbb{A}_r(\boldsymbol{\Theta}(t))|} h_{ik}^2 \tag{3.29}$$

The selection is conducted over the columns where each column index represents a transmitter beam, in the available transmitter and receiver channel gain matrix $\mathbf{H}_A(\boldsymbol{\Theta}(t))$. Algorithm 2 performs transmitter beam set selection, similar to Algorithm 1, which involves engaging all available receivers. The algorithm starts with a single-beam GSSK transmission and, in the each subsequent iteration, selects the next column of matrix $\mathbf{H}_a$ that maximises condition (3.29). It tests the condition $P_{bit} < P_{bit,0}$ until either the BER threshold is met or all available transmitters beams are engaged.

Algorithm 2: Maximal SNR Criterion Based Set Selector

Input: $\mathbb{A}_{\mathrm{t}}(\mathbf{\Theta}(t))$,$\mathbb{A}_{\mathrm{r}}(\mathbf{\Theta}(t)), \mathbf{H}_{\mathrm{A}}(\mathbf{\Theta}(t))$;

Define: $P_{\mathrm{bit},0}$ as the upper BER threshold, element of matrix $\mathbf{H}_{\mathrm{A}}(\mathbf{\Theta}(t))$ as h_{ik};

Set: $\mathbb{E}_{\mathrm{t,r}}(\mathbf{\Theta}(t)) = \{\mathbb{A}_{\mathrm{r}}(\mathbf{\Theta}(t)) \cup \varnothing\}$, $P_{\mathrm{bit}} = 0$, $l = 1$, $k_{l=0} = 0$

while $P_{\mathrm{bit}} < P_{\mathrm{bit},0} \wedge l \leq |\mathbb{A}_{\mathrm{t}}(\mathbf{\Theta}(t))|$ **do**

  Select: $\mathbf{H}_{\mathrm{A}}(\mathbf{\Theta}(t))$ column $k_l \in k = \{1, 2, ..., |\mathbb{A}_{\mathrm{t}}(\mathbf{\Theta}(t))|\}$ such that:

$$k_l = \underset{k \neq k_{(l-1)}}{\mathrm{argmax}} \sum_{i=1}^{|\mathbb{A}_{\mathrm{r}}(\mathbf{\Theta}(t))|} h_{ik}^2$$

  Set: $\tilde{\mathbb{E}}_{\mathrm{t,r}}(\mathbf{\Theta}(t)) = \{\mathbb{E}_{\mathrm{t,r}}(\mathbf{\Theta}(t)) \cup m_{k_l} \in \mathbb{A}_{\mathrm{t}}(\mathbf{\Theta}(t))\}$

  Estimate P_{bit} for the selected set $\tilde{\mathbb{E}}_{\mathrm{t,r}}(\mathbf{\Theta}(t))$

  if $P_{\mathrm{bit}} > P_{\mathrm{bit},0} \wedge l == 1$ **then**

    return $\mathbb{E}_{\mathrm{t,r}}(\mathbf{\Theta}(t)) = \varnothing$

    break

  else if $P_{\mathrm{bit}} > P_{\mathrm{bit},0} \wedge l > 1$ **then**

    return $\mathbb{E}_{\mathrm{t,r}}(\mathbf{\Theta}(t)) = \tilde{\mathbb{E}}_{\mathrm{t}}(\mathbf{\Theta}(t)) \setminus \{m_{k_l}\}$

    break

  else

    continue

  end

  return $\mathbb{E}_{\mathrm{t,r}}(\mathbf{\Theta}(t)) = \tilde{\mathbb{E}}_{\mathrm{t,r}}(\mathbf{\Theta}(t)), F(\mathbf{\Theta}(t)) = F(\mathbb{E}_{\mathrm{t,r}}(\mathbf{\Theta}(t)))$

end

Number of operations for Algorithm 2 can be shown to be (see Appendix B):

$$N_{\mathrm{SNR}}^{\mathrm{ops}}(\mathbb{E}_{\mathrm{t},\kappa}(\mathbf{\Theta}(t))) = |\mathbb{A}_{\mathrm{t}}(\mathbf{\Theta}(t))||\mathbb{A}_{\mathrm{r}}(\mathbf{\Theta}(t))|N_{\mathrm{bit}}^2 + |\mathbb{A}_{\mathrm{t}}(\mathbf{\Theta}(t))||\mathbb{A}_{\mathrm{r}}(\mathbf{\Theta}(t))|N_{\mathrm{bit}} + |\mathbb{A}_{\mathrm{t}}(\mathbf{\Theta}(t))|^2. \quad (3.30)$$

As can be seen from (3.30) the number of operations is only dependent on the number of available receivers and transmitter beams. The time complexity asymptotically tends to:

$$\lim_{|\mathbb{A}_{\mathrm{t}}(\mathbf{\Theta}(t))| \to \infty} N_{\mathrm{SNR}}^{\mathrm{ops}}(\mathbb{E}_{\mathrm{t},\kappa}(\mathbf{\Theta}(t))) = O(|\mathbb{A}_{\mathrm{t}}(\mathbf{\Theta}(t))|^2), \quad (3.31)$$

and

$$\lim_{|\mathbb{A}_{\mathrm{r}}(\mathbf{\Theta}(t))| \to \infty} N_{\mathrm{SNR}}^{\mathrm{ops}}(\mathbb{E}_{\mathrm{t},\kappa}(\mathbf{\Theta}(t))) = O(|\mathbb{A}_{\mathrm{r}}(\mathbf{\Theta}(t))|). \quad (3.32)$$

While the number of operations in (3.31) asymptotically tends towards $O(|\mathbb{A}_{\mathrm{r}}(\mathbf{\Theta}(t))|^2)$, the third term in (3.30) begins to dominate over the first two terms when $|\mathbb{A}_{\mathrm{t}}(\mathbf{\Theta}(t))| =$

272 with $|\mathbb{A}_{\mathrm{r}}(\boldsymbol{\Theta}(t))| = 1$ and at $|\mathbb{A}_{\mathrm{t}}(\boldsymbol{\Theta}(t))| = 4080$ with $|\mathbb{A}_{\mathrm{r}}(\boldsymbol{\Theta}(t))| = 15$. Therefore, for all practical scenarios, the number of operations of Algorithm 2 exhibits a linear relationship with both $|\mathbb{A}_{\mathrm{r}}(\boldsymbol{\Theta}(t))|$ and $|\mathbb{A}_{\mathrm{t}}(\boldsymbol{\Theta}(t))|$. The discussed linear dependency can be clearly observed in Figures 3.8 and 3.9.

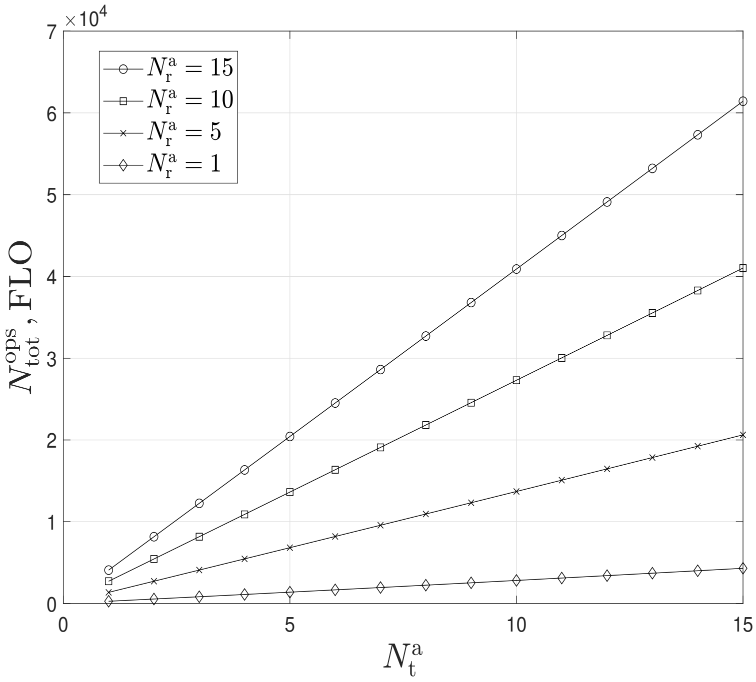

Figure 3.8: Number of floating point operations (FLO) required perform maximal SNR based set selection for various fixed $N_{\mathrm{r}}^{\mathrm{a}}$ dependent on $N_{\mathrm{t}}^{\mathrm{a}}$.

Compared to Algorithm 1, the number of operations required to select $\mathbb{E}_{\mathrm{t,r}}(\boldsymbol{\Theta}(t))$ can be orders of magnitude lower for an arbitrarily high number of receivers and transmitters. In scenarios with around 10 transmitter beams and receivers, the algorithm incurs a latency penalty in the order of tens of nanoseconds.

The primary drawback of using maximal SNR as a transmitter beam set selection criterion is its lack of differentiation towards different transmitter beam optical powers observed at the receiver. For example, a maximal SNR selection criterion based algorithm might choose 2 transmitter beams, that together maximise (3.29). However, the difference between these selected beams can sometimes be arbitrarily small. In such cases, the Euclidean distance between symbols representing bit vectors like "10" and

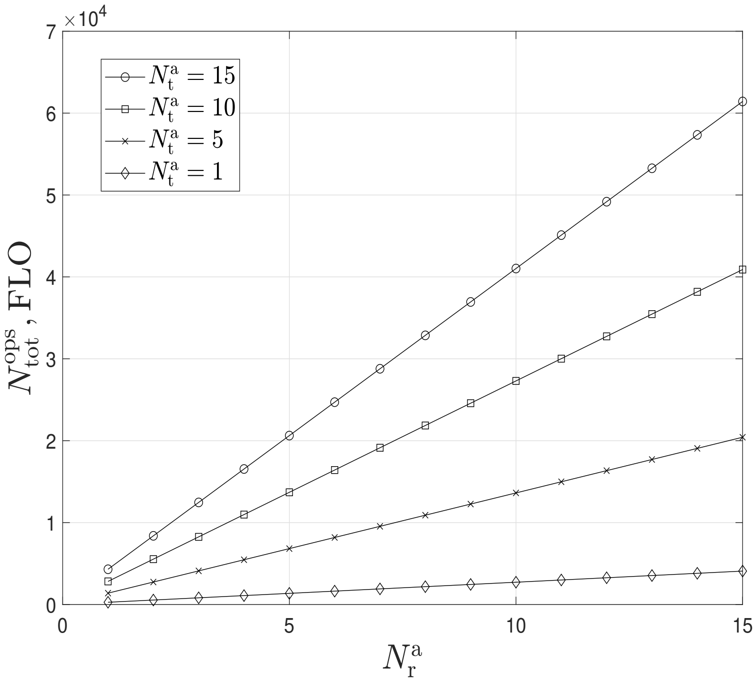

Figure 3.9: Number of floating point operations (FLO) required to perform maximal SNR based set selection for various fixed N_t^a dependent on N_r^a.

"01" approaches 0 while the bit error probability will tend towards 0.5, assuming equal symbol probabilities. Care must be taken in the design of an optical transmission and reception system that would impose physical constraints that prevent such selections.

Optimal GSSK Channel Ratio Set Selector

So far, the beam selection algorithms have either been very exhaustive and selective on the inter-symbol Euclidean distances such as Algorithm 1 leading to high computational complexity costs. Or, in contrary, as Algorithm 2 has displayed they lack granularity towards the inter-symbol spacing, focusing on a single common value such as overall link SNR. However, we can exploit the properties of optical GSSK to design a more computationally efficient algorithm than the maximal minimum Euclidean distance one, while accounting for the required beam distingushability with improved granularity compared to Algorithm 2.

Consider an N_t^e-beam GSSK link. The number of symbols in the alphabet required to transmit any data sequence is $2^{N_\mathrm{t}^\mathrm{e}}$. The maximum optical power P is received when $\{\forall x_i \in \mathbf{x}_{k=2^{N_\mathrm{t}^\mathrm{e}}-1} : x_i = P_H\}$ and minimum P_0 when $\{\forall x_i \in \mathbf{x}_{k=0} : x_i = P_L\}$. For each symbol $\mathbf{x}_k$ there is a corresponding optical power level received $P_k = \sum_{i=1}^{N_\mathrm{t}^\mathrm{e}} x_{ik}$. The symbol optical power levels form a one-dimensional array of increasing values akin to the points on a line of length $L = P - P_0$ measured in watt.

It is well-known that to maximise the minimal distance between points on a line, they should be uniformly distributed with their spacing given by:

$$\delta = \frac{L}{2^{N_\mathrm{t}^\mathrm{e}} - 1}. \tag{3.33}$$

The symbol power levels then are distributed as: $P_0, P_0 + \delta, P_0 + 2\delta, ..., P_0(2^{N_\mathrm{t}^\mathrm{e}} - 1)\delta$. Because of uniform point distribution we can write the following:

$$P_k - P_{k-1} = P_2 - P_1 = \delta, \tag{3.34}$$

assuming GSSK encoding, P_2 and P_1 correspond to symbols $\mathbf{x}_{k=2} = [P_L, P_L, ..., P_H, P_L]$ and $\mathbf{x}_{k=1} = [P_L, P_L, ..., P_L, P_H]$ as measured at the receiver. We can write then that:

$$P_2 = aP_1, \tag{3.35}$$

where a is some proportionality coefficient. Inserting (3.35) into (3.34) we get:

$$\begin{aligned} P_k - P_{k-1} = P_1(a-1) &= \delta, \\ P_1(a-1) &= P_1 - P_0, \\ a &= 2 + \frac{P_0}{P_1}. \end{aligned} \tag{3.36}$$

The second term in (3.36) resembles the inverse of extinction ratio r_e. It can be shown that in the limit of a single transmitter and receiver link, a becomes $1/r_\mathrm{e}$ of the transmitter beam source. If we assume a perfect extinction ratio of the source, where $P_0 = P_L = 0$, then $a = 2$ correspondingly. In practice, however, a can vary substantially with the extinction ratio, which can potentially affect the performance of the adaptive algorithm.

Based on the expressions above, to maximise symbol spacing, each successive transmitter beam added to the engaged set under test $\tilde{\mathbb{E}}_{\mathrm{t,r}}(\boldsymbol{\Theta}(t))$ should transmit optical power, which at the receiver is half of the previously added beam. Since all transmitter beams emit the same optical power P_{H} or P_{L}, the distinguishability between them relies on the differences in receiver and transmitter beam channel gains. The algorithm should select the first transmitter beam to maximise (3.29) while each subsequent l^{th} transmitter beam minimises the following:

$$\Delta_{h_{k(l),k(l-1)}} = \sum_{i=1}^{|\mathbb{A}_{\mathrm{r}}(\boldsymbol{\Theta}(t))|} |\frac{h_{ik_{(l-1)}}^2}{h_{ik}^2} - a|^2. \tag{3.37}$$

Algorithm 3 (see the next page) performs transmitter beam selection similarly to Algorithm 2. Like the maximal SNR based condition set selector, Algorithm 3 engages all available receivers in the selection process. Each matrix column index one-to-one matches an available transmitter beam index. The algorithm starts with a single beam GSSK transmission selection based on the maximum SNR by solving (3.29). In each subsequent iteration, the algorithm selects the next matrix $\mathbf{H}_{\mathrm{a}}$ column that minimises condition (3.37). The algorithm tests $P_{\mathrm{bit}} < P_{\mathrm{bit},0}$ and continues adding transmitter beams to the set under test until it either meets the BER threshold or engages all available transmitter beams. This approach ensures that each additional beam maintains uniformly spaced optical transmission power levels at the receiver, resembling the maximal minimum Euclidean distance-based transmitter beam selection.

Algorithm 3: Optimal GSSK Channel Ratio Criterion Set Selector

Input: $\mathbb{A}_{\mathrm{t}}(\mathbf{\Theta}(t))$,$\mathbb{A}_{\mathrm{r}}(\mathbf{\Theta}(t)), \mathbf{H}_{\mathrm{A}}(\mathbf{\Theta}(t))$;
Define: $P_{\mathrm{bit},0}$ as the upper BER threshold, element of matrix $\mathbf{H}_{\mathrm{A}}(\mathbf{\Theta}(t))$ as h_{ik};
Set: $\mathbb{E}_{\mathrm{t,r}}(\mathbf{\Theta}(t)) = \{\mathbb{A}_{\mathrm{r}}(\mathbf{\Theta}(t)) \cup \varnothing\}$, $P_{\mathrm{bit}} = 0$, $l = 1$, $a = 2$
while $P_{\mathrm{bit}} < P_{\mathrm{bit},0} \wedge l \leq |\mathbb{A}_{\mathrm{t}}(\mathbf{\Theta}(t))| \wedge k_l \leq |\mathbb{A}_{\mathrm{t}}(\mathbf{\Theta}(t))|$ **do**
  if $l == 1$ **then**
    Select: $\mathbf{H}_{\mathrm{A}}(\mathbf{\Theta}(t))$ column $\tilde{k} \in \mathbb{K} = \{1, 2, ..., |\mathbb{A}_{\mathrm{t}}(\mathbf{\Theta}(t))|\}$ such that:

$$\tilde{k} = \underset{k \in \mathbb{K}}{\operatorname{argmax}} \sum_{i=1}^{|\mathbb{A}_{\mathrm{r}}(\mathbf{\Theta}(t))|} h_{ik}^2$$

    Set: $\tilde{\mathbb{E}}_{\mathrm{t,r}}(\mathbf{\Theta}(t)) = \{\mathbb{E}_{\mathrm{t,r}}(\mathbf{\Theta}(t)) \cup m_{\tilde{k}} \in \mathbb{A}_{\mathrm{t}}(\mathbf{\Theta}(t))\}$
    Estimate P_{bit} for the selected set $\tilde{\mathbb{E}}_{\mathrm{t,r}}(\mathbf{\Theta}(t))$
    if $P_{\mathrm{bit}} > P_{\mathrm{bit},0}$ **then**
      return $\mathbb{E}_{\mathrm{t,r}}(\mathbf{\Theta}(t)) = \varnothing$
      break
    else
      Set: $l = l + 1$, $\mathbb{K} = \mathbb{K} \setminus \{\tilde{k}\}$
      continue;
    end
  else
    Set: $k_0 = \tilde{k}$
    Select: $\mathbf{H}_{\mathrm{A}}(\mathbf{\Theta}(t))$ column $\tilde{k} \in \mathbb{K}$ such that:

$$\tilde{k} = \underset{k \in \mathbb{K}}{\operatorname{argmin}} \sum_{i=1}^{|\mathbb{A}_{\mathrm{r}}(\mathbf{\Theta}(t))|} |(\frac{h_{ik_0}}{h_{ik}})^2 - a|^2$$

    Set: $\tilde{\mathbb{E}}_{\mathrm{t,r}}(\mathbf{\Theta}(t)) = \{\tilde{\mathbb{E}}_{\mathrm{t,r}}(\mathbf{\Theta}(t)) \cup m_{\tilde{k}} \in \mathbb{A}_{\mathrm{t}}(\mathbf{\Theta}(t))\}$
    Estimate P_{bit} for the selected set $\tilde{\mathbb{E}}_{\mathrm{t,r}}(\mathbf{\Theta}(t))$
    if $P_{\mathrm{bit}} > P_{\mathrm{bit},0}$ **then**
      return $\mathbb{E}_{\mathrm{t,r}}(\mathbf{\Theta}(t)) = \tilde{\mathbb{E}}_{\mathrm{t,r}}(\mathbf{\Theta}(t)) \setminus \{m_{\tilde{k}}\}$
      break
    else
      Set: $l = l + 1$, $\mathbb{K} = \mathbb{K} \setminus \{\tilde{k}\}$
      continue
    end
  end
end
return $\mathbb{E}_{\mathrm{t,r}}(\mathbf{\Theta}(t)) = \tilde{\mathbb{E}}_{\mathrm{t,r}}(\mathbf{\Theta}(t)), F(\mathbf{\Theta}(t)) = F(\mathbb{E}_{\mathrm{t,r}}(\mathbf{\Theta}(t)))$

The number of operations for Algorithm 3 to select $|\mathbb{E}_{\mathrm{t,r}}(\boldsymbol{\Theta}(t))|$ engaged transmitter beams can be shown to be (see Appendix B):

$$N^{\mathrm{ops}}_{\mathrm{Alg3}}(\mathbb{E}_{\mathrm{t},\kappa}(\boldsymbol{\Theta}(t))) = |\mathbb{A}_{\mathrm{t}}(\boldsymbol{\Theta}(t))||\mathbb{A}_{\mathrm{r}}(\boldsymbol{\Theta}(t))|N^2_{\mathrm{bit}} + |\mathbb{A}_{\mathrm{t}}(\boldsymbol{\Theta}(t))||\mathbb{A}_{\mathrm{r}}(\boldsymbol{\Theta}(t))|N_{\mathrm{bit}}$$
$$+|\mathbb{A}_{\mathrm{t}}(\boldsymbol{\Theta}(t))|^2 + \sum_{i=1}^{|\mathbb{E}_{\mathrm{t}}(\boldsymbol{\Theta}(t))|-1} (2(|\mathbb{A}_{\mathrm{t}}(\boldsymbol{\Theta}(t))|-i)|\mathbb{A}_{\mathrm{r}}(\boldsymbol{\Theta}(t))|N_{\mathrm{bit}}(1+N_{\mathrm{bit}})+(|\mathbb{A}_{\mathrm{t}}(\boldsymbol{\Theta}(t))|-i)^2). \tag{3.38}$$

As can be seen in (3.38) the first three terms represent the number of operations needed for maximal SNR condition based selection. In fact, in the case of a single beam selection, the number of operations for Algorithm 3 is reduced to that of Algorithm 2. In the sum term, we can observe that, for most practical scenarios, the number of operations depend linearly on the number of available transmitter beams and receivers.

The number of required operations, depending on the number of engaged transmitter beams, is illustrated in Figure 3.10. Here the number of available transmitter beams is set to 15. It is evident that the number of operations rapidly increases until $N^{\mathrm{e}}_{\mathrm{t}} = 5$. This slowing of increase can be attributed to the decreasing contribution from sum terms with a greater number of engaged transmitter beams. As more transmitter beams are engaged in the link, fewer beams need to be evaluated for the next selection, resulting in reduced search space and computational resources.

Figure 3.10 shows that the number of operations in Algorithm 3 is larger than in Algorithm 2. Still, it is orders of magnitude smaller than that of Algorithm 1, which allows for transmitter beam selection from a large pool of available transmitters accommodating a wider scope of use case scenarios. In the case when $N^{\mathrm{a}}_{\mathrm{r}} = 15$ and $N^{\mathrm{a}}_{\mathrm{t}} = 15$ the expected latency incurred by Algorithm 3 is in the range of a few hundred nanoseconds to microseconds.

Similar dependency for the number of required operations on the number of available receivers for the fixed number of engaged transmitter beams is shown in Figure 3.11. So far we have presented a mathematical framework and introduced the adaptive

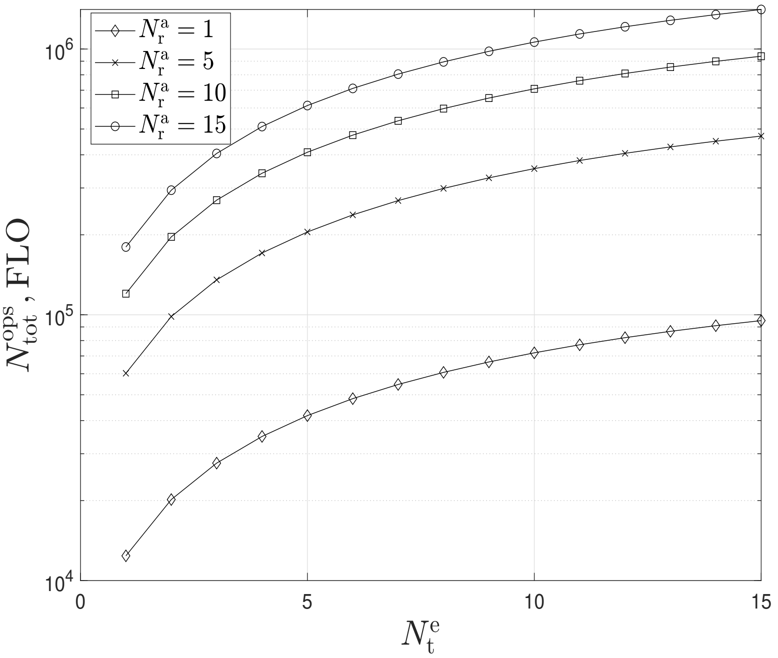

Figure 3.10: Number of floating point operations (FLOs) required to perform optimal GSSK channel ratio set selection for various fixed $N_{\rm r}^{\rm a}$ dependent on $N_{\rm t}^{\rm e}$.

GSSK algorithm. The critical component of this adaptive algorithm is the set selector, which, for each unique engaged transmitter beam and receiver set, determines the codebook to be used in GSSK data transmission. We've explored various set selection criteria, including maximisation of mutual information, maximal minimum Euclidean distance, maximal SNR, and optimal GSSK channel ratio, and compared their computational complexity. To comprehensively assess the performance of adaptive GSSK with different set selector algorithms, we also need to consider factors such as connectivity loss and achievable data throughput.

To this end we need to introduce a simulation optical test setup in which we will implement the adaptive GSSK algorithm and evaluate its performance for various set selector criteria.

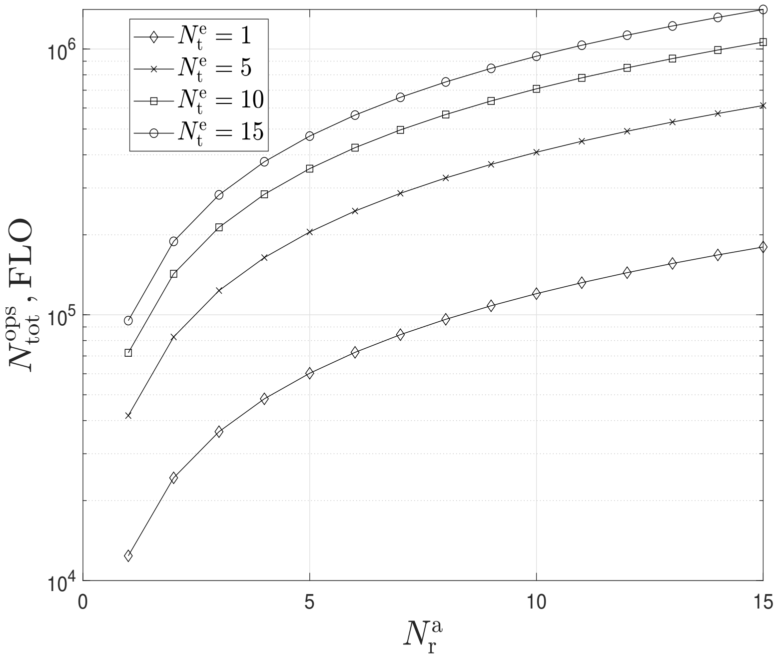

Figure 3.11: Number of floating point operations (FLOs) required to perform optimal GSSK channel ratio set selection for various fixed N_t^e dependent on N_r^a.

3.4 Simulation Optical Test Setup

In this study, we will delve into the performance evaluation of the adaptive GSSK algorithm within the context of two different optical test scenarios. The first scenario assumes a LoS indoor VLC scenario for mobile users. The scenario is characterised by non-directionality, signifying that the alignment of transmitter beams and the receivers along their distance vector is not perfectly aligned with their respective optical axis. The receiver end is embedded into portable UE allowing users the freedom to move around the room, while the transmitting end is incorporated into a fixed ceiling AP.

The objective of scenario is to investigate the capability of the adaptive GSSK algorithm in maintaining seamless connectivity, achieving high data throughput and retaining acceptable latency within set limits. The scenario considers various set selection algorithms described in the previous section. The VLC optical front-end is selected with the aim to support 10 Gbit/s downlink data throughput. Uplink is not considered in this study. Both scenarios model a single user communication link.

In the second scenario, we investigate a directional infrared OWC link. In this configuration embedding of both transmitter end and receiver within a small factor device is considered. The compact device is characterized by a diameter of less than a centimeter. Such setup emulates a directional user-to-user device data transmission or a device-to-device connection, particularly relevant in the context of IoT applications or backhaul. The primary objective of this scenario is to assess the capability of the adaptive GSSK algorithm facilitating high data throughput device communication, aiming for the average throughput of 10 Gbit/s. The scenario considers a fixed distance and target coverage radius, while adhering to the latency constraints.

3.4.1 Hemispherical Transceiver MIMO-VLC Channel

In the initial scenario, we consider a configuration where both UE and AP are embedded onto hemispherical surfaces for angle diversity. This geometric arrangement is deliberately chosen to optimise LiFi link coverage in indoor environment all while adhering to the constraint of employing a singular AP and UE. The UE is equipped with an angle-diverse hemispherical receiver, comprising multiple segmented receiver photodiode cells and an embedded decoder. On the other hand, the AP features an angle-diverse hemispherical transmitter, equipped with multiple segmented transmitter micro-LED cells and an embedded encoder.

The set selector can be embedded either on the transmitter or receiver end or it can be hosted by a third-party device. For the purposes of our simulations we assume perfect channel sate information at the set selector and time synchronisation, and the adaptive GSSK transmission follows the block diagram in Figure 3.2. Whilst such conditions are idealistic, in indoor LoS scenario synchronisation can be achieved using clock recovery [262]. The impact of noisy channel estimation, however, can negatively impact the beam selection algorithm, the impact of which has been described in Chapter 5. Additionally, we assume that the communication link between the set selector and the encoder/decoder is assumed to be perfect.

As the scenario considers indoor environment we can assume that atmospheric scintillation has a negligible impact on the data transmission. Additionally, we consider an environment devoid of obstructions, where the scenario analyses an empty room use case with a single UE and a single fixed AP. The channel condition parameter in this scenario $\theta'_{ij}(t)$ between i^{th} engaged receiver photodetector cell and j^{th} engaged LED cell beam can be simplified to:

$$\theta'_{ij}(t) = [\mathbf{r}_{ij}(t), \boldsymbol{\Omega}_i(t)].$$

As previously mentioned the object's orientation with respect to the global co-ordinate axes are described using three Euler angles using successive elementary rotations about the global co-ordinate axes. These elementary rotations are represented by the multiplication of 3 elementary rotation matrices. Importantly, in this context the matrix multiplication is non-commutative, which means that there are 6 possible ways to arrange the sequence of successive rotations.

In this work, we adhere to the World Wide Web Consortium (WC3) specification [253] for the order of rotations. The intrinsic rotation orders are then given as: $(z \to x' \to y'')$ here $x'y'z'$ and $x''y''z''$ are the local co-ordinate systems rotated about z-axis, which is followed by a rotation about x'-axis. The elementary rotations are pitch $\beta \in [-\pi, \pi)$ corresponding to the rotation about x-axis, roll $\gamma \in [-\frac{\pi}{2}, \frac{\pi}{2})$ corresponding to the rotation about y-axis and yaw $\alpha \in [0, 2\pi)$ corresponding to the rotation about z-axis. The elementary rotations are shown in Figure 3.12.

By applying the Euler's rotation theorem, the rotation matrix for given angles α, β, γ can be written as [253]:

$$\mathbf{R}(\alpha, \beta, \gamma) = \begin{bmatrix} \cos\alpha\cos\gamma - \sin\alpha\sin\beta\sin\gamma & -\sin\alpha\cos\beta & \sin\alpha\sin\beta\cos\gamma + \cos\alpha\sin\gamma \\ \cos\alpha\sin\beta\sin\gamma + \sin\alpha\cos\gamma & \cos\alpha\cos\beta & \sin\alpha\sin\gamma - \cos\alpha\sin\beta\cos\gamma \\ -\cos\beta\sin\gamma & \sin\beta & \cos\beta\cos\gamma \end{bmatrix}.$$

A normal vector of i^{th} (j^{th}) receiver photodetector cell (LED cell beam) is $\mathbf{n}_i = [n_{1,i}, n_{2,i}, n_{3,i}]$ or $\mathbf{n}_j = [n_{1,j}, n_{2,j}, n_{3,j}]$, the rotated normal vector depending on the UE orientation is given as $\mathbf{n'}_i = [n'_{1,i}, n'_{2,i}, n'_{3,i}]$. The rotated normal vector can be

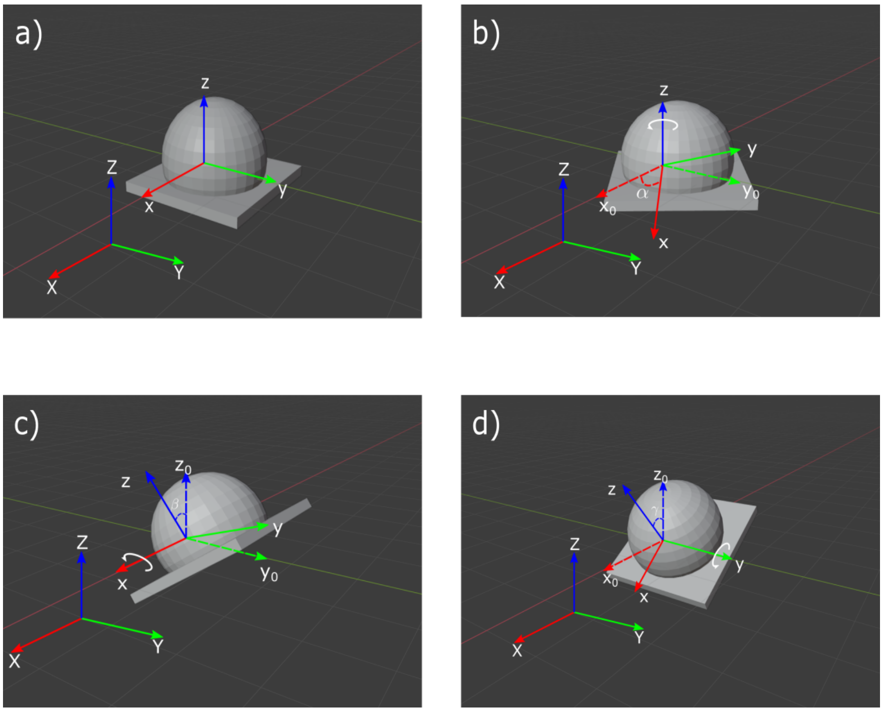

Figure 3.12: Orientations of a hemisphere: a) aligned to global axes, b) yaw rotation with angle α, c) pitch rotation with angle β, d) roll rotation with angle γ. Figure reproduced from [263].

expressed as:

$$\mathbf{n}_i' = \mathbf{R}(\alpha, \beta, \gamma)\mathbf{n}_i.$$

In this particular scenario, the MIMO hemispherical micro-LED (photodetector) cell arrangement for transmitter (receiver) and the geometry of the channel model is illustrated in Figures 3.13a and 3.13b, respectively. For the receivers avalanche photodiodes are considered. The data transmission over the LoS VLC channel for given channel state conditions $\mathbf{\Theta}'(t)$ at time instant t within the room is characterised by $N_{\mathrm{r}}^{\mathrm{e}}(\mathbf{\Theta}'(t)) \times N_{\mathrm{t}}^{\mathrm{e}}(\mathbf{\Theta}'(t))$ dimension optical DC channel gain matrix $\mathbf{H}_{0,\mathrm{e}}(\mathbf{\Theta}'(t))$ given by (3.11).

Assuming Lambertian emitters for the transmitter beam sources, each element of this matrix denoted as $h_{ij}(\theta'(t))$, represents the optical DC channel gain between i^{th} engaged receiver photodetector cell and j^{th} engaged LED cell beam and is defined as [73]:

$$h_{ij}(\theta'(t),\lambda) = \frac{m_{\text{lens}}+1}{2\pi d_{ij}^2(\mathbf{r}_{ij}(t))} A_{\text{PD}} G_{ij}^{\text{filter}}(\theta'(t),\lambda) G_{\text{con}} \times \cos^{m_{\text{lens}}}(\varphi_{ij}(\mathbf{r}_{ij}(t)) \cos(\psi_{ij}(\theta'(t))\text{rec}\left(\frac{\psi_{ij}(\theta'(t))}{\Psi_c}\right). \tag{3.39}$$

The angles φ_{ij} and ψ_{ij} are given by the following expressions [194]:

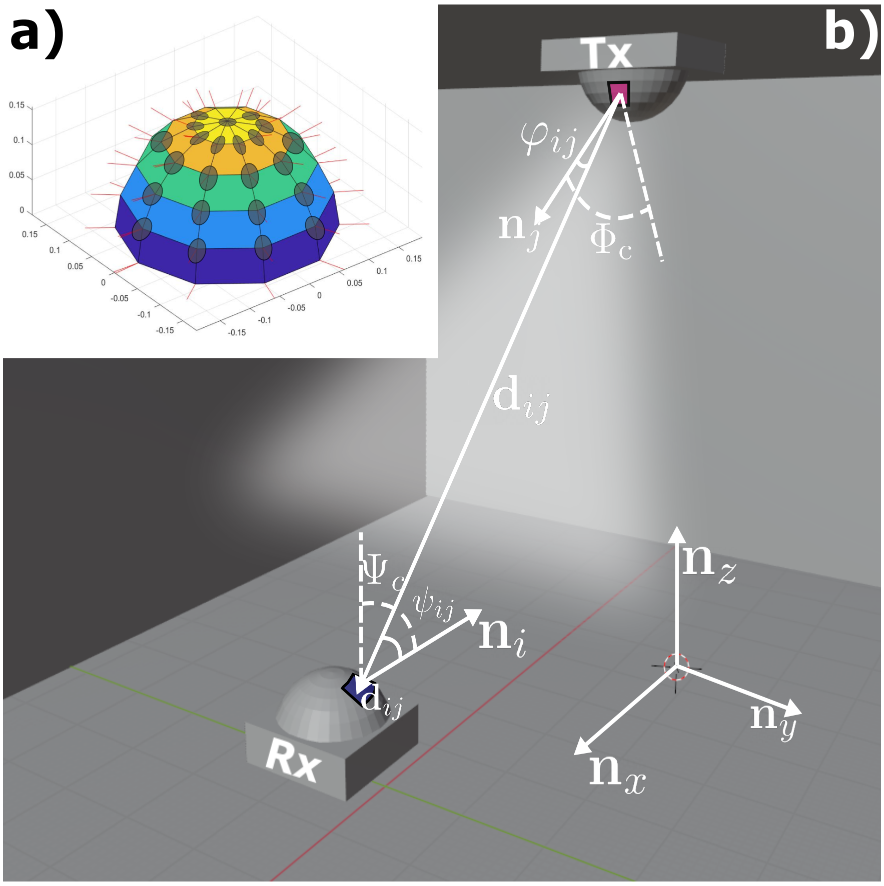

Figure 3.13: a) The arrangement of transmitter beam sources or receivers (indicated with dark ellipses) on a hemispherical transmitter (receiver) surface, b) The geometrical representation of the hemispherical channel link model, "Rx" indicates the UE and "Tx" - the AP.

$$\varphi_{ij}(\mathbf{r}_{ij}(t)) = \arccos\left(\frac{\mathbf{n}_j \cdot \mathbf{r}_{ij}(t)}{d_{ij}(\mathbf{r}_{ij}(t))}\right),$$
$$\psi_{ij}(\theta'(t)) = \arccos\left(\frac{\mathbf{n}_i(\mathbf{\Omega}_i(t)) \cdot \mathbf{r}_{ij}(t)}{d_{ij}(\mathbf{r}_{ij}(t))}\right).$$

The LoS constraint for the photodetector and LED cells is modelled with the rectangular functions [194]:

$$\begin{aligned}
\operatorname{rec}\left(\frac{\psi_{ij}}{\Psi_c}\right) &= 1 \qquad\qquad \psi_{ij} \leq \Psi_{\mathrm{c}}, \\
\operatorname{rec}\left(\frac{\psi_{ij}}{\Psi_c}\right) &= 0 \qquad\qquad \psi_{ij} > \Psi_{\mathrm{c}},
\end{aligned}$$

here Ψ_{c} is the acceptance angle of the optical concentrator. The $G_{ij}^{\mathrm{filter}}(\theta'(t))$ – optical gain from the optical bandpass filter at the receiver end, which is given as [153]:

$$G_{ij}^{\mathrm{filter}}(\theta'(t)) = T_{\mathrm{filter}}(\lambda_{ij}^{\psi}(\theta'(t))),$$

here $T_{\mathrm{filter}}(\lambda_{ij}^{\psi}(\theta'(t)))$ is the transmissivity of the band-pass filter at the angle of incidence ψ relative to the surface normal of the filter. $\lambda_{ij}^{\psi}(\theta'(t))$ corresponds to the central wavelength of the transmission passband accounting the shift [153]:

$$\lambda_{ij}^{\psi}(\theta'(t)) = \lambda\sqrt{(1-(\frac{n_0}{n_{\mathrm{filter}}})^2 \sin^2 \psi_{ij}(\theta'(t))},$$

here n_0 is the refractive index of the external medium, n_{filter} is the refractive index of the optical bandpass filter and λ is the central wavelength of the transmission passband at the incidence angle ψ normal to the filter's surface. A_{PD} is the photoactive area of a photodetector cell. Lambertian order m_{LED} is given as [194]:

$$m_{\mathrm{LED}} = -\frac{\ln 2}{\ln\left(\cos\left(\Phi_{1/2}\right)\right)},$$

where $\Phi_{1/2}$ - half intensity angle of an LED. The compound parabolic optical concentrator gain G_{con} is given as [73]:

$$G_{\mathrm{con}} = \frac{n_{\mathrm{con}}^2}{\sin^2\left(\Psi_{\mathrm{c}}\right)},$$

where n_{con} is the refractive index of the photodetector cell optical concentrator.

Photocurrent generated in the i^{th} receiver cell of APDs due to the incident optical power emitted by the j^{th} transmitter beam at a specific receiver location $\mathbf{r}$ is [53]:

$$I_{ij}(\theta'(t), \lambda) = P_{\text{opt}}^{\text{lens}}(B) h_{ij}(\theta'(t), \lambda) H(B) R(\lambda) M_{\text{APD}}, \tag{3.40}$$

here avalanche photo-diode responsivity is given by $R(\lambda)$, multiplication factor is M_{APD} and $H(B)$ is photodiode frequency response given at the centre frequency. The optical power $P_{\text{opt}}^{\text{lens}}(B)$ after condenser lens on the cell is [264]:

$$P_{\text{opt}}^{\text{lens}}(B) = \frac{(m_{\text{LED}} + 1) D_{\text{lens}}^2}{8d'^2} T_{\text{lens}} P_{\text{opt}}(B),$$

where D_{lens} is the condenser lens diameter, d' is the distance between micro-LED array and lens and T_{lens} - transmissivity of the lens. The half intensity angle of the condenser lens is given as [264]:

$$\Phi_{1/2}^{\text{lens}} = \frac{D_{\text{LED}}}{2d'},$$

here D_{LED} - diameter of the LED array. The Lambertian order of the beam after passing the condenser lens is given as [264]:

$$m_{\text{lens}} = -\frac{\ln 2}{\ln\left(\cos\left(\Phi_{1/2}^{\text{lens}}\right)\right)}.$$

The received electrical power at i^{th} photodetector cell from j^{th} transmitter is [194]:

$$P_{ij}^{\text{elec}}(\theta'(t), \lambda) = \frac{I_{ij}^2(\theta'(t), \lambda) G_{\text{TIA}}^2}{R_{\text{Load}}},$$

here G_{TIA} is transimpedance amplifier (TIA) gain and R_{Load} - the photodetector's cell load resistance of 50 ohms.

The electrical SNR γ_{ij} is given as [194]:

$$\gamma_{ij}^{\text{elec}}(\theta'(t), \lambda) = \frac{P_{ij}^{\text{elec}}(\theta'(t), \lambda)}{\sigma_{ij}^2(\theta'(t), \lambda)}. \tag{3.41}$$

We assume the use case scenario within well-illuminated office conditions, where the primary source of noise is shot noise due to the incident photons from background illumination and signal at j^{th} transmitter beam at i^{th} receiver is expressed as [194]:

$$\sigma_{ij}^2(\theta'(t),\lambda) = 2qM_{\text{APD}}^2 F_{\text{APD}} R(\lambda) B P_{\text{bg}}(\theta'(t)) + \frac{I_{ij}(\theta'(t),\lambda)}{M_{\text{APD}} R(\lambda)}) \frac{G_{\text{TIA}}^2}{R_{\text{Load}}}, \tag{3.42}$$

here F - excess noise factor of an APD and P_{bg} - incident background optical power collected over a photodetector cell area. Using 450 nm CWL 50 nm bandpass filter [265] we evaluate that about 93 % of background optical noise is filtered out.

The thermal Johnson-Nyquist noise was evaluated to be 2 orders of magnitude lower than the background shot noise at 300 K temperature. If high-sensitivity and low input current density TIAs such as the 1.4 GHz Semtech NT25L51 [266] are employed, the TIA noise is also two orders of magnitude lower than the combined shot noise from the signal and ambient lighting. Consequently, only the shot noise contribution is relevant to the link's performance.

Optical Test Setup

We now describe the test setup and the optical front-end for the VLC mobile use case scenario. The experimental setup encompasses a room measuring $4 \times 4 \times 3$ m in dimensions. Within this room, the AP is fixed to the ceiling, and positioned precisely at the central co-ordinates of the room: $\mathbf{r}_{\text{AP}} = [2\mathbf{e}_1, 2\mathbf{e}_2, 3\mathbf{e}_3]$. The AP is oriented downward aligning itself with the global z-axis. The UE is situated at the ground level $z = 0$. The UE is free to be moved along the XY-plane of the room. We initially test the GSSK link performance in a fixed orientation scenario. Here the UE orientation in regards to the global z-axis ($\mathbf{n}_z$) is fixed. Later, we assume a random position and orientation model for the UE.

In our experimental setup both the receivers at the UE and transmitter beam sources on the AP end are deployed and uniformly distributed on $r = 0.1$ m radius hemispheres. At the transmitter end, as depicted in Figure 3.14 there are total 41 transmitter beam source cells (as illustrated in Figure 3.13a). These cells emit Lambertian beams. Each cell consists of multiple blue GaN micro-LED arrays from [109] with a central wavelength (CWL) $\lambda_{\text{CWL}} = 450$ nm and -6 dB one-sided spectral elec-

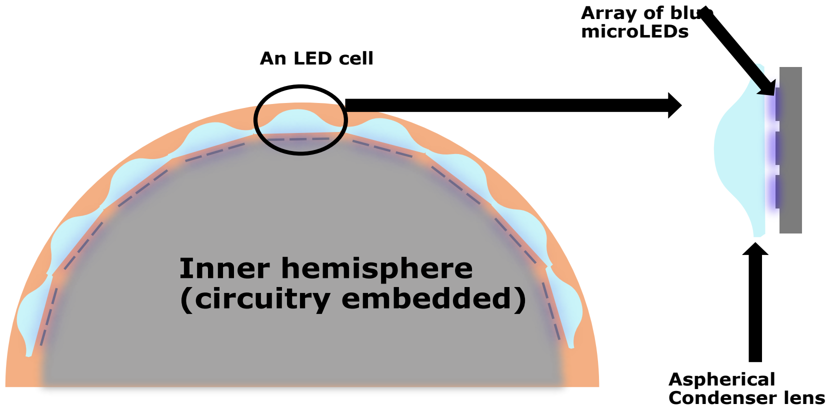

Figure 3.14: AP layout with transmitter beam source (micro-LED) cells shown.

trical modulation bandwidth of $B = 980\,\mathrm{MHz}$. The maximum emitted optical power of each individual 3×3 array is $P_{\mathrm{array}} = 10\,\mathrm{mW}$ and half-intensity angle $\Phi_{1/2} = 60$ deg. For each transmitter beam cell we assume a condenser lens with variable parameters. For the simulations we vary the half-intensity angle of the lens. The optical emission power at the lens $P_{\mathrm{opt}}^{\mathrm{lens}}$ is set to $1\,\mathrm{W}$. The extinction ratio of the transmitter is assumed to be 10.

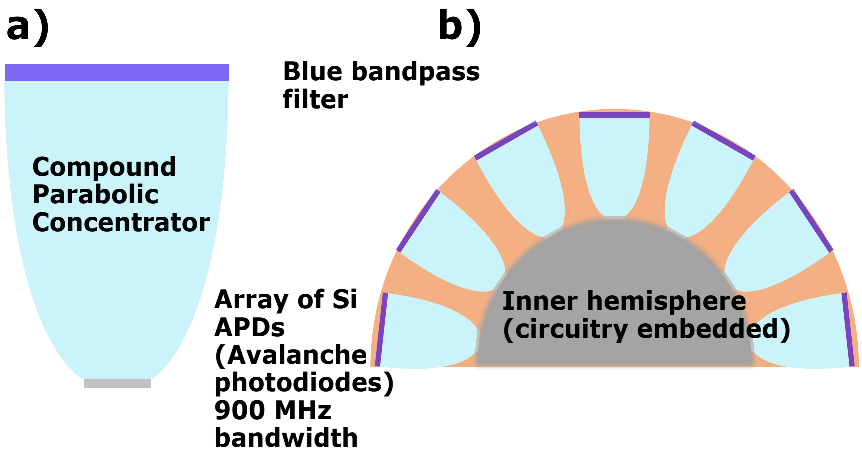

Figure 3.15: a) Diagram of a single receiver cell, b) receiver layout.

On the receiver end, we incorporate 41 receiver cells with each cell consisting of 25×25 Silicon APD arrays. While such arrays are very expensive to produce, deployment of large Silicon photodiode arrays such as in silicon photomultipliers (SiPMs) is well know, with manufacturers like Onsemi producing up to 12×12 arrays [267]. A CPC is

Table 3.1: Receiver cell optical front-end elements and their key parameters.

Component	Model	Key Parameter Values
Photodiode	Hamamatsu Si APD S12023 [268]	Cutoff frequency: $f_{\mathrm{APD}} = 0.9$ GHz Spectralresponse range: $\lambda \in (400 : 1000$ nm$)$ Photosensitivity: $R(\lambda_{450\ \mathrm{nm}}) = 0.04$ A/W Photosensitive area: $\varnothing = 0.2$ mm Multiplication factor: $M_{\mathrm{APD}} = 50$ Excess noise factor: $F_{\mathrm{APD}} = 3$.
Optical Concentrator	4.34mm Output Dia., Compound Parabolic Concentrator (Edmundoptics) [269] [3]	Acceptance angle: $\Psi_{\mathrm{c}} = 25$ deg Refractive index: $n_{\mathrm{con}} = 1.47$
Optical Filter	450nm CWL, 25mm Dia. Hard Coated OD 4.0 50nm Bandpass Filter (Edmundoptics) [265]	Central wavelength $\lambda_{\mathrm{CWL}} = 450$ nm FWHM: $\Delta\lambda = \pm 25$ nm Maximum transmittance: $T_{\mathrm{filter}} = 0.94$

mounted on top of these arrays, such that the array is located on the exit aperture of the CPC. A blue band-pass filter is considered on top of each CPC as shown in Figure 3.15. The overview of the receiver optical front-end elements is given in Table 3.1. For background illumination we assume a uniform 500 lux background illumination. The colour temperature is 3000 K, which is based on standard domestic LED spectrum [270]. These specific illumination and colour temperature values have been chosen to replicate typical office working conditions, as recommended by [271].

The spectral efficiency of the link depending on $\theta'(t)$ is given as:

$$\eta(\theta'(t)) = \log_2 |\mathbb{X}(\theta'(t))| = N_{\mathrm{t}}^{\mathrm{e}}(\theta'(t)),\ \eta(\theta'(t)) \in \mathbb{N}. \tag{3.43}$$

We assume FEC with 7% (line rate of 93 % compared to uncoded case) overhead at

[3] No longer available at Edmundoptics.

3.8×10^{-3} BER [261], which is frequently used in VLC as upper FEC limit [272, 273], therefore the maximum data throughput that can be achieved for a given bandwidth B is:

$$C_{\text{data}}^{\text{peak}}(\theta'(t), B) = 2 \times 0.93\eta(\theta'(t))B = 1.86\eta(\theta'(t))B. \tag{3.44}$$

3.4.2 Directional Infrared Transceiver MIMO-OWC Channel

For this scenario, we model that both the UE and the AP as being embedded on flat, planar surfaces. This setup simulates mobile to mobile or stationary device-to-device communication scenario. Both transmitter beam emitters and receivers are distributed on regular square lattices. Within this framework we consider two distinct arrangements of the transmitter beam sources as represented in Figure 3.16.

In the "close" arrangement, as illustrated in Figure 3.16a, the transmitter beam sources are distributed in a compact square lattice with a spacing denoted as s_0. Importantly, this spacing s_0 is less than the spacing of the beam centroids at the receive plane, represented as s. This configuration is designed to model a scenario where the transmitter end consists of small form factor devices. To achieve the desired spacing of the beam centroids s at the receiver plane, we assume a passive beam steering and deflection mechanism such as through the implementation of wedge prisms [274].

In the "sparse" arrangement, depicted in Figure 3.16b, the transmitter beam sources are spatially separated in a square lattice with spacing $s_0 = s$. This configuration is designed to simulate a scenario where the transmitter end consists of large form factor devices, such as displays or multiple APs. The (x, y) co-ordinates of the transmitter beam sources precisely correspond to the (x, y) co-ordinates of the transmitter beam centroids at the receive plane.

The receive plane is separated from the transmitter plane by a distance of $z = 1\,\text{m}$. The target area, representing the intended coverage at the receive plane is set to $20 \times 20\,\text{cm}^2$. For the simulations in "close" scenario we fix $s_0 = 1\,\text{cm}$, which is constrained by the convex lens diameter. In both scenarios variable s is adjusted. For the simulations we evaluate different square lattices of transmitter beam sources, including 3×3, 5×5, 7×7 and 9×9 configurations.

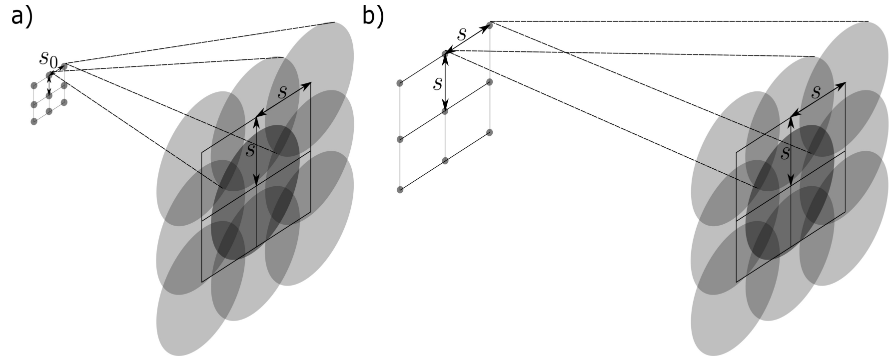

Figure 3.16: a) "Close" arrangement scenario, b) "sparse" arrangement scenario.

Each receiver contains a single Si APD with a convex lens mounted on top to concentrate light. The spacing between different receivers in a square lattice is 1.6 mm, which is determined by the aperture diameter of receiver lenses. For the simulations, we explore various square lattice configurations of receivers, including 1×1, 2×2, 3×3 and 4×4 arrays. In the simulations, the co-ordinates (x, y) of the receiver array are treated as variables constrained within the target area. The orientation of both the receiver array and the transmitter beam array is fixed and aligned with the optical z-axis.

Transmitter Design

We model a transmitter beam source as a square array of size $N \times N$ composed of multiple VCSEL chips positioned in front of a convex lens, as depicted in Figure 3.17. This Figure is generated by Zemax OpticStudio, which we employ for ray-tracing various irradiance distributions of the VCSEL array at different locations: the receive plane, the exit aperture of the lens and at a distance $z = 10\,\text{cm}$, corresponding to the Most Hazardous Position (MHP) [88]. The consideration of MHP for MPE evaluation is essential in laser eye safety assessments.

For the VCSEL chips in the array we use $\lambda = 850\,\text{nm}$ Optowell SM85-1AH001 [275] VCSELs. The main parameters of the chips used in the simulations are summarised in Table 3.2.

The convex lens selected for this setup is Thorlabs ACL108U [276] with an aperture

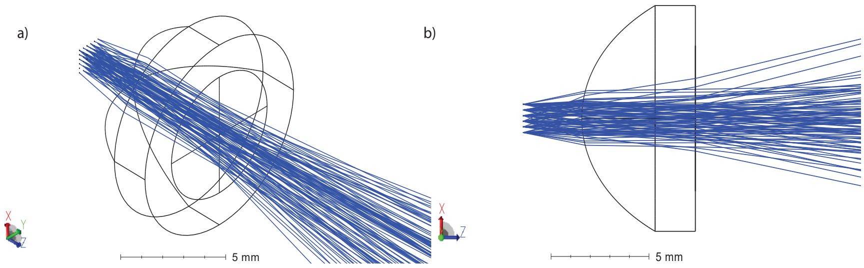

Figure 3.17: a) Isometric projection of the transmitter beam source and ray diagram array, b) side-view and ray diagram of the transmitter beam source.

Table 3.2: OWC transmitter beam source VCSEL chip parameters.

Parameter	Value
Wavelength, λ, nm	850
Divergence angle, Θ_{VCSEL}, deg	18
Optical output power P_{VCSEL}, mW	3
Spacing between chips s_{array}, μm	250

diameter of 1 cm and a focal length of $f_{\mathrm{lens}} = 8$ mm. We chose this lens to maximise the apparent source size of the transmitter beam for laser eye safety considerations, while also taking into account the limited form factor required for mobile devices.

As previously mentioned, it is crucial to consider laser eye safety constraints. To address this concern, we evaluate MPE using the procedure described in [88]. This evaluation involves comparing the peak irradiance obtained from the ray-tracing simulations at the MHP with the MPE values to ensure that our design meets the laser eye safety constraints. We conduct this assessment for various sizes of chip arrays and array distances from the lens. Our objective is to determine the optimal number of VCSELs that can maximise the irradiance from the transmitter beam source at the receiver plane while adhering to the MPE constraints. We have determined that the highest irradiance levels are attained with a 6×6 VCSEL chip array, producing an output optical power: $P_{\mathrm{array}} = 108$ mW. The optimal distance between the array and the lens is found to be 3 mm.

To accommodate for extended simulation times, we have fitted the single-beam irradiance distribution results at the far field ($z = 1, \mathrm{m}$), generated in Zemax OpticStudio, with an approximate Gaussian fit, as illustrated in Figure 3.18. These results are provided along the optical axis of the beam. The beam profile is provided along the x axis

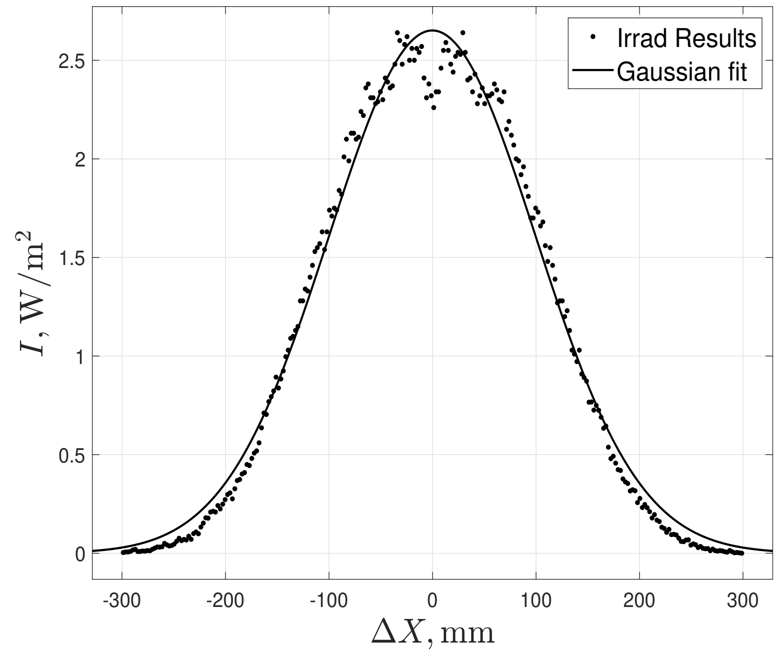

Figure 3.18: Irradiance distribution at the receive plane, x-axis projection.

at the receiver. We assume symmetrical (identical) Gaussian beam profile when viewed along y axis. The analytical fit follows expression as defined by MathWorks MATLAB as [277]:

$$I_{\mathrm{beam}}(x) = A_i e^{-(\frac{x-b_i}{c_i^2})^2}. \tag{3.45}$$

We can extended (3.45) straightforwardly to 2D as follows:

$$I_{\mathrm{beam}}(x, y) = A_i e^{-(\frac{x-b_i}{c_i^2})^2} e^{-(\frac{y-b_i}{c_i^2})^2}. \tag{3.46}$$

The analytical fit parameters and fitting statistics are summarised in Table 3.3. We employ the analytical fit approximation of the Gaussian irradiance distribution to describe the transmitter beam at the target area. In the case of beam steering, we assume that optical aberrations have a negligible impact on the beam profile for beams located

Table 3.3: Irradiance Gaussian fit parameters and fitting statistics.

	A_i, W/m^2	b_i, mm	c_i, mm
	2.651	-0.1966	141.2
95% Confidence interval	(2.623, 2.679)	(-1.4,1.007)	(139.5,142.9)
SSE = 2.514			
R^2 = 0.989			
Adjusted R^2 = 0.989			

further away from the central optical axis of the transmitter device. For a beam in the square lattice situated at n_x and n_y lattice units away from the optical axis centre, the parameter b_i is calculated as $b_i = \sqrt{(sn_x)^2 + (sn_y)^2}$.

Receiver Design

We model a receiver array as a $N \times N$ sized square array comprised of Si APDs (Hamamatsu S14643-02) [278] with convex lenses for concentration as depicted in Figure 3.19 with the ray diagram generated in Zemax OpticStudio. As an example, we illustrate

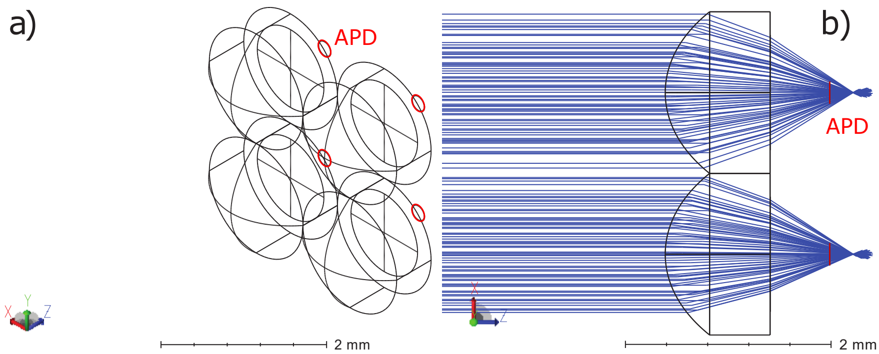

Figure 3.19: a) Isometric projection of the discrete component receiver array, b) side-view and ray diagram of the array. Red circles are used to indicate the APD position.

a 2×2 discrete component receiver array in the figure. The Si APDs, represented as small circles in the isometric projection, are positioned before the focal length of the lenses, as depicted in the ray diagram in Figure 3.19(b). This arrangement is designed to ensure that the FoV of the receivers fits within the specified coverage area.

We have chosen the Thorlabs 354140-B lens for the receiver [279]. This lens has a focal length of 1.5 mm and an aperture diameter of 1.6 mm. Our selection of this lens is based on its ability to offer optimal optical concentration for defocused receivers within the specified target area.

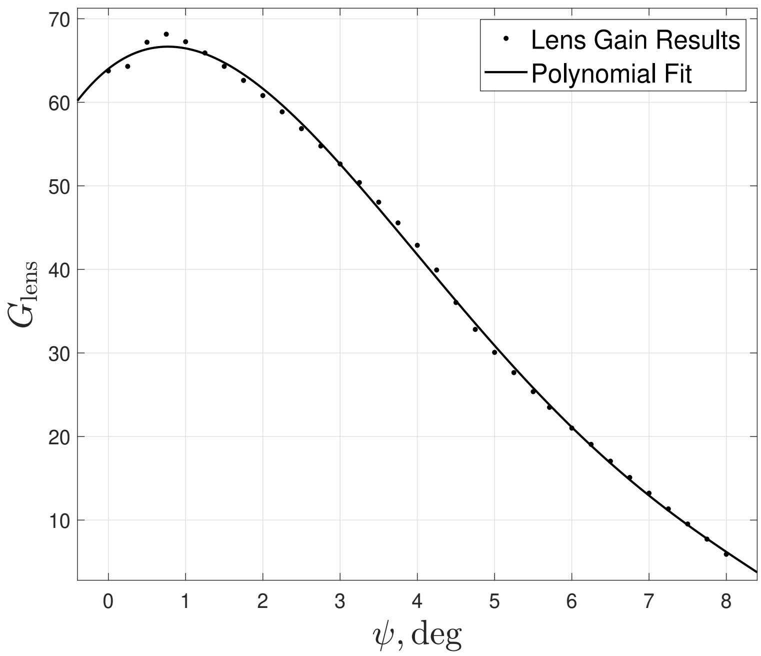

Figure 3.20: Receiver Lens Gain Dependency on the Incidence Angle.

Similar to the approach used for the transmitter model, and to account for long simulation times, we model the lens gain (optical concentration gain) as a function of the incidence angle, ψ. This is achieved by conducting ray tracing simulations for a single receiver-convex lens pair. These simulations generate an irradiance distribution at the receiver's photo-active area using a test source with arbitrary optical power. We then compare the total optical power integrated over the receiver area, denoted as A_{Rx}, to the reference optical power without a convex lens, denoted as P_{ref}, for the given incidence angle ψ. We define the lens gain, which is related to the flux concentration gain [280] as follows:

$$G_{\text{lens}}(\psi) = \frac{P_{\text{lens}}(\psi)}{P_{\text{ref}}(\psi)} = \frac{\int_{A_{\text{Rx}}} I_{\text{lens}}(x, y, \psi) dxdy}{\int_{A_{\text{Rx}}} I_{\text{ref}}(x, y, \psi) dxdy}.$$

We present the analytical polynomial fit of the lens gain results obtained from the ray-tracing simulations in Figure 3.20. The analytical fit follows expression:

$$G_{\text{lens}}(\psi) = p_1\psi^4 + p_2\psi^3 + p_3\psi^2 + p_4\psi + p_5.$$

The analytical fit parameters and fitting statistics are summarised in Table 3.4.

Table 3.4: Lens gain polynomial fit parameters and fitting statistics.

	p_1	p_2	p_3	p_4	p_5
	-0.0267	0.6684	-5.451	7.255	64.01
95 % Confidence interval	(-0.0382, -0.0151)	(0.4816, 0.8552)	(-6.438, -4.465)	(5.357, 9.152)	(62.95, 65.07)
SSE = 13.96					
$R^2 = 0.999$					
Adjusted $R^2 = 0.999$					

The peaking of the lens gain in Figure 3.20 at a non-normal incidence angle is due to the non-uniform irradiance hotspots located outside the FoV of the photodiode at a normal incidence. These hotspots originate from the spherical aberration of the lens where meridional rays intersect optical axis at a longer focal length compared to the paraxial rays [281].

The received optical power at the i^{th} receiver in the array from j^{th} transmitter beam at $z = 1\,\text{m}$ distance and (x, y) co-ordinate can be written as:

$$P_{ij}(x, y) = I_j(x, y)A_{\text{Rx}}G_{\text{lens}}(\psi_{ij}).$$

The parameters of the Si APDs and TIA are provided in Table 3.5. The Si APDs were selected to offer maximal bandwidth at $\lambda = 850\,\text{nm}$ while maximizing the photoactive area. To optimise signal amplification while reducing the excessive shot noise, the avalanche multiplication gain was set $M = 30$ (with reverse voltage of 75 V assumed). The primary criterion for selecting the TIA was a bandwidth exceeding 2 GHz to match the bandwidth of APDs, along with minimal input-referred noise. In this scenario, we assume the absence of a wavelength filter at the receiver, as the impact of background illumination noise is negligible at $\lambda = 850\,\text{nm}$. For indoor scenarios, this assumption is valid when LEDs are considered for background illumination [282].

Table 3.5: OWC receiver opto-electronic front-end component parameters.

Component	Model	Key Parameter Values
Photodiode	Hamamatsu Si APD S14643-02 [278]	Cutoff frequency: $f_{\mathrm{APD}} = 2$ GHz Spectralresponse range: $\lambda \in (400 : 1000$ nm$)$ Photosensitivity: $R(\lambda_{850\text{ nm}}) = 0.04$ A/W Photosensitive area: $\varnothing = 0.2$ mm Multiplication factor: $M_{\mathrm{APD}} = 30$ Excess noise factor: $F_{\mathrm{APD}} = 2.774$.
TIA	Analog Devices TIA ADN2880 [283]	Bandwidth: $B_0 = 2.5\,$GHz Input refered noise $\sigma_{\mathrm{TIA},I,0} = 315\,$nA Transimpedance Gain: $G_{\mathrm{TIA}} = 4400\,\Omega$

In contrast to the VLC hemispherical model scenario, the TIA noise is comparable to the signal shot noise while the background illumination is negligible. The input-referred noise is provided for $B = 2.5\,$GHz. From this, the input-referred noise density can be determined as $6.3\,\mathrm{pA}/\sqrt{\mathrm{Hz}}$. After adjusting for the modulation bandwidth of 2 GHz, we calculate using (3.47) the input-referred noise to be $\sigma_{\mathrm{TIA},I} = 282\,$nA where $\sigma_{\mathrm{TIA},I,0} = 315\,$nA, $B_0 = 2.5\,$GHz and $B_1 = 2\,$GHz.

$$\sigma_{\mathrm{TIA},I} = \sigma_{\mathrm{TIA},I,0}\sqrt{\frac{B_1}{B_0}}. \tag{3.47}$$

The generated peak-to-peak voltage by j^{th} transmitter beam at i^{th} receiver at point (x, y) in the plane of transmitter and receiver:

$$V_{ij}(x, y, \lambda) = \frac{1}{2}P_{ij}(x, y)R(\lambda)M_{\mathrm{APD}}G_{\mathrm{TIA}}, \tag{3.48}$$

with factor 1/2 due to $-3\,$dB bandwidth of the Si APD at $B = 2\,$GHz modulation bandwidth.

The total noise (expressed in volts) in this case is given as:

$$\sigma_{ij} = \sqrt{\sigma^2_{\mathrm{TIA}} + \sigma^2_{\mathrm{shot},ij}}, \tag{3.49}$$

where:

$$\sigma^2_{\mathrm{TIA}} = \sigma^2_{\mathrm{TIA},I} G^2_{\mathrm{TIA}}, \tag{3.50}$$

the shot noise is calculated as:

$$\sigma^2_{\mathrm{shot},ij} = 2qM^2_{\mathrm{APD}} F_{\mathrm{APD}} R(\lambda) B P_{ij} G^2_{\mathrm{TIA}}. \tag{3.51}$$

Chapter 4

Computer Simulation Results and Analysis

4.1 Union Bound Approximation

To achieve the maximal data throughput distribution across a wide range of measurement points, such as different room positions and orientations, we need to evaluate BER for given location and orientation based on the transmitter beam and receiver set selection. Typically, we conduct BER evaluations using Monte Carlo simulations, involving a minimum of 10^6 bit realizations for the given MIMO channel. This gives a good overhead and accuracy to test for target BER of 3.8×10^{-3} at FEC condition. However, for an extremely large number of data points, computational requirements can become prohibitively time-consuming.

Alternatively, we can approximate BER using the upper union bound (3.19) for faster evaluation. When channel coding is not employed, the union bound can serve as a reasonable approximation of the BER. We validate this assumption through Monte Carlo computer simulations, considering at least 10^7 bit realizations for a single-user link for a further enhanced precision. The union bound approximation applies generally to the GSSK data transmission, therefore it is also applicable for the adaptive GSSK algorithm evaluation.

A fixed orientation and position is chosen for the receiver which is situated beneath the AP at $\mathbf{r} = [2\mathbf{e}_1, 2\mathbf{e}_2, 0\mathbf{e}_3]$ with the hemisphere aligned upwards along the global z-axis. To determine the engaged beam set, we employ the maximal minimum Euclidean distance beam selector. We vary the cardinality of the engaged beam set selection from 1 to 6 and evaluate the BER using both Monte Carlo simulations and analytical union bound. The number of engaged receivers remains fixed at $N_\mathrm{r}^\mathrm{e} = 6$. The optical power of individual transmitter beams is varied to set different pairwise channel SNR levels. The SNR can vary among different transmitter-receiver pairs due to factors such as differences in transmitter beams, receiver inclination angles, and distances. For this reason, we calculate the average SNR from all the transmitter-receiver pairs considered:

$$\tilde{\gamma}_\mathrm{elec} = 10\log\left(\frac{1}{N_\mathrm{r}^\mathrm{e} N_\mathrm{Tx}} \sum_{i=0}^{N_\mathrm{r}^\mathrm{e}-1} \sum_{j=0}^{N_\mathrm{Tx}-1} \gamma_{ij}^\mathrm{elec}\right).$$

The BER versus the average electrical SNR per receiver is depicted in Figure 4.1. The

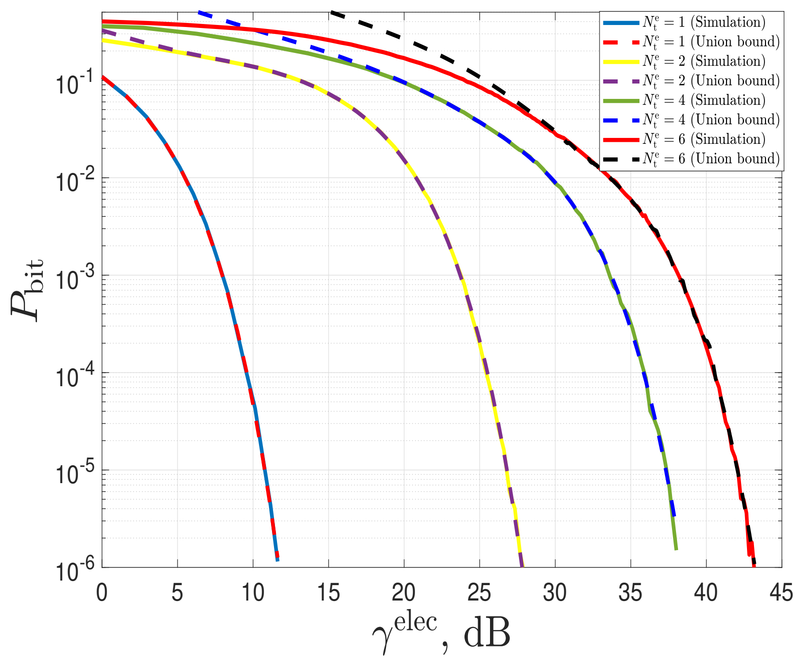

Figure 4.1: BER performance versus average electrical SNR per receiver for $N_\mathrm{r}^\mathrm{e} = 6$ engaged receivers.

results are presented with analytical union bounds shown as dashed lines and Monte

Carlo simulations as solid lines.

As observed in Figure 4.1, the union bound approximation closely aligns with the results obtained from Monte Carlo simulations across a range of cardinalities for engaged transmitter beams. Significant disparities between simulation and analytical results only emerge when BER values exceed the target FEC limit by two orders of magnitude, and this occurs when the number of engaged beams is greater than 2. Consequently, for BER evaluations, the union bound approximation is both applicable and will be employed for the remainder of the simulations.

4.2 Fixed Orientation Hemispherical MIMO-VLC Scenario

We can now assess the achievable data throughput of adaptive GSSK using the set selectors with different selection criteria. We explore various transmitter beam half-intensity angles (by adjusting the convex lens half-intensity angle) while keeping the remaining front-end parameters constant. The simulations are conducted on a 202×202 square grid with a step size of $\Delta_{x,y} = 2\,\mathrm{cm}$. This grid spans from $x_0 = -2\,\mathrm{m}$ to $x = 2\,\mathrm{m}$ and from $y_0 = -2\,\mathrm{m}$ to $y = 2\,\mathrm{m}$.

4.2.1 Maximal Minimum Euclidean Distance Set Selector

The spatial distribution of the maximum achievable data throughput in the xy plane of the room, obtained with different transmitter beam half-intensity angles using the maximal minimum Euclidean distance-based set selector following Algorithm 1, is presented in Figures 4.2 (a-d). These figures reveal that the spatial distribution of achievable data throughput exhibits two notable characteristics.

Firstly, it varies significantly in uniformity, ranging from highly non-uniform to nearly uniform. Secondly, the distribution follows various symmetrical geometrical patterns, each with a 36-degree symmetry, corresponding to the azimuthal placement of transmitter beam sources. This highlights a strong dependency of the data throughput distributions on the transmitter beam half-intensity angle.

The maximum achievable data throughput, as depicted in the figures, exhibits sig-

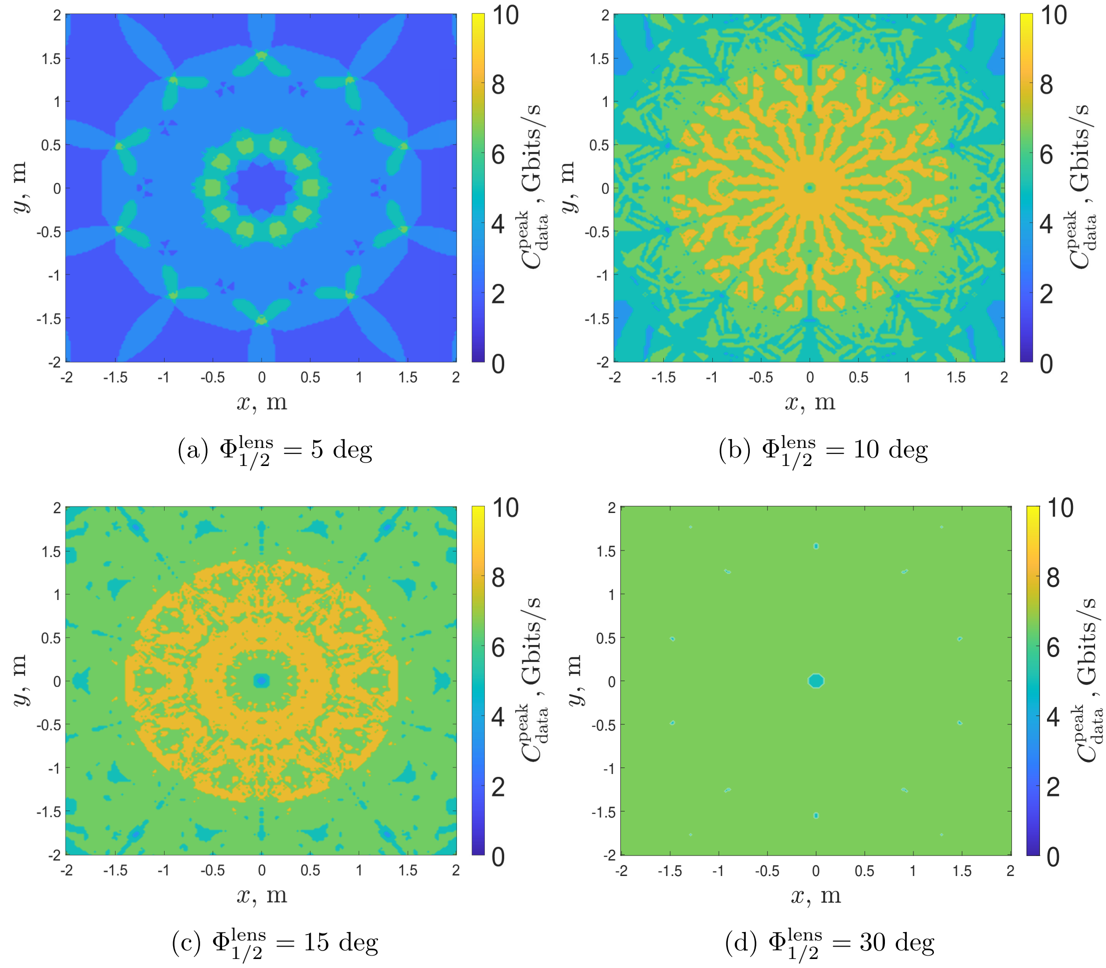

(a) $\Phi_{1/2}^{\text{lens}} = 5$ deg

(b) $\Phi_{1/2}^{\text{lens}} = 10$ deg

(c) $\Phi_{1/2}^{\text{lens}} = 15$ deg

(d) $\Phi_{1/2}^{\text{lens}} = 30$ deg

Figure 4.2: Room maximum achievable data throughput distribution for various values of $\Phi_{1/2}^{\text{lens}}$ and when using the maximal minimum Euclidean distance set selection criterion.

nificant variations depending on the transmitter beam half-intensity angle and spatial user equipment coordinates. This range spans from a minimum of 1.674 Gbit/s to a maximum of 8.37 Gbit/s. To determine the mean maximal data throughput achievable in this scenario for a given transmitter half-intensity angle, we calculate it as follows:

$$\mathrm{E}(C_{\mathrm{data}}^{\mathrm{peak}}) = \frac{1}{N_x N_y} \sum_{i=0}^{N_x} \sum_{j=0}^{N_y} C_{\mathrm{data}}^{\mathrm{peak}}(x_0 + \Delta_{x,y} i, y_0 + \Delta_{x,y} j), \tag{4.1}$$

here N_x and N_y are number of grid points along x and y axis respectively. The standard deviation of the maximal data throughput can be calculated as:

$$\sigma(C_{\mathrm{data}}^{\mathrm{peak}}) = \sqrt{\sum_{i=0}^{N_x} \sum_{j=0}^{N_y} \frac{C_{\mathrm{data}}^{\mathrm{peak}}(x_0 + \Delta_{x,y} i, y_0 + \Delta_{x,y} j) - \mathrm{E}(C_{\mathrm{data}}^{\mathrm{peak}})}{N_x N_y - 1}}. \tag{4.2}$$

The mean maximal data throughput and standard deviation is given in Table 4.1. As shown in the table, the mean data throughput experiences a rapid increase from 2.9 Gbit/s at 5 deg to 6.43 Gbit/s at 10 deg. With a further increase in the half-intensity angle, there is only a modest increase in mean data throughput, and the results plateau from $\Phi_{1/2}^{\mathrm{lens}} = 15$ deg to $\Phi_{1/2}^{\mathrm{lens}} = 40$ deg, after which the data throughput gradually begins to decline. The peak mean data throughput, $\mathrm{E}(C_{\mathrm{data}}^{\mathrm{peak}}) = 6.98$ Gbit/s, is observed at a half-intensity angle of $\Phi_{1/2}^{\mathrm{lens}} = 15$ deg. In this case, the adaptive GSSK algorithm most frequently engages 4 beams. A further increase in the half-intensity angle leads to a slow decrease in the average number of engaged beams that can support a link within the given BER FEC constraint.

To analyse these results of mean data throughput dependence on the half-intensity angle, we examine the geometrical distribution presented in Figures 4.2 (a-d). Firstly, we observe a region of low data throughput in the middle of the room, which corresponds to users being directly under the AP. In this scenario, all neighbouring beams within the FoV have nearly identical irradiance at the receiver. When the half-intensity angles of the transmitter beams are very narrow, as in the case of $\Phi_{1/2}^{\mathrm{lens}}$, the nearest neighbouring beams are also narrow. Due to the roll-off in the Lambertian irradiance pattern, these narrow beams cannot be selected as the engaged beam, and the only available option

Table 4.1: Mean data throughput and standard deviation for various $\Phi_{1/2}^{\text{lens}}$ and maximal minimum Euclidean distance set selector.

$\Phi_{1/2}^{\text{lens}}$, deg	Mean Data Throughput: $\mathrm{E}(C_{\text{data}}^{\text{peak}})$, Gbit/s	Standard Deviation: $\sigma(C_{\text{data}}^{\text{peak}})$, Gbit/s
5	2.9	0.3
10	6.43	0.14
15	6.98	0.21
20	6.7	0.16
25	6.67	0.17
30	6.69	0.08
35	6.68	0.16
40	6.62	0.27
45	6.5	0.4

is the beam aligned with the global z-axis.

However, as we increase the half-intensity angle, the next nearest neighbouring beams become available for the engaged beam selection, leading to an increase in data throughput at the centre of the room. As we move radially outward from the centre, two observations become evident. Firstly, there is an increase in the local data throughput. Secondly, a symmetric radial pattern of varying data throughput emerges. In this pattern, the local minima in data throughput correspond to regions with increased overlapping of neighbouring beams.

In the hemispherical Lambertian irradiance model, when considering a single receiver, the channel gain ratio between two nearest neighbouring transmitter beams, denoted as j and $j+1$, at the i^{th} receiver can be approximated at the distances considered in the simulation. This approximation holds when $\psi_{ij} \approx \psi_{i(j+1)}$ and $d_{ij} \approx d_{i(j+1)}$, and it can be expressed as:

$$\frac{h_{i(j+1)}}{h_{ij}} = (\frac{\cos\varphi_{i(j+1)}}{\cos\varphi_{ij}})^m = (\frac{\cos\varphi_{i(j+1)}}{\cos\varphi_{ij}})^{-\frac{\ln 2}{\cos\Phi_{1/2}^{\text{lens}}}}. \tag{4.3}$$

The j^{th} transmitter beam represents the primary engaged transmitter beam, which is always selected in engaged beam sets with non-zero cardinality. In a singular engaged beam selection, this beam will consistently maximise the link SNR. Each neighbouring transmitter beam is defined in relation to the j^{th} transmitter beam.

Recalling the previous discussion on the optimal channel ratios (as discussed in Section 3.3.2), we understand that the ideal optimal channel level spacing can be achieved when $h_{i(j+1)} = 0.5h_{ij}$. Assuming this condition, we can analytically solve (4.3) for $\Phi_{1/2}^{\text{lens}}$ to obtain the optimal half-intensity angle condition:

$$\Phi_{1/2}^{\text{lens}} = \cos^{-1}(\frac{\cos\varphi_{i(j+1)}}{\cos\varphi_{ij}}),$$

which when the j^{th} transmitter beam is aligned with i^{th} receiver beam, such that $\varphi_{ij} = 0$, reduces to:

$$\Phi_{1/2}^{\text{lens}} = \varphi_{i(j+1)}. \tag{4.4}$$

Similarly solving (4.3) for the next selected transmitter beam applying condition $h_{i(j+2)} = 0.5h_{i(j+1)} = 0.25h_{ij}$ we get the optimal half-intensity angle condition:

$$\Phi_{1/2}^{\text{lens}} = \cos^{-1}(\sqrt{\frac{\cos\varphi_{i(j+2)}}{\cos\varphi_{ij}}}),$$

For a general $j+N$ engaged transmitter beam the optimal half-intensity angle condition is:

$$\Phi_{1/2}^{\text{lens}} = \cos^{-1}(\sqrt[N]{\frac{\cos\varphi_{i(j+N)}}{\cos\varphi_{ij}}}),$$

Additionally the half-intensity angle has to be a positive number such that:

$$\Phi_{1/2}^{\text{lens}} > 0.$$

This leads to a system of equations when $j + N$ engaged transmitter beams are considered for the optimal half-intensity angle in GSSK transmission:

$$\begin{cases} \Phi_{1/2}^{\text{lens}} = \cos^{-1}(\frac{\cos\varphi_{i(j+1)}}{\cos\varphi_{ij}}) \\ \Phi_{1/2}^{\text{lens}} = \cos^{-1}(\sqrt{\frac{\cos\varphi_{i(j+2)}}{\cos\varphi_{ij}}}) \\ \vdots \\ \Phi_{1/2}^{\text{lens}} = \cos^{-1}(\sqrt[N]{\frac{\cos\varphi_{i(j+N)}}{\cos\varphi_{ij}}}) \\ \Phi_{1/2}^{\text{lens}} > 0 \end{cases}. \tag{4.5}$$

As evident from (4.5), the system of equations is non-linear and strongly depends on the relative positions of the j^{th} transmitter beam and the i^{th} receiver. This suggests that it is extremely unlikely to produce a singular or a set of half-intensity angle values that achieve the ideal GSSK channel ratios except for a few particular configurations. However, (4.5) also indicates the existence of a mean half-intensity angle or a set of angles that, on average, optimizes GSSK channel ratios, even if it doesn't reach the ideal ratio tuple of $0.5, 0.25, ..., 2^{-N}$. To further analyse this behavior, we delve deeper into our simulation model.

In our hemispherical system, two neighbouring transmitter beams are spaced in angular space $\Delta\varphi_{j,j+1} = \phi_{j+1} - \varphi_j = 18$ deg apart, following the direction of inclination of the hemisphere. The next-nearest neighbours, denoted as $j+2$, are spaced $\Delta\varphi_{j,j+2} = 36$ deg relative to the j^{th} transmitter beam, extending along the azimuth of the hemisphere. The third-nearest neighbours, denoted as $j+3$, are spaced $\Delta\varphi_{j,j+3} = 39.4$ deg relative to the j^{th} transmitter beam. For simplicity, assuming an aligned single transmitter and receiver pair with $\varphi_{ij} = 0$ deg, we illustrate the channel ratios of the first, second, and third nearest neighbour transmitter beams relative to the j^{th} transmitter beam as a function of the half-intensity angle. These ratios are shown in Figure 4.3

The dashed line describes the ratio of channel gain for the j^{th} transmitter at angle $\Phi_{1/2}^{\text{lens}}$ relative to the $\Phi_{1/2}^{\text{lens}} = 5\,\text{deg}$ given as:

$$\frac{h_{ij}(m)}{h_{ij}(m(\Phi_{1/2}^{\text{lens}} = 5\text{ deg}))} = \frac{m+1}{m(\Phi_{1/2}^{\text{lens}} = 5\text{ deg}) + 1} \cos^{m - m(\Phi_{1/2}^{\text{lens}} = 5\text{ deg})} \varphi_{ij}. \tag{4.6}$$

In the plot, the labels $k=1$, $k=2$, and $k=3$ correspond to the first, second, and third neighbours, respectively. From the figure, it is evident that the optimal channel condition $h_{i(j+1)} = 0.5h_{ij}$ is achieved when $\Phi_{1/2}^{\text{lens}} = \Delta\varphi_{j,j+1}$, as expected from (4.4). As we further increase the half-intensity angle of the transmitter beams, the channel ratio of each neighbour relative to the j^{th} transmitter beam tends asymptotically toward 1, while the optical power reaching the receiver rapidly decreases to just 1.64% at $\Phi_{1/2}^{\text{lens}} = 45$ deg compared to the 5 deg half-intensity angle. However, it's important to note that, as indicated by (4.3), the curves depend on the angle of the primary j^{th}

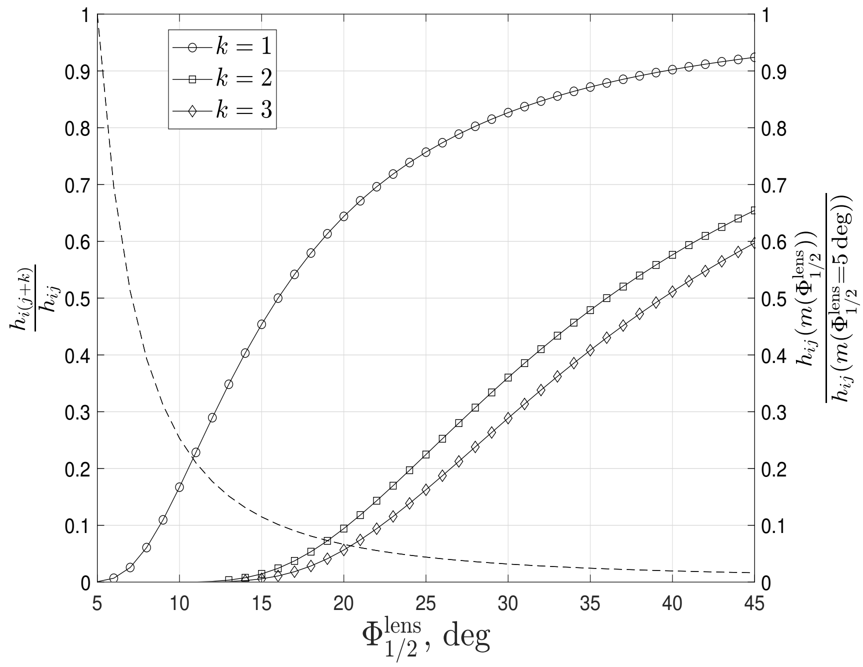

Figure 4.3: Channel ratios of $k = 1$, $k = 2$, $k = 3$ nearest neighbours relative to the primary transmitter beam for various values of $\Phi_{1/2}^{\text{lens}}$. Dashed line indicates the channel gain of the primary transmitter beam relative to $\Phi_{1/2}^{\text{lens}} = 5$ deg.

transmitter beam with respect to the i^{th} receiver, and the optimal half-intensity angle for up to the N^{th} engaged beam is determined by (4.5).

By examining the curves in Figure 4.3 and (4.5), we can observe an expected convex behavior of achievable data throughput when channel gain is considered as a function of the transmitter beam half-intensity angle, for every relative position of the receivers to the transmitters. Firstly, due to the relative decrease of channel gain with increasing half-intensity angle. Secondly, there is an interplay between different neighbour channel ratios. At low half-intensity angles, the beam overlap is too minimal, while at high half-intensity angles, the overlap becomes too significant. It's important to note that finding an exact single global solution for (4.5) might not always be feasible, even in the case of only two engaged beams. However, we can reasonably conclude that while we may not achieve the ideal GSSK channel ratio in every case, we can, on average, find a set of engaged beams that minimizes the overall difference between the channel ratios of the selected beams and the ideal GSSK ratio conditions within the room.

Additionally, since we are considering the mean maximal data throughput, we can anticipate that different half-intensity angles may maximise the mean data throughput. This is evident in the results presented as a data throughput plateau in Table 4.1. Therefore, the convex behavior does not necessarily imply finding a single specific half-intensity angle that maximises the mean data throughput; instead, it suggests that a set of half-intensity angles can be identified that, on average, maximise the mean data throughput.

While it is difficult to precisely specify this interval, we can argue that it is bounded. As observed from the dashed line in Figure 4.3, the optical power received from the j^{th} transmitter beams rapidly decreases as we increase the half-intensity angle. This upper bound limits the domain within which the peak mean maximal data throughput can be achieved, primarily due to the SNR constraint. Additionally, as the half-intensity angle increases, all of the channel ratios tend to approach unity, contributing to the overall performance degradation.

When multiple receivers are added, the ideally GSSK transmission is described by a system of equations, such as (4.5), for each receiver, respectively. However, in cases where the AP and UE are sufficiently far apart—typically when the distance is at least an order of magnitude larger than the dimensions of the devices—we can assume that $\psi_{ij} \approx \psi_{i(j+1)}$, $d_{ij} \approx d_{i(j+1)} \approx d_{(i+1)j}$, and $\varphi_{ij} \approx \varphi_{(i+1)j}$. This implies that beam j and its respective neighbours can be aligned along the distance vector connecting the AP and the UE. In such cases, the presence of multiple receivers does not significantly affect the channel ratios of neighbouring beams. Instead, it primarily impacts the array gain and, consequently, the SNR. This, in turn, would be expected to shift the upper bound of the plateau.

The lower bound (observed at $\Phi_{1/2}^{\text{lens}} = 5$ deg) can be attributed to the significantly low optical channel ratios relative to the j^{th} transmitter beam, primarily due to contributions from the nearest neighbours. In this scenario, the optical power received from the neighbouring beams is insufficient to reliably distinguish between different GSSK symbols in the presence of noise. This limitation arises because Lambertian irradiance patterns quickly attenuate as φ_{ij} exceeds 5 deg.

This behavior leads to the peaking phenomenon, which we observed in the half-intensity angle range from $\Phi_{1/2}^{\text{lens}} = 15$ deg to $\Phi_{1/2}^{\text{lens}} = 40$ deg. As shown in Figure 4.3, at these half-intensity angles, the channel ratios from the 2nd and 3rd nearest neighbours are significantly lower compared to the nearest neighbour. However, the SNR is high enough to compensate for this disparity. In the middle of the plateau, the channel ratios from the 2nd and 3rd nearest neighbours relative to the first neighbouring beam have considerably improved, effectively compensating for the rapid SNR decrease. Nevertheless, beyond a certain point, the poor channel ratios and further SNR decline contribute to a gradual reduction in mean data throughput.

In addition to mean data throughput, the uniformity of the data throughput distribution is another important performance metric. Ideally, we aim to maximise both metrics. To assess the degree of uniformity in the spatial distribution of data throughput, we can employ entropy as a characterization measure. The entropy of data throughput distribution is defined as [284]:

$$\mathrm{H}(C_{\text{data}}^{\text{peak}}) = - \sum_{\min(C_{\text{data}}^{\text{peak}})}^{\max(C_{\text{data}}^{\text{peak}})} p_{C_{\text{data}}^{\text{peak}}} \ln \left(\frac{p_{C_{\text{data}}^{\text{peak}}}}{w_{C_{\text{data}}^{\text{peak}}}} \right), \tag{4.7}$$

here $p_{C_{\text{data}}^{\text{peak}}}$ - the frequency or the number of counts of the given peak data throughput and $w_{C_{\text{data}}^{\text{peak}}}$ - a constant bin width. The bin width is set to 1, and corresponds to a step size of the number of engaged transmitter beams. In this context, entropy is measured in nats. The peak data throughput distributions, as shown in Figure 4.2, consist of discrete values based on the number of engaged beams, which can range from 1 to 5. Consequently, we can group all of the results into 5 equally sized bins. In a perfectly uniform data throughput distribution, we would expect the entropy to be 0. The upper limit of entropy occurs when the peak data throughput samples on the simulation grid are drawn from a uniform distribution of size 5, resulting in an entropy limit of 1.609 nat.

In Figure 4.4, we present the mean data throughput and its spatial distribution entropy as functions of the beam half-intensity angle. The standard deviation of the

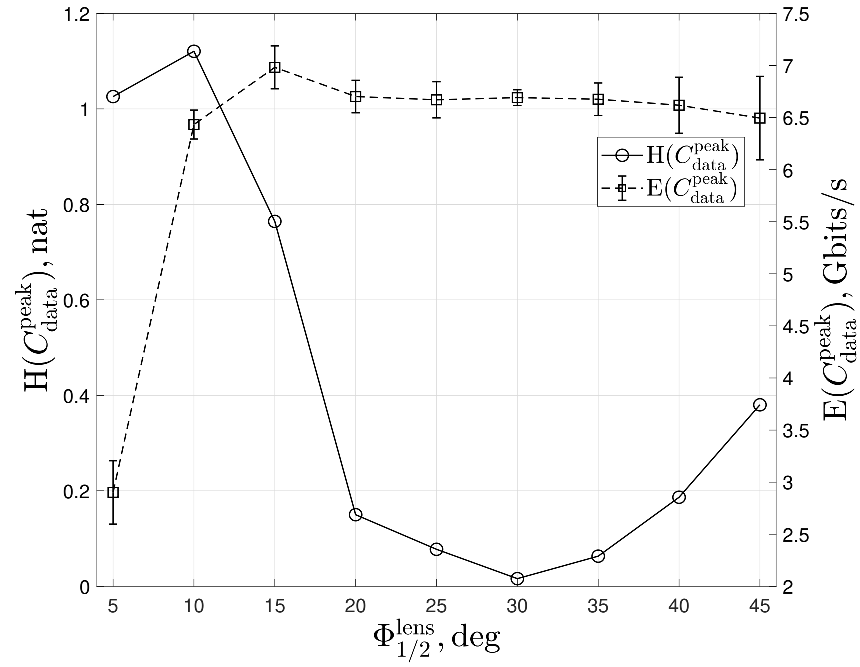

Figure 4.4: Mean data throughput and spatial entropy for various values of $\Phi_{1/2}^{\mathrm{lens}}$ using maximal minimum Euclidean distance set selector.

mean data throughput is represented by y error bars on the $\mathrm{E}(C_{\mathrm{data}}^{\mathrm{peak}})$ curve. As depicted in the figure, for small half-intensity angles ($5-10\,\mathrm{deg}$), the distribution entropy is high, resulting in a heterogeneous geometrical distribution of hot and cold spots, as also evident in Figures 4.2 (a-b). With a further increase in the half-intensity angle, the distribution becomes significantly more homogeneous without incurring a penalty in the mean data throughput. The best user experience occurs at the half-intensity angle of $\Phi_{1/2}^{\mathrm{lens}} = 30$ deg where the mean data throughput is only 4.15% smaller than the maximum at $\Phi_{1/2}^{\mathrm{lens}} = 15$ deg, while the entropy is close to $0\,\mathrm{nat}$ ($0.02\,\mathrm{nat}$), which indicates a near uniform data throughput across the room.

The observation regarding entropy aligns with our earlier discussions. This behavior appears to be related to the selection of neighbouring beams for the link. At very low half-intensity angles (ranging from 5 to 10 degrees), only the nearest neighbours are available for selection. Moreover, the number of available nearest neighbours varies significantly with the spatial coordinates of the UE due to the rapid roll-off of the

Lambertian irradiance pattern. In many spatial locations, the set selection is limited to just 2 beams due to the symmetry of the nearest neighbours. However, in some areas where beam overlap is more substantial, especially in proximity to the AP, there are more available neighbours with high SNRs, enabling the achievement of high local data throughput.

As we further increase the half-intensity angle, the dependency of the irradiance pattern on spatial coordinates decreases, leading to more uniform local maximal data throughput. However, this decrease in pattern dependency also results in lower distinguishability among the first selected j^{th} transmitter and its nearest neighbours, leading to reduced local data throughput peaks. The overall trade-off is that with larger half-intensity angles, more neighbours ($k = 2$ and $k = 3$) become available for beam selection at any location, providing a substitute for the nearest neighbour ($k = 1$) in GSSK transmission. On average, this enhanced availability compensates for the lower SNR and poorer channel ratios, keeping the mean data throughput constant while minimizing the distribution entropy.

In simpler terms, when the half-intensity angle grows from very low, the mean data throughput quickly approaches the peak mean data throughput. This increase arises through the significant presence of hot spots, resulting in a higher peak-to-average data throughput ratio. However, there are also a substantial number of cold spots, leading to high spatial distribution entropy and a heterogeneous data throughput distribution. In contrast, at higher half-intensity angles, the number of both hot and cold spots decreases, tending toward a more homogeneous data throughput distribution, which corresponds to the selection of all 4 beams.

As the half-intensity angle increases further (from 35 deg onwards), the distinguishability between the first selected j^{th} transmitter and its nearest neighbours, as well as SNR, decreases. In such cases, the number of beams available for a GSSK link also decreases. However, this decrease is not uniform across the room, resulting in the emergence of local cold spots where neighbouring beam overlap is higher, and mutual channel ratios are worse. Consequently, this leads to an increase in spatial distribution entropy and a decrease in mean data throughput.

4.2.2 Maximal SNR Set Selector

In Figures 4.5 (a-d), we observe the maximal data throughput spatial distribution using the maximal SNR-based selector, following Algorithm 2. While the spatial distribution in 4.5 (a) follows similar general patterns as in Figure 4.2 (a), the difference between the two methods quickly becomes more pronounced with increasing half-intensity angle. In comparison to the maximal Euclidean-based selection, all the distributions in Figures 4.5 (a-d) exhibit substantial heterogeneity with pronounced hot and cold spots. Furthermore, clear data throughput minima can be observed spatially in regions with high neighbouring beam overlap, exhibiting a 36-degree symmetry. Additionally, in Figures 4.5 (c,d), we observe a faster decline in data throughput with increasing half-intensity angle compared to Figures 4.2 (c,d).

The mean data throughput as a function of half-intensity angle is presented in Table 4.2. It is notable that a lower peak data throughput of 5.46 Gbit/s is achieved at a half-intensity angle of 10 deg, which corresponds to 78.22% of the peak mean maximal data throughput achieved by the Euclidean-based set selector. Furthermore, when compared to the maximal minimum Euclidean distance case, the peak data throughput peaks at small half-intensity angles and afterwards rapidly decreases, reaching only 2.25 Gbit/s at $\Phi_{1/2}^{\mathrm{lens}} = 45\,\mathrm{deg}$.

Algorithm 2 primarily favors the selection of neighbouring beams to maximise the mean SNR at the receivers. In cases where a single aligned receiver is used, this tendency limits the maximum number of engaged transmitter beams to just 2. The algorithm consistently selects the nearest neighbours due to their nearly identical received optical power. As a result, only the j^{th} transmitter beam and one of its nearest neighbours are typically chosen. However, in various spatial regions, the symmetry of nearest neighbours can be disrupted due to misalignments between the receivers and the j^{th} transmitter beam. In such regions, data throughput hot spots emerge, similar to what is observed in the maximal Euclidean selection case.

As discussed earlier, when the half-intensity angles are narrow (i.e., $\Phi_{1/2}^{\mathrm{lens}} < 15$ deg), the received optical powers from the nearest neighbour transmitter beams can vary significantly with the spatial coordinates of the UE. This phenomenon helps explain the

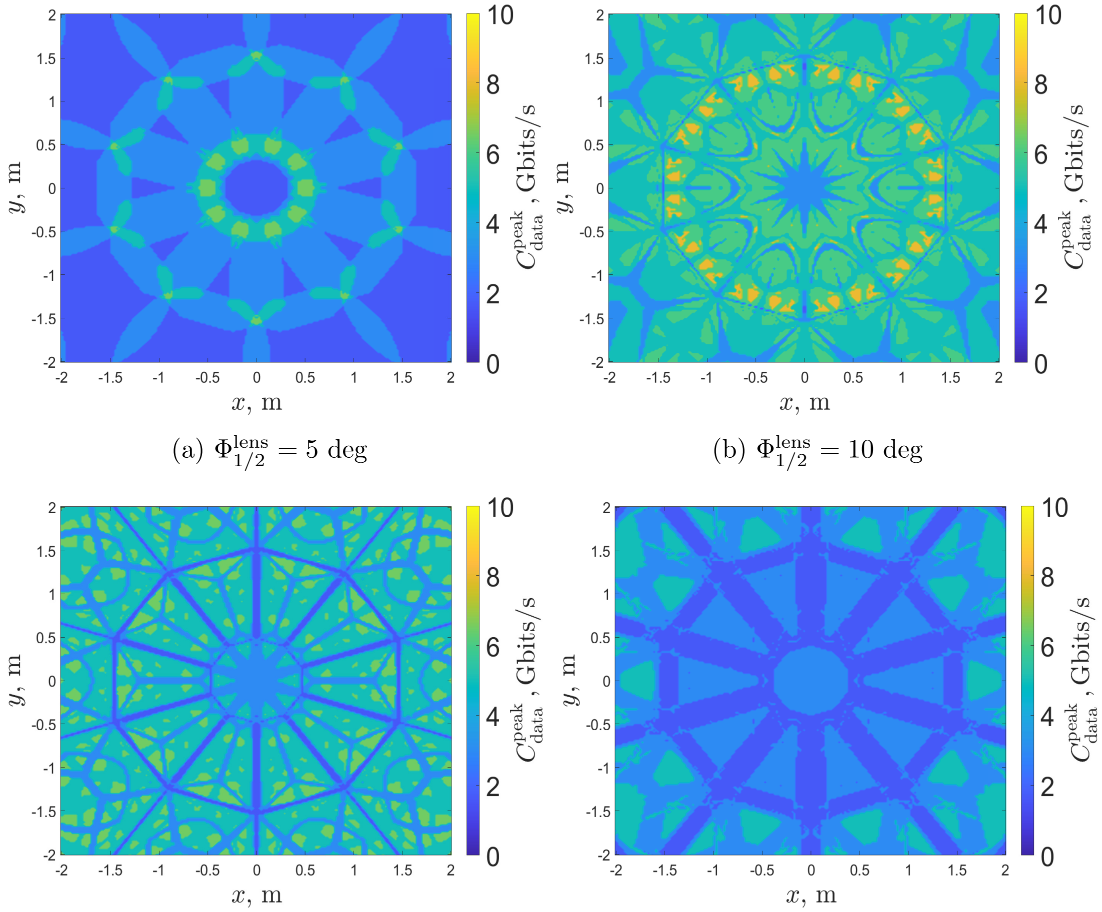

(a) $\Phi_{1/2}^{\text{lens}} = 5$ deg

(b) $\Phi_{1/2}^{\text{lens}} = 10$ deg

(c) $\Phi_{1/2}^{\text{lens}} = 15$ deg

(d) $\Phi_{1/2}^{\text{lens}} = 30$ deg

Figure 4.5: Room maximum achievable data throughput distribution for various values of $\Phi_{1/2}^{\text{lens}}$ and when using the maximal SNR set selection criterion.

Table 4.2: Mean data throughput and standard deviation for various $\Phi_{1/2}^{\mathrm{lens}}$ and maximal SNR set selector.

$\Phi_{1/2}^{\mathrm{lens}}$, deg	Mean Data Throughput: $\mathrm{E}(C_{\mathrm{data}}^{\mathrm{peak}})$, Gbit/s	Standard Deviation: $\sigma(C_{\mathrm{data}}^{\mathrm{peak}})$, Gbit/s
5	2.84	0.31
10	5.46	0.17
15	4.63	0.17
20	4.06	0.21
25	3.51	0.21
30	3.06	0.22
35	2.71	0.17
40	2.42	0.1
45	2.25	0.11

lower half-intensity angle peaking behavior and the overall lower peak mean maximal data throughput. In these scenarios, the engaged beam set selection based on SNR is limited to the nearest neighbours and heavily depends on the presence of hot spots. In such regions, the asymmetry between the nearest neighbour irradiance patterns creates favorable conditions for selecting multiple beams based on the maximal SNR criterion. However, once the half-intensity angle becomes wide enough, and the symmetry of optical power among nearest neighbour transmitter beams is restored (i.e., irradiance patterns become more uniformly spread) regardless of the UE's relative position to the AP, the maximal data throughput experiences a rapid decline.

Figures 4.5(a-d) suggest a high spatial distribution entropy, which we have plotted alongside the mean data throughput in Figure 4.6. In the previously discussed Euclidean case, the range of high peak mean data throughput was achieved correlated with low spatial entropy. However, in the maximal SNR case, we observe that high mean data throughput is achieved with high spatial entropy. The entropy roll-off is strongly correlated with the mean data throughput roll-off, which tends toward a single-beam selection. It is clear from the figure that when using maximal SNR-based selection, high mean data throughput cannot be achieved with high homogeneity. This demonstrates the limitation of the maximal SNR condition selection in the context of nearest neighbour asymmetry, which results in increased heterogeneity of the data throughput distribution in the room.

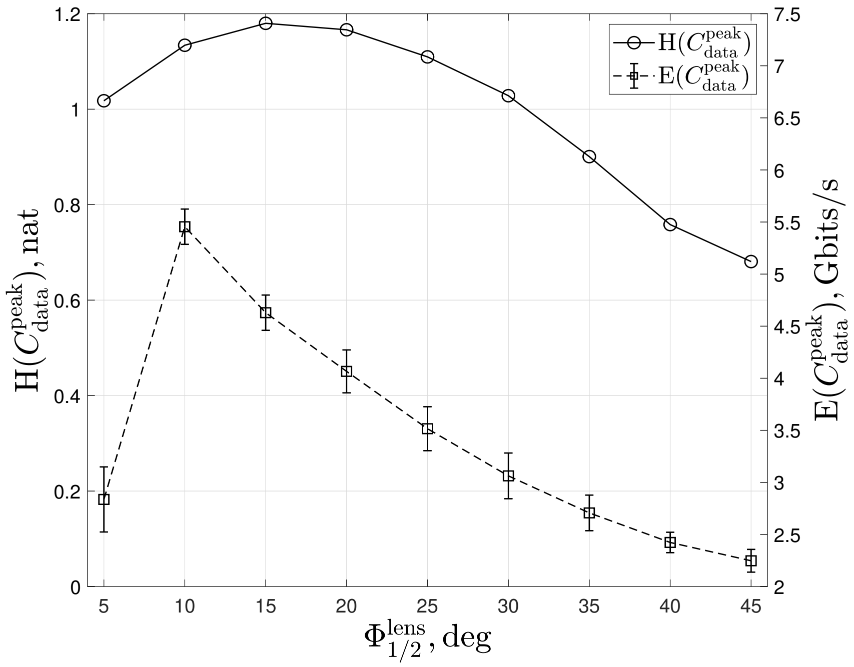

Figure 4.6: Mean data throughput and spatial entropy for various values of $\Phi_{1/2}^{lens}$ using maximal SNR set selector.

4.2.3 Optimal GSSK Channel Ratio Set Selector

In Figures 4.7(a-d), we see maximal data throughput spatial distribution using the optimal GSSK channel-ratio-based set selector following Algorithm 3. We can observe that the set selector's performance at $\Phi_{1/2}^{lens} = 5$ deg is very similar to that of the maximal SNR and maximal minimum Euclidean-based selectors. As the half-intensity angle increases, the spatial distribution in Figure 4.7(b) begins to resemble the results obtained under maximal SNR conditions, characterized by cold spot areas where nearest neighbour overlap is highest. However, in contrast to the maximal SNR case, the optimal GSSK channel ratio case exhibits a considerably slower roll-off in data throughput. Nonetheless, the distributions still maintain a higher level of heterogeneity compared to the maximal minimum Euclidean case.

We can conclude from these results that the optimal ratio-based set selector, at low half-intensity angles, performs the same nearest neighbour selection as the maximal SNR and maximal minimum Euclidean distance-based set selectors. However, it yields

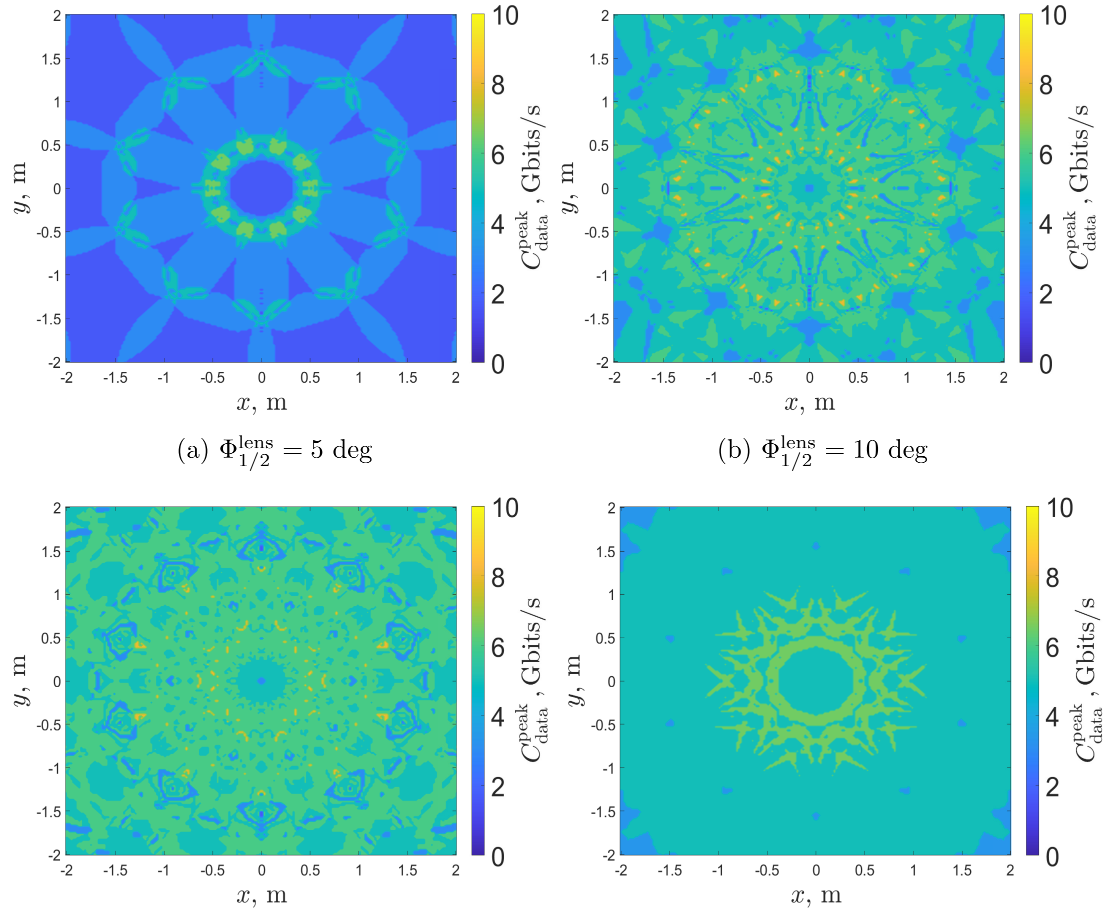

(a) $\Phi_{1/2}^{\text{lens}} = 5$ deg

(b) $\Phi_{1/2}^{\text{lens}} = 10$ deg

(c) $\Phi_{1/2}^{\text{lens}} = 15$ deg

(d) $\Phi_{1/2}^{\text{lens}} = 30$ deg

Figure 4.7: Room maximum achievable data throughput distribution for various values of $\Phi_{1/2}^{\text{lens}}$ and optimal GSSK channel ratio set selection criterion.

a slightly smaller achievable maximal data throughput at $\Phi_{1/2}^{\text{lens}} = 5$ deg compared to the other two methods at low half-intensity angles. Furthermore, while the optimal ratio selection outperforms maximal SNR condition-based selection, it does not achieve the data throughput performance of the Euclidean one. We consider this limitation to be due to the SNR of further neighbours. After selecting the highest j^{th} SNR beam, the algorithm proceeds to select each subsequent $j+1$ neighbouring beam with the average channel gain per receiver as close as possible to $1/2$. This suggests that in the limit of high SNR and a large number of available beams, the algorithm should yield similar performance to the Euclidean-based selection.

We assert that in this limit, there will exist a tuple of channel gains with relative ratios similar to the condition and absolute values well above the noise floor. However, if we consider limited channel resources and the number of beams, noting that each subsequent beam has only half of the channel gain relative to the previous one, the algorithm runs out of available beams with enough SNR faster than the Euclidean-based selector, as the algorithm ignores SNR contribution in the selection. In contrast, the maximal minimum Euclidean distance criterion-based set selector chooses the engaged beam set based on both the most optimal ratios for the given SNR of all beams. In that sense, the maximal minimum Euclidean distance criterion takes into account the noise floor, whereas the optimal ratio-based selector does not.

The optimal ratio based selector benefits from the selectivity based on the distinguishability of different beams, however, it lacks in terms of selectivity based on the SNR of the beams.

Table 4.3: Mean data throughput and standard deviation for various $\Phi_{1/2}^{\text{lens}}$ and optimal GSSK channel ratio set selector.

$\Phi_{1/2}^{\text{lens}}$, deg	Mean Data Throughput: $\mathrm{E}(C_{\text{data}}^{\text{peak}})$, Gbit/s	Standard Deviation: $\sigma(C_{\text{data}}^{\text{peak}})$, Gbit/s
5	2.76	0.29
10	5.44	0.15
15	5.91	0.12
20	5.64	0.18
25	5.35	0.32
30	4.92	0.25
35	4.56	0.23
40	4.06	0.33
45	3.68	0.3

Comparing the results in Table 4.3 to those in Table 4.1, we observe that the performance of the optimal ratio and maximal minimum Euclidean distance set selectors achieves a mean peak data throughput at a significantly lower half-intensity angle of $\Phi_{1/2}^{\text{lens}} = 15$ deg. The peak mean data throughput is 5.91 Gbit/s, which is about 85% of the peak mean maximal data throughput achieved by the Euclidean-based set selector and 1.08 higher than the mean data throughput achieved by the maximal SNR-based set selector.

Figure 4.8 displays the mean data throughput and spatial distribution entropy as

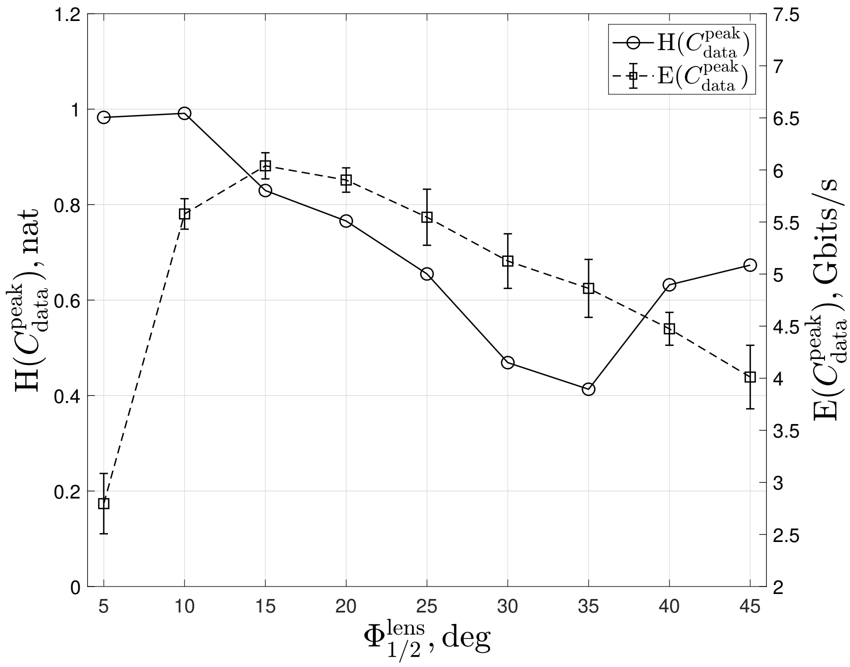

Figure 4.8: Mean data throughput and spatial entropy for various values of $\Phi_{1/2}^{\mathrm{lens}}$ using optimal GSSK channel ratio set selector.

functions of the half-intensity angle for the optimal GSSK channel ratio set selector. Similar to the SNR-based and maximal minimum Euclidean-based set selectors, a high degree of spatial entropy is present at low half-intensity angles due to the limited availability of nearest neighbours and their dependence on local spatial coordinates. As we increase the half-intensity angle, the mean data throughput peaks at still relatively high spatial entropy, resembling the case of the maximal SNR set selector. However, we observe a sharp decline in entropy, similar to the Euclidean set selector case, before the mean data throughput has significantly declined.

Furthermore, the minimum spatial entropy is observed at the slightly higher half-intensity angle as in the Euclidean distance set selector case. This demonstrates that concerning the trade-off between data throughput and spatial entropy, the optimal GSSK channel ratio set selector exhibits intermediate properties compared to the maximal SNR and maximal minimum Euclidean distance-based criteria set selectors. The spatial entropy, however remains significantly higher than in the case of maximal minimum Euclidean distance set selector. In terms of user experience, the best mean data throughput and uniformity trade-off is within the range of $30-35$ deg half-intensity angles.

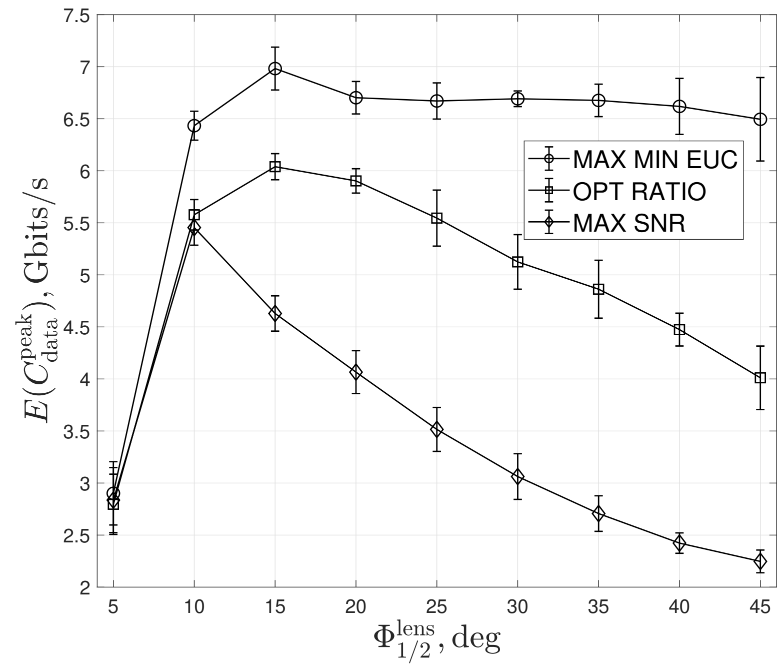

Figure 4.9: Mean data throughput comparison.

4.2.4 Performance Comparison of the Algorithms

We can summarize the comparison of the three different beam set selectors in terms of mean maximal data throughput in Figure 4.9. The set selector based on maximal minimum Euclidean distance provides the highest and stable mean data throughput over a wide range of half-intensity angles. In comparison, the maximal SNR-based set selector peaks at a lower mean data throughput and half-intensity angle, with a quicker roll-off. The optimal GSSK channel ratio selector yields intermediate results between the other two methods.

We can further compare the performance by calculating the relative difference of the mean data throughput achieved by different set selectors compared to the maximal

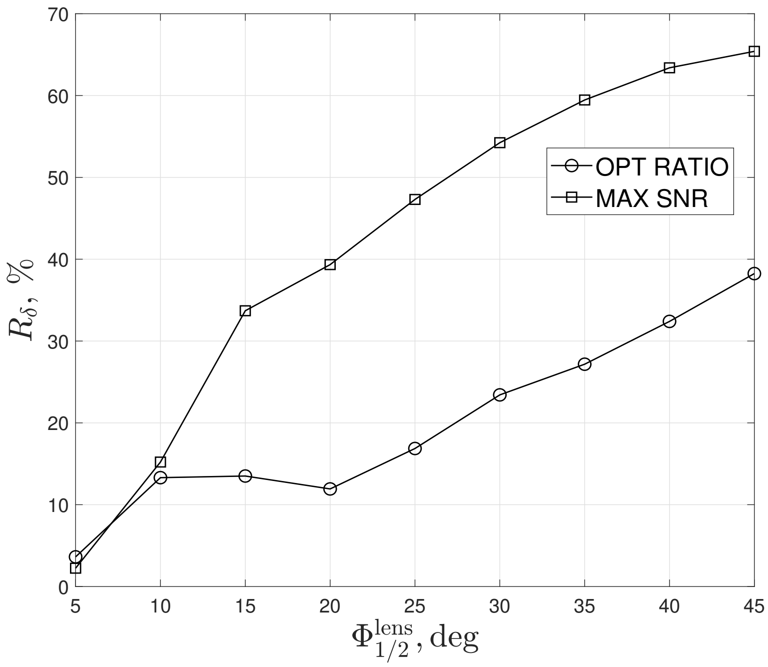

Figure 4.10: Relative throughput difference of set selectors compared to the maximal minimum Euclidean distance set selector.

minimum Euclidean distance-based one as follows:

$$R_\delta = \frac{\mathrm{E}(C^{\text{peak}}_{\text{data,Euclidean}}) - \mathrm{E}(C^{\text{peak}}_{\text{data,test}})}{\mathrm{E}(C^{\text{peak}}_{\text{data,Euclidean}})} \cdot 100\%, \tag{4.8}$$

here $C^{\text{peak}}_{\text{data,test}}$ is the mean maximal data throughput achieved by adaptive GSSK with set selectors using either the maximal SNR or optimal GSSK channel ratio criteria. The relative throughput difference of both criteria compared to the maximal minimum Euclidean distance criterion is shown in Figure 4.10.

As seen in the Figure, the relative throughput of the maximal SNR set selector, increases with half-intensity angle compared to the Euclidean-based. Whilst at $\Phi_{1/2}^{\text{lens}} = 45$ deg, the relative throughput approaches 70%. At this point, the SNR set selector can only support a single beam almost everywhere, while both the optimal ratio and maximal minimum Euclidean-based selectors support between $2-3$ and $3-4$ beams, respectively. For the optimal GSSK channel ratio set selector, the difference grows nearly linearly after $\Phi_{1/2}^{\text{lens}} = 20$ deg reaching nearly 40% at $\Phi_{1/2}^{\text{lens}} = 45$ deg. However, a small local minimum is also observed, where the relative throughput of the optimal ratio set selector compared to the maximal minimum Euclidean distance one is slightly above 10% at $\Phi_{1/2}^{\text{lens}} = 20$ deg.

Figure 4.11 displays the spatial data throughput distribution entropy plotted against the mean data throughput for all three set selectors. Generally, the bottom right corner of the Figure corresponds to overall better user performance, which is represented by higher data throughput and uniformity. In contrast, top left corner corresponds to overall worse user performance, which is represented by lower data throughput and high heterogeneity of the data throughput.

Firstly, we observe that for the maximal minimum Euclidean distance set selector, the entropy results cluster at lower right corner. As discussed earlier, the lowest entropy is achieved at the highest mean data throughput, which corresponds to 0.02 nat at 6.69 Gbit/s.

In contrast, the entropy for the maximal SNR set selector follows a distinct curve, exhibiting a strong correlation with mean data throughput. Here, the maximal SNR set selector achieves peak mean data throughput at the expense of high spatial entropy, reaching 1.13 nat at 5.46 Gbit/s. The lowest entropy of 0.68 nat, is coincides with lowest mean data throughput at 2.25 Gbit/s. The maximal SNR set selector exhibits the highest spatial entropy among all three selectors while achieving the lowest peak mean data throughput.

For the optimal GSSK channel ratio set selector, the entropy results cluster primarily between 4.01 Gbit/s and 6.04 Gbit/s, with the lowest entropy of 0.41 nat occurring at 4.86 Gbit/s. At peak mean data throughput, the spatial entropy is 0.83 nat. The highest optimal ratio selector exhibits similar clustering properties to the Euclidean distance based set selector but within a lower mean data throughput interval, with a higher entropy and a higher point spread.

We can summarise the results above in Table 4.4. Together with Figure 4.11 they demonstrate that the best results in simultaneous terms of peak mean data throughput and homogeneity of throughput are achieved using the maximal minimum Euclidean

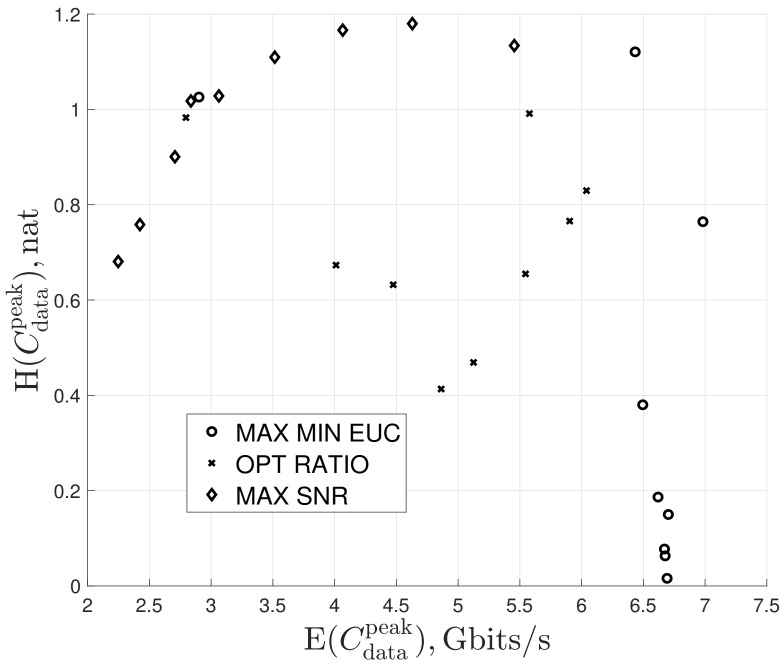

Figure 4.11: Spatial entropy vs mean data throughput.

distance set selector. The maximal SNR condition based set selector in comparison achieves lower peak mean data throughput at higher heterogeneity of data throughput. As can be seen, the relative data throughput at comparable spatial entropy is only 65.4%, while at relative data throughput difference of 15.21% the spatial entropy is approximately 1.5 times larger than for the Euclidean set selector. This demonstrates that the set selector follows an undesirable trade-off between both performance metrics - either achieving a high mean data throughput at the expense of homogeneity or achieving a high homogeneity at the expense of mean data throughput. The optimal GSSK channel ratio set selector provides an intermediate choice between the two, with a better trade off between the two performance metrics achieving only 1.09 times worse homogeneity at 13.5% relative data throughput difference as compared to the maximal Euclidean set selector case.

For all three adaptive GSSK algorithms no connectivity loss is observed at any half-intensity angle. We define a connectivity loss as a position and orientation realisation within the simulation parameters for which no beam selection can be performed within the BER requirements.

Table 4.4: Comparison of peak mean data throughput and spatial entropy.

	Maximal minimum Euclidean distance set selector	Maximal SNR set selector	Optimal GSSK channel ratio set selector
Peak mean data throughput, Gbit/s	6.98	5.46	6.04
Spatial entropy at peak mean data throughput, nat	0.76	1.13	0.83
Relative throughput difference, %	0	15.21	13.5
Minimal spatial entropy, nat	0.02	0.68	0.41
Peak mean data throughput at minimal spatial entropy, Gbit/s	6.69	2.25	4.86
Relative throughput difference at minimal spatial entropy, %	0	65.4	27.2

4.3 Random Orientation Hemispherical MIMO-VLC Scenario

In comparison to the fixed orientation scenario, the user does not have a fixed orientation relative to the global z-axis. Instead, we assume for our simulations a random orientation and position model. In this setup, for each iteration, we randomly generate a user's position in the room from a uniform distribution with $X \sim U(0,4)$ for the x-coordinate and $Y \sim U(0,4)$ for the y-coordinate, while keeping $z = 0$. As for the user's orientation, we model it based on statistics from a dynamic walking scenario, where user orientation Euler angles are drawn from Gaussian distributions: $A \sim \mathcal{N}(\mu_\alpha, \sigma_\alpha^2)$ for yaw α, $B \sim \mathcal{N}(\mu_\beta, \sigma_\beta^2)$ for pitch β, and $G \sim \mathcal{N}(\mu_\beta, \sigma_\beta^2)$ for roll.The parameters for the normal distributions, based on the dynamic user walking scenario from [285], are provided in Table 4.5.

The orientation statistics are based on the experimental measurements of 40 participants, which are representative of the cases where users use their smartphones in landscape or portrait mode in walking conditions [286] justifying the consideration of random orientation. The orientation of the AP transmitter beam sources is assumed to be fixed.

Table 4.5: UE orientation statistics from [285].

Angle	Mean, μ, deg	Standard deviation, σ, deg
Yaw α	-90	10
Pitch β	28.81	3.26
Roll γ	-1.35	5.42

During each iteration, we perform a beam selection using each of the three beam set selector algorithms based on the given position and orientation realization. BER is evaluated using the union bound approximation for the engaged sets, and the maximal data throughput is estimated. We repeat this process for 10^4 random position and orientation realizations for each transmitter beam half-intensity angle. For each set of half-intensity angle simulations, we calculate the mean maximal data throughput and standard deviation. We assume memory-less model, where each angle and position sample is drawn independent from the previous one. While in principle, the model differs from the dynamic walking scenario in [285, 286], we can consider that each sample is a snapshot of link performance, which has settled to a stable state. This assumption is sensible considering that the channel coherence time can be up to few hundreds of milliseconds long, which exceeds the beam selection algorithm time.

The comparison between the performance of the three different beam set selectors in a random orientation scenario, in terms of mean maximal data throughput, is depicted in Figure 4.12.

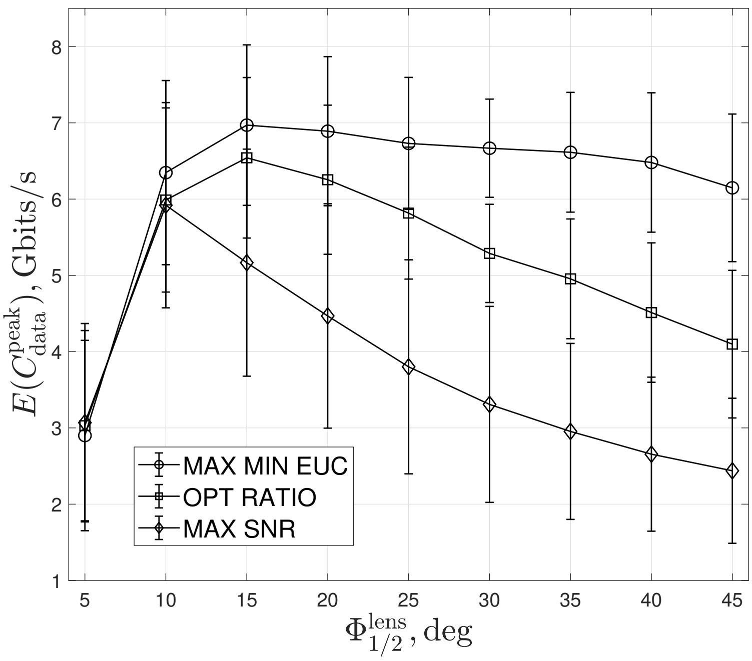

Figure 4.12: Mean data throughput comparison in random orientation scenario.

Figure 4.12 illustrates that the behavior of the curves closely resembles that of the fixed orientation case. There is a minor increase in mean data throughput, accompanied by a significantly higher standard deviation. This standard deviation increase is expected due to the random orientation statistics of the UE.

Likewise, the relative throughput of both the maximal SNR-based criterion set selector and the optimal GSSK channel ratio set selector, as shown in Figure 4.13,

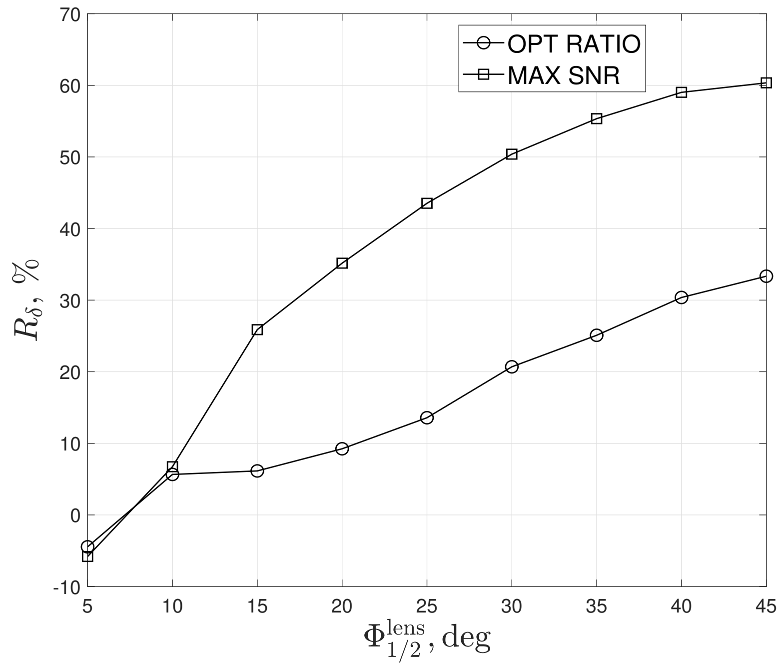

Figure 4.13: Relative throughput difference of set selectors compared to the maximal minimum Euclidean distance set selector in random orientation scenario.

closely resembles that of the fixed orientation case. This suggests that the addition of random orientation primarily increases the standard deviation of mean maximal data throughput for all tested half-intensity angles, while the mean data throughput and relative throughput remain relatively similar.

In the random orientation case, it is not possible to represent results with spatial distributions. Nonetheless, we can still calculate the entropy of the results, from the measurement frequency, which is depicted relative to the peak mean data throughput in Figure 4.14. Here, we observe that the addition of random orientation roughly retains the same entropy compared to the fixed orientation model. Furthermore, we also note that the comparison between different set selectors remains valid even when random orientation is assumed.

For all three adaptive GSSK algorithms the connectivity loss of about 1% of random realisations is observed at $\Phi_{1/2}^{\text{lens}} = 45$ deg[4].

[4]Connectivity loss refering to the case, where no transmitter beams can be engaged in the link.

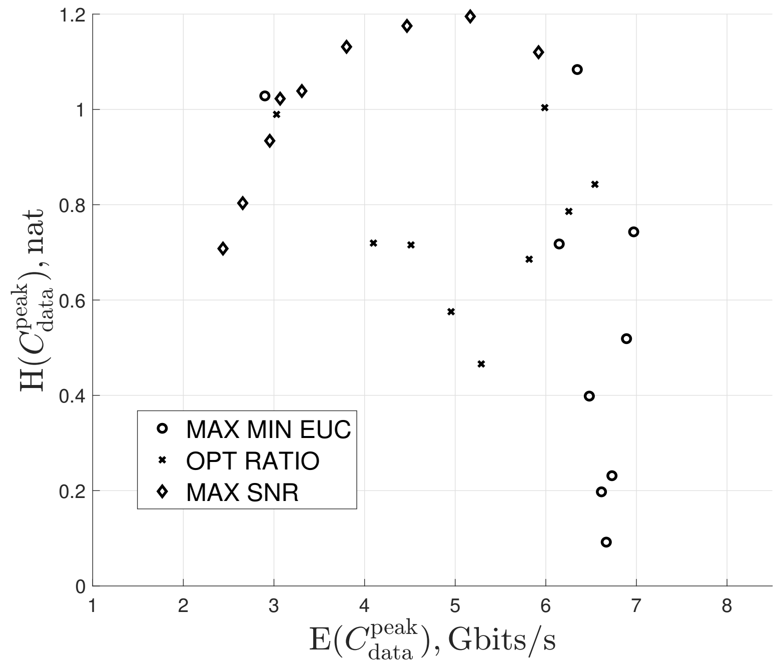

Figure 4.14: Distribution entropy vs mean data throughput in random orientation scenario.

In light of the results discussed thus far, we can draw the following conclusions:

- The adaptive GSSK system demonstrates no connectivity loss in GSSK transmission for any spatial region and all tested half-intensity angles within the model parameters when the user orientation is fixed. In the case of random orientation, no connectivity loss was observed in all iterations and for all tested half-intensity angles for all set selectors until $\Phi_{1/2}^{\mathrm{lens}} = 45\,\mathrm{deg}$. The connectivity loss of only about 1% was observed at half-intensity angle of $\Phi_{1/2}^{\mathrm{lens}} = 45\,\mathrm{deg}$. It's worth noting that in a fixed allocation GSSK scenario, connectivity loss would be expected when the engaged transmitter beam exits the FoV of the engaged receivers.

- The best results of peak mean data throughput and spatial homogeneity are achieved with the maximal minimum Euclidean distance-based set selector for adaptive GSSK. However, the set selector suffers from very high computational complexity, which grows exponentially with the search space of all available transmitter beam combinations, leading to a high latency penalty when multiple available transmitter beams are considered.

- The maximal SNR criterion-based set selector for adaptive GSSK has the lowest computational complexity among the three selectors, scaling linearly with the number of available transmitter beams. However, it demonstrates significantly lower performance in peak and roll-off mean maximal data throughput for both fixed and random user orientations. This lower performance is further characterized by high spatial distribution entropy, indicating high data throughput heterogeneity. Additionally, there is a strong correlation between data throughput and heterogeneity, resulting in a trade-off between data throughput and distribution homogeneity.

- The best GSSK performance can be achieved when all GSSK symbol levels are equidistant from each other. This condition occurs, as described when deriving the optimal GSSK channel ratio condition, when the channel gains for the j^{th} engaged transmitter beam and its $j^{\text{th}}+1$ neighbour channel gain at the i^{th} engaged receiver satisfy the relationship:

$$h_{ij+1} = 0.5h_{ij}.$$

Based on this condition, we propose a set selection algorithm, which we term as the optimal GSSK channel ratio criterion set selector. When the j^{th} engaged transmitter beam is aligned with the i^{th} engaged receiver, this leads to a half-intensity angle condition (for a Lambertian emitter) for two engaged beams:

$$\Phi_{1/2}^{\text{lens}} = \Delta\varphi_{ij+1} = \varphi_{ij+1} - \varphi_{ij}.$$

Generally, for N engaged beams, the optimal half-intensity angle that maximises the mean maximal data throughput is determined by a non-linear equation system, denoted as Equation (4.5). In practice, this system may be unsolvable when the relative orientation between transmitters and receivers can vary. Nevertheless, it provides insight into the mean optimal half-intensity angle for different numbers of engaged beams, allowing us to estimate an interval where mean maximal data throughput is achieved.

- The optimal GSSK channel ratio criterion set selector for adaptive GSSK provides an intermediate solution between the two other selectors. The selector's complexity benefits from the square dependency on the number of engaged transmitters, requiring multiple orders of magnitude fewer operations than the maximal minimum Euclidean distance criterion set selector. While the set selector does not match the mean data throughput of the maximal Euclidean distance-based one, it significantly improves it compared to the maximal SNR set selector. Furthermore, it provides a significantly better data throughput vs. homogeneity trade-off compared to the maximal SNR-based set selector. This makes the set selector well-suited for practical adaptive GSSK implementations, especially when considering a large number of available transmitter beams in the GSSK link.

4.4 Device-to-device Infrared MIMO-OWC Scenario

We will now discuss the data throughput performance in a device-to-device infrared MIMO-OWC scenario.

4.4.1 Close Spacing Scenario

In the first scenario, the transmitter beam sources are closely spaced. In this case, the (x, y) coordinates of the transmitter beam centroids on the receiver plane do not necessarily match the (x, y) coordinates of the transmitter beam sources on the transmitter plane. The spacing between the transmitter beam sources is fixed at 1 cm, while the transmitter beam centroid spacing is treated as a variable.

In such a scenario, we simulate handheld device-to-device communication, where transmitter beam sources are closely spaced together, with the minimum spacing determined by their convex lens diameters.

The spatial distributions of maximal data throughput at the receiver plane are shown in Figures 4.15 (a-f). In these figures, the left-side images correspond to different spacing transmitter beam square grids, which provide maximal coverage radius R_{cov} that is frequently used in wireless link performance analysis. Here we condition coverage radius (in mm) to correspond to the area of a spatial region on the receiver plane where the maximal achievable data of each location in the region is at least 10 Gbit/s.

Generally this coverage area can be much larger than the $20 \times 20\,\text{cm}^2$ target area. However, we only plot the subset of the this coverage area constrained to the target area for a fair comparison between different transmitter grids with different achievable coverage radii. On the right side, the images correspond to different transmitter beam square grid spacings that achieve peak mean maximal data throughput. These figures are presented for a fixed 2×2 receiver grid.

We can primarily observe from the Figures that, with adaptive GSSK, high data throughput can be achieved using an ordinary symmetrical square lattice of transmitter beams. This lattice is capable of achieving data throughput exceeding 10 Gbit/s within a 2 GHz bandwidth. By carefully adjusting the transmitter beam spacing to

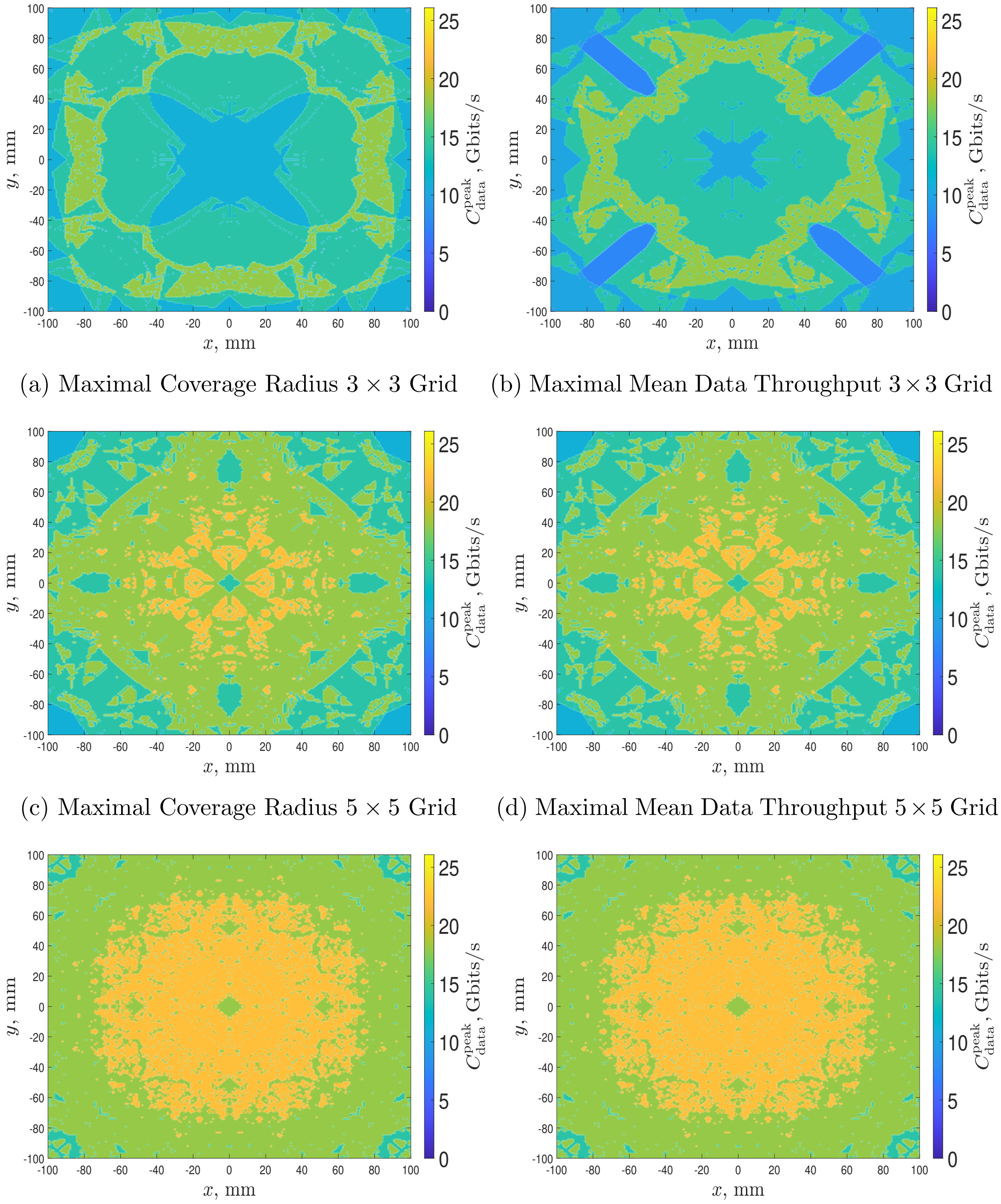

(a) Maximal Coverage Radius 3×3 Grid

(b) Maximal Mean Data Throughput 3×3 Grid

(c) Maximal Coverage Radius 5×5 Grid

(d) Maximal Mean Data Throughput 5×5 Grid

(e) Maximal Coverage Radius 9×9 Grid

(f) Maximal Mean Data Throughput 9×9 Grid

Figure 4.15: Achievable data throughput in close spacing scenario at target area for various grid sizes. Left side Figures conditioned on maximal coverage radius. Right side Figures conditioned on maximal mean data throughput.

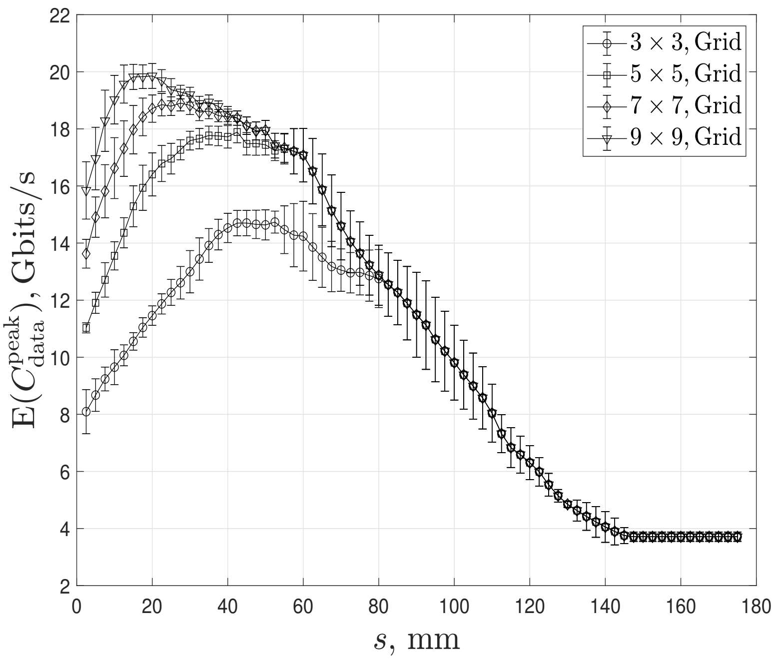

Figure 4.16: Mean peak data throughput as a function of transmitter beam spacing for various grids in close spacing scenario.

match the given beam parameters and design, conditions can be established where the optimal GSSK channel ratio set selector can effectively utilise nearest and next-nearest neighbours to select an engaged multiple beam set that meets the link performance requirements for BER.

As expected, the data throughput distributions exhibit a 90-degree rotational symmetry, characteristic of a square lattice. We also observe an intricate geometric distribution of hotspots (areas with higher data throughput than the mean) and cold spots (areas with lower data throughput than the mean). This geometric arrangement is particularly pronounced for 3×3 and 5×5 transmitter beam grids but becomes less distinct for the 9×9 transmitter beam grid. However, in all three cases, a common feature is a cold spot in the middle of the target area, which is characterized as a highly symmetrical point towards which all the radii of transmitter beams can be drawn towards, which represents a high interference/low distinguishability region.

Furthermore, the Figures demonstrate that increasing the number of available transmitter beams in the transmitter beam square lattice leads to higher achievable maximal data throughput and coverage radius. This observation is supported by Figures 4.16 and 4.17. Additionally, as the number of grid beams increases, both the peak mean maximal data throughput and coverage radius shift toward lower grid spacing. Specifically, for mean data throughput, the shift is from 52.5 mm for a 3×3 grid to 20 mm for a 9×9 grid. In the case of maximal coverage radius, the shift is from 50 mm for a 3×3 grid to 10 mm for a 9×9 grid.

As discussed in the previous section, the inclusion of more distant neighbours allows for larger engaged beam set selections when the beams are closely spaced within the target area, resulting in higher SNR. The Gaussian beam roll-off, combined with the high SNR at certain spacings, ensures the most optimal neighbour channel ratio among these distant beams. Conversely, when dealing with a low number of neighbours, the options for selections are limited. In such cases, to include more selected beams in the link, the spacing between neighbours must be increased to achieve optimal selection of beam channel ratios. In both scenarios, we observe a consistent decrease in mean data throughput and coverage radius as beam spacing increases. This reduction is primarily attributed to the SNR roll-off. Figure 4.16 illustrates a similar convexity property as seen with Lambertian beams.

From Figure 4.16, we can observe that the most significant increase in mean achievable data throughput occurs when we increase the transmitter beam grid elements from 3×3 to 5×5. Further increasing the number of transmitter beam grid elements contributes less to the peak mean data throughput. This behaviour represents the limited channel budget, which can be utilised, which asymptotically tends to a single peak mean data throughput.

Further analysing the Figures in 4.15, we observe that only for the 3×3 grid does maximal coverage radius differ from maximal mean data throughput within the given target area. In general, maximizing mean data throughput does not necessarily lead to maximal coverage radius. For instance, in Figure 4.15 (b), mean data throughput is higher compared to Figure 4.15 (a) due to increased data throughput in the central area. However, the presence of four symmetric 'cold spots'—areas with reduced achievable

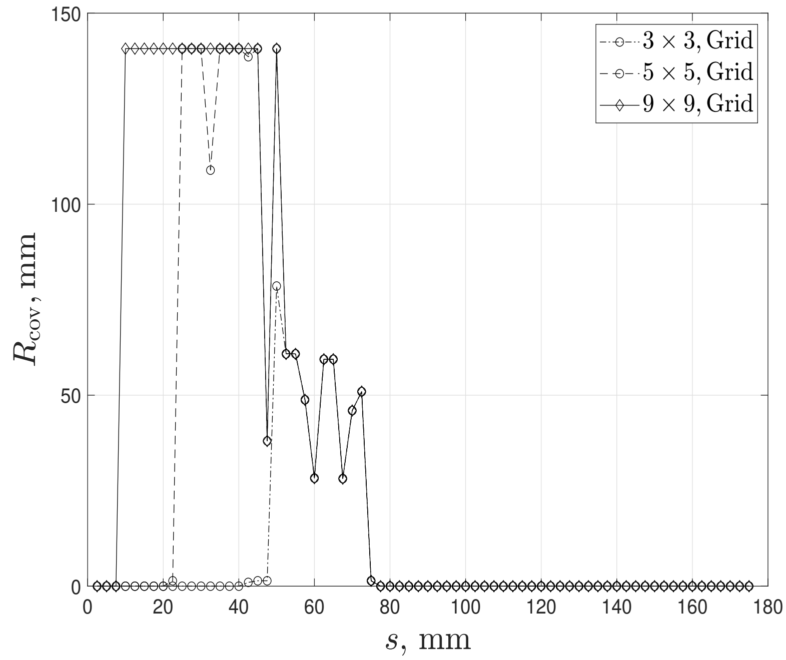

Figure 4.17: Coverage radius as a function of transmitter beam spacing for various grids in close spacing scenario.

peak data (under 10 Gbit/s) throughput—leads to reduced coverage radius. Varying the beam grid spacing, hot and cold spots can be generated, as shown particularly well in Figure 4.15 (c), where channel ratios and various beam SNRs vary significantly from point to point. This phenomenon explains the local minima observed in Figure 4.17, such as at 30 mm for the 5×5 grid, where a sudden local minimum is observed.

In Figure 4.17, as expected, the best coverage radius is achieved with the 9×9 grid, which, except for occasional minima due to cold spots, maintains maximum coverage radius from $s = 7.5$ mm to $s = 50$ mm. In contrast, the 3×3 transmitter beam grid cannot achieve maximal coverage radius for the given target area at any s

Another noteworthy feature is that increasing the number of transmitter beams in the grid improves the uniformity of data throughput within the coverage radius for maximal mean data throughput. Analysing the standard deviation in Figure 4.16, we observe that the standard deviation (represented by y error bars) of data throughput distributions is minimal near their respective maxima.

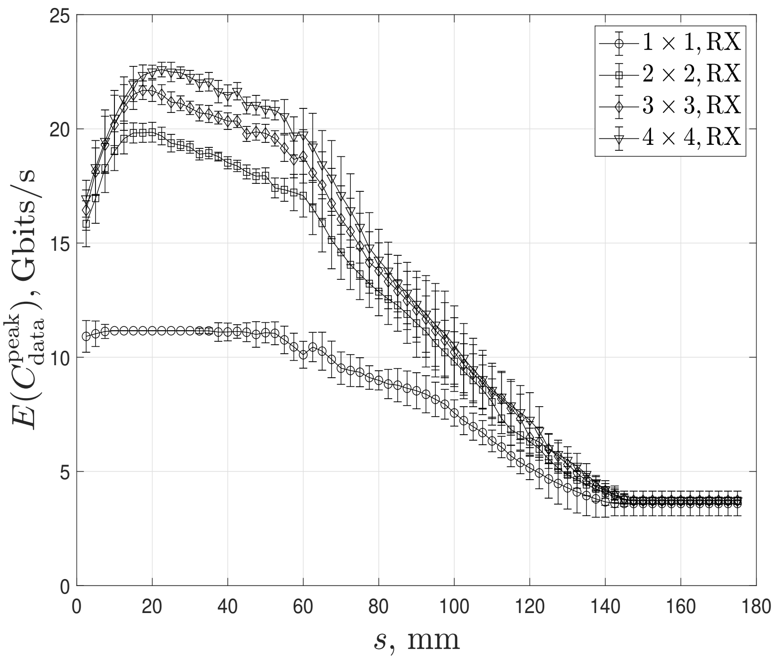

Figure 4.18: Mean peak data throughput as a function of transmitter beam spacing for various receiver grids in close spacing scenario.

The mean achievable data throughput's dependency on the number of receivers for different transmitter beam spacing (s) is illustrated in Figure 4.18, with the transmitter beams arranged in a 9×9 square grid. As expected, due to the array gain, the mean achievable data throughput increases with the number of receivers in the link. The most significant increase occurs when transitioning from a 1×1 square grid of receivers to a 2×2 grid. We observe that mean data throughput of up to 22 Gbit/s (22.6 Gbit/s) can be achieved, with a mean spectral efficiency of $E(\eta) = 6.08$ bit/s/Hz for a 4×4 receiver grid.

Similarly to the number of transmitter beams in the grid, we observe that further increase in number of receivers in the grid have diminishing impact to the achievable mean data throughput with larger receiver grids. By increasing the number of receivers, we can increase the SNR and consequently the number of the selectable neighbouring beams, which suffice minimum required channel ratios. However, because we limit the number of such beams to 9×9 at some point further increase in SNR cannot allow for more neighbouring beam inclusion in the engaged beam set. For example, if we compare 2×2 and 4×4 RX grids, the spectral efficiencies are $E(\eta) = 5.34\,\text{bit/s/Hz}$ and $E(\eta) = 6.08\,\text{bit/s/Hz}$ - we can add on average 0.74 beams more in the engaged sets due to the increased SNR, while comparing 3×3 and 4×4 RX grids we see increase of only 0.25 additional transmitter beams on average.

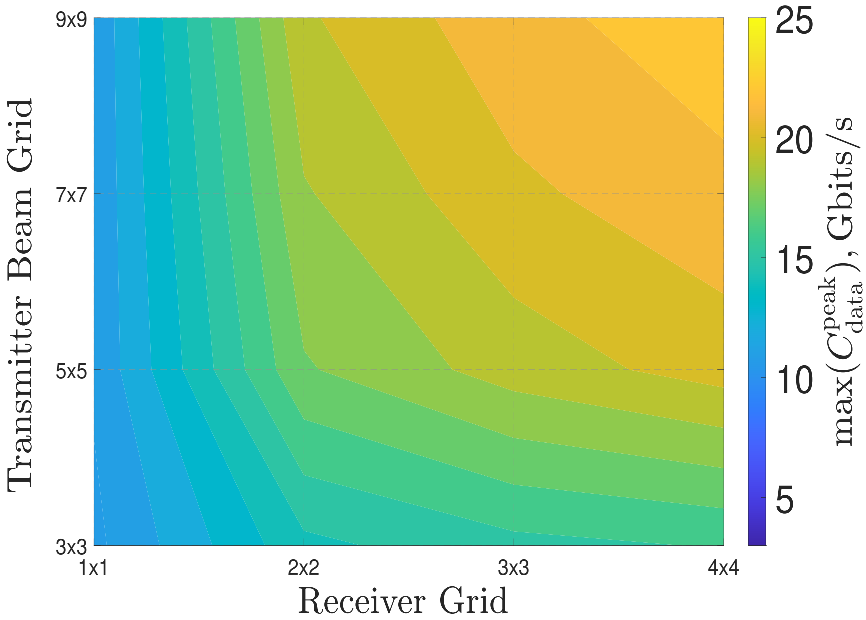

Figure 4.19: Maximum mean peak data throughput as a function of transmitter beam and receiver grids in close spacing scenario.

By combining the analysis of Figures 4.16 and 4.18, we can summarize the maximal mean data throughput achievable based on both the number of transmitter beams and receivers in the square lattice in Figure 4.19. As expected, the highest maximal mean data throughput is achieved when both the transmitter beam grid and receiver grid dimensions are maximal. For instance, a 2×2 receiver grid achieves a maximal data throughput of $19.85\,\text{Gbit/s}$ with a 9×9 transmitter beam grid, resulting in a mean spectral efficiency of $E(\eta) = 5.34\,\text{bit/s/Hz}$. Furthermore, we observe that the fastest increase in maximal mean data throughput occurs along the diagonal of the plot, which is expected since an increase in both parameters promotes both the diversity of neighbour selection and higher SNR.

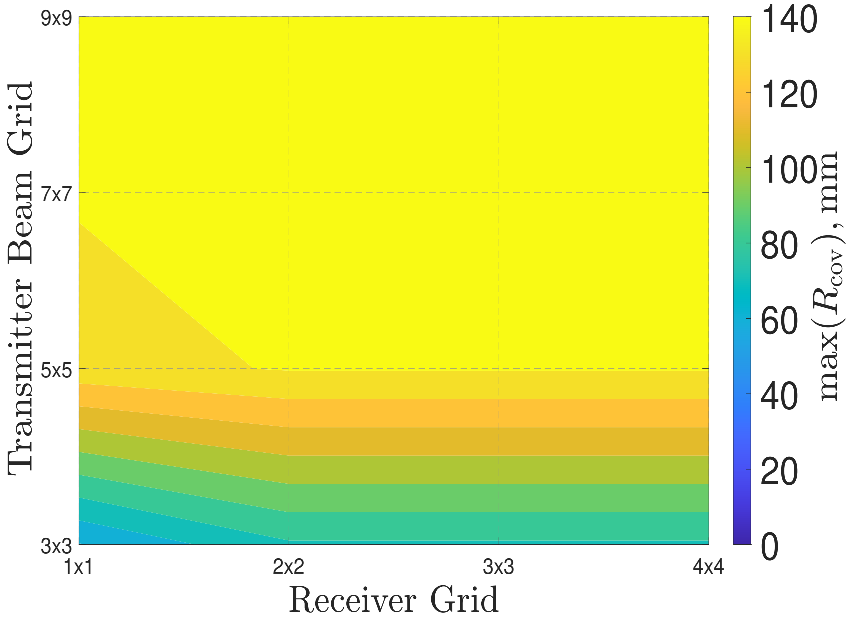

Figure 4.20: Maximum coverage radius as a function of transmitter beam and receiver grids in close spacing scenario.

The dependency of maximal coverage radius on the numbers of transmitters and receivers in their grids is depicted in Figure 4.20. We observe that the maximal coverage radius for the given target area can already be achieved with a 5×5 transmitter beam grid. Furthermore, the target coverage radius can be achieved with a single receiver, provided that the transmitter beam grid is at least 7×7.

4.4.2 Sparse Spacing Scenario

Now, let's consider the scenario where the transmitter beam sources are spatially separated shown in Figure 3.16 b). In this case, the (x, y) coordinates of the transmitter beam centroids on the receiver plane match the (x, y) coordinates of the transmitter beam sources on the transmitter plane. Furthermore, as discussed in subsection 3.4.2 the transmitter beam sources are spatially separated in a square lattice with spacing $s_0 = s$. The separation of the transmitter beam sources enhances the spatial diversity of the GSSK link, which we expect to improve the achievable data throughput.

The spatial distributions of maximal data throughput at the receiver plane are

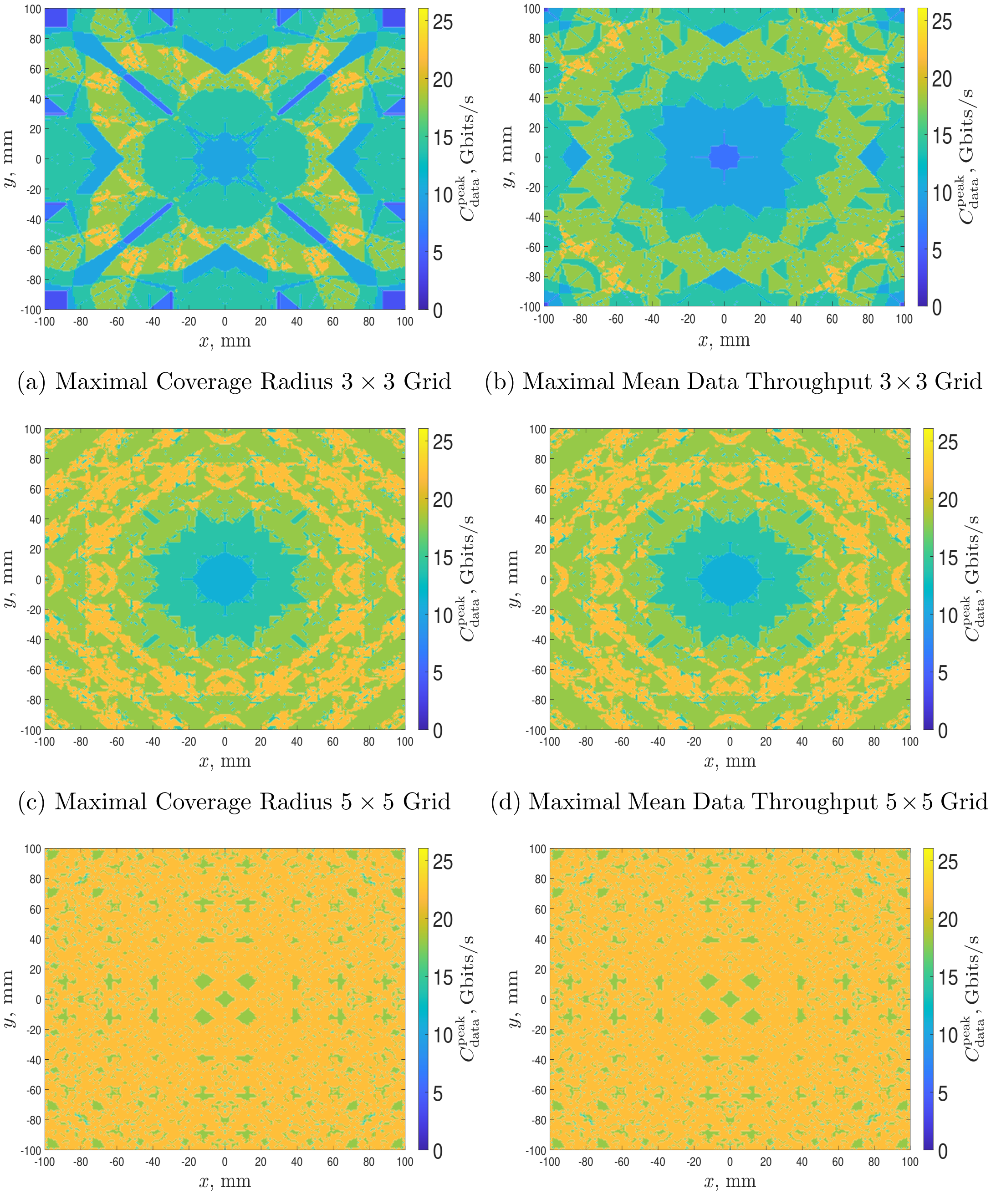

(a) Maximal Coverage Radius 3×3 Grid
(b) Maximal Mean Data Throughput 3×3 Grid
(c) Maximal Coverage Radius 5×5 Grid
(d) Maximal Mean Data Throughput 5×5 Grid
(e) Maximal Coverage Radius 9×9 Grid
(f) Maximal Mean Data Throughput 9×9 Grid

Figure 4.21: Achievable data throughput in sparse spacing scenario at target area for various grid sizes. Left side Figures conditioned on maximal coverage radius. Right side Figures conditioned on maximal mean data throughput.

presented in Figures 4.21 (a-f). As in the previous scenario, the left-side spatial distributions are obtained with the transmitter beam spacing that maximises coverage radius, while the right-side figures correspond to the transmitter beam spacing that yields peak mean maximal data throughput. These figures are generated for a fixed 2×2 receiver grid.

Similar to the closely spaced arrangement discussed earlier, the data throughput distributions exhibit elaborate and symmetrical patterns, each characterised by a 90-degree rotational symmetry. However, due to the spatial separation, the incidence angle ψ at the receiver for the transmitter beams varies considerably, resulting in significant modifications to the data throughput pattern.

In comparison to the closely spaced transmitter beam source arrangement, as shown in Figure 4.15, the data throughput in the spatial arrangement is increased. This increase is particularly evident in Figure 4.15 (e). Furthermore, we observe that only in Figures 4.15 (e-f) do the results for maximal coverage radius and maximal mean data throughput match. This illustrates that the introduction of larger spatial separation and the modification of the incidence angle between the transmitter beam sources and receivers can lead to new local hot and cold spots.

Figure 4.22 confirms our observation that the mean maximal data throughput increases in the sparse spacing of the transmitter beam sources compared to the close spacing case. The maximum data throughput observed here is 21.52 Gbit/s, achieved with a 9×9 grid. However, we also notice a faster decrease in mean data throughput with increased spacing, as expected due to the larger separation between beam sources resulting in greater incidence angles of different beams at the receiver plane.

For instance, at a grid spacing of $s = 20\,\text{mm}$, the farthest neighbour in the lattice is located at a distance of $r = \sqrt{(20 \times 4)^2 + (20 \times 4)^2} = 113.13\,\text{mm}$ from the target area centre, resulting in an incidence angle of approximately 6.447 deg. Meanwhile, the beam half-width half-maximum is 104.55 mm. The combined effect of reduced lens gain at such incidence angles and Gaussian beam roll-off significantly diminishes the SNR of the far neighbour beams, limiting their participation in set selection, especially at the periphery of the target area.

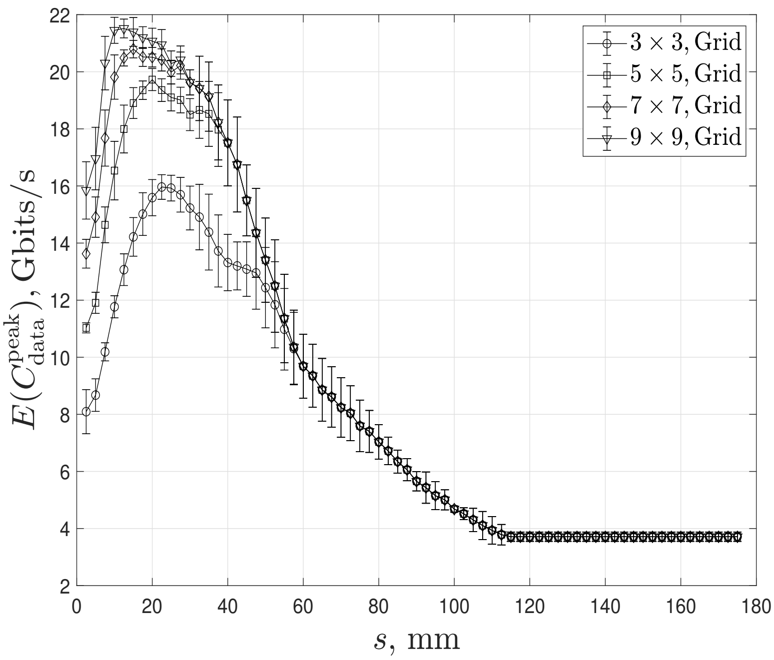

Figure 4.22: Mean peak data throughput as a function of transmitter beam spacing for various grids in sparse spacing scenario.

Figure 4.23 shows that both the 9×9 and 5×5 transmitter beam square grids can achieve maximal coverage radius for the given target area. When compared to Figure 4.17, we observe that the maxima of coverage radii have shifted toward smaller grid spacing values. However, for the 3×3 grid, we see a decrease in coverage radius when a sparse grid of transmitter beams is used. Additionally, we notice a reduction in the interval for the 9×9 and 5×5 grids. For the 9×9 grid, the maximal coverage radius has decreased from $\Delta s = 42.5\,\mathrm{mm}$ in the close spacing scenario to $\Delta s = 22.5\,\mathrm{mm}$ in the sparse spacing scenario. As discussed previously, we attribute this observation to the separation of transmitter beam sources, leading to a faster SNR roll-off.

The dependency of mean achievable data throughput on the number of receivers for different transmitter beam spacing (s) is illustrated in Figure 4.24. In this scenario, similar to the previous one, the transmitter beams are arranged in a 9×9 square grid. The maximal achievable mean data throughput has increased to 23.8 Gbit/s compared to 22.6 Gbit/s in the case of closely spaced transmitter beam sources. Similarly to

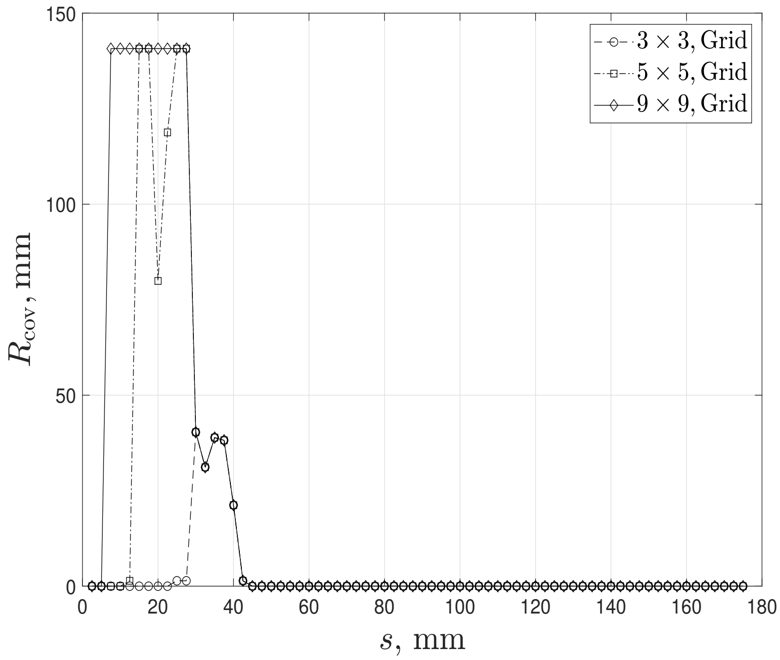

Figure 4.23: Coverage radius as a function of transmitter beam spacing for various grids in sparse spacing scenario.

what we observed in Figures 4.22 and 4.23, we notice a faster roll-off in mean data throughput. At 23.8 Gbit/s, the mean spectral efficiency is $E(\eta) = 6.4$ bit/s/Hz; to further increase it, the set selector should engage at least 7 transmitter beams.

Comparing the results to the close spacing scenario, we observe a substantial improvement in the maximal mean achievable data throughput when comparing the 4×4 grid to the 3×3 grid. This improvement can be attributed to a larger number of eligible neighbouring transmitter beams that satisfy the condition of the optimal channel ratio criterion. This increase in eligibility results from the angle diversity of the separated transmitter beam sources. In this case, the limiting condition is primarily the SNR rather than the channel ratio. Therefore, by increasing the number of receivers, the necessary SNR threshold is reached to support an additional average of 0.38 transmitter beams in the engaged link.

In Figure 4.25, we notice a similar dependency of the maximal mean data throughput on the receiver and transmitter beam grids as observed in the close spacing scenario.

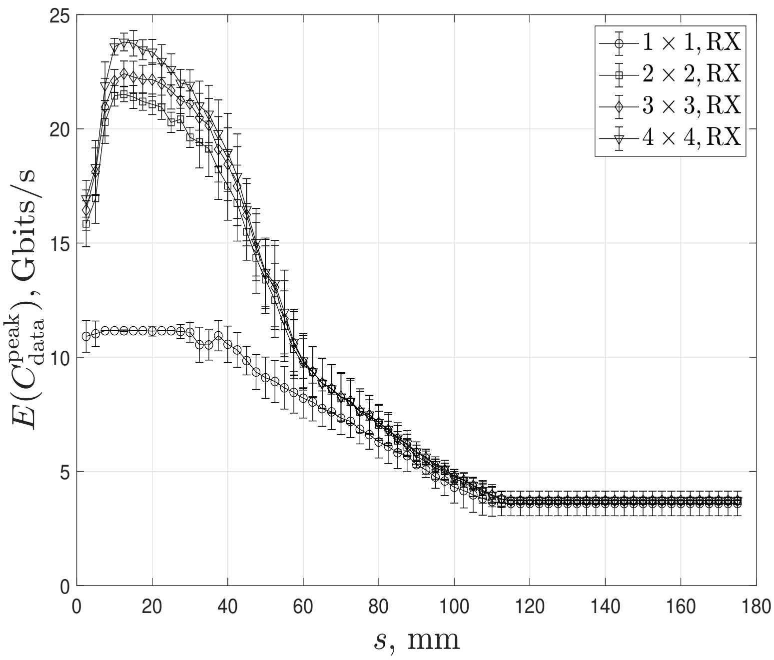

Figure 4.24: Mean peak data throughput as a function of transmitter beam spacing for various receiver grids in sparse spacing scenario.

However, when compared to Figure 4.19, we observe that further increasing the number of transmitter beams in the grid does not lead to a significant increase in the maximal achievable data throughput. This can be observed in the Figure as a large plateau of data throughput in the top-right corner.

Figure 4.26 illustrates the maximal coverage radius depending on the numbers of transmitters and receivers in their respective grids. We can observe that the maximal achievable coverage radius is very similar to the close spacing scenario. In contrast to Figure 4.20, the coverage radius for the 3×3 grid is reduced overall.

The summary of main findings in terms of achievable maximal mean data throughput and maximal coverage radius is given in Table 4.6.

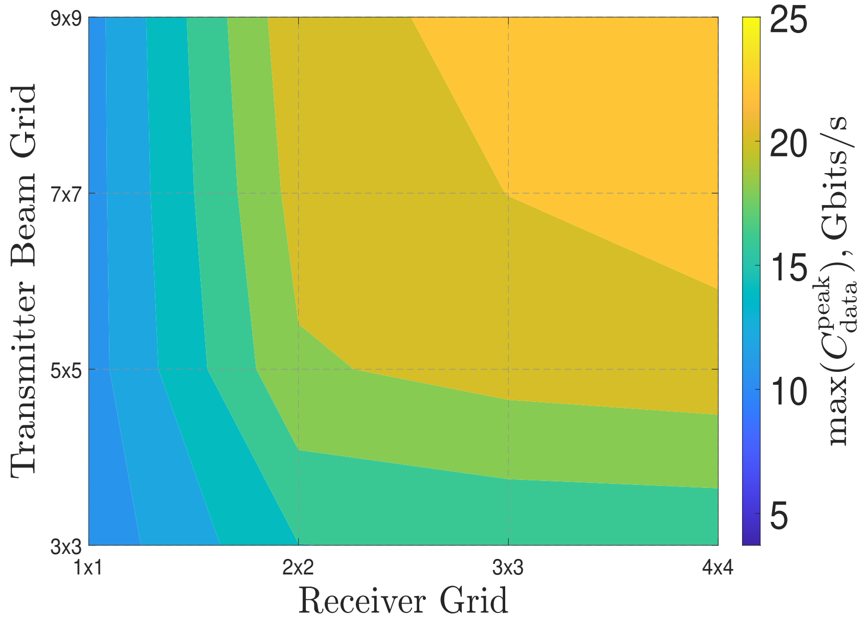

Figure 4.25: Maximum mean peak data throughput as a function of transmitter beam and receiver grids in sparse spacing scenario.

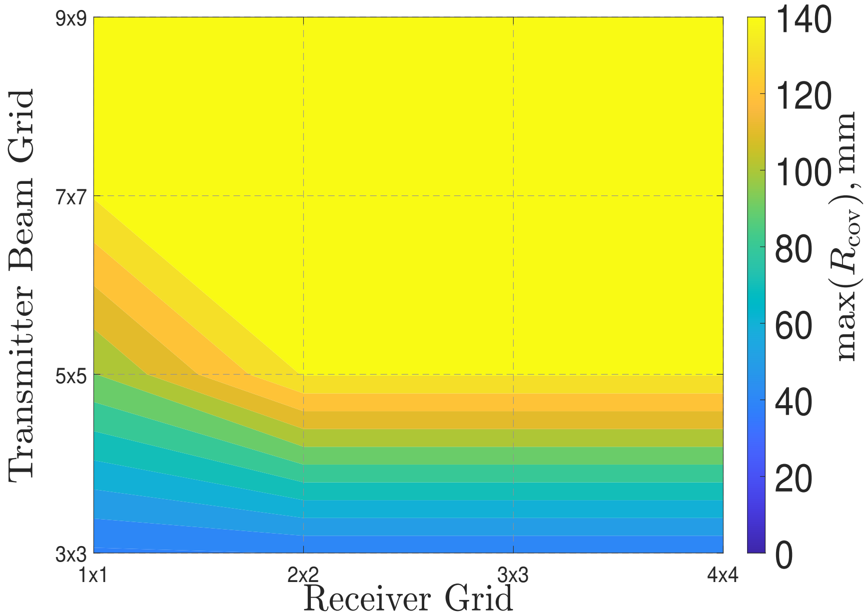

Figure 4.26: Maximum coverage radius as a function of transmitter beam and receiver grids in sparse spacing scenario.

Table 4.6: Maximal mean data throughput and maximal coverage radius comparison of close and sparse beam spacing scenarios.

	2×2 Receiver Grid	4×4 Receiver Grid
Maximal mean data throughput $\max(E(C_{\text{data}}^{\text{peak}}))$, Gbit/s (Close transmitter beam spacing)	19.85	22.6
Maximal coverage radius $\max(R_{\text{cov}})$, mm (Close transmitter beam spacing)	140.72	140.72
Maximal mean data throughput $\max(E(C_{\text{data}}^{\text{peak}}))$, Gbit/s (Sparse transmitter beam spacing)	21.52	23.8
Maximal coverage radius $\max(R_{\text{cov}})$, mm (Sparse transmitter beam spacing)	140.72	140.72

We can summarise the key findings of infrared adaptive GSSK link performance in the device-to-device, aligned scenario with the following points:

- Very high data throughput ($>$ 10Gbit/s) can be achieved in a device-to-device infrared link at a considerable distance of 1 m and coverage diameter of nearly 30 cm using adaptive GSSK with low computational complexity optimal GSSK channel ratio criterion set selector.

- A high data throughput GSSK link can be achieved using a simple symmetric square lattice arrangement of transmitter beams. Achieving the necessary symmetry breaking to engage multiple transmitter beams can be done by spacing the lattice transmitter beam locations appropriately relative to the beam dimensions at the receive plane.

- The appropriate spacing can be arranged both by steering or deflecting the beams at the receiver plane of very closely spaced transmitter beam sources or by spatially separating transmitter beam sources without beam steering. The first scenario corresponds to a small form factor portable transmitter device embedding transmitter beams. The second scenario corresponds to a large form factor device, for example, a screen or display with transmitter beams sparsely arranged on its surface.

- A sparse arrangement of transmitter beam sources achieves higher data throughput than a close arrangement. In both cases, a grid of at least 5×5 transmitter beams is required to achieve the necessary coverage radius of the target area. When using a grid of at least 3×3 receivers, a mean data throughput of over 20 Gbit/s can be achieved.

4.5 Energy Efficiency Evaluation

In this section, we briefly discuss the energy efficiency of the simulated designs, focusing on the opto-electronic front-end. The evaluation of power consumption due to the DSP relies heavily on both the DSP implementation of the adaptive GSSK algorithm, encoding, decoding and FEC, as well as the processing unit itself. Likewise, the power consumption analysis of the networking layer is beyond the scope of this study. Therefore, in this work, we limit our assessment to the lower bound of energy efficiency in the opto-electronic front-end.

To analyse the power consumption of the transmitter beam, we consider a simple optical emitter (VCSEL or microLED) driver circuitry in Figure 4.27 similar to those discussed in [89, 287, 288]. Here, the OOK signal is modulated by controlling the

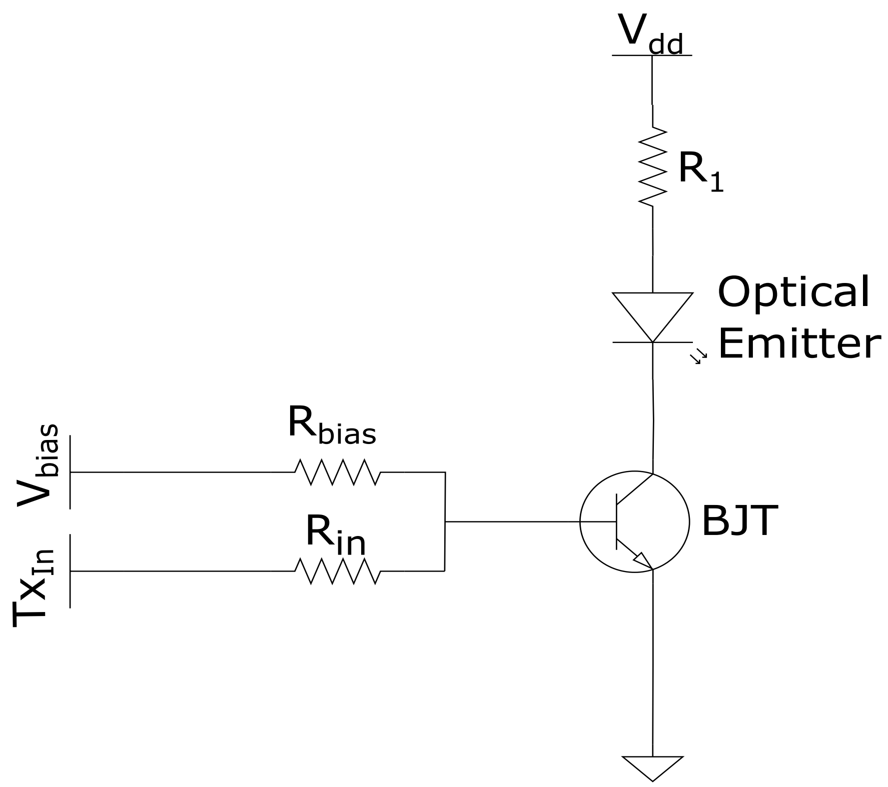

Figure 4.27: GSSK transmitter beam source array driver circuitry.

collector-emitter current flowing through the NPN BJT. To maintain a fast frequency response of the emitter, a constant bias current is applied to the base of the BJT at the direct current (DC) level of the signal. The modulated OOK signal is applied from the TX_{In} pin.

The base current of the BJT is chosen such that the minimum base-emitter current aligns with the threshold current of the emitter. Before the emitter, a current-limiting resistor R_1 is connected in series with both the emitter and the BJT. Here, TX_{IN} represents the OOK voltage signal originating from a digital device, such as an FPGA, which controls the base-emitter current through resistor R_{in}. The low state of TX_{IN} corresponds to the collector current being equal to the threshold current of the VCSEL (microLED), while the high state corresponds to the operational forward current of the VCSEL (microLED).

In practice, however, arrays of VCSELs or microLEDs, as shown in Figure 4.28, must be utilised to achieve the required optical output power while ensuring the appropriate bandwidth. In such cases, VCSEL chips (microLEDs) are arranged in an $N_1 \times N_2$ matrix [197]. To compensate for the increased capacitance resulting from N_2 parallel columns, we choose the number of rows $N_1 = N_2$.

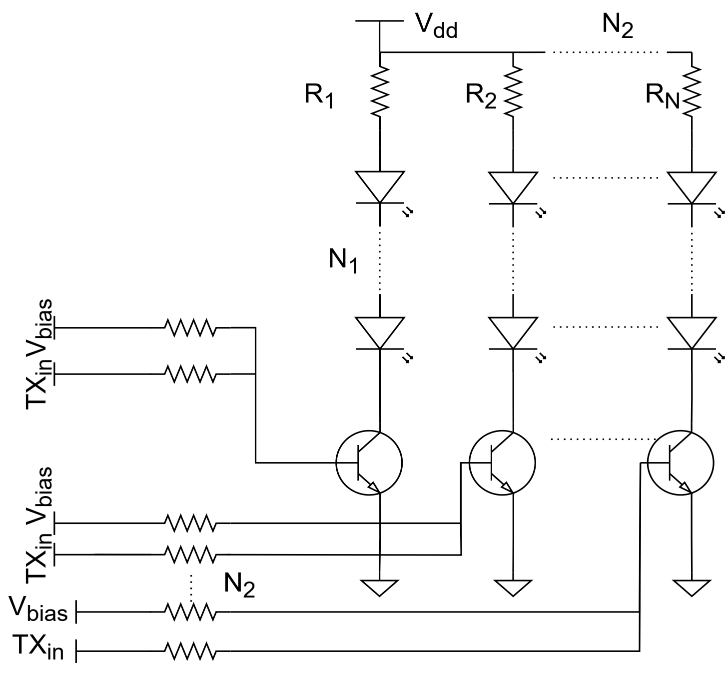

Figure 4.28: GSSK transmitter beam source driver circuitry. For microLED array $N_1 = N_2 = 10$, for VCSEL array $N_1 = N_2 = 6$.

For the hemispherical VLC MIMO setup discussed in subsection 3.4.1, we have determined that we need to arrange microLED chips, each containing 9 microLEDs connected in series [109], into a 10×10 microLED-chip array. Whilst such number is very large, it nevertheless has been demonstrated using complementary metal-oxide semiconductor (CMOS) technology that massive microLED arrays of hundreds of microLEDs can be developed for high speed connectivity [289]. The high optical requirement in this use case stems from the fact that the link distance is quite large typically within 3 m to 4 m leading to a large illumination area over which 900 MHz modulated signal must be transmitted.

Each chip emits optical power: $P_{\mathrm{opt}} = 10\,\mathrm{mW}$. The threshold current, representing a logical '0' symbol, is $I_{\mathrm{low}} = 1\,\mathrm{mA}$ (emitting $P_{\mathrm{opt}} = 1\,\mathrm{mW}$), while a logical '1' symbol draws $I_{\mathrm{high}} = 34.8\,\mathrm{mA}$ current (emitting $P_{\mathrm{opt}} = 10\,\mathrm{mW}$). For each chip, the required bias voltage is $V_{\mathrm{bias}} = 31\,\mathrm{V}$ [109]. To drive 10 microLED chips connected in series, the total voltage required is $V_{\mathrm{bias,tot}} = 31 \times 10 = 310\,\mathrm{V}$. The bias current for a microLED chip is set at the optimal point of $I_{\mathrm{bias}} = 25.4\,\mathrm{mA}$. Assuming equal symbol probabilities in the signal, for I_{RMS} evaluation, we approximate the OOK signal as a sine waveform. In this case, I_{RMS} can be calculated as:

$$I_{\mathrm{RMS}} = \sqrt{I_{\mathrm{bias}}^2 + \frac{(I_{\mathrm{high}} - I_{\mathrm{low}})^2}{2}}. \tag{4.9}$$

We calculate I_{RMS} for the microLED chip to be $I_{\mathrm{RMS}} = 34.88\,\mathrm{mA}$. The electrical power required to drive I_{RMS} over 10 microLED chips connected in series is given by:

$$P_{\mathrm{elec,series}} = I_{\mathrm{RMS}} V_{\mathrm{bias,tot}} = 10.81\,\mathrm{W}, \tag{4.10}$$

which we need to multiply by the 10 parallel series of microLED chips resulting in a total electrical power drawn by a 10×10 microLED chip array itself as $P_{\mathrm{elec,array}} = 108.12\,\mathrm{W}$.

To drive the OOK signal, as seen in Figure 4.28, we need a BJT in the given architecture that can handle the peak collector-emitter current of $I_{\mathrm{high}} = 34.8 \times 10 = 348\,\mathrm{mA}$. Unfortunately, there are no off-the-shelf BJTs that can handle such a current at a modulation frequency of 900 MHz. However, among the available off-the-shelf BJT components, we find that the multicomp PRO 2N5179-NRC [290] is the best-suited option. It has a maximum collector-emitter current of 50 mA and a power dissipation of $P_{\text{elec,BJT}} = 300\,\text{mW}$. The maximum DC gain of the BJT is 250.

Considering Figure 4.28, we need at least seven 900 MHz BJTs to support the collector-emitter current. This also means that multiple pairs of R_{bias} and R_{In} resistors need to be connected in parallel, with each pair of resistors connected to its respective BJT.

For each BJT, the TX_{in} generated base-emitter current swing is $\Delta I\text{base} = 0.11\,\text{mA}$ to drive the collector-emitter current. We assume the $V_{\text{TX}_{\text{In}}}$ voltage swing, $\Delta V_{\text{TX}_{\text{In}}} = 2\,\text{V}$, with $V_{\text{TX}_{\text{In}}} \in \{-1, 1\}\,\text{V}$ to accommodate the output pin operating range of typical digital devices. Based on this, we calculate $R_{\text{In}} = 18.6\,\text{k}\Omega$ and $R_{\text{bias}} = 6.9\,\text{k}\Omega$. The collector-emitter voltage of the BJT is $V_{\text{BJT}} = 12\,\text{V}$ [290], while V_{bias} is set to 1 V. The power dissipated by a single R_{In} is $P_{\text{elec},R_{in}} = 53.7\,\mu\text{W}$, and by a single R_{bias} is $P_{\text{elec},R_{\text{bias}}} = 145.1\,\mu\text{W}$. The total power dissipated by all R_{In} is $P_{\text{elec},R_{\text{in,tot}}} = 375.9\,\mu\text{W}$, and by all R_{bias} is $P_{\text{elec},R_{\text{bias,tot}}} = 1.02\,\text{mW}$.

We set $V_{\text{dd}} = 330\,\text{V}$ for which different off-the-shelf power supplies are available. The voltage drop across resistors $R_1, R_2, ...R_N$ can be calculated as $V_{R_i} = V_{\text{dd}} - V_{\text{BJT}} - V_{\text{bias,tot}} = 8\,\text{V}$. The resistance of $R_1, R_2...R_N$ is calculated to be $230\,\Omega$. The dissipated electrical power by a resistor R_i can then be calculated to be $P_{\text{elec},R_i} = 279.62\,\text{mW}$ with a total power dissipated from resistors $R_1, R_2...R_N$: $P_{\text{elec},R_{\text{tot}}} = 2.796\,\text{W}$.

The total electrical power dissipation contributions of a single transmitter beam source can be summed as follows:

$$\begin{aligned} P_{\text{elec,Tx,tot}} &= P_{\text{elec,array}} + P_{\text{driver}} = P_{\text{elec,array}} + P_{\text{elec},R_{\text{tot}}} + P_{\text{elec},R_{\text{bias,tot}}} \\ &\quad + P_{\text{elec},R_{\text{in,tot}}} + 7P_{\text{elec,BJT}} = 108.12\,\text{W} + 2.796\,\text{W} + 1.02 \times 10^{-3}\,\text{W} \\ &\quad + 0.38 \times 10^{-3}\,\text{W} + 2.1\,\text{W} = 108.12\,\text{W} + 4.9\,\text{W} = 113.02\,\text{W}. \end{aligned} \tag{4.11}$$

As can be seen from calculation in (4.11) the total electrical power dissipation of transmitter beam is estimated to be $P_{\text{elec,Tx,tot}} = 113.02\,\text{W}$. The driver circuitry dissipates 4.9 W to generate 1 W optical output power, resulting in an efficiency of only

$1/113.02 = 0.88\%$ in converting electrical power to optical power.

As can be seen, even without evaluating the RX end, the power consumption of high-bandwidth microLED-based LEDs, even with a single beam engaged in the hemispherical VLC model, is unacceptably high. This is primarily due to the high voltage required to drive individual microLED chips, resulting in excessive power consumption when the arrayed solution is introduced. The reason for high voltage is in series connection of microLEDs, which reduces the capacitance by a factor of 9, boosting the bandwidth necessary to achieve the target. However, the trade-off is much higher required drive voltage to overcome 9-fold increase impedance of the micro-LEDs while retaining the same forward current.

Referring to the results in Table 4.6 we can achieve a peak mean data throughput of 6.98 Gbit/s using a maximal Euclidean beam set selector, which requires approximately 4 engaged beams on average. This implies a mean TX power consumption of 452.08 W. We can now evaluate the mean energy efficiency of the transmitter end for peak mean data throughput:

$$\mathrm{EE} = \frac{P_{\mathrm{elec,Tx,tot}}}{\max(\mathrm{E}(C_{\mathrm{data}}^{\mathrm{peak}}))} = \frac{452.08}{6.98} = 64.77\,\mathrm{nJ/bit}, \tag{4.12}$$

compared to existing communication standards, the energy efficiency of the proposed VLC hemispherical MIMO model falls significantly short of the target of $\mathrm{EE} = 1\,\mathrm{nJ/bit}$.

The energy efficiency results of the VLC model highlight the challenges of achieving high-speed and energy-efficient adaptive GSSK links in VLC. The primary obstacle to achieving high-speed indoor connectivity is the absence of high-bandwidth transmitter beam sources capable of providing both high optical power output and bandwidth. As demonstrated in [67, 109], one approach involves increasing the bandwidth of microLEDs and arranging them in arrays to achieve the desired optical power output while maintaining bandwidth. However, this approach comes with a drawback of significantly high power consumption, which is required to draw the necessary forward current at very high biasing voltages. As an alternative, a more advantageous approach is to employ multi-carrier modulation techniques using O-OFDM, as it necessitates lower bandwidth requirements to achieve equivalent data throughput [214,215]. This enables the use of transmitter beam sources with a lower $-3\,\mathrm{dB}$ bandwidth but higher optical output power. This is because the beam output power is proportional to the emission area, which leads to typically a higher junction and a parasitic capacitance of the source [291].

In OWC, the situation is different. The infrared spectral region offers readily available high-bandwidth transmitter beam sources, such as VCSELs, which provide comparable optical output power to microLEDs. This leads to a more favorable trade-off between bandwidth and optical power a topic we will now explore as we analyse the energy efficiency of the directional infrared MIMO-OWC scenario.

As discussed in subsection 3.4.2 the optimal VCSEL array is a 6×6 array generating $0.108\,\mathrm{mW}$ of optical power. Each individual VCSEL chip emits $P_{\mathrm{opt}} = 3\,\mathrm{mW}$ optical power. The threshold current for the VCSEL representing the logical $'0'$ symbol, is $I_{\mathrm{low}} = 0.6\,\mathrm{mA}$ (emitting $P_{\mathrm{opt}} = 0.3\,\mathrm{mW}$), while logical 1 symbol draws $I_{\mathrm{high}} = 6\,\mathrm{mA}$ current (emitting $P_{\mathrm{opt}} = 3\,\mathrm{mW}$). For each VCSEL chip, the required bias voltage is $V_{\mathrm{bias}} = 2.2\,\mathrm{V}$. To drive 6 VCSEL chips connected in-series the total voltage required is $V_{\mathrm{bias,tot}} = 2.2\times6 = 13.2\,\mathrm{V}$. The bias current for the VCSEL chip is set to $I_{\mathrm{bias}} = 3.3\,\mathrm{mA}$. I_{RMS} for the VCSEL chip to be $I_{\mathrm{RMS}} = 3.81\,\mathrm{mA}$. The electrical power required to drive I_{RMS} over 6 VSCEL chips connected in series is $P_{\mathrm{elec,VCSELs}} = 50.33\,\mathrm{mW}$. When multiplied by the 6 parallel series of VCSEL chips, the total electrical power drawn by the 6×6 VCSEL chip array itself is $P_{\mathrm{elec,array}} = 0.3\,\mathrm{W}$.

To drive the OOK signal, as seen in Figure 4.28 we need a single BJT in the given architecture that can allow for the peak collector-emitter of $I_{\mathrm{high}} = 6\times6 = 36\,\mathrm{mA}$. From the off-the-shelf BJT components, we find Rohm Semiconductor 2SC5662 [292], which is the only one that satisfies $2\,\mathrm{GHz}$ bandwidth (the BJT transition frequency is $3.2\,\mathrm{GHz}$) and supports the maximum collector-emitter current with $50\,\mathrm{mA}$ limit and has relatively low power dissipation of $P_{\mathrm{elec,BJT}} = 150\,\mathrm{mW}$. The maximum DC gain of the BJT is 270.

Compared to VLC hemishperical MIMO scenario, we only need a single BJT to support the collector-emitter current, leading to a single R_{bias} and R_{In} resistor connected in parallel. For the BJT the $\mathrm{TX_{in}}$ generated base-emitter current swing is $\Delta I_{\mathrm{base}} = 0.12\,\mathrm{mA}$ to drive collector-emitter current. We assume the same $V_{\mathrm{TX_{In}}}$ voltage swing $\Delta V_{\mathrm{TX_{In}}} = 2\,\mathrm{V}$ and $V_{\mathrm{TX_{In}}} \in \{-1, 1\}\,\mathrm{V}$. Based on the base current and voltage swing we calculate $R_{\mathrm{in}} = 16.67\,\mathrm{k\Omega}$ and $R_{\mathrm{bias}} = 13.64\,\mathrm{k\Omega}$. The collector-emitter voltage of the BJT is $V_{\mathrm{BJT}} = 3.25\,\mathrm{V}$ while V_{bias} is set to $1\,\mathrm{V}$. The power dissipated by R_{in} is: $P_{\mathrm{elec},R_{in}} = 120\,\mu\mathrm{W}$, while by R_{bias} is: $P_{\mathrm{elec},R_{\mathrm{bias}}} = 73.33\,\mu\mathrm{W}$.

We set $V_{\mathrm{dd}} = 17\,\mathrm{V}$ for which different off-the-shelf voltage adaptors are available for this purpose. The voltage drop across resistors $R_1, R_2, ...R_N$ can be calculated as $V_{R_i} = V_{\mathrm{dd}} - V_{\mathrm{BJT}} - V_{\mathrm{bias,tot}} = 0.55\,\mathrm{V}$. The resistance of $R_1, R_2...R_N$ is calculated to be $91.67\,\Omega$. The dissipated electrical power by a resistor R_i can be calculated to be $P_{\mathrm{elec},R_i} = 1.33\,\mathrm{mW}$ with the total power dissipated over resistors $R_1, R_2...R_N$: $P_{\mathrm{elec},R_{\mathrm{tot}}} = 8\,\mathrm{mW}$.

The total electrical power dissipation contributions of a single transmitter beam source can be summed as follows:

$$P_{\mathrm{elec,Tx,tot}} = P_{\mathrm{elec},R_{\mathrm{tot}}} + P_{\mathrm{elec},R_{\mathrm{bias,tot}}} + P_{\mathrm{elec},R_{\mathrm{in,tot}}} + P_{\mathrm{elec,BJT}} + P_{\mathrm{elec,array}}. \tag{4.13}$$

The total electrical power dissipation of the transmitter beam is estimated then to be $P_{\mathrm{elec,Tx,tot}} = 0.46\,\mathrm{W}$, with the driver circuitry dissipating $0.16\,\mathrm{W}$ (representing 34.7% of the total transmitter power consumption) to generate $0.108\,\mathrm{W}$ optical output power. The estimated electrical to optical power conversion efficiency is 23.47%.

Referring to the results in Table 4.6, we can achieve a maximal mean data throughput of 21.52 Gbit/s for the 2×2 receiver grid and 23.8 Gbit/s for the 4×4 receiver grid in a sparse arrangement. To achieve this data throughput, an average of 5.78 and 6.4 beams need to be engaged, respectively. The mean power consumption of the transmitter end is then calculated to be 2.66 W and 2.94 W, respectively. Applying (4.12), we calculate the mean transmitter energy efficiency for both receiver grids to be 123.69 pJ/bit. The same energy efficiency is calculated for the close transmitter beam spacing scenario.

We observe that the mean evaluated energy efficiency in this scenario for the transmitter end falls significantly below the 1 nJ/bit threshold. To assess the energy efficiency of the receiver, we examine a typical OWC receiver circuitry in Figure 4.29.

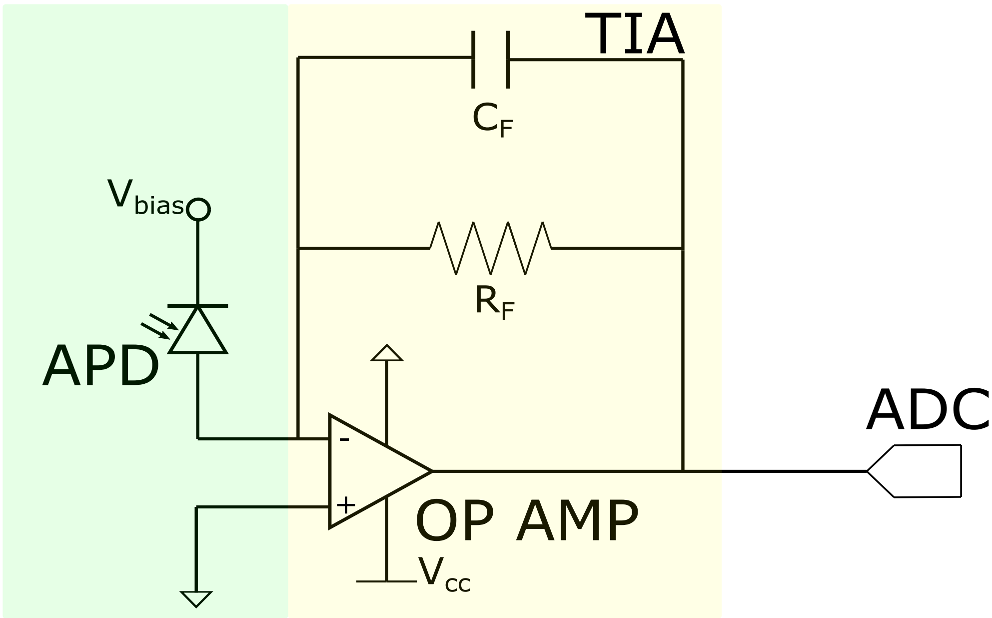

Figure 4.29: Receiver circuit.

The primary source of power consumption in the receiver circuit stems from the TIA and ADC, whereas the power dissipation from the APDs is considerably lower, given the small photocurrent generated (which we estimate to be in the order of tens of μA on average). We assume there are N_{RX} channels at the input and output of the ADC. For each channel, we have a dedicated APD and TIA. Each channel is then routed to the input of the DSP chip, where decoding is performed using maximum likelihood. The total power consumption of the receiver can be expressed as follows:

$$P_{\mathrm{elec,Rx,tot}} \approx N_{\mathrm{Rx}} P_{\mathrm{elec,TIA}} + P_{\mathrm{elec,ADC}}. \tag{4.14}$$

For the receiver front-end, we require an ADC that supports as many channels as possible while providing a minimum sampling rate of 4 GSPS and minimal power consumption. We have selected the Analog Devices AD9209 Quad ADC [293], which offers four channels at the required sampling rate from the available off-the-shelf devices. As previously discussed, we use the Analog Devices ADN2880 TIA [283] to achieve the necessary TIA gain at a bandwidth of 2 GHz. The power consumption of each selected device is summarised in Table 4.7.

Table 4.7: Receiver opto-electronic front-end components.

Component	Model	Power consumption, mW
TIA	Analog Devices TIA ADN2880 [283]	70
ADC	Analog Devices Quad ADC AD9209 [293]	5470 (typical)

The power consumption of the 2×2 receiver array is $P_{\text{elec,Rx,tot}} \approx 5.75\,\text{W}$, while for the 4×4 receiver array, 4 ADCs are required to capture 16 channels, resulting in the receiver power consumption of $P_{\text{elec,Rx,tot}} \approx 23\,\text{W}$.

The mean energy efficiency for the 2×2 receiver array in the close transmitter beam spacing scenario is 289.67 pJ/bit and in the sparse transmitter beam spacing scenario, it is 254.42 pJ/bit. For the 4×4 receiver array the mean energy efficiency in the close transmitter beam spacing scenario is 1068.77 pJ/bit and in the sparse transmitter beam spacing scenario, it is 966.39 pJ/bit.

We observe that, due to the need for multiple ADCs in the 4×4 receiver array, the energy efficiency is approximately three times worse than that of the 2×2 receiver array, despite the higher peak mean data throughput. This makes the 2×2 array a more preferable design choice in terms of energy efficiency.

The total power consumption of the opto-electronic front-end link can be determined by summing up the contributions from the transmitter and receiver ends: $P_{\text{elec,tot}} = P_{\text{elec,Tx,tot}} + P_{\text{elec,Rx,tot}}$. The total mean link energy efficiency, denoted as $\text{E}(\text{EE}_{\text{link}})$, where E(.) denotes expectation, can be calculated using (4.12), where the total electrical power consumed is divided by the mean peak data throughput. The results for 2×2 and 4×4 receiver grids in both the close and sparse scenarios are provided in Table 4.8.

As evident from the table, the best energy efficiency is achieved when using a 2×2 receiver array instead of a 4×4 array. Although there is a reduction in peak mean

Table 4.8: Peak mean data throughput and energy efficiency comparison for close and sparse OWC device-to-device scenarios.

Receiver Grid & Scenario	$P_{\text{elec,Tx,tot}}$, W	$P_{\text{elec,Rx,tot}}$, W	$P_{\text{elec,tot}}$, W	$\max(\mathrm{E}(C_{\text{data}}^{\text{peak}}))$, Gbit/s	$\mathrm{E}(\mathrm{EE}_{\text{link}})$, pJ/bit
2x2 (Close)	2.46	5.75	8.21	19.85	413.17
2x2(Sparse)	2.8	5.75	8.55	22.6	378.12
4x4 (Close)	2.66	23	25.66	21.52	1192.47
4x4 (Sparse)	2.94	23	25.94	23.8	1090.08

data throughput, it is limited to 7.76% and 5.04% compared to the 4×4 receiver array in close and sparse transmitter spacing scenarios, respectively. In contrast, the improvement in energy efficiency achieved in comparison to the 4×4 array case is approximately 2.88 and 2.89 times for close and sparse scenarios. In both scenarios, the mean peak data throughput exceeds the target of 10 Gbit/s, but only with the 2×2 array is the mean energy efficiency of the opto-electronic front-end considerably less than 1 nJ/bit. Therefore, for further analysis, we exclusively consider the 2×2 receiver array.

The calculated mean energy efficiency for the opto-electronic front-end provides a lower bound on the achievable mean energy efficiency in the device-to-device OWC scenario compared to the VLC scenario. If we set an upper limit on energy efficiency at 1 nJ/bit, the remaining power consumption margin that can be allocated to DSP and the networking layer is 11.64 W for the close transmitter beam spacing scenario and 14.05 W for the sparse scenario. Notably, this margin exceeds the power consumption of the opto-electronic front-end.

The power consumption of the DSP and networking layer depends on the specific DSP device or chip (e.g., FPGA) and the implementation of DSP and networking layer functions. Nevertheless, the high energy efficiency of the opto-electronic front-end and the ample power consumption margin illustrate a scenario where an adaptive GSSK-based link could be efficiently employed for a high-energy-efficiency link with energy consumption below 1 nJ/bit and high data throughput exceeding 10 Gbit/s, allowing for a high speed adaptive mobile device-to-device communication based on GSSK.

Based on the power consumption analysis, we observe that the primary source of power consumption is the ADC, constituting approximately $64 - 66\%$ of the dissipated power in the link. Additionally, it is noteworthy that the power consumption at the transmitter end is more than two times lower than that at the receiver end.

The higher receiver power consumption is a drawback when considering a discrete 4-channel receiver solution, which necessitates use of four TIAs and a 4-channel ADC. However, there is a potential to significantly reduce the number of discrete devices and channels by designing a bespoke 2×2 array with the same collective photoactive area and bandwidth as in the case of four individual APDs.

For example, if a 2×2 receiver array is designed with the same bandwidth and photoactive area but as a single channel, a lower power consumption single-channel ADC, such as the Texas Instruments ADC12J4000 [294] with a sampling rate of 4 GSPS and power consumption of 2.2 W, can be used. In such a case, transmitter power consumption would become comparatively similar, while the receiver power consumption would be decreased. The energy efficiency could potentially increase to 238.1 pJ/bit and 224.1 pJ/bit for close and sparse transmitter beam spacing scenarios, respectively if a bespoke array is considered. Further improvements in energy efficiency can be achieved with higher concentration gain receiver optics.

For OWC, we selected a transmission wavelength of $\lambda = 850$ nm for several reasons. One of the main reasons are the readily off-the-shelf options for this wavelength include high-bandwidth avalanche photodiodes with a bandwidth of ≥ 2 GHz and a sufficiently large photoactive area of ≥ 0.1 mm, such as those offered by Hamamatsu [268, 278]. Moreover, 850 nm wavelength sources are readily available with optical power exceeding ≥ 2.5 mW, and high-bandwidth VCSELs at this wavelength exhibit superior electrical-to-optical conversion efficiency compared to alternatives like micro-LEDs.

However, it's worth noting that the use of 850 nm wavelength does have limitations in terms of SNR due to stringent eye safety constraints [88], which are most restrictive at this wavelength. Substantially higher SNR can be achieved by opting for sources and receivers operating at $\lambda = 940$ nm or $\lambda = 1310$ nm, which have more relaxed laser eye safety constraints.

During the time of this study, however, there were limited or no off-the-shelf options available for high-power, high-bandwidth transmitter beam sources and high-bandwidth, simultaneously with large photoactive area receivers (receiver arrays) at wavelengths other than 850 nm, which led us to consider the 850 nm design.

Further research and development in long wavelength solutions can significantly increase the data throughput and energy efficiency of adaptive GSSK link at larger communication distance and coverage area by boosting the individual beam SNR within the laser eye safety constraints.

Finally, we perform a comparative analysis of the energy efficiency of the adaptive GSSK link, as described in section 4.4, with commonly used M-QAM [53] and DCO-OFDM [125] modulation techniques in VLC and OWC links. We maintain the same channel conditions for all three links, and our target data throughput is set at 22.32 Gbit/s. To evaluate the analytical BER of M-QAM, we employ the following expression [295]:

$$P_{\mathrm{bit,QAM}} = \frac{4(\sqrt{M}-1)}{\sqrt{M}\log_2(M)} Q(\sqrt{\frac{3\log_2(M)}{M-1}\gamma_{\mathrm{b(elec)}}}) + \frac{4(\sqrt{M}-2)}{\sqrt{M}\log_2(M)} Q(3\sqrt{\frac{3\log_2(M)}{M-1}\gamma_{\mathrm{b(elec)}}}), \tag{4.15}$$

where M - modulation order, $\gamma_{\mathrm{b(elec)}}$ - SNR per bit. For $B = 2\,\mathrm{GHz}$ a $64-\mathrm{QAM}$ is required, therefore $M = 64$. We maintain a fixed receiver position, and multiple transmitter beams are directed toward a single (x, y) coordinate at a distance of $z = 1\,\mathrm{m}$. In the case of adaptive GSSK, we require the engagement of 6 beams to achieve the desired spectral efficiency for the target data throughput. To estimate the number of transmitter beams needed to support a $64-\mathrm{QAM}$ link at the FEC limit, we evaluate (4.15) and compare it with the FEC constraints [261]. The calculation steps and for the evaluation of QAM BER values for various numbers of engaged transmitter beams are provided in Appendix C.

To assess the power consumption of the transmitter beams modulated with M-QAM, it is imperative to account for the DAC and voltage amplifier necessary to modulate a 6×6 VCSEL array with QAM signals [193]. In our analysis, we consider the MAXIM MAX19693 DAC [296], which consumes 1.8 W of power and operates at 4.4 GSPS. Additionally, for the voltage amplifier, we utilise the Texas Instruments

LMH6401 [297], which has a power consumption of 0.345 W.

We have determined that a minimum of 4 beams is required to achieve the necessary SNR within the FEC limit for a 64-QAM system. The root mean square current through the VCSEL array is calculated to be $I_{\text{RMS}} = 22.7\,\text{mA}$ with a bias voltage of 13.2 V across the VCSEL array. For a single transmitter beam, the VCSEL array consumes $P_{\text{elec,array}} = 0.3\,\text{W}$. Assuming that a single voltage amplifier and DAC drive 4 transmitter beam VCSEL arrays, the total transmitter power consumption is then [193]:

$$P_{\text{elec,Tx,tot}} = P_{\text{elec,DAC}} + 4P_{\text{elec,array}} + P_{\text{volt,amp}} = 3.34\,\text{W}. \tag{4.16}$$

We employ DCO-OFDM with adaptive bit loading for carriers up to $B = 2\,\text{GHz}$ due to the ADC's sampling rate limitation. The calculation steps are based on expressions from [125]. SNR per bit is evaluated same as for QAM with the calculation steps described in Appendix C. Based on our analysis, we estimate that the DCO-OFDM link would require at least 4 transmitters and have a total transmitter power consumption of approximately 3.57 W. In contrast, the adaptive GSSK link, with 6 engaged transmitter beams, would consume around 2.76 W in total. These findings are summarised in Table 4.9 for easier reference. Maximum achievable data throughput is set to 22.32 Gbit/s as it corresponds to the maximum achievable value in the GSSK link for a fair comparison between techniques.

Table 4.9: Peak mean data throughput, power consumption and energy efficiency comparison between $64-$QAM, DCO-OFDM and adaptive GSSK.

	$P_{\text{elec,Tx,tot}}$, W	$P_{\text{elec,Rx,tot}}$, W	$P_{\text{elec,tot}}$, W	$C_{\text{data}}^{\text{peak}}$ Gbit/s	EE, pJ/bit
64-QAM	3.34	5.75	9.09	22.32	407.26
DCO-OFDM	3.57	5.75	9.32	22.32	417.56
Adaptive GSSK	2.76	5.75	8.51	22.32	381.27

As shown in Table 4.9, the adaptive GSSK link stands out as the most energy-efficient choice when compared to 64-QAM and DCO-OFDM. The primary reason for this difference is the absence of a DAC in the driver circuitry of adaptive GSSK, which reduces power consumption by 1.8 W. Additionally, the computational complexity of the DSP is considerably lower for adaptive GSSK compared to QAM and DCO-OFDM.

In particular, at the encoding end, adaptive GSSK utilises a simple OOK modulation for driving the transmitter beams after serial-to-parallel conversion. This design choice significantly reduces the computational demands, contributing to the link's overall energy efficiency.

While adaptive GSSK demands more transmitter beams for data transmission to achieve the same spectral efficiency as 64-QAM and DCO-OFDM, the simplified driver circuitry more than compensates for this requirement. Moreover, the use of a two-level modulation at each individual transmitter offers an inherent advantage. It makes the signal less susceptible to distortions caused by the non-linearity of individual VCSEL IV (current-voltage) curves. This characteristic contributes to the robustness of adaptive GSSK, particularly in scenarios where optical power levels may vary due to factors such as temperature fluctuations of the transmitter beam source. Furthermore, the design implementation complexity is considerably lower than for the multi carrier schemes such as DCO-OFDM.

4.6 Summary

Adaptive GSSK algorithm is analysed in the indoor VLC and OWC scenarios. The algorithm performs transmitter beam set selection and spectral efficiency adjustment based on the channel conditions. The number of engaged transmitter beams in the link is not fixed and adjusts based on the local channel conditions to maximise the data throughput of the link. Three different criteria for selecting transmitter beam sets are investigated for the algorithm: maximal minimum Euclidean distance, optimal GSSK channel ratio, and maximal SNR. The set selectors based on the three criteria are compared in the VLC hemispherical transceiver downlink scenario with fixed and random orientation. The transmitter and receiver opto-electronic front-end is selected to maximise data throughput.

In the fixed orientation scenario the peak mean data throughput averaged over $4 \times 4 \times 3$ room achieves the best results using maximal minimum Euclidean distance criterion set selector at 6.98 Gbit/s while the optimal GSSK channel ratio set selector achieves 86.5% of that at 6.04 Gbit/s. The maximal SNR set selector performs the worst out of the three, achieving a data throughput of 78.2% at 5.46 Gbit/s. Furthermore, the maximal Euclidean set selector achieves the best data throughput performance at the lowest spatial entropy of its spatial distribution, while the maximal SNR produces the worst spatial entropy at the peak mean data throughput. Optimal GSSK channel ratio set selector provides intermediate performance.

The results in the random orientation scenario are similar to those in the fixed orientation scenario. While the maximal Euclidean distance set selector outperforms the other two, its computational complexity exceeds the others by approximately five orders of magnitude, potentially introducing millisecond-scale latency. Such latency is highly undesirable in a mobile use case scenario. Combined with data throughput and spatial entropy the optimal GSSK channel ratio set selector provides the best trade-off of the 3 set selectors in terms of data throughput and spatial entropy vs computational complexity.

In the OWC MIMO device-to-device scenario, we employ an adaptive GSSK system based on the optimal GSSK channel ratio set selector. The transmitter beams and receivers are arranged in square grids of varying size and spacing. Two scenarios of transmitter beam source arrangement are investigated - close spacing and sparse spacing. In the close spacing scenario, the transmitter beam source spacing is fixed at 1 cm, while the transmitter beam spacing at the receive plane is variable. In the sparse spacing scenario, the transmitter beam source spacing is set to be variable and equal to the transmitter beam spacing at the receive plane. At a 1 m link distance and a $20 \times 20\,\mathrm{cm}^2$ coverage area, the mean peak data throughput of 19.85 Gbit/s at the coverage area is achieved for the close spacing scenario and the 2×2 receiver array. For the sparse scenario and the 2×2 receiver array - 22.6 Gbit/s can be achieved. For the 4×4 receiver array 21.52 Gbit/s and 23.8 Gbit/s can be achieved for the close and the sparse spacing respectively. In the both cases full $20 \times 20\,\mathrm{cm}^2$ coverage is achievable.

The power consumption and energy efficiency of the opto-electronic front-end are evaluated using the adaptive GSSK algorithm for both VLC and OWC scenarios. For the VLC scenario, the transmitter's power consumption is evaluated. The power consumption of solely transmitter end yields 452.08 W to transmit 6.98 Gbit/s mean data throughput. The results show a mean energy efficiency of the transmitter's opto-electronic front-end of 64.77 nJ/bit, which falls significantly short of the target of 1 nJ/bit and does not achieve the required 10 Gbit/s mean data throughput. The primary source of the high power consumption is low energy efficiency of micro-LED arrays when designed for high bandwidth solution, with a fixed spectral efficiency tied to the number of engaged beams in the link. The choice fell on the micro-LEDs due to their high achievable bandwidth required for a high data rate GSSK link. However, because microLEDs are typically low optical power emitting, an implementation for large distance and coverage VLC links is challenging. In this work we see that such implementation comes with a major energy efficiency drawback. This indicates that a high-speed VLC link utilising the adaptive GSSK or GSSK in general in an indoor scenario is not practical, particularly in the context of green telecommunications.

An alternative, which can be considered for high speed VLC solutions is to use laser diodes instead of microLEDs, which can offer similar bandwidth but provide a higher optical emission power. However, when designing a VLC link based on laser diodes care should be taken for laser eye safety considerations, which can also limit the maximum transmitter optical power available.

In the OWC device-to-device scenario, both the transmitter and receiver opto-electronic front-ends consume only 8.21 W and 8.55 W to transmit data at rates of 19.85 Gbit/s and 22.6 Gbit/s for a 2×2 receiver array in close and sparse spacing, respectively.The results show mean energy efficiency values of 413.17 pJ/bit and 378.12 pJ/bit for close and sparse spacing. For 4×4 receiver array the energy efficiency exceeds 1 nJ/bit due to the multiple ADCs required for the link. These results demonstrate the feasibility of using the adaptive GSSK algorithm in an OWC directional device-to-device scenario, showing both high peak data throughput and energy efficiency.

The energy efficiency of the adaptive GSSK link, which utilises six engaged beams i.e, operates at a rate of 6 bit/s/Hz with a data throughput of 22.32 Gbit/s, is compared to an equivalent $64-$QAM and DCO-OFDM link using the same opto-electronic front-end. The adaptive GSSK link outperforms the $64-$ QAM and DCO-OFDM links in terms of energy efficiency with an energy consumption of 381.27 pJ/bit, compared to 407.26 pJ/bit for $64-$ QAM and 417.56 pJ/bit for DCO-OFDM. The adaptive GSSK link requires 0.58 W less transmitter electrical power compared to $64-$QAM and 0.81 W less compared to DCO-OFDM. Although the GSSK link requires six beams compared to four beams in $64-$ QAM and DCO-OFDM, the absence of a DAC in the GSSK link compensates for the extra beams in the link and reduces power consumption below that of QAM and DCO-OFDM.

This study has demonstrated the potential and limitations of adaptive GSSK for achieving high data throughput and energy efficiency in VLC and OWC applications. For indoor VLC links, the implementation of the adaptive GSSK algorithm is not feasible for high-speed applications. However, for device-to-device OWC links, the adaptive GSSK algorithm can achieve high data throughput and energy efficiency, outperforming multi-carrier schemes such as DCO-OFDM. Furthermore, the implementation complexity and cost of adaptive GSSK link is low compared to other multi-carrier schemes as no DAC is required. Additionally, the driver circuitry for GSSK can be designed in a relatively straightforward way.

Lastly, the GSSK is not affected by non-linear transfer characteristics of the transmitter. While optimal beam set selectors like those based on maximal minimum Euclidean distance achieve best data throughput, the trade-off is a significant increase in the computational complexity of the link. Low-complexity transmitter beam set selectors, such as those based on the optimal GSSK channel ratio criterion, offer a good trade-off between achievable data throughput, uniformity, and computational complexity.

Chapter 5

Adaptive GSSK Algorithm Simulink Implementation

5.1 Introduction

For a practical implementation of GSSK in OWC and VLC mobile wireless links, where the user is free to move, the use of adaptive GSSK modulation and beam selection is essential. In pursuit of this, algorithms for beam selection, employing various criteria [225, 234, 240], and adaptive modulation [226] have been proposed for both RF and OWC/VLC applications. Although a practical realisation of a GSSK link using FPGAs in OWC has been demonstrated [221,222], there is a substantial lack of research on the implementation of a GSSK algorithm that integrates both adaptive modulation and beam selection for FPGA platforms.

Such implementation necessitates the use of adaptive codebooks in conjunction with a beam selection algorithm. Proposals for codebook algorithms have been made for rate-adaptable probabilistic constellation shaping encoders [130], background subtraction in video surveillance [298], an adaptive space-time coding and spatial multiplexing detector implementation on FPGA [299], real-time video coding [300], and, more recently, for learning-based adaptive intelligent reflective surfaces with limited feedback codebooks [301].

Furthermore, adaptive modulation algorithms suitable for FPGA implementation in

OWC/VLC links have been advanced for OFDM [302] and rate-adaptive Low-Density Parity-Check (LDPC)-coded modulation [303]. In the domain of RF, proposals for FPGA-based precoding and antenna selection algorithms include symbol-level precoding for multi-user multi-antenna communication systems [304], neural network-based phased array antennas [305], and eigenbeam MIMO-OFDM with transmit antenna selection [306].

In this chapter, we present a Hardware Description Language (HDL)-synthesisable implementation of an adaptive GSSK algorithm using MathWorks Simulink. The implemented algorithm integrates beam selection based on a maximal minimum Euclidean distance criterion [234] with an adaptive codebook of varying spectral efficiency.

The algorithm model and its constituent DSP modules, implemented in MathWorks Simulink, along with their principles of operation, are described. The algorithm's performance, in terms of achievable spectral efficiency, is evaluated across scenarios involving four available transmitter beams and four receivers for varying link electrical SNR. Moreover, three distinct scenarios of transmitter beam channel ratios are investigated to assess the performance dependency of the algorithm on channel conditions. An estimation of the latency associated with beam selection is also provided.

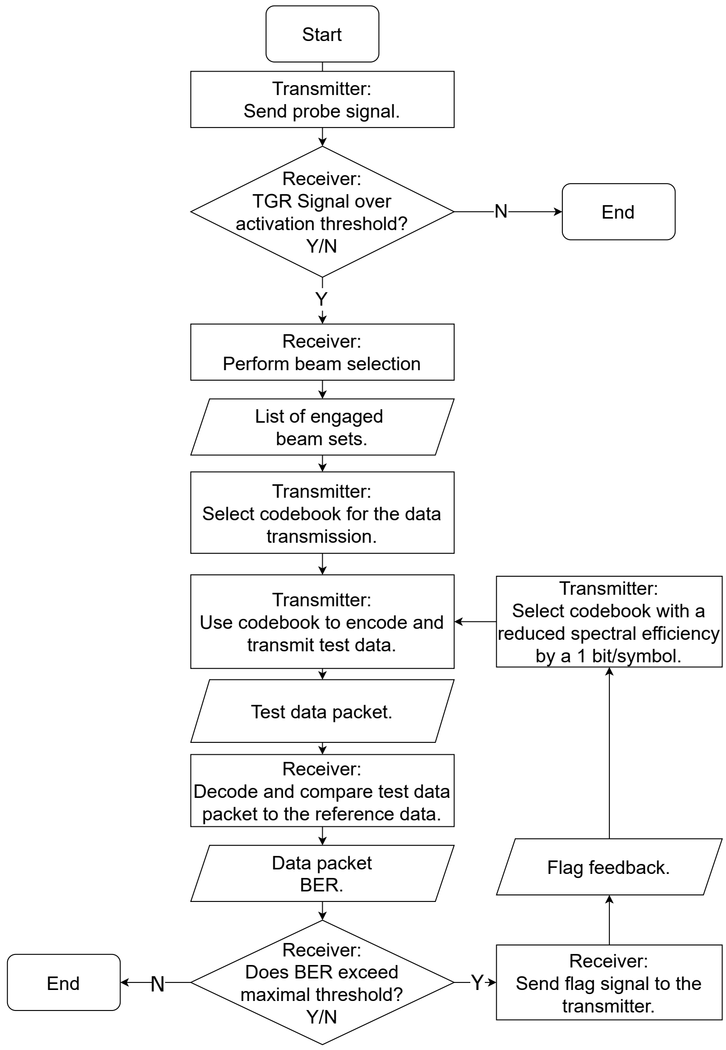

Figure 5.1: Block diagram of adaptive GSSK algorithm.

5.2 Algorithm Simulink Model

The flowchart of the algorithm operation is shown in Figure 5.1. The algorithm operates in the following manner: initially, the transmitter dispatches a probe signal towards the receiver. Upon reception, this probe signal prompts the receiver (or receivers) to activate. Subsequently, the receiver ascertains the set of available transmitter beams, denoted as $\mathbb{A}_t$, and measures the signal strength of each constituent beam m_j within $\mathbb{A}_t$.

Beam selection at the receiver is conducted based on the criterion of maximal minimum Euclidean distance [234]. This criterion is favoured due to its superior BER performance compared to other previously considered criteria, rendering it particularly well-suited for GSSK links that have a limited number of available transmitter beams (< 5). Upon determining the optimal beam sets for all possible spectral efficiencies in the link, characterised by $\{1, 2, \ldots, |\mathbb{A}_{\mathrm{t}}|\}$ bit/symbol engaged beam combinations, the receiver communicates the selected transmitter beam set information back to the transmitter via a feedback channel, which may be either wired or wireless, encoded as a 16-bit vector.

At this juncture, the transmitter encoder utilises the beam set information to select the appropriate codebook for data transmission. This selection includes the determination of the quantity and the specific constituency of transmitter beams to be engaged for GSSK data transmission. Subsequently, the encoder transmits a data packet over the optical wireless channel, comprising training bits and test data. The receiver, already in possession of the test data as a known reference, decodes the incoming packet and assesses its BER.

Should the packet's BER surpass the predefined maximum threshold, the receiver transmits a flagging signal back to the encoder via the feedback channel, prompting a reduction in spectral efficiency by deactivating one transmitter beam and selecting with a reduced number of constellation points in the symbol alphabet.

The encoder then transmits the next data packet, this time with a diminished symbol alphabet. This iterative process persists until the BER conforms to the requisite targets. The adjustment of data transmission and GSSK modulation is executed on a packet-by-packet basis. For the purposes of our model, we assume a maximum of four available transmitters within the link. While beam selection input occurs at a singular receiver, the data reception and decoding process engages four receivers.

Figure 5.2 illustrates the overall block diagram of the adaptive GSSK algorithm for the implementation in MathWorks Simulink.

The algorithm is divided into two parts, which is the transmitter part denoted with TX and receiver part denoted with RX. The transmitter algorithm consists of following

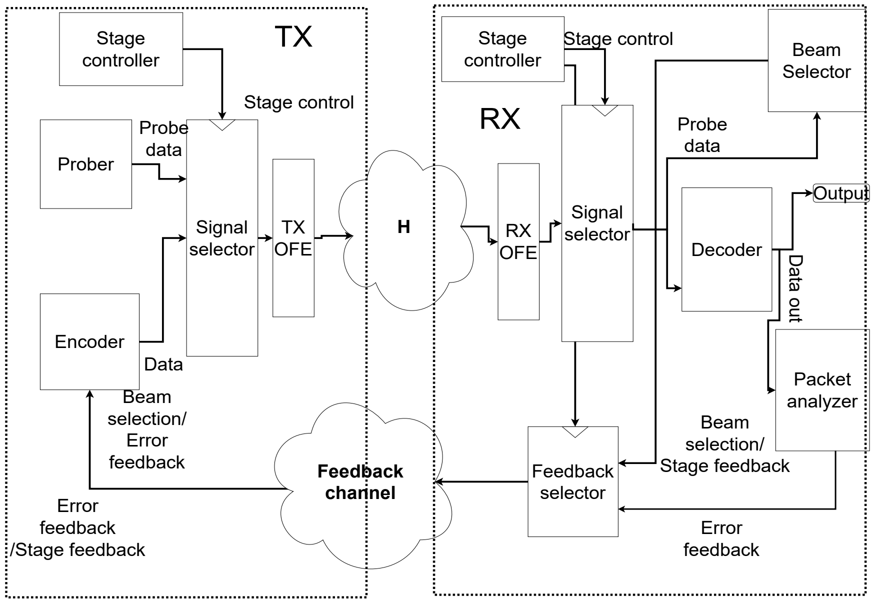

Figure 5.2: Block diagram of adaptive GSSK algorithm.

modules:

- Prober module: this module is responsible for generating the trigger signal and probe data to be transmitted to the receiver. The probe data serves the dual purpose of activating the receiver and transmitting channel state information regarding the available transmitter beams for selection.

- Encoder module: this module performs the function of encoding serial binary data into GSSK symbols. In addition to this primary encoding task, it also includes the insertion of training bits and GSSK identification bits at the outset of data packets. These identification bits are necessary for the receiver's determination of the spectral efficiency associated with the utilised codebook. In the scope of this work, we assume predetermined test data for transmission. In the case of real data, the encoder module would require modification with an additional input port for that data.

- Stage controller: within this module, the control over the transmitter's transmission mode is managed, allowing for transitions between probing packets and data transmission packets. This entails switching between the inputs from the encoder and prober to output towards optical-front-end.

The receiver part of algorithm is composed of the following modules:

- Beam selector module: this module, upon receiving input from the prober module, executes beam selection utilising the maximal minimum Euclidean beam selector algorithm. It concurrently selects beams across all available cardinalities of engaged beam sets, producing an engaged beam set for each level of spectral efficiency with the maximum being contingent on the quantity of available beams and minimum being a single beam. Feedback is then relayed to the transmitter to inform encoding processes.

- Decoder module: the module is responsible for decoding GSSK data symbols, this module employs a codebook derived from the identification and training bits, and uses a maximal likelihood algorithm to reconstruct serial data.

- Packet analyser module: This module is tasked with comparing the decoded packet bits against a known reference to estimate the BER. If the BER exceeds the predetermined threshold, the module flags the packet and communicates with the transmitter encoder over the feedback channel to modify the signal's spectral efficiency—for instance, reducing from four engaged beams to three.

- Stage controller: this module determines the operational mode of the receiver, choosing between beam selection and signal decoding.

- Feedback selector: depending on the stage of operation, this module decides the content of the feedback data transmitted via the feedback channel to the transmitter encoder. During the probing stage, the feedback consists of all engaged beam set list, while during the data transmission stage, a flag signal is sent.

Each module incorporates HDL coder-compatible component blocks to facilitate an FPGA-implementable design. The discussion will now continue with a more detailed exploration of each module, beginning with those pertaining to the transmitter.

Prober Module

The Prober Module serves a dual purpose. Firstly, it activates the receiver and transmits probing data over a designated channel. From this probing data, the receiver can derive two essential pieces of information. It can, firstly, ascertain the number of available transmitters within the link, represented as $|\mathbb{A}_{\mathrm{t}}|$. Secondly, the receiver can gauge the signal strength associated with each individual transmitter beam. For a more detailed visual representation of this process, we refer to Figure 5.3.

In the figure presented, we observe the idealised, noise-free temporal waveform of the probing data as it is received. The initial pulse represents the probe trigger signal, denoted by TGR. This signal is utilised to activate the receiver when the generated voltage V_{TGR} meets or exceeds the threshold $V_{\mathrm{min,act}}$, with $V_{\mathrm{min,act}}$ signifying the minimal activation voltage for the receiver. Concurrently, during the transmission of the TGR pulse, all transmitter beams are switched to a high state.

Subsequently, a sequence of transmitter activation patterns ensues. In this sequence, the prober emits a series of pulses at every other sample point. During each of these

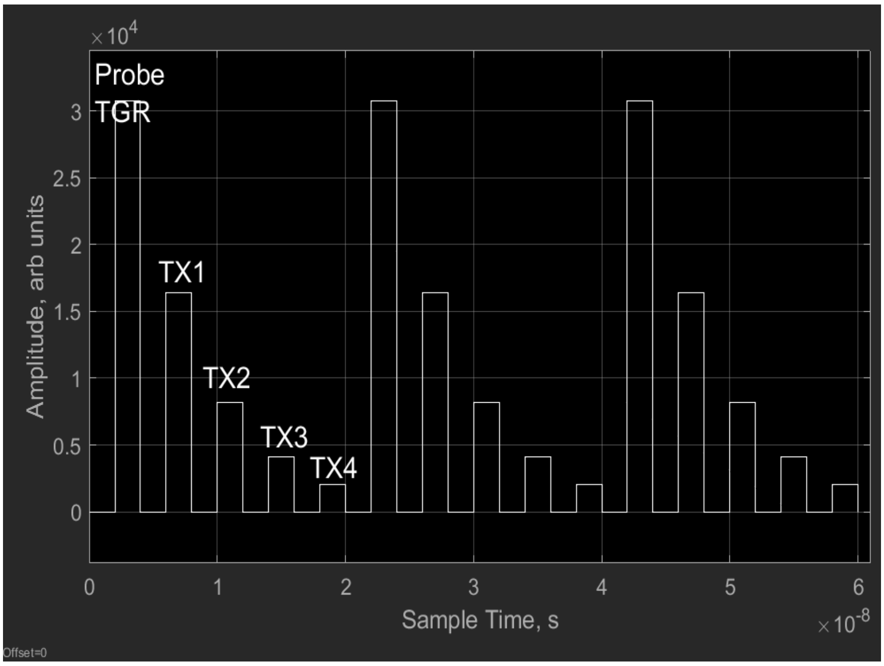

Figure 5.3: Probe waveform in Simulink.

pulses, a single transmitter beam is set to the high state. It's noteworthy that all transmitter beams emit an identical optical power during their respective allocated pulse.

Each pulse from the transmitter, denoted as TX_j, traverses the channel and undergoes distinct levels of attenuation, contingent upon the channel gain between the i^{th} receiver and j^{th} transmitter, symbolised as h_{ij}. Consequently, at the receiver's end, each pulse from the transmitter beams is manifested as a unique signal voltage level. A transmitter pulse is acknowledged by the receiver if $V_{\text{TX}j}$ meets or surpasses V_{min}, which represents the threshold voltage for signal registration. The sequence of transmitter beam activation pulses is capable of being replicated arbitrarily many times to ensure reliability. For the purpose of our simulations, we have elected to model this with 3 repetitions to keep latency due to the beam selection low.

Implementing the prober module within Simulink is a straightforward process. It requires merely an HDL counter block characterised by a sample time, denoted as T_{samp}, and a period, T_{count}. This counter block can then be interfaced with a Look-Up Table (LUT). Within the LUT, individual counter values are mapped to specific activation patterns of the transmitter beams, thereby generating the requisite probe waveform.

When dealing with a configuration of four transmitter beams, it is feasible to employ a 4-bit mapping system. In this mapping, each bit, denoted by the j^{th} position, signifies the state of the corresponding j^{th} transmitter. To create a probing sequence of pulses using the prober, which relies on the counter block, we can utilise the mapping demonstrated for the first three pulses, as presented in Table 5.1.

Table 5.1: Activation pattern counter mapping.

Counter count	Activation Pattern $\mathbf{b} = \{b_1, b_2, b_3, b_4\}$	Label
1	$\{1111\}$	TGR
2	$\{0000\}$	-
3	$\{1000\}$	TX_1
4	$\{0000\}$	-
5	$\{0100\}$	TX_2

The emitted power is set for each j^{th} transmitter during each sample to:

$$P(b_j) = \begin{cases} P_{\text{H}} & b_i = 1 \\ 0 & b_i = 0. \end{cases} \tag{5.1}$$

The implementation of the module in the Simulink is given in Appendix D.

Encoder Module

After the receiver completes the beam selection, and the transmitter receives the set of all selected engaged beam sets $\mathbb{M}$, represented as a 16-bit vector at the input, the encoder leverages this information to accomplish two main tasks. First, it determines the number of engaged beams for data transmission, which in turn establishes the GSSK constellation size. Second, the encoder identifies which transmitter beams should be engaged for the data transmission, prerequisite for the mapping of serial input binary data onto the selected transmitter beams.

The mapping of serial binary data to the GSSK symbols, denoted as $\mathbf{x}_{\text{GSSK}}$, for any combination of engaged transmitter beams can be executed by combining the engaged beam set, represented in our case as a 4-bit vector, with a 4-bit serial binary data vector. In $\mathbf{x}_{\text{in}}$, the first four significant bits signify the engaged beams, denoted as $\mathbf{m} = \{m_1, m_2, m_3, m_4\}$, while the four least significant bits represent the data bits $\{n_1, n_2, n_3, n_4\}$ to be mapped into a GSSK symbol. In our scenario, the GSSK symbol mapping to the transmitters is represented as $b_{\text{GSSK}} = \{b_1, b_2, b_3, b_4\}$, adhering to a one-to-one mapping rule as described in Equation (5.1). Other mapping rules can be also considered such as Gray coding.

To illustrate this mapping process, we provide an example in Table 5.2, showcasing a 2-beam GSSK scenario where the 1st and 3rd transmitters are engaged in data transmission. Generally, any mapping can between different engaged beam vectors and GSSK symbols with different alphabet cardinalities can be established using look-up tables. Additionally, it is important to note that the same mapping principle applies for other combinations and different numbers of engaged transmitter beams.

Table 5.2: GSSK symbol mapping example

$\mathbf{x}_{\text{in}} = \{m_1, m_2, m_3, m_4, n_1, n_2, n_3, n_4\}$	$\mathbf{b}_{\text{GSSK}} = \{b_1, b_2, b_3, b_4\}$
1010 0000	0000
1010 0001	0010
1010 0010	1000
1010 0011	1010

The encoder at the first iteration data packet uses $\tilde{\mathbf{m}}_1$ from the engaged beam set list $\mathbb{M}$ which in turn is generated by the beam selector for each spectral efficiency using information from the probing module. The beam vector from the list is satisfies:

$$\tilde{\mathbf{m}}_1 = \arg\max_{\mathbf{m}\in\mathbb{M}} \sum_{i=1}^{i=4} m_i, \tag{5.2}$$

which ensures that the highest spectral efficiency GSSK link is probed first and all of the engaged beams selected by the beam selector are used by the encoder. The encoder utilises the established mapping to transmit the training bits, followed by the random bit test data with the bit-to-symbol mapping determined by the quantity of engaged transmitter beams and the chosen beam mapping.

Based on this engaged beam set and the type of mapping shown in Table 5.2 a packet of data is generated as demonstrated in Figure 5.4. For example, each training and data symbol in the demonstrated packet is represented by $\mathbf{x}_{\text{in}}$ scaled by the channel. In the packet example a noiseless channel is assumed. If for the next data packet the encoder has received a flag feedback signal from the receiver of an excessive BER, next $\tilde{\mathbf{m}}_2$ is selected such that:

$$\tilde{\mathbf{m}}_2 = \arg\max_{\mathbf{m}\in\mathbb{M}':\mathbb{M}'=\mathbb{M}\cap\tilde{\mathbb{M}}_1} \sum_{i=1}^{i=4} m_i, \tag{5.3}$$

where $\tilde{\mathbb{M}}_1$ is given by $\tilde{\mathbb{M}}_1 = \{\tilde{\mathbf{m}}_1\}$. This ensures that encoder uses the next lower spectral efficiency engaged beam vector generated by the beam selector. In such case a similar data packet is generated, however, the GSSK symbols from different spectral efficiency alphabet are used with mapping established using appropriate look up table.

Examining the Figure in more detail, we see that the packet commences with Iden-

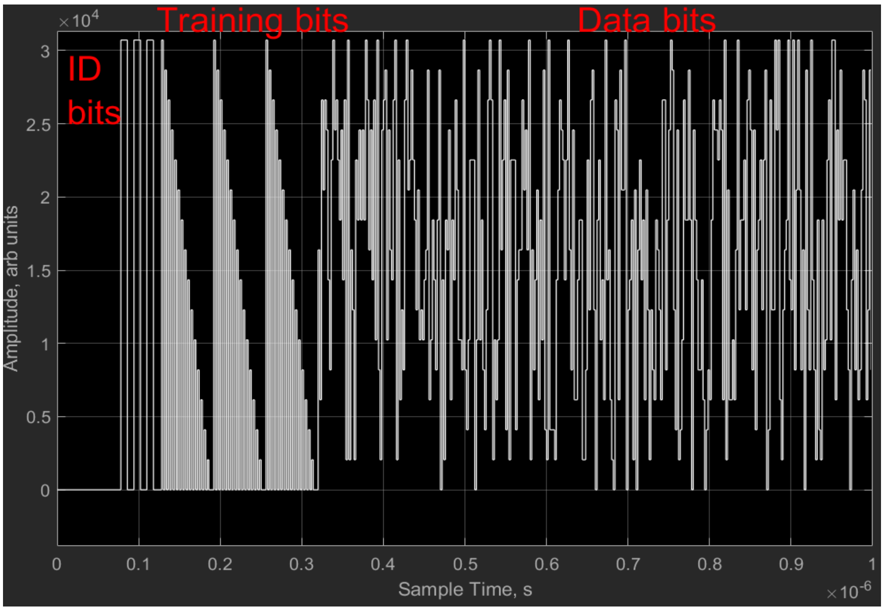

Figure 5.4: Example waveform of test data packet of 4 beam GSSK in Simulink.

tification (ID) bits. These bits signify the number of transmitter beams active in the link. This is done by the following procedure. The ID bit preamble has been allocated a certain time slot (in simulation represented by the first 25 samples). The determination of how many transmitter beams are engaged in the link is done based on how many pulses are fit within the preamble time slot, which is determined by the pulse width in the pulse train. For example, in the OOK case, the pulse width is 1 sample long. For 2-GSSK the width is 2 samples long and for 3-GSSK and 4-GSSK - 3 and 4 samples respectively. Therefore, the number of pulses at the receiver during the ID bit stage can be as high as 11 for OOK and as low as 3 for 4-GSSK.

The receiver, upon detecting a certain number of rising edges based on the number of pulses received in the ID bit preamble conditioned upon a threshold U_{act} ascertains the specific type of GSSK mapping employed during the data reception phase. Subsequently, predicated on this identification, the receiver's decoder selects the appropriate sub module to employ for codebook assembly throughout the training and decoding processes.

The ID bits are succeeded by the training bits, wherein each GSSK training symbol realisation is transmitted three times to improve the decoding accuracy. The receiver calculates the mean signal strength for each symbol to establish the codebook reference levels necessary for decoding the data bits. Subsequently, the data bits are encoded using the same mapping principle as detailed in Table 5.2.

The Simulink module implementation is detailed in Appendix E. It involves the utilisation of an HDL counter for the internal module clock, along with multiple LUTs and multiport switches.

Beam Selector

As previously discussed, the link connection begins with the probing stage initiated by the prober module. The receiver, relying on the prober sequence, measures the signal strength at the receiver for N_t^a beams. Using the signal strengths obtained from the probe data, the beam selector employs Euclidean beam selection to identify the set $\mathbb{M}$ of engaged transmitter beam sets of $\mathbb{E}_{\mathrm{t},i}$ for various cardinalities. The selected sets are then transmitted to the encoder over the feedback channel at the transmitter as a 16-bit vector. Depending on the error feedback state of the transmitter, the encoder can encode data bits as 4-beam, 3-beam, 2-beam GSSK, or as a Non-Return-to-Zero On-Off-Keying (NRZ-OOK) signal.

We will now consider Algorithm 1 from Chapter 3 for the DSP implementation of the beam selector in Simulink. Recall that the Euclidean distance, denoted as $d_{(\mathbf{x}_k,\mathbf{x}_{k'})}$, between symbols $\mathbf{x}k$ and $\mathbf{x}_{k'}$ can be calculated as follows:

$$d_{(\mathbf{x}_k,\mathbf{x}_{k'})} = \mathbf{H}\Delta_{\mathbf{x}_k,\mathbf{x}_{k'}} = \mathbf{H}(\mathbf{x}_k - \mathbf{x}_{k'}), \tag{5.4}$$

where $\mathbf{H}$ is the $N_\mathrm{t}^\mathrm{a} \times N_\mathrm{r}^\mathrm{a}$ channel matrix. For the DSP implementation of the algorithm based on the Euclidean distance it is useful to express Equation (5.4) in a matrix form for a simultaneous calculation of all mutual Euclidean distances for the given engaged beam set:

$$\Delta(\mathbb{E}_{\mathrm{t},i}) = \mathbf{X}_{\mathbb{E}_{\mathrm{t},i}}\mathbf{H}_{\mathbb{E}_{\mathrm{t},i}} - (\mathbf{X}_{\mathbb{E}_{\mathrm{t},i}}\mathbf{H}_{\mathbb{E}_{\mathrm{t},i}})^\mathrm{T}, \tag{5.5}$$

where $\mathbf{X}_{\mathbb{E}_{t,i}(\mathbf{R})}$ is given as:

$$\mathbf{X}_{\mathbb{E}_{t,i}} = \begin{bmatrix} \mathbf{x}_0 \\ \mathbf{x}_1 \\ \cdots \\ \mathbf{x}_{|\mathbb{X}|-1}, \end{bmatrix},$$

here $\mathbf{x_i}$ represents a single GSSK symbol. The maximal minimum Euclidean distance criterion can be expressed for a given engaged number of transmitter beams $|\mathbb{E}_t| = a$ as:

$$\mathbb{E}'_{t,i}(\mathbf{R}) = \arg \max_{\mathbb{E}_{t,i}(\mathbf{R}) \in \mathcal{E}_t(\mathbf{R})} \min \Delta(\mathbb{E}_{t,i}(\mathbf{R}))_{j,j' \in j \neq j'} : \tag{5.6}$$
$$|\mathbb{E}_{t,i}(\mathbf{R})| = a.$$

The beam selector chooses the engaged beam set for each cardinality, which satisfies Equation (5.6), and the engaged beam sets with varying cardinalities are subsequently consolidated into a unified list denoted as $\mathbb{M}$. This list is then encoded as a 16-bit vector and transmitted through the feedback channel to the transmitter encoder.

The implementation of the beam selector, utilising the symbol matrices and estimating Equation (5.5) in Simulink, is provided in Appendix F.

Decoder

The receiver's decoder module comprises several stages, with the initial stage being the identifier stage. In this stage, the identifier employs the input ID bits to ascertain the type of GSSK transmission that should occur, determined by the number of engaged beams in the link. To achieve this, the identifier tracks the rising edges of the ID bit rectangular pulse signals within a specified time interval, calculating the total count of rising edges. This count is subsequently compared to a predetermined reference value. Based on this reference comparison, the identifier activates a specific decoder module for training and decoding purposes.

The enabled module corresponding to a specific type of GSSK transmission is tailored to a particular constellation alphabet size and training sequence required for acquiring its reference value. During the training sequence, this module establishes a decoding alphabet based on the input training bits. Each symbol's strength value is determined as the average of three realizations of the same symbol during the training phase.

Once the training stage is concluded, the decoder proceeds to process serial data symbols and simultaneously calculates the Euclidean distances of each received symbol when compared to the alphabet reference. Subsequently, the decoder generates an output signal that multiplexes all these Euclidean distances and outputs them to the maximal likelihood estimator. For instance, in the scenario of a 4-engaged-beam GSSK transmission, the decoder will produce 16 multiplexed Euclidean distances for each received data symbol to be utilised by the maximal likelihood estimator.

In our configuration, we employ four receivers, each equipped with its dedicated decoder module. The Euclidean distances from all four receivers' inputs are aggregated at the maximal likelihood estimator. For every received symbol $\mathbf{x}_k$, the combined Euclidean distance concerning its comparison with the reference symbol $\mathbf{x}_{k'}$ is expressed as follows:

$$d_{kk'} = \sqrt{\sum_{i=1}^{4} d_{ikk'}^2}. \tag{5.7}$$

The estimated symbol $\mathbf{x}_k''$ is determined using the maximal likelihood estimator by the following equation:

$$\mathbf{x}_k'' = \arg\min_{\mathbf{x_{k'}}} d_{kk'}. \tag{5.8}$$

Subsequently, the estimated symbol is represented as a 4, 3, 2, or 1-bit vector, depending on the type of GSSK transmission.

This vector is then transmitted to the packet analyser, where it undergoes a comparison with the known reference. This comparison is executed by estimating Hamming distance between the bits of the known reference from those of the decoded symbol vector. The resulting output is accumulated in memory during the data packet transmission process. Upon concluding the data packet, the analyser assesses the accumulated count of bit errors per received bits in comparison to the threshold value $P_{\text{bit,max}}$. If the number of errors surpasses the threshold, the analyser sends a flagging feedback signal over the feedback channel to the transmitter encoder, signaling the need to reduce the spectral efficiency of the signal. However, if the number of errors remains below the threshold, the data transmission of subsequent packets will continue to use the same GSSK encoding. We set the BER threshold value of a data packet to the FEC limit of $P_{\text{bit,max}} = 3.8 \times 10^{-3}$.

The implementation of the decoder in Simulink is given in Appendix G.

5.2.1 Simulation Results

Figure 5.5 illustrates a time-dependent decoder output waveform for data packets. In this particular instance, the GSSK link offers four available beams; however, the link's SNR only permits a reliable communication using a 2-beam GSSK link that maintains an acceptable BER. The algorithm initially evaluates a four-beam GSSK data packet, and the decoded data is then compared to a predefined reference through the packet analyser module. Subsequently, the analyser transmits a feedback bit vector to the encoder, directing it to reduce the number of engaged beams in the upcoming test data packet. As a result, the transmitter sends data packets with a spectral efficiency of $\eta = 3\,\mathrm{bit/s/Hz}$ and, subsequently, with a spectral efficiency of $\eta = 2\,\mathrm{bit/s/Hz}$

In our simulations, we employ a sampling rate of 500 MSamp/s, which considers applications with a data throughput of $1-2$ Gbit/s of the GSSK link. At this sampling rate we introduce a latency of 70 ns attributable to the beam selection algorithm when

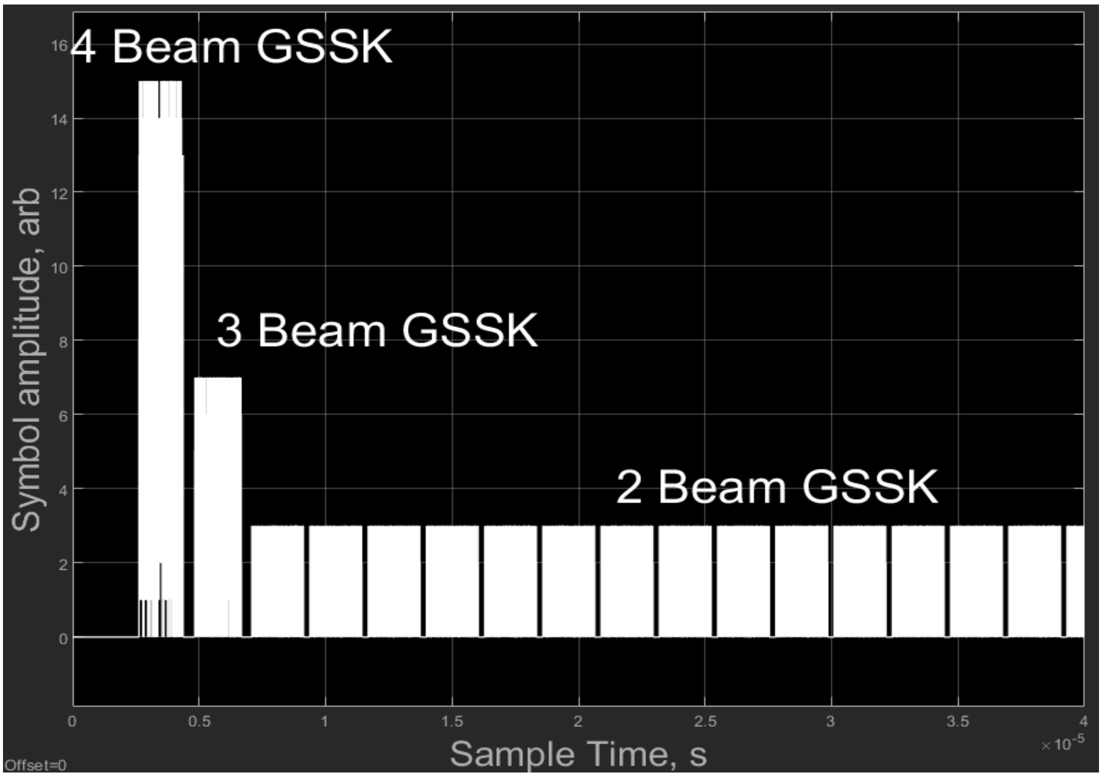

Figure 5.5: Simulated packet waveforms in Simulink.

the maximum of four available beams is taken into account. The latency, however can substantially increase. Revisiting the discussion from the previous chapter regarding the computational complexity of the maximal minimum Euclidean distance set selector, it becomes evident that the computational load of the beam selector is expected to grow exponentially as the number of engaged transmitter beams increases.

In scenarios where a substantial number of transmitter beams are available, it is advisable to employ less computationally intensive beam selection methods, such as the optimal GSSK channel ratio beam selector. However, it should be noted that a comprehensive study on the scalability of such algorithms for a large number of transmitter beams within Simulink falls beyond the scope of this work.

Each data packet transmitted by the encoder comprises 1150 samples, corresponding to a duration of $2.3\,\mu$s. This specific sample count is chosen to ensure that the packet contains at least 1000 bits, which is necessary for measuring the BER at the FEC threshold. The latency encountered until a stable state of data transmission is established can fluctuate between $2.3\,\mu$s and $9.2\,\mu$s, depending on the frequency of adjustments to the number of engaged beams. Additionally, the latency is influenced by the sampling rate.

The performance of the algorithm and the link, in terms of achievable spectral efficiency, is highly dependent on the link SNR. In our simulations, we assume that the four receivers are closely spaced, ensuring that the SNR at each individual receiver is approximately the same. To estimate the signal SNR from the received data packet waveforms, as depicted in Figure 5.4, we compute the root mean square of the signal voltage, denoted as $V_{\text{signal,rms}}$, from the random data samples. For each SNR measurement, we introduce random noise with the same noise power to the received signal at each receiver. Subsequently, we calculate the root mean square of the noise voltage from the samples, denoted as $V_{\text{noise,rms}}$, and the electrical SNR is determined by the following expression:

$$\gamma_{\text{elec}} = 20\log\left(\frac{V_{\text{signal,rms}}}{V_{\text{noise,rms}}}\right). \tag{5.9}$$

In our analysis of spectral efficiency dependence on electrical SNR, we consider three different scenarios with varying transmitter beam channel ratios at the receivers. These

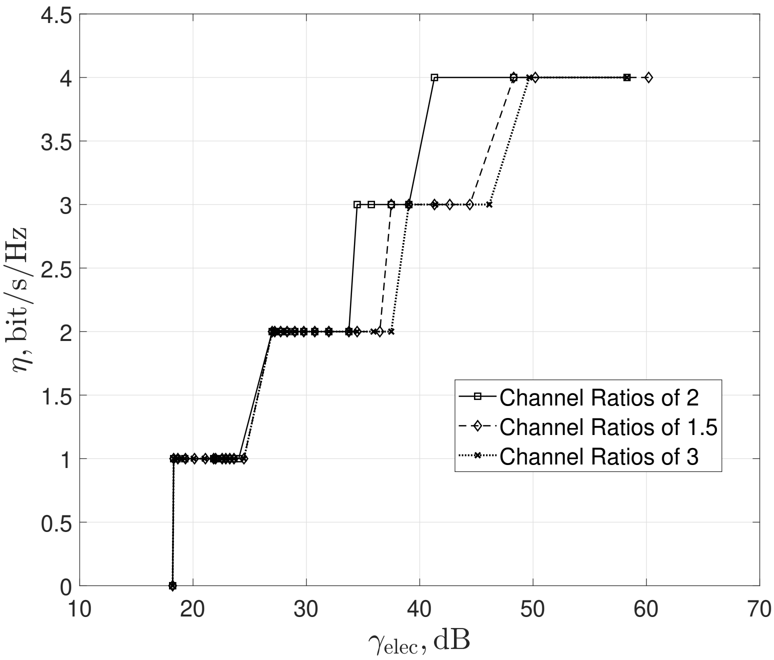

Figure 5.6: Achievable η vs γ_{elec} for noiseless beam selection.

cases are characterized by perfect channel ratios of 2, implying that $\frac{h_{i1}}{h_{i2}} = \frac{h_{i2}}{h_{i3}} = \frac{h_{i3}}{h_{i4}} = 2$, channel ratios of 1.5, and channel ratios of 3.

Figure 5.6 provides a visualization of the achievable link spectral efficiency as a function of the electrical SNR for the given link, assuming ideal channel state information for beam selection.

From the Figure, it is evident that the algorithm requires a minimum electrical SNR of at least 18.29 dB or an optical SNR of 9.15 dB to operate within the permissible BER. We also observe that the channel ratios of different beams do not have a discernible impact on the minimum required electrical link SNR.

However, as we analyse the increase of spectral efficiency with increasing electrical SNR, a substantial difference becomes apparent among the different cases. As expected from our previous chapter's discussion, the ideal channel ratios outperform the other cases. In the scenario with ideal channel ratios, the minimum electrical SNR needed to achieve the maximum spectral efficiency for the setup is lowest at 41 dB. Furthermore, in this case, there is a significant gap of between $8 - 9$ dB in electrical SNR compared to the other cases.

Among the three cases analysed, it is notable that the channel ratios of 3 exhibit the poorest spectral efficiency performance concerning electrical SNR. This difference in performance can be attributed to the low SNR of the first and second weakest transmitter beams, which exhibit significantly lower signal strength compared to the noise floor, even when the Euclidean mutual distances between the transmitter beams are increased. In contrast, although the mutual Euclidean distances are the lowest for channel ratios of 1.5, the slightly improved performance is observed compared to the case with channel ratios of 3. This improvement can be attributed to the enhanced SNR of the first and second weakest transmitter beams in the 1.5 channel ratio scenario.

These results highlight that the algorithm's performance can be significantly influenced by channel state conditions and beam distinguishability, especially when high spectral efficiency is considered. It is worth noting that the minimum spectral efficiency, in contrast, is primarily dependent on the individual beam SNR.

The lower SNR limit of the algorithm can be attributed to several factors. Firstly, despite having ideal channel state information for beam selection, the channel state information estimated from the training bits is subject to noise. This noise in the estimated channel state information can significantly impact the decoding performance and contribute to an increase in BER as the link SNR decreases.

Another limiting factor to consider is the noise level relative to the activation threshold levels for each decoding stage, including receiver activation itself and the transition from the ID stage to the training stage. In scenarios with strong noise, there is a probability of triggering an out-of-sync stage, which can result in the receiver becoming desynchronized with the input data, immediately leading to decoding breakdown.

To enhance performance, we have the option to further optimize the triggering levels of different stages. Additionally, we can consider increasing the length of the training sequence, although this comes with the trade-off of introducing higher packet overhead due to the extended training.

Up to this point, we have assumed that the channel state information for beam selection is perfect. However, in reality, it will be subject to the same noisy channel

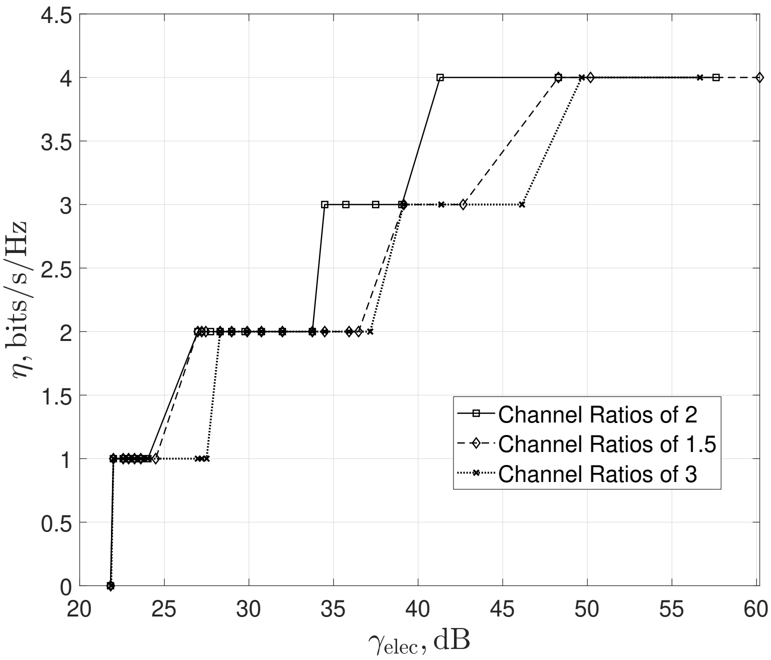

Figure 5.7: Achievable η vs γ_{elec} for noisy beam selection.

conditions as the transmitted data packets. In such cases, one can anticipate a degradation in spectral efficiency performance relative to the link's electrical SNR. Figure 5.7 provides an illustration of the achievable link spectral efficiency for a given electrical SNR when considering noisy channel state information for beam selection.

An initial observation from the Figure is a shift in the minimum required electrical SNR, which increases by approximately 3.7 dB to reach 21.99 dB. This shift can be attributed to errors in the Euclidean distance estimation within the beam selector caused by the noisy channel state information. In such scenarios, there is an elevated probability that the strongest signal transmitter beam (necessary for OOK transmission) will not be selected promptly leading to degraded performance. One approach to reduce the minimum required electrical SNR is to increase the length of the probing signal, incorporating more transmitter beam pulses to decrease the error probability. However, this comes with a trade-off in the form of increased latency due to the beam selection process.

Another significant observation from the Figure is the widening gap in spectral efficiency of $\eta = 2\,\mathrm{bit/s/Hz}$ between channel ratios of 3 and the other cases. However, for the remaining spectral efficiencies, the performance closely resembles the noiseless beam selection scenario. This discrepancy can be attributed to the fact that during the probing stage, the SNRs of weaker transmitter beams are substantially lower in the case of channel ratios of 3 compared to the other two cases. This lower SNR results in additional errors during the beam selection process.

We can conclude that the presence of noise can indeed impact the beam selection process, notably degrading algorithm performance, particularly at lower spectral efficiencies. However, higher spectral efficiencies at higher SNRs appear to be less affected. To mitigate the effect of noise during the beam selection stage, one effective approach is to increase the length of the probing stage. In our current setup, the beam selection process only takes 70 ns, which is two orders of magnitude shorter than the data packet length and occurs only once at the beginning of the algorithm. Assuming that the channel coherence time extends to hundreds of milliseconds, extending the beam selection length by including more repetitions of the probing stage waveform can help reduce the impact of noise during the beam selection stage, while maintaining negligible effects on latency.

To reduce the ideal minimum SNR requirement and enhance spectral efficiency performance concerning the link's electrical SNR, longer training sequences are necessary, which in turn incur a larger overhead. In such cases, maintaining the required data throughput demands an increase in the number of data bits within each packet. It's worth noting that while our work did not consider the baseline wander effect, increasing the number of bits in the data packet is expected to amplify the impact of baseline wander on the link's performance. This is primarily due to the presence of lower-frequency, long binary sequences of '1's and '0's. Consequently, it's advisable to consider wander mitigation techniques such as Manchester coding in these scenarios.

Lastly, it is important to note that in this work, we operated under the assumption of ideal feedback information transmission from the receiver to the transmitter. In a real-world scenario, the feedback channel is noisy, which can potentially further degrade the spectral efficiency performance of the system.

5.3 Summary

In this chapter, we have presented the Simulink model of the adaptive GSSK algorithm designed for FPGA implementation. This algorithm utilises the maximal minimum Euclidean distance beam selection criterion and is composed of multiple modules integrated into both the receiver and transmitter components. The beam selection process occurs at the receiver, and the selected beam sets are subsequently communicated back to the transmitter. One key feature of the algorithm is its ability to dynamically adjust the number of engaged beams in the link based on the data packet's BER.

During our simulations, we utilised 4 transmitter beams and 4 receivers. The latency penalty incurred by the algorithm due to the beam selection is minimal, at only 70 ns. However, it is anticipated to increase exponentially with a higher number of engaged beams in the link. In such scenarios, alternative beam selection criteria like optimal GSSK channel ratio should be explored.

Furthermore, we observed that the latency introduced by the training and spectral efficiency adjustment ranges from $2.3\,\mu$s to $9.2\,\mu$s, depending on the number of spectral efficiency adjustments being made.

The minimum required electrical SNR, considering noisy channel state information for the beam selection, is determined to be 21.99 dB. The performance of the algorithm is notably influenced by the beam distinguishability, with this dependence becoming more pronounced as spectral efficiency increases.

To enhance the algorithm's achievable spectral efficiency performance relative to electrical SNR, several potential improvements can be considered. These include optimizing the trigger levels within the decoder modules and increasing the length of probing and training sequences, taking into account the trade-off with latency.

Chapter 6

Freeform Receiver Concentrator

6.1 Introduction

As already demonstrated in Chapter 2, the performance of OWC or VLC links heavily depends on the opto-electronic front-end, which can often require the design and implementation of customized optical and opto-electronic elements. While a considerable improvement in data throughput and energy efficiency can be achieved using modulation techniques such as GSSK, the opto-electronic front-end can significantly limit the achievable performance. In many applications, such performance targets demand for high data throughput, long-distance transmission, and wide coverage necessitates, in conjuction with a modulation technique, the use of high-bandwidth photodiodes and optics with high optical concentration for the receiver.

However, it is a well recongised fact that that the bandwidth of photodiodes exhibits an inverse relationship with their size or diameter [155]. This reduction in size results in a diminished photoactive area of the photodiode, leading to a deterioration in SNR. In order to counteract the loss of active area, it becomes necessary to increase the optical concentration gain of the receiver optics. However, with this approach a problem quickly becomes apparent: as the concentration gain of the receiver optics is increased, the receiver's FoV decreases, resulting in reduced coverage [67, 307].

This trade-off is visually represented in Figure 6.1. For instance, in Figure 6.1a), this trade-off is illustrated within the context of imaging optics, where concentration is achieved through the use of lenses, such as a plano-convex lens. In scenarios where the incident beams are paraxial, optimal placement for the photodiode is at location 1, which corresponds to the focal point. This position allows for the capture of the majority of incident light.

However, when an incident angle deviates from the optical axis of the system, the focal point shifts in a transversal direction, resulting in no signal reception at the photodiode. To address this issue, the photodiode must be adjusted toward the lens into the defocused range [67]. In this scenario, the FoV of the receiver is conserved, but the concentration ratio decreases.

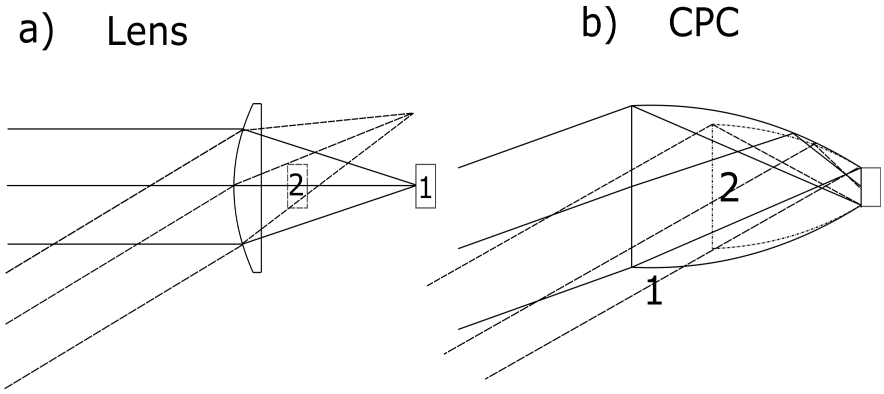

Figure 6.1: Concentration *vs.* FoV trade-off in a) imaging optics (lens), b) non-imaging optics (CPC).

A comparable trade-off is also evident in non-imaging optics. This relationship is depicted in Figure 6.1b) using the example of a CPC. In this case, the field of view FoV of the receiver is confined by the acceptance angle of the concentrator. When the acceptance angle of the CPC is increased, the length and size of the input aperture decrease, leading to a reduction in optical concentration. This behavior is a consequence of the well-known concentration limit of 2D CPCs: [156, 308, 309]:

$$C_{\mathrm{opt}} = \frac{A_{\mathrm{in}}}{A_{\mathrm{out}}} = \frac{n_{\mathrm{con}}^2}{\sin^2 \Psi_{\mathrm{c}}}, \tag{6.1}$$

here A_{in} is area of the input aperture, A_{out} is the area of exit aperture of the CPC, n_{con} is the refractive index of the CPC material and Ψ_{c} is the acceptance half-angle of the CPC.

Both cases illustrate the conservation of étendue, which can be expressed as [310]:

$$\pi A_{\text{in}} \sin^2 \alpha = n\pi A_{\text{PD}} \sin^2 \beta, \tag{6.2}$$

where A_{in} is the input aperture area, A_{PD} is the photodiode area, n is the refractive index of medium in which the photodiode is immersed, α is the maximum incident solid angle at the input aperture and β is the maximum incident solid angle at the photodiode.

To mitigate the impact of the reduced optical concentration on SNR, one approach is to enlarge the input aperture of optical elements to capture more incident light. However, this results in an increase in the size of the receiver, which is undesirable for compact, form-factor-constrained devices.

Non-imaging optics, such as CPCs, offer advantages including a generally superior gain vs. FoV trade-off and greater robustness against misalignment [155]. However, for especially small receivers (less than a mm in scale), the alignment and installation of a CPC on top and in contact of a photodiode can pose a significant practical and mechanical challenge. On the other hand, conventional imaging optics are typically simpler to manufacture and can achieve a more compact form factor compared to CPCs [311]. Moreover, aligning and installing imaging optics in front of a photodiode is considerably simpler, especially when dealing with compact receivers.

Moreover, there are potential advantages in creating custom-designed receiver concentrators for compact devices by applying methodologies developed for prescribed irradiance freeform optics [312] to enhance the optical concentration beyond the limits of imaging optics while retaining no-contact characteristics of the design with a photodiode. As such, we can explore alternative ways in designing optical concentrators.

In this chapter, we illustrate that by leveraging conventional freeform optics techniques employed in far-field irradiance pattern generation [312], we can devise an optical concentrator composed of multiple distinct lenslets, referred to as a "lenslet array". This array is designed to try to mitigate the limitations of both imaging and non-imaging optics, offering an improved trade-off between FoV and gain compared to imaging optics while simultaneously reducing production and implementation complexity when compared to CPCs.

To substantiate our approach, we initially validate the methodology using the Linear Assignment Problem (LAP) employed in freeform optics design [312]. This validation process focuses on the development of a straightforward on-axis (paraxial) concentrator, akin to conventional imaging optics such as plano-convex or Fresnel lenses. Subsequently, we introduce a freeform lenslet concentrator tailored for a receiver with a 10 deg FoV within the context of mobile OWC. We then proceed to discuss the comparative advantages and limitations of this novel concentrator when juxtaposed with conventional imaging and non-imaging optics represented in the study by a convex lens and an CPC.

Another approach to improve the SNR involves expanding the photoactive area of the receiver while maintaining the same bandwidth. This can be achieved by implementing multiple photodiodes organized in an array configuration, more precisely in an $M \times M$ square matrix array [146]. In the realm of high data throughput solutions, the utilisation of photodiode arrays represents a prominent avenue of research and development in OWC, VLC and LiFi.

Hence, our discussion on imaging, non-imaging, and freeform optical concentrators extends beyond the context of single photodiodes to encompass arrays of photodiodes. We delve into the examination of how various concentrators/lenses with different irradiance distributions incident on the array impact the trade-off between FoV and gain. Furthermore, we analyse the dependence of photocurrent on photodiode size within the array for different irradiance distributions. These investigations lead to the proposition of an adapted model for assessing photocurrent in the link budget modeling of OWC links, which employ photodiode arrays.

6.2 Freeform Optical Concentrators

Freeform optics refer to a diverse class of optical and micro-optical devices, characterized by their lack of rotational symmetry in surface shape [313]. The research field known as freeform optics has gained prominence in the last two decades [313]. In a 2004 publication, Rodgers and Thompson provided an early description of a toroidal aspherical lens with an anamorphic optical surface as a freeform optic [314]. However, it is worth noting that there are prior instances of non-symmetrical lenses predating the 2004 publication [313]. Examples include hypergonar lenses [315], Alvarez lenses [316], and even commercial products such as the Polaroid viewfinder [317]. In recent years, the deployment of freeform optics has significantly increased in various applications, including biosensing, remote sensing, transportation, military applications, and manufacturing [313]. This growth has been facilitated by advances in ultraprecision machining technology [313].

Formally, freeform surfaces are defined as surfaces lacking rotational or translational invariance. This design approach transcends the limitations imposed by spherical surfaces, rotationally symmetrical aspheres, off-axis conics, and toroids [313]. Notably, freeform surfaces are not constrained to spatial continuity. Mathematically, they can be described using either local or global representations [313]. Locally freeform surfaces can be effectively represented by splines [318], radial basis functions [319], and wavelets [320]. On the global representation, freeform surfaces can be represented using mathematical tools such as Zernike polynomials [313, 321–323], Zernike differences [324, 325], Forbes polynomials [326], off-axis aspheres [325], and Chebyshev and Legendre polynomials [325, 327, 328].

Various design methods are employed for freeform optics, including but not limited to solving Monge-Ampère partial differential equations [329–332], Oliker's supporting ellipsoids [333], ray mapping methods [312,334–338] and Simultaneous Multiple Surface (SMS) method [339–341].

Various types of freeform optics designs have been developed for applications in solar concentration for photovoltaics and imaging. These designs encompass a wide range of optical components, including freeform mirrors [342, 343], freeform lenses [344, 345], multifold Kohler concentrators with Fresnel lenses [159, 346–348], XR freeform optics [349, 350], trough freeform reflector type concentrators [351, 352], aplanatic freeform concentrators [353], freeform Cassegrain concentrator [354] and even planar metasurface type freeform lenses [355].

In recent years, there has been a growing interest in the development of optical freeform concentrators for LiFi receivers. Examples of innovative designs include freeform compound concentrators [356, 357], non-rotationally symmetric freeform Fresnel lenses [158, 358], freeform multipath lenses [359, 360], TIR lens [361] and multi-cell freeform diversity receiver [362, 363].

6.3 Freeform Lenslet Array Design Methodology

We will now delve in-detail into the calculation of the freeform lenslets utilised in this study. In many instances, the freeform surface is defined through the solution of the highly nonlinear Monge-Ampère (MA) partial differential equation [329,364]. However, solving this equation presents a significant theoretical and computational challenge, necessitating the development of various finite-difference methods and iterative least-squares approaches to address it [365, 366].

Alternatively, it has been demonstrated that several inverse optical problems can be reformulated as Monge-Kantorovich Mass Transportation Problems (MTP) with a specific cost function, which are notably simpler to solve than the MA equation [336]. Moreover, the MTP can be discretized and represented as an LAP [336]. However, it's worth noting that the design of a refractive lenslet in the near-field non-paraxial case cannot be cast as an MTP. Nevertheless, as shown by Bykov et al. in [312], the eikonal function can be calculated using LAP to solve the MTP with a cost function that corresponds to the distance between points on the S and T surfaces using their iterative algorithm.

In our study, we employ the method and iterative algorithm as elucidated in the work in [312] to construct individual lenslets for the array. Subsequently, we combine these lenslets together for the fulfillment of target irradiance at the receiver plane. Originally, the method described in [312] was developed for calculating the surface of optical elements under prescribed irradiance conditions in the far-field with diverging rays. However, in this work, we adapt this method for designing a compact optical element optimized for near-field concentration. This adaptation highlights its applicability in crafting slender, concentrating imaging optics suitable for mobile OWC and LiFi applications. Our investigation primarily focuses on equal area lenslets.

LAP for a Single Lenslet Design

Our principal approach to designing a compact freeform refractive receiver optical element with specific functionality involves dividing the element into an array of segmented freeform lenslets, as depicted in Figure 6.2. The freeform surface of each lenslet is independently computed. The overall optical response of the element at the output target plane, given a particular input irradiance and angle of incidence distribution at the input aperture of the element, is expressed as the sum of individual lenslet responses. This approach often leads to an optimization problem where the goal is to determine a set of lenslets that best match the target irradiance. In this study, we assume that the optical element possesses a single freeform surface, with the other surface being flat, and we also consider the utilisation of a flat photodetector.

We commence the design process by selecting an optical configuration tailored to the specific use-case scenario and the desired functionality of the element, such as a collimated on-axis beam scenario with a light concentration function. Subsequently, we define input (source) and output (target) domains, denoted as $\mathbb{S}$ and $\mathbb{T}$, which encompass the respective freeform surface S and the photodetector target surfaces T_{PD}. Input irradiance distribution E_0 and output target irradiance distribution E_{t} are specified on their respective domains.

The surface S is characterized by the equation $z = s(x, y)$, while T_{PD} is defined as $z = t(x, y) = t_d$, with t_d representing the fixed distance between the input aperture of the array and the photodetector. It is crucial to emphasize that the surface T_{PD} is situated above S, indicating that $t(x, y) > s(x, y)$. The collective freeform surface of

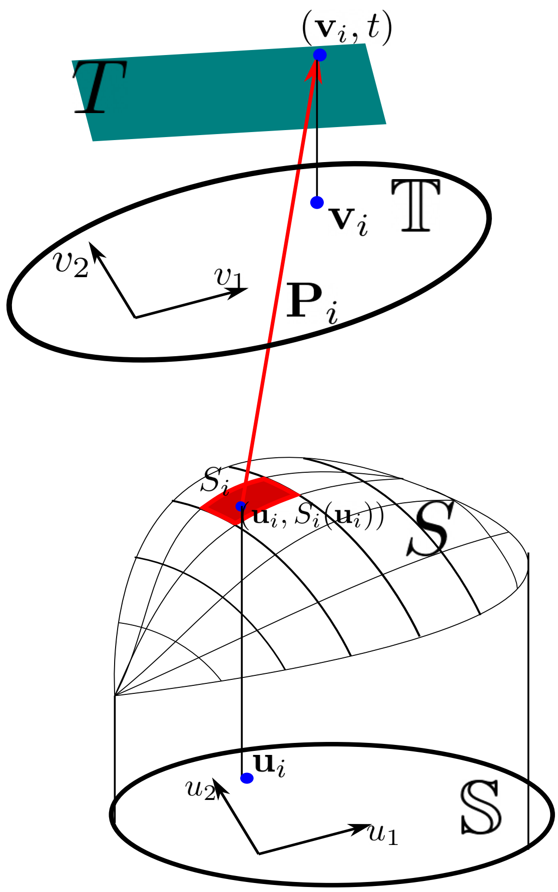

Figure 6.2: Subdivision of the lens surface S into smaller lenslets S_i. Here a point on the lenslet surface S_i is mapped by $\mathbf{P}_i$ to the photodetector target surface T_{PD}.

the array S is reconstructed as the union of the individual lenslet surfaces:

$$S = \bigcup_{i=1}^{N} S_i \in \mathbb{S}, \tag{6.3}$$

where S_i is surface of the i^{th} lenslet, N is number of lenslets. The co-ordinates (x, y) of the points lying on the surfaces S and T are described by vectors $\mathbf{u} = (u_1, u_2) \in \mathbb{S}$ and $\mathbf{v} = (v_1, v_2) \in \mathbb{T}$ respectively, $\mathbf{u}$ and $\mathbf{v}$ are defined in separate co-ordinate systems. A lenslet surface S_i is defined as a set of 3D vectors $(\mathbf{u}_i, s_i(\mathbf{u}_i))$ such that $u_{1,i} \in [\frac{-l_1}{2} + \Delta_{u_1,i}; \Delta_{u_1,i} + \frac{l_1}{2}]$ and $u_{2,i} \in [\frac{-l_2}{2} + \Delta_{u_2,i}; \Delta_{u_2,i} + \frac{l_2}{2}]$, where is the i^{th} lenslet off-set along u_1 and u_2 axis from the centre of lens and l_1, l_2 are half-widths of a lenslet. The off-set should be selected such that for any pair of lenslet surfaces

$\{S_i, S_j\} \in \mathbb{S} : \forall \mathbf{u}_i, \mathbf{u}_j : \mathbf{u}_i \neq \mathbf{u}_j \in \mathbb{S}$, i.e. that no two lenslet surfaces overlap.

We can now formulate the inverse problem, which is to design N individual freeform lenslets such that their unity is defined by (6.3) $S : E_0(\mathbf{u}) \in \mathbb{S} \mapsto E_t(\mathbf{v}) \in \mathbb{T}$ where:

$$E_t(\mathbf{v}) = \sum_{i=1}^{N} E_i(\mathbf{v}) \in \mathbb{T}, \tag{6.4}$$

where $E_i(\mathbf{v})$ is the irradiance generated on T by the i^{th} lenslet defined on $\mathbb{S}$.

Identifying a configuration of N lenslets that satisfies the conditions specified in Equation (6.4) is a non-trivial task, primarily due to the multitude of possible ways to distribute the target irradiance among individual lenslet contributions. This complexity gives rise to an optimization problem, involving the goal to find a set of partitioned irradiances that minimizes the optical path length for the rays traversing the optical system.

Nevertheless, within the context of OWC and LiFi, the primary performance benchmarks for receiver optics are centered on the optical concentration ratio C_{opt} and the acceptance angle Ψ_{c} rather than image quality. This shift in emphasis provides greater flexibility in the design of imaging at the photodetector. It allows for the selection of a relatively simple-shaped target irradiance distribution (e.g., a rectangle, square, or circle) with uniform distribution characteristics, fixed at a central position relative to and aligned with the optical axis of the system. In such scenarios, all lenslets can be tailored to converge toward the same irradiance target at the centre of the target plane:

$$E_i(\mathbf{v}) = \frac{E_t(\mathbf{v})}{N} = \frac{E}{N} \in \mathbb{T}.$$

Here $v_1 \in [-\frac{w_1}{2}; \frac{w_1}{2}]$ and $v_2 \in [-\frac{w_2}{2}; \frac{w_2}{2}]$, where w_1, w_2 are half-widths of the target rectangle (or square) and E is the uniform irradiance of the target.

On the other hand, the incident irradiance can exhibit notable variations from one lenslet to another. For example, a narrow Gaussian beam with low divergence will yield a considerably non-uniform irradiance distribution determined by the spot size across the array. However, in this study, we make the assumption of a communication link where the transmitter beam source is situated at a substantial distance from the lenslet array with a high enough divergence, such that the beam size significantly surpasses the dimensions of the array itself. This assumption enables us to approximate the incident irradiance distribution as uniform.

An evident limitation of the inverse mapping problem is its exclusive reliance on the input and specified output irradiance, without considering the incidence angle of the beams in the radiance space. The method is predicated on a paraxial scenario, where the incident beams are nearly parallel to the optical axis of the optical system. A comprehensive mapping problem would necessitate the inclusion of input and prescribed radiances at the input aperture and the target area, respectively. However, we postpone the exploration of this aspect to future research.

We will now provide a brief description of the LAP for MTP and iterative algorithm from [312] used to calculate a single lenslet.

For a given input $E_{0,i}(\mathbf{u}_i)$ and output $E_{t,i}(\mathbf{v})$ irradiance for a single lenslet, the MTP solution is the mapping $\mathbf{P}_i : \mathbb{S} \mapsto \mathbb{T}$ where points $\mathbf{u}_i$ on the lenslet surface S_i are mapped to the points $\mathbf{v}_i = \mathbf{P}_i(\mathbf{u}_i)$ on the surface T. This mapping preserves the light flux and minimizes the functional [312]:

$$\mathcal{C}(\mathbf{P}_i) = \int_{\mathbb{S}} \rho(\mathbf{u}_i, \mathbf{P}_i(\mathbf{u}_i)) E_{0,i}(\mathbf{u}_i) d\mathbf{u}_i, \tag{6.5}$$

here the cost function $\rho(\mathbf{u}_i, \mathbf{P}_i(\mathbf{u}_i))$ for target distance $t(\mathbf{v}_i)$ and i^{th} lenslet height $s_i(\mathbf{u}_i)$ is given as [312]:

$$\begin{aligned} \rho(\mathbf{u}_i, \mathbf{v}_i) =& \sqrt{|\mathbf{v}_i - \mathbf{u}_i|^2 + [t(\mathbf{v}_i) - s_i(\mathbf{u}_i)]^2} \\ =& \sqrt{|\mathbf{v}_i - \mathbf{u}_i|^2 + [t - s_i(\mathbf{u}_i)]^2}. \end{aligned} \tag{6.6}$$

It is important to emphasize that the cost function is defined as the Euclidean distance in $\mathbb{R}^3$ between points on the lenslet and target surfaces. The preservation of light flux is guaranteed by the following expression [312]:

$$E_0(\mathbf{u}_i) = E(\mathbf{P}_{\Phi,i}(\mathbf{u}_i)) J_{\mathbf{P}_{\Phi,i}}(\mathbf{u}_i), \tag{6.7}$$

where $P_{\Phi,i} : \mathbb{S} \mapsto \mathbb{T}$ is the mapping for which the light flux conservation holds and $J_{\mathbf{P}_{\Phi,i}}(\mathbf{u}_i)$ is the Jacobian of the co-ordinate transformation $(v_{1,i}, v_{2,i}) = (P_{\Phi,1,i}(\mathbf{u}_i), P_{\Phi,2,i}(\mathbf{u}_i))$ given as [312]:

$$J_{\mathbf{P}_{\Phi,i}}(\mathbf{u}_i) = \left| \frac{\partial P_{\Phi,1,i}}{\partial u_{1,i}} \frac{\partial P_{\Phi,2,i}}{\partial u_{2,i}} - \frac{\partial P_{\Phi,1,i}}{\partial u_{2,i}} \frac{\partial P_{\Phi,2,i}}{\partial u_{1,i}} \right|. \tag{6.8}$$

As shown in [312], the discrete version presented in Equation (6.5) can be reformulated as an LAP. In this approach, the input $E_{0,i}(\mathbf{u}_i)$ and output $E_{t,i}(\mathbf{v}_i)$ irradiance distributions are divided into M equal flux cells on the lenslet and photodetector surfaces. As a result, for each lenslet indexed by i, the following equality is valid for any pair of cells $(\sigma_{i,j} \subset \mathbb{S}, \tau_{i,k} \subset \mathbb{T})$: [312]:

$$\int_{\sigma_{i,j}} E_{0,i}(\mathbf{u}_i) d\mathbf{u}_i = \int_{\tau_{i,j}} E_{t,i}(\mathbf{v}_i) d\mathbf{v}_i = P_{\text{cell}}, \tag{6.9}$$

where P_{cell} is the radiant power contained by the cell.

In the straightforward scenario where the irradiance is uniform at both the input aperture of a lenslet and at the photodetector, a simple partition of the $\mathbb{S}$ domain within the lenslet boundaries and $\mathbb{T}$ into a grid of M equal rectangles is sufficient. However, in situations where the irradiance cannot be assumed to be uniform, a more comprehensive approach to cell division, as elucidated in [312], should be employed.

Once the lenslet surface is discretized into a grid of M equal flux cells, any energy-conserving mapping, denoted as $\mathbb{S} \mapsto \mathbb{T}$ for the i^{th} lenslet, can be expressed through permutations of M indices $(k_1, k_2, \ldots, k_M)$. These indices determine to which target cells $\tau_{i,k}$ the lenslet cells $\sigma_{i,j}$ are mapped. The optimal mapping, $\mathbf{v}_i = \mathbf{P}_i(\mathbf{u}_i)$, can be determined by solving the linear assignment problem [312]:

$$\mathcal{C}_d(k_1, ...k_N) = \sum_j \rho(\mathbf{u}_{i,j}, \mathbf{v}_{i,k_j}) \rightarrow \text{min}. \tag{6.10}$$

Once the mapping $\mathbf{v}_i = \mathbf{P}_i(\mathbf{u}_i)$ is determined, the eikonal function of a lenslet $\Phi(\mathbf{u}_i)$ can be reconstructed by numerically integrating equation [312]:

$$\nabla\Phi(\mathbf{u}_i) = \frac{\mathbf{P}_i(\mathbf{u}_i) - \mathbf{u}_i}{\rho(\mathbf{u}_i, \mathbf{P}_i(\mathbf{u}_i))} + \nabla s_i(\mathbf{u}_i) \frac{t - s_i(\mathbf{u}_i)}{\rho(\mathbf{u}_i, \mathbf{P}_i(\mathbf{u}_i))}, \tag{6.11}$$

here $\nabla = (\frac{\partial}{\partial u_{1,i}}, \frac{\partial}{\partial u_{2,i}})$.

Once the eikonal function $\Phi(\mathbf{u}_i)$ is reconstructed, the local surface height or Sagitta (Sag) of the optical element, denoted as $s_{\text{el},i}(\mathbf{u}_i)$, of the lenslet can be calculated using the thin lens approximation [312]:

$$s_{\text{el},i}(\mathbf{u}_i) = \frac{1}{n_0 - 1}(\Phi_i(\mathbf{u}_i) - s_i(\mathbf{u}_i)), \tag{6.12}$$

here n_0 is refractive index of the optical element. Subsequently, a ray tracing is executed on the calculated optical element to determine the intermediate output irradiance, denoted as $E^j_{t,i}(\mathbf{v})$, for the j^{th} iteration. To assess the degree of correspondence between the intermediate output irradiance and the specified output irradiance, a quality parameter δ^j is defined as follows [312]:

$$\delta^j = \int_{\tau_{i,j}} (E^j_{t,i}(\mathbf{v}_i) - E_{t,i}(\mathbf{v}_i))d\mathbf{v}_i. \tag{6.13}$$

The irradiance produced by the calculated optical element is deemed to be in good agreement with the specified irradiance when $\delta^j < \varepsilon$, where ε represents a tolerance value determined by the design requirements.

The freeform surface of the lenslet then can be calculated using the iterative algorithm proposed in the study [312] as follows:

1. Initialise the algorithm, set $s_i(\mathbf{u}_i) = 0$ and $s_{\text{el},i}(\mathbf{u}_i) = 0$.

2. Calculate the mapping $\mathbf{v}_i = \mathbf{P}_i(\mathbf{u}_i)$ by solving (6.10).

3. Reconstruct the eikonal function $\Phi(\mathbf{u}_i)$ on $z = s_i(\mathbf{u}_i)$.

4. Calculate the optical element height $s_{\text{el},i}(\mathbf{u}_i)$ from (6.12).

5. Conduct a ray-tracing calculation to ascertain the irradiance generated on the photodetector surface by the lenslet. If the discrepancy between the irradiance and the specified value remains within the defined tolerance limit ε, set $s_i(\mathbf{u}_i) = s_{\text{el},i}(\mathbf{u}_i)$, and proceed to the subsequent lenslet. However, if the deviation exceeds the tolerance limit, return to step 2 for further adjustments.

After computing all the lenslets, the freeform lenslet array can be reconstructed using Equation (6.3).

6.4 Proof of Concept Paraxial Concentrator

In this section, we first introduce a proof-of-concept design for a lenslet array using the proposed method. This design features an optical concentrator of significantly reduced sagitta when compared to commercially available lenses and offers straightforward light concentration and focusing functionality. We conduct a performance evaluation comparing it with a conventional plano-convex lens of equivalent input aperture and focal strength. It's essential to note that this design is based on the assumption of a well-aligned transmitter-receiver link and is tailored for applications with a narrow FoV of less than 1 deg.

In the later chapter, we will present a lenslet array designed to accommodate a broader Field of View (FoV) of 10 deg. We will then conduct a comparative analysis of its performance in terms of optical concentration, benchmarking it against a CPC and a common convex lens.

Optical setup

For the sake of simplicity, we consider an incident collimated monochromatic beam with uniform irradiance, $E_0 = 11.83 \times 10^4\,\mathrm{W/m^2}$, having a square shape that we aim to focus onto a smaller square area on the photodetector. The photodetector's dimensions are set at $10 \times 10\,\mu\mathrm{m}^2$, an individual lenslet measures $200 \times 200\,\mu\mathrm{m}^2$, and the lenslet array encompasses $1 \times 1\,\mathrm{mm}^2$, segmented into $N = 25$ lenslets. The distance between the input aperture of the array and the photodetector is $t = 2\,\mathrm{mm}$. The incident beam possesses a wavelength of 850 nm, and the total optical power is $P_{\mathrm{opt}} = 0.1\,\mathrm{W}$, integrated over the input aperture of the array. The material chosen for the array is PMMA (polymethyl methacrylate), with $n_0(\lambda = 850\,\mathrm{nm}) = 1.484$ [367]. We utilise a grid consisting of 45×45 square cells for the equal flux divisions in our calculations for each lenslet.

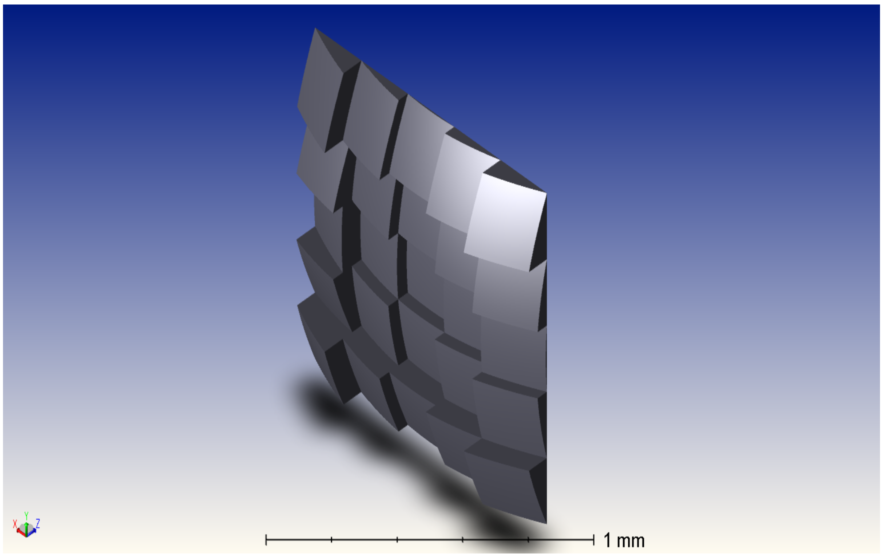

Figure 6.3: Calculated thin refractive freeform lenslet array in Zemax optic studio.

Design Example & Performance Analysis

The optical freeform refractive element is designed using MATLAB and subsequently exported to Zemax Optic Studio software for ray-tracing analysis. The resultant lenslet array is depicted in Figure 6.3, demonstrating a slender optical refractive element with a maximum thickness at the edges of 159 μm and only 10 μm at the central lenslet. One can observe an overall curvature of the array, which is inverted compared to a plano convex lens but similar to a Fresnel lens.

Figure 6.4 presents a comparison of thickness between the lenslet array and a standard plano-convex lens with an effective input aperture diameter of 1 mm, an effective focal length of 2 mm, and a thickness of d = 0.8 mm chosen to match the freeform lenslet array in terms of input aperture diameter and effective focal length.

As depicted in Figure 6.4, the proposed lenslet array's thickness is approximately five times less than that of a typical plano-convex lens. This reduction results in a significant decrease in the optics' fill factor, which carries substantial significance for devices with stringent form factor requirements. For instance, a LiFi module integrated into a smartphone must adhere to stringent size and thickness limitations, typically within a few milimetres. Consequently, many commercially available optical components are incompatible with such compact modules.

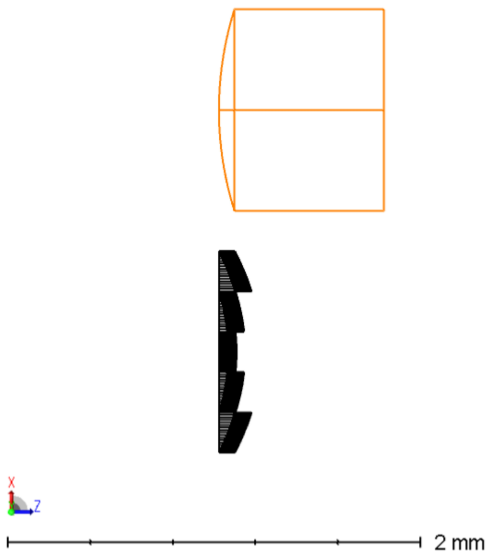

Figure 6.4: Illustration of a thickness comparison between a standard plano-convex lens and the lenslet array in yz-plane.

In Figure 6.5, as illustrated in the ray diagram, it is evident that the lenslet array effectively converges light at a distance of 2mm from the input aperture of the array.

The resulting target irradiance at the photodetector, generated by the lenslet array, is depicted in Figure 6.6. In this figure, it becomes apparent that the simulated irradiance distribution deviates significantly from the prescribed one. Qualitatively, it can be observed that multiple square irradiances produced by different lenslets are positioned at various focal lengths. Moreover, some of the irradiances exhibit notable astigmatism.

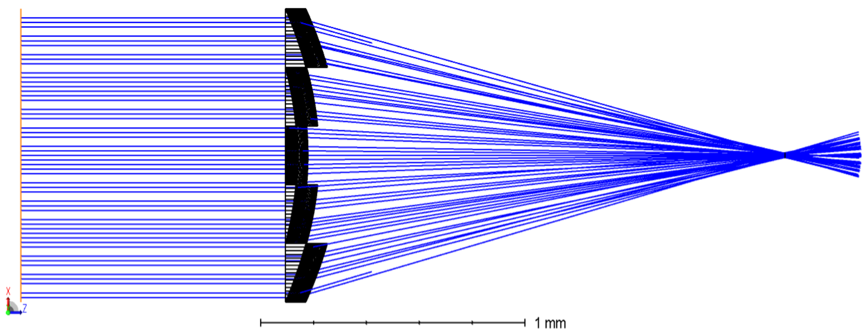

Figure 6.5: Ray diagram of the calculated lenslet array

.

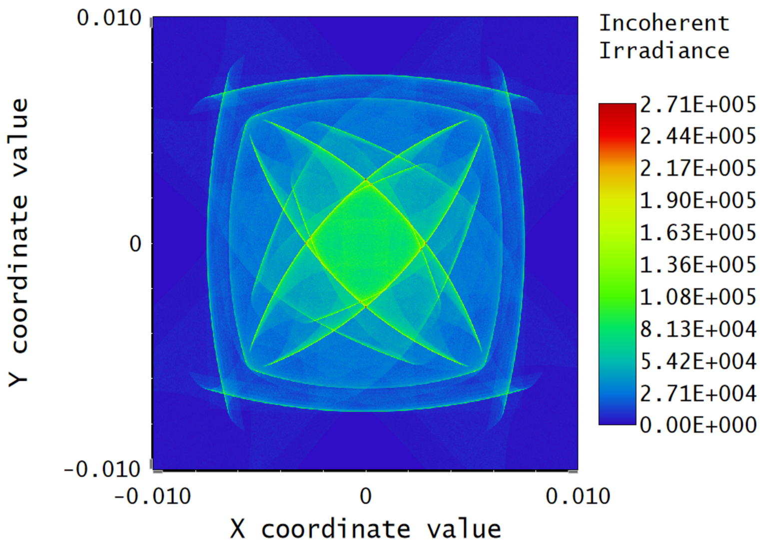

Figure 6.6: Irradiance at the photodetector surface. The x and y co-ordinates are given in mm and the irradiance in W/cm^2.

Let us delve into the origins of these aberrations. We will initiate our analysis by investigating the contribution from the central lenslet. Figure 6.7 displays the irradiance distribution generated by the central lenslet. It is evident that the lenslet focuses light into a slightly curved/aberrated square region with dimensions of $10 \times 10\,\mu\text{m}^2$, featuring nearly uniform intensity in the centre and hotspots at the corners. As anticipated, the resulting irradiance closely aligns with the prescribed irradiance (further optimization should be considered), thus validating the design process outlined in Section 6.3.

Figure 6.7 suggests that the outer lenslets of the array are likely to produce more stretched and aberrated irradiance contributions, as observed in Figure 6.6. To gain a deeper understanding of the sources of these aberrations, we perform a comparison between a single off-axis lenslet with an offset of $\Delta = -0.4\,\text{mm}$ from the array centre along the x-axis and the central lenslet in the ray diagram presented in Figure 6.8.

As evident in the diagram, the off-axis lenslet experiences a tangential focal shift due to the Petzval field curvature toward the lenslet aperture, resulting in beam defocusing. In this scenario, the images of objects are distributed across a curved surface where the tangential and sagittal surfaces converge [368]. Simultaneously, the sagittal focus remains unchanged, as depicted in Figure 6.9. The difference between the two focal

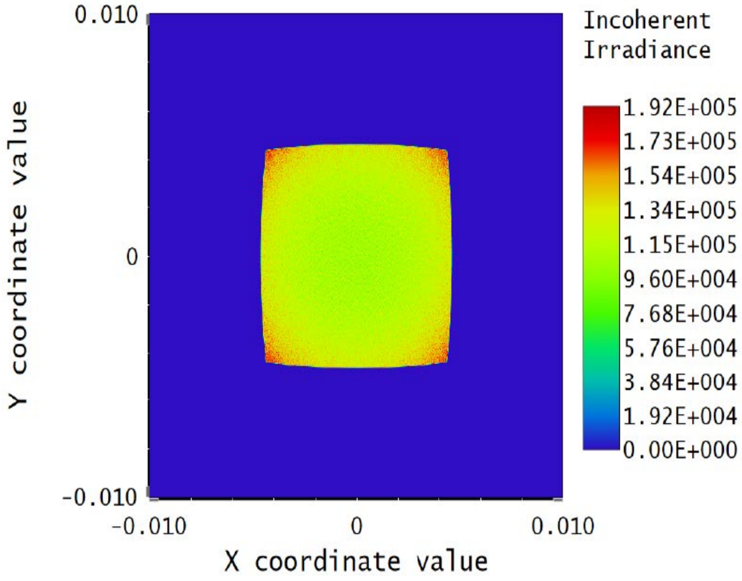

Figure 6.7: Irradiance at the photodetector surface produced by the central lenslet. The x and y co-ordinates are given in mm and the irradiance in W/cm^2.

points gives rise to the apparent astigmatism observed in Figure 6.6.

The Petzval field curvature presents a substantial challenge when designing flat, low f-number light-collecting freeform refractive elements. This challenge arises because the Petzval curvature is equal to the focal length of the array [368]. Hence, a smaller focal length of the concentrator results in a reduced Petzval curvature radius and more stretched wavefront at the periphery. One potential solution to mitigate this issue may involve the utilisation of another lenslet array with a negative focal length [369], designed to counteract the field curvature effects of the initial array.

As an alternative, the use of a meniscus lens [369] in combination with an aperture stop positioned in front of the array can be considered to correct the field curvature effect. However, it is important to note that this approach may not be ideal, as it could lead to an increased size of the optical system, thereby offsetting the advantages of the lenslet array in terms of thickness and form factor.

It is indeed possible to mitigate the defocusing effects caused by the Petzval curvature by individually adjusting the target distance for each lenslet. This adjustment can be made so that the lenslet's circle of least confusion aligns with the same distance as the central lenslet's focal length. However, the challenge persists in dealing

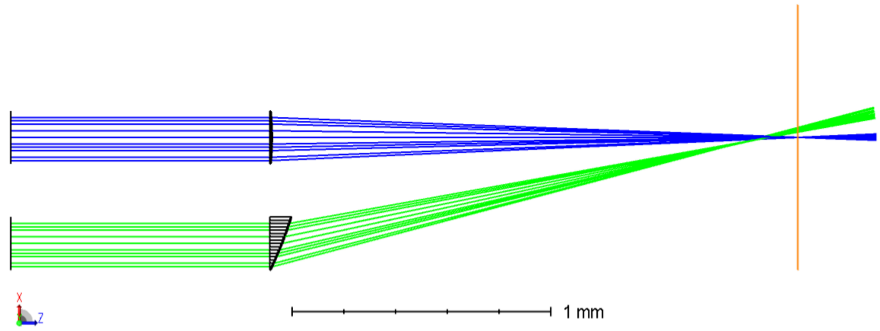

Figure 6.8: Ray diagram for the central and the edge lenslets - blue rays belonging to the on-axis central lenslet, and the green - off axis lenslet, xz projection.

with the increased separation between tangential and sagittal foci at larger angles with respect to the optical axis, resulting in astigmatism that reduces the efficiency of the lens with a low f-number. Consequently, a more comprehensive approach to developing a thin freeform correcting lenslet array is essential for achieving high-quality light concentration and imaging.

As emphasized in the preceding discussion, the method enables the design of a concentrating array of lenslets for receivers. However, it is crucial to acknowledge that the method is not immune to the constraints typically associated with imaging optics, which encompass a range of optical aberrations.

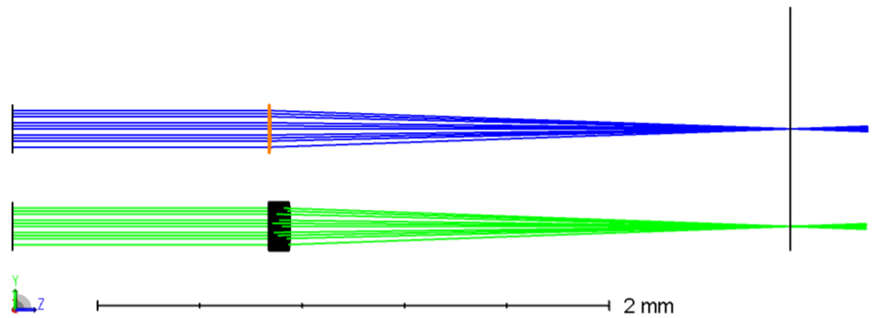

Figure 6.9: Ray diagram for the central and the edge lenslets - blue rays belonging to the on-axis central lenslet, and the green - off axis lenslet,yz projection.

Optical Concentration Performance of the Array

As expounded upon in the preceding section, the imaging quality of the optical element at the photodetector surface takes on a secondary role within the context of OWC and LiFi. Instead, the foremost criteria for evaluating the optical front-end of the receiver revolve around the optical concentration ratio and the receiver's FoV.

The optical concentration ratio can be determined by the division of the optical power received by the photodetector (P_{opt}) when using a concentrating optic by the power received without any such optic (P_{ref}) [280]:

$$C_{\text{opt}} = \frac{P_{\text{opt}}}{P_{\text{ref}}}. \tag{6.14}$$

The optical concentration ratio for the lenslet array is computed as $C_{\text{opt,array}} = 8796$. In contrast, the optical concentration for a plano-convex lens with identical dimensions is $C_{\text{opt,lens}} = 10000$. Consequently, it can be inferred that the freeform lenslet array demonstrates performance comparable to that of a traditional plano-convex lens in terms of optical concentration, all while maintaining a substantially slimmer profile.

Furthermore, it is important to acknowledge that the present lenslet array has the potential for further enhancement through optimization. Utilising a merit function and introducing minor adjustments to address the existing astigmatism, it is conceivable to further enhance the concentration performance of the array.

Comparison to a Single Lenslet

The chief advantage of a lenslet array, in contrast to a single lens, lies in its capacity to yield refractive optical elements specific to the scenario functionalities. Nonetheless, for the evaluation of a basic function such as light concentration, it is valuable to gauge the performance of the lenslet array against a single lens designed using the same methodology. This individual lens shares the same target irradiance and dimensions as those of the entire array.

Assuming an identical optical setup and incident optical power to those employed for the lenslet array, we employ the same lenslet methodology to design a single lens

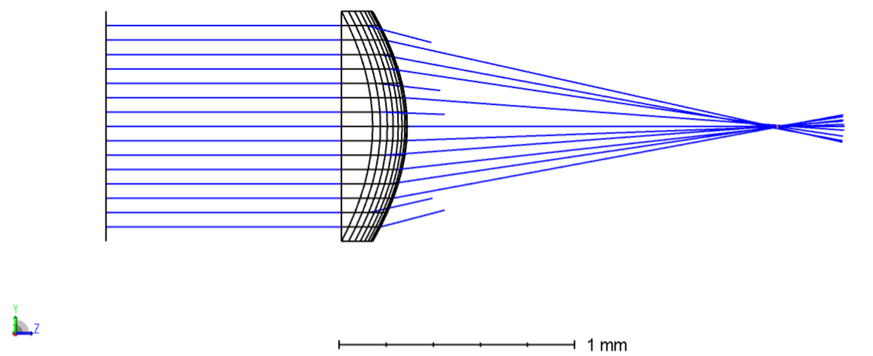

Figure 6.10: Ray diagram for a single freeform lens.

with a square area of $1 \times 1, \mathrm{mm}^2$. The ray diagram for this single freeform lens is presented in Figure 6.10. It is evident that the method faithfully reproduces a basic plano-convex lens in the context of a single lenslet.

As depicted in Figure 6.10, the concentration at the focal point of the single freeform methodology designed lens is notably inferior to that achieved by a lenslet array. Furthermore, in comparison to the lenslet array, the single freeform lens is designed with a maximum thickness of 279 μm at the centre, compared to array's 159 μm at the edges. In contrast, the lenslet array exhibits characteristics similar to those of a Fresnel lens. The compromised performance in terms of optical concentration is further evidenced by the irradiance distribution at the photodetector, as presented in Figure 6.11.

The optical concentration gain is calculated to be $C_{\text{opt,single}} = 5811.7$. This value is considerably lower than that of the lenslet array. Additionally, there is a notable presence of stray light outside the central circle in the case of the singly designed lens.

To understand the fundamental difference between the shape of a single freeform lens and an array of lenslets, it's essential to consider that the input and output domains are continuous. The integrability condition (6.11) requires that the mapping $\mathbf{v} = \mathbf{P}(\mathbf{u})$ and the surface S should be continuous, at least locally. In a model where no discontinuities are permitted, the most optimal shape mapping for focusing tends to resemble that of a plano-convex lens. This resemblance can be observed in the sagitta distribution of the freeform lens in Figure 6.12.

The abrupt edges of the freeform lens can contribute significantly to the presence of

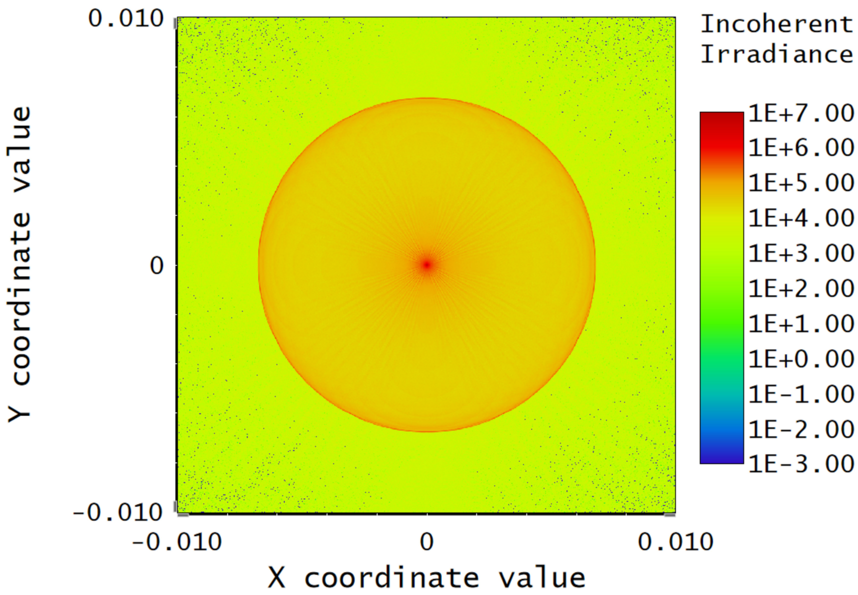

Figure 6.11: Irradiance at the photodetector surface for a single freeform lens. The x and y co-ordinates are given in mm and the irradiance in W/cm^2. We use log10 scale for better clarity.

stray light in Figure 6.11. This accounts for the substantially lower optical concentration ratio observed in the single freeform lens compared to the lenslet array. Although performance could potentially improve by calculating the freeform lens on a circular area instead of square, the resulting lens would still be over 75% thicker than the array.

Comparison to a Fresnel Lens

As previously mentioned, the freeform lenslet array closely resembles a Fresnel lens due to the presence of sharp discontinuities. When used for straightforward light concentration in the near-paraxial regime, the design behaves akin to a Fresnel-type lens. However, it's important to highlight that a lenslet array offers greater versatility as an optical element compared to a traditional Fresnel lens. It can be customized to fulfill various functionalities.

These functionalities are not limited to specific applications and can include, among other possibilities, MIMO communication. In MIMO systems, multiple beams carrying distinct information bits could be designed to be mapped to different photoactive areas of the receiver based on the incidence angle. Additionally such mapping could be used

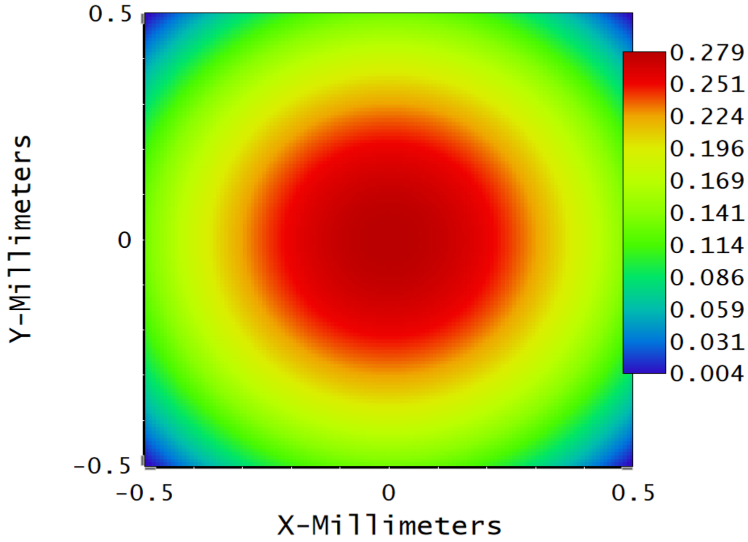

Figure 6.12: Sagitta distribution of the calculated freeform lens, the colourscale denotes the sagitta of the lens given in mm.

to reduce inter-symbol interference between different beams, improving overall communication performance. Furthermore, by accurately adjusting the refractive index of each individual lenslet, a wavelength-dependent mapping can be implemented. This capability can be particularly advantageous in communication links that utilise wavelength multiplexing, allowing for efficient management of different wavelengths and enhancing the versatility of the optical system.

Additionally, it's essential to highlight that, unlike a conventional Fresnel lens, a lenslet array may lack rotational symmetry. For instance, different regions of the array can have distinct mapping characteristics: one region may focus incident irradiance into a triangular shape, while another region may produce a square shape. This non-symmetrical behavior can lead to a diverse and versatile surface solution across various regions of the array.

Furthermore, the non-symmetrical characteristics of a lenslet array offer opportunities for tailoring the output irradiance to match the shape of a particular photodiode or a photodiode array. This customization can significantly improve the received optical power and, consequently, enhance the SNR.

6.5 10 Deg FoV Lenslet Array

We now present the design for a 10 deg FoV receiver freeform concentrator, which is illustrated in Figure 6.13, and was originally presented in [370]. The selected 10 deg FoV corresponds well to a scenario where access point located at the ceiling (approximately 3 m high) would provide a coverage of 1 m in diameter. The primary concept behind this design is the utilisation of a hemispherical lens as the Primary Optical Lenslet (POL). The POL is primarily responsible for generating the majority of the optical gain. Surrounding the perimeter of the POL, we distribute Secondary Optical Lenslets (SOL) that are smaller in size compared to the POL.

These SOLs essentially function as curved wedge prisms with a slightly convex shape, designed to enhance the focal strength of the rays focused onto the PD and into the POL. The SOLs significantly increase the FoV of the receiver by redirecting edge rays that would otherwise not be captured by the POL. Each individual lenslet is computed using the method described in Section 6.3, implemented in MATLAB, followed by optimization and ray-tracing analysis conducted in Zemax Optic Studio.

We have developed this design with a mobile use case scenario in mind, where the receiver is integrated into a device with strict form factor constraints. The device's maximum allowable height is limited to 3.5 mm, and its width is set at 8 mm. Each SOL features a slightly convex outer surface with the curvature pointing towards the centre of the optical axis, which coincides with the centre of the POL. As illustrated in Figure 6.14, we have included the sagitta distributions for three different SOLs.

The lenslet array comprises a total of 12 SOLs and 1 POL. Each SOL measures $2 \times 1.72\,\text{mm}^2$ in size, with a maximum height of 3.04 mm on the sides and 3.32 mm in the corners. The POL's dimensions are set at $3 \times 3\,\text{mm}^2$ with a height of 3.4 mm. For visual reference, the resulting array design is depicted in Figure 6.15.

The ray diagram for our design is presented in Figure 6.16. In this Figure, we consider an incidence angle of $\psi_\text{i} = 0$ deg, aligning it with the optical axis. The POL efficiently concentrates light at its focal plane, located at a distance of $f_\text{con} = 1.5\,\text{mm}$ from the exit aperture, as shown in the figure. The orange line in the diagram represents the receiver plane.

Comparing this design to a simple convex lens of same size, we observe that the point spread of the beam is considerably larger. This phenomenon can be attributed to the SOL, which have slightly different optical strengths than the POL. These differences contribute to a more defocused irradiance distribution in contrast to a simple convex lens. Additionally, our design results in a larger beam spot at the focal plane of the array in comparison to a convex lens.

It's worth noting that we also observe some losses due to internal reflections and stray light caused by discontinuities. These factors reduce the overall concentration efficiency of the array.

The receiver's target area measures $1 \times 1\,\mathrm{mm}^2$, and the half-acceptance angle, which we have set to be $5,\mathrm{deg}$, is defined as the angle at which the optical concentrated power at the receiver plane drops below 90% of the maximum optical concentration achieved at normal incidence. The full FoV is $10,\mathrm{deg}$.

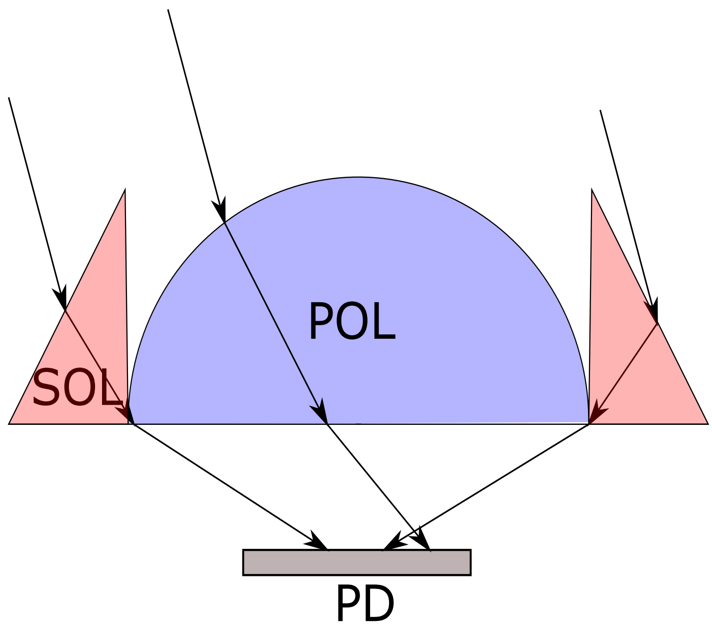

Figure 6.13: Diagram of side-view of freeform lenslet array design for limited size factor imaging concentration. POL denotes primary optical lenslet, while SOL denotes secondary optical lenslet. PD denotes photodetector. Figure from [370].

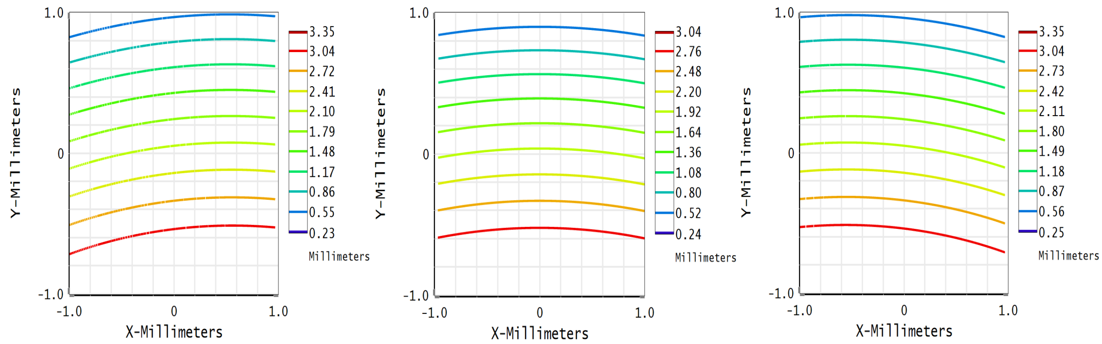

Figure 6.14: The sag distribution of a single lenslet array side SOLs.

For this design, we've selected polycarbonate as the material, with a refractive index of $n_{\text{con}} = 1.5855$ [371]. This choice of material enhances the optical concentration achieved by the receiver.

The increased spot size enhances the receiver's tolerance to misalignment while the increased optical surface of SOLs compensates for the lower concentration ratio due to the apparent defocusing.

Optical Test Setup

For the incident beam, we consider a uniform irradiance distribution with optical power incident at the input aperture of the array at 1.2×10^{-5} W. We assume the use of a VCSEL source located at a distance of $z = 1$ m, emitting an optical power of $P_{\text{opt}} = 10$ mW. In our ray tracing analysis, we employ 5×10^{7} rays. We do not account for any background or additional illumination in our simulations.

Parameters of Imaging and Non-Imaging Optical Elements

For the purpose of comparing our design to imaging and non-imaging optics, we conducted simulations using Zemax Optic Studio, focusing on a convex lens and a CPC.

In the case of the convex lens, we set the thickness to the maximum height of the lenslet array, which is 3.4 mm, and the diameter to 8 mm. The receiver plane is positioned 1.5 mm away from the exit aperture of the lens. This configuration places the receiver before the lens, in what we refer to as the defocused region.

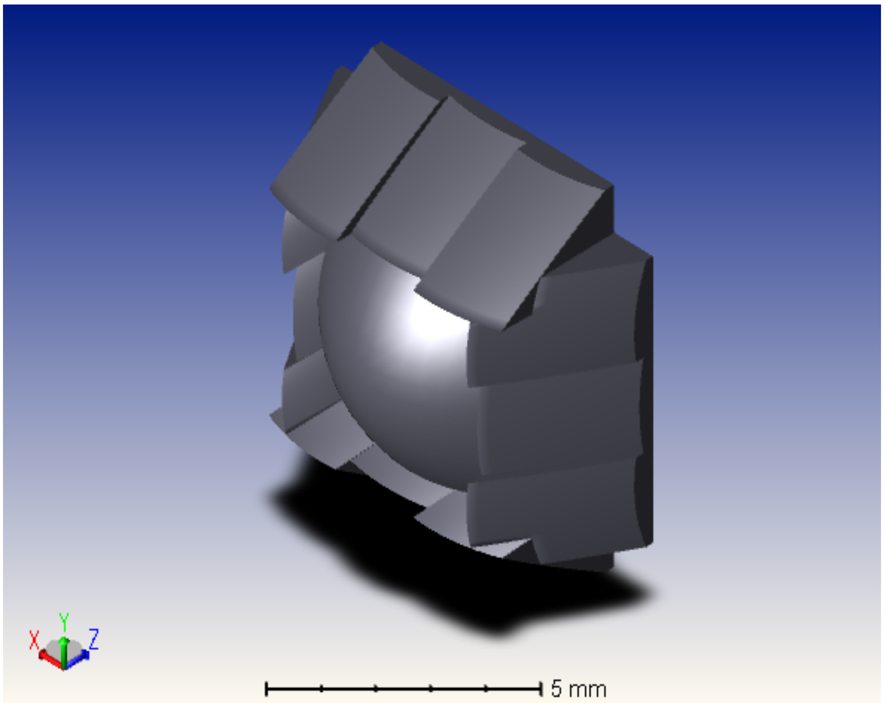

Figure 6.15: Freeform lenslet array in isotropic projection. Figure from [370].

For the CPC, we specified the key parameters as follows: the height, H_{CPC}, was set to 4.9 mm (resulting from 3.4 mm + 1.5 mm), and the receiver plane is located at the exit aperture of the CPC. To achieve a 10 deg FoV, we set the half-acceptance angle of the CPC to 5 deg. Additionally, the exit aperture of the CPC was designed to match the area of $1 \times 1\,\mathrm{mm}^2$.

Irradiance Distributions

The ray diagram of the resultant lenslet array is shown in Figure 6.16. The irradiance distributions at the receiver plane for the optical elements under examination are depicted in Figure 6.17. The left column plots show irradiance values for normal incidence $\psi_{\mathrm{i}} = 0$, while the right column plots display irradiance values at the FoV limit. A logarithmic scale is applied.

In Figures 6.17a and 6.17b, we observe the non-uniform irradiance pattern characteristic of the CPC, featuring substantial variations in hot and cold areas, representing areas of low and high irradiance, respectively. Moreover, we note a significant change in the distribution's shape when non-normal incidence is taken into account. While the non-uniformity in CPC irradiance may not have a pronounced impact on SNR for a single photodiode, we will demonstrate that it plays a substantial role when considering an array of photodiodes.

Figures 6.17c and 6.17d depict a distinctly different behavior. In this case, the freeform lenslet array concentrator generates a beam with a more uniform distribution, resulting in a defocused spot, as anticipated in the ray diagram shown in Figure 6.16. This result matches with the expecation of the prescribed target irradiance at the receiver using lenslet array design methodology. While the concentrator irradiance was prescribed to a single focused spot, a more complicated target irradiance could be set, where different incident beams could be concentrated to different PDs in the array. Such functionality of the concentrating optics could benefit a system utilising GSSK as a transmission protocol by providing another way of improving distinguishability between beams in the link and enhacing the spectral efficiency.

A similar irradiance distribution is observed in the case of the defocused convex

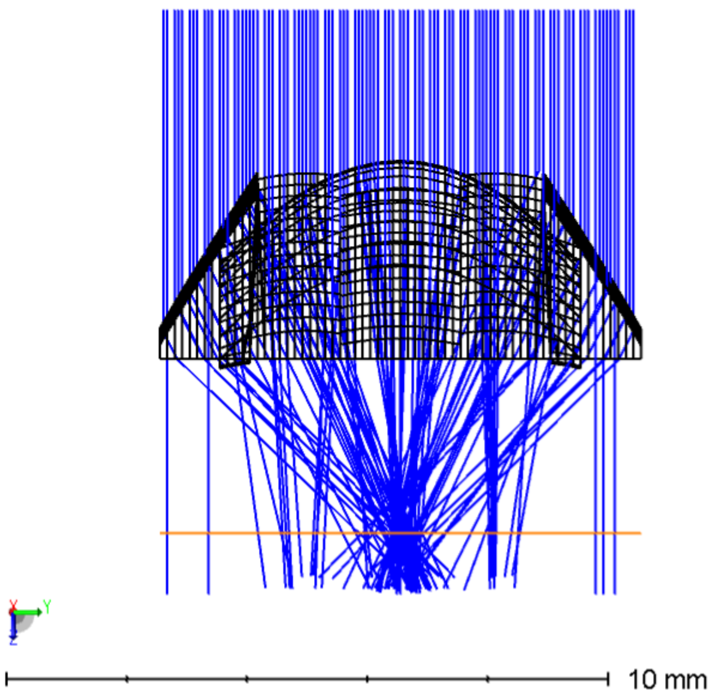

Figure 6.16: Ray diagram of the lenslet array. Figure from [370].

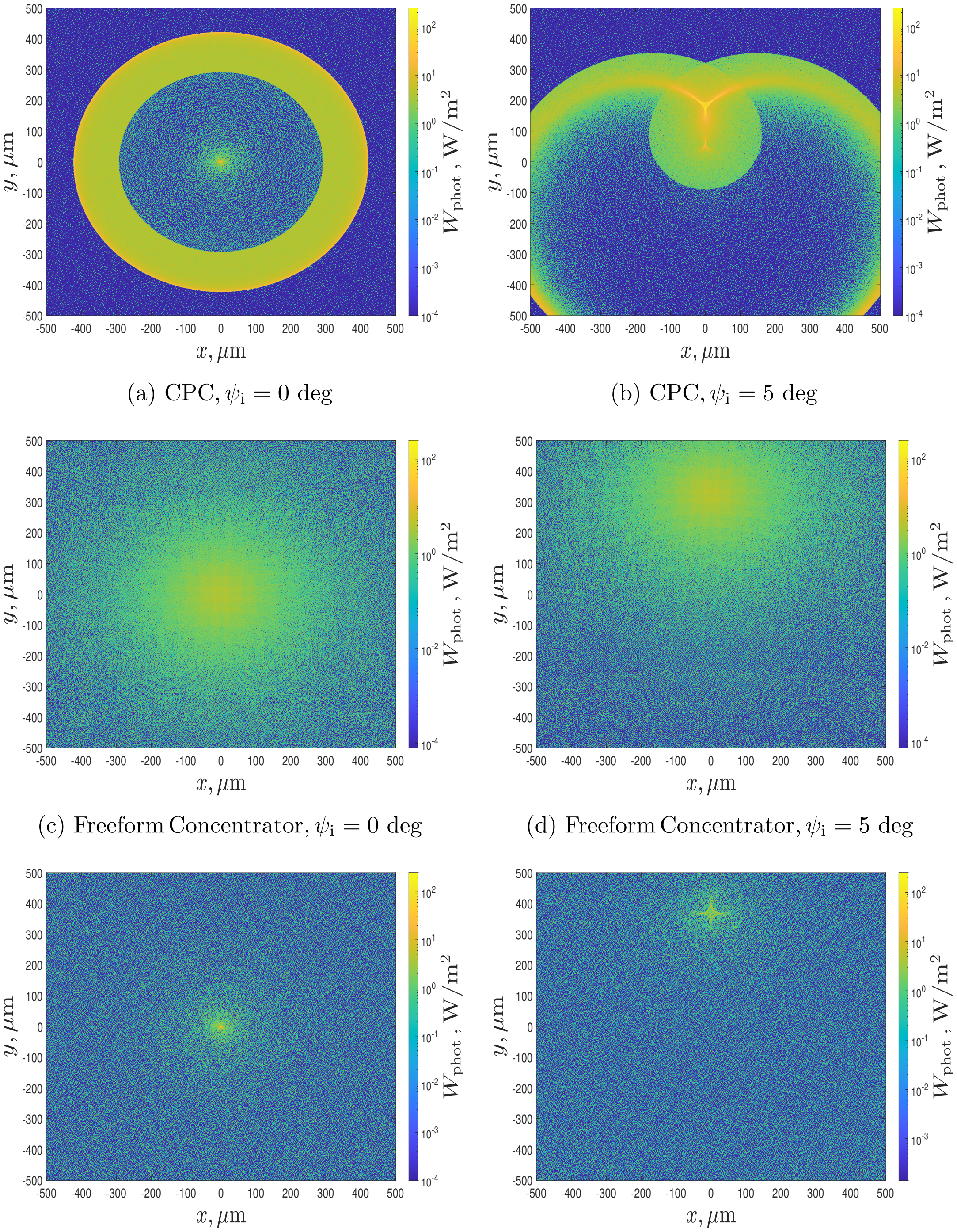

(a) CPC, $\psi_{\mathrm{i}} = 0$ deg

(b) CPC, $\psi_{\mathrm{i}} = 5$ deg

(c) Freeform Concentrator, $\psi_{\mathrm{i}} = 0$ deg

(d) Freeform Concentrator, $\psi_{\mathrm{i}} = 5$ deg

(e) Convex Lens $\psi = 0$ deg

(f) Convex Lens $\psi = 5$ deg

Figure 6.17: Irradiance distributions of various optical elements at the receiver plane. Figure from [370].

lens; however, the spot size is considerably smaller. This observation suggests that in the case of the convex lens, the receiver distance is close to the focal point of the lens. Consequently, both the freeform concentrator and the convex lens have similar focal lengths and, correspondingly, similar f-numbers when the same lens height/thickness is maintained. Nevertheless, the irradiance distribution already hints at an enhanced optical concentration in the freeform lenslet array concentrator. However, in comparison to the CPC, the concentrated optical power is smaller.

Radiance Distributions

Often overlooked, but equally crucial, is the radiance distribution in the angular space at the receiver, which describes the incidence angles ψ_{r} of refracted rays at the receiver. It is well-established that the relative responsivity of the photodiode $R_{\mathrm{PD,rel}}$ can be approximated using the cosine law as follows [372]:

$$R_{\mathrm{PD,rel}} = \frac{R_{\mathrm{PD}}(\psi_{\mathrm{r}} = \psi)}{R_{\mathrm{PD}}(\psi_{\mathrm{r}} = 0)} = \cos\psi. \tag{6.15}$$

The cosine law dependency primarily arises from polarization-sensitive Fresnel reflections occurring at the interface of the photodiode surface with air or other materials [373].

The radiance distributions at the receiver plane for the optical elements under examination are presented in Figure 6.18. The left column plots display radiance values for normal incidence $\psi_{\mathrm{i}} = 0$ deg, while the right column plots show radiance values at the FoV limit. A logarithmic scale is applied. In Figures 6.18a and 6.18b, we observe a non-uniform radiance pattern, which is a characteristic feature of the CPC. Additionally, both figures exhibit a small hotspot at the centre, indicating normal incidence at the receiver. Notably, a substantial number of incident rays arrive at the receiver plane from highly oblique angles. Consequently, according to (6.15), a significant portion of incident photons is expected to be reflected at the photodiode semiconductor-polycarbonate interface.

Compared to the CPC case, the freeform lenslet array concentrator in Figures

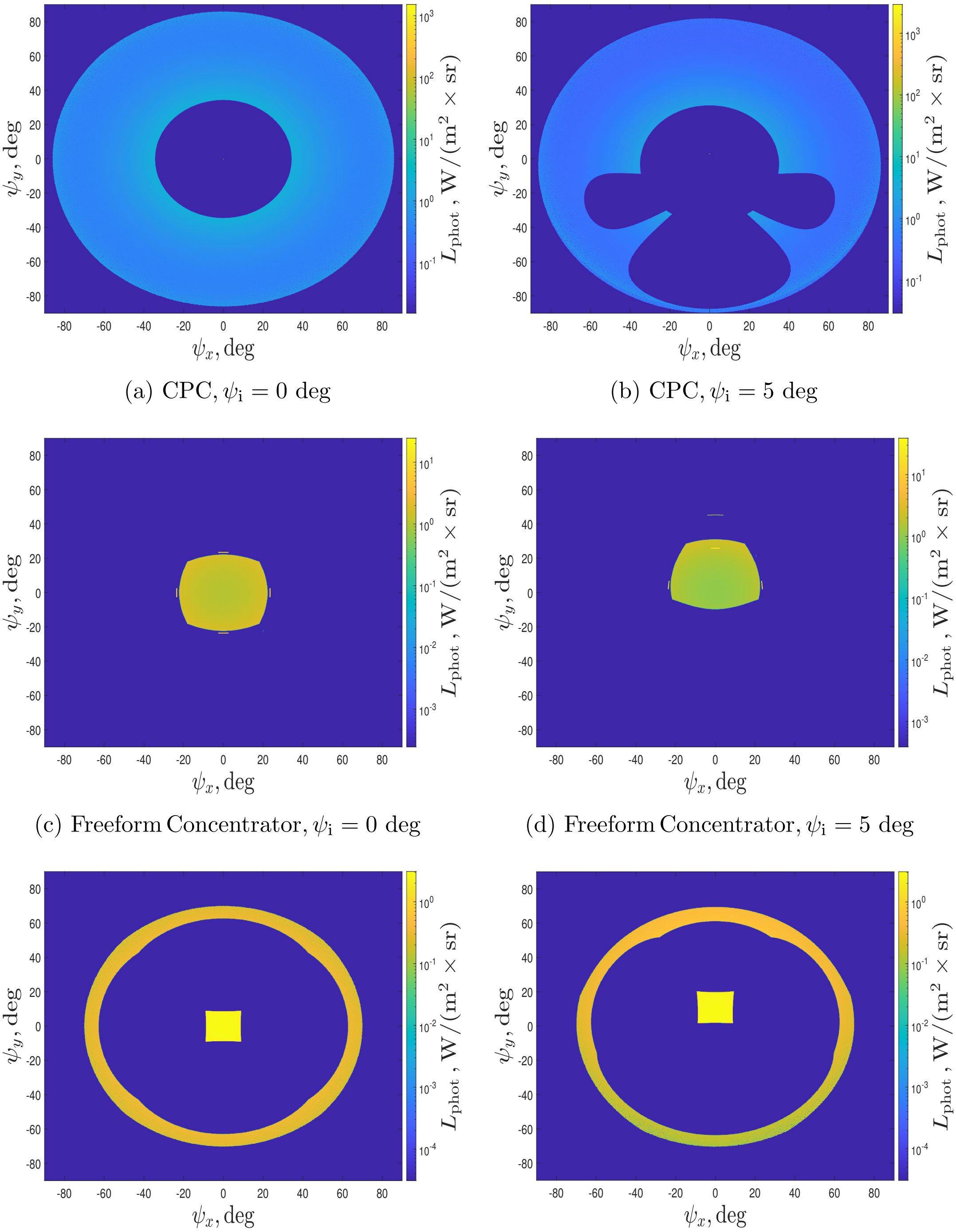

(a) CPC, $\psi_{\mathrm{i}} = 0$ deg

(b) CPC, $\psi_{\mathrm{i}} = 5$ deg

(c) Freeform Concentrator, $\psi_{\mathrm{i}} = 0$ deg

(d) Freeform Concentrator, $\psi_{\mathrm{i}} = 5$ deg

(e) Convex Lens $\psi_{\mathrm{i}} = 0$ deg

(f) Convex Lens $\psi_{\mathrm{i}} = 5$ deg

Figure 6.18: Radiance distributions of various optical elements at the receiver plane.

6.18c and 6.18d refracts rays toward the photodetector at much smaller angles. The majority of radiance is concentrated in the area defined by $\psi_x \in \{-20, 20\}$ deg and $\psi_y \in \{-20, 20\}$ deg, with some stray light artifacts observed outside this region.

In the case of the defocused convex lens, we observe an even more confined area of radiance in the centre of Figures 6.18e and 6.18f. However, there is also a distinct disc of radiance emanating from high incidence angles. This disc corresponds to rays refracted from the edge of the lens, exhibiting significant spherical aberration. To mitigate this effect, an aperture stop could be introduced for the convex lens, although this would result in some sacrifice of the concentrated optical power. Interestingly, while the freeform concentrator does exhibit stray light and back reflections, we do not observe a similar circular radiance distribution there.

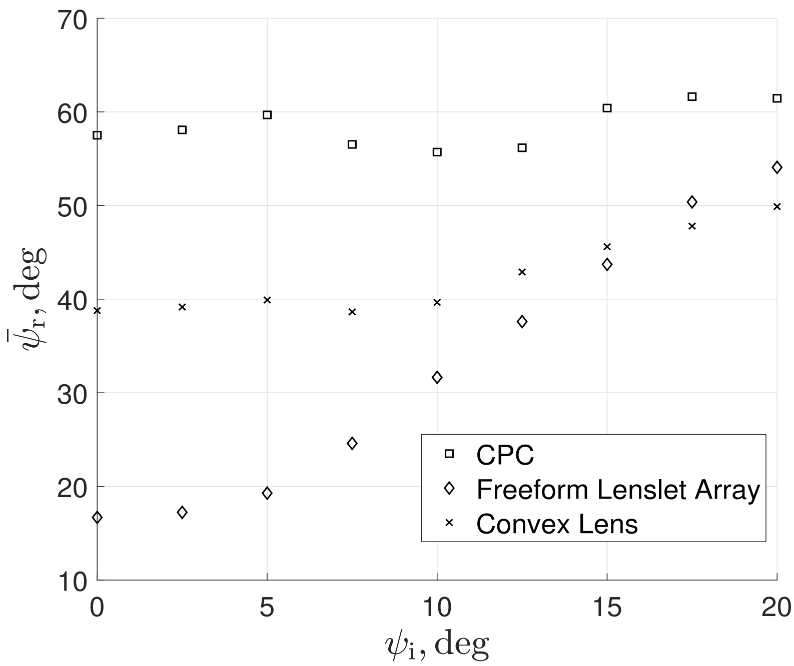

Figure 6.19: Mean refracted incidence angle *vs.* incidence angle.

To assess the influence of radiance on the relative responsivity of the photodiode, it is necessary to ascertain the mean incidence angle of the refracted rays at the receiver plane based on the radiance distribution. The mean refracted incidence angle can be calculated as follows:

$$\bar{\psi}_{\mathrm{r}} = \frac{\int_{-\pi/2}^{\pi/2} \int_{-\pi/2}^{\pi/2} L_{\mathrm{phot}}(\psi_{\mathrm{r}}) \psi_{\mathrm{r}} d\psi_x d\psi_y}{\int_{-\pi/2}^{\pi/2} \int_{-\pi/2}^{\pi/2} L_{\mathrm{phot}}(\psi_{\mathrm{r}}) d\psi_x d\psi_y}, \tag{6.16}$$

where $\psi_{\mathrm{r}} = \sqrt{\psi_x^2 + \psi_y^2}$. The mean incidence angle of the refracted rays as a function of the incidence angle at the input aperture of the optics for all three concentrating optics is illustrated in Figure 6.19.

As can be seen from it, $\bar{\psi}_{\mathrm{r}}$ is highest for the CPC, while for the freeform lenslet array, it is the lowest. The results for the convex lens fall in between, primarily due to refraction at the lens edge.

By inserting the calculated $\bar{\psi}_{\mathrm{r}}$ into (6.15), we can determine the mean relative sensitivity of the photodiode. Figure 6.20 illustrates the dependence of mean relative sensitivity on ψ_{i}.

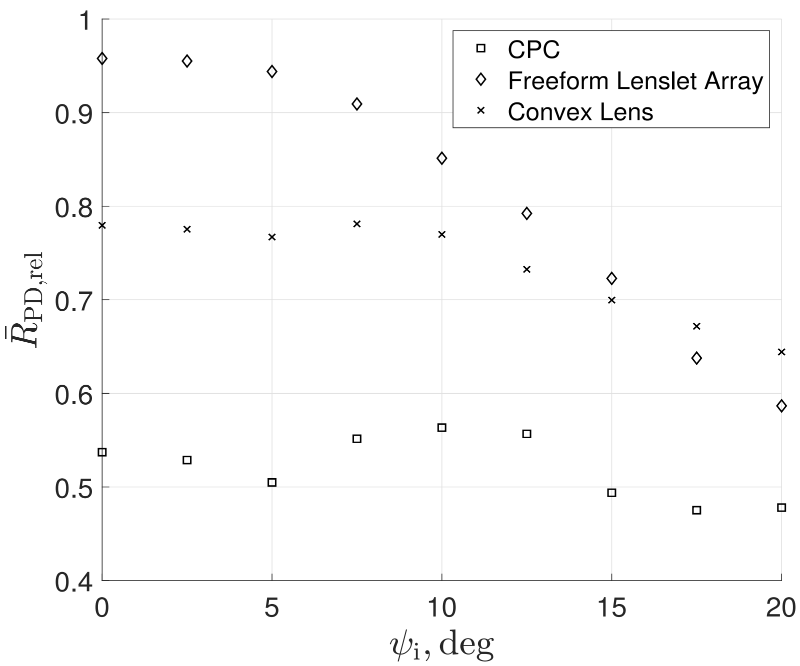

Figure 6.20: Mean relative photodiode responsivity *vs.* incidence angle.

As evident from the figure, the CPC exhibits the lowest mean relative responsivity, primarily attributed to the very high mean incident refracted angle of the rays impacting the photodiode surface. In fact, the efficiency is only approximately $50 - 55\%$ within the FoV. On the other hand, the freeform lenslet array maintains a stable efficiency of around 95%, while the convex lens achieves an approximate $\bar{R}_{\mathrm{PD,rel}}$ of 78%.

From this, we can conclude that there is a significant loss of optical power due to the Fresnel reflections at the CPC-photodiode interface, which can amount to nearly 50% if not considered in the optical design. To mitigate these reflections and, consequently, reduce the losses, the use of index-matching materials is necessary. However, this approach increases the complexity, as it requires precise alignment of a small CPC with a photodiode, along with the proper insertion of the index-matching material at their interface. This task becomes even more challenging when dealing with sub-millimetre diameter photodiodes where alignment and installment challenges are apparent.

This observation highlights two significant practical advantages of the freeform lenslet array over the CPC: there is no need for direct contact between the lenslet array and the photodiode, and there is no requirement for index-matching materials, to mitigate the loss from Fresnel reflections.

Gain vs Incidence Angle

In addition to the FoV, optical concentration gain is a critical parameter for receiver optical elements in OWC, VLC, and LiFi. To compare the gain of the three receiver optical elements, we utilise expression (6.14).

The dependency of optical concentration gain on the incidence angle (not corrected for the mean incidence angle) is illustrated in Figure 6.21.

As anticipated from the irradiance results, the CPC outperforms both the freeform lenslet array and the convex lens by a substantial margin. The gains within the FoV roughly follow a ratio of 2. This observation demonstrates that, although inferior to the CPC, the freeform lenslet array surpasses a basic convex lens in terms of optical concentration when the same size and FoV are taken into account.

However, when we incorporate the results of mean relative responsivity into the calculation of optical concentration gain, the performance gap between the CPC and the freeform lenslet array noticeably diminishes, as depicted in Figure 6.22.

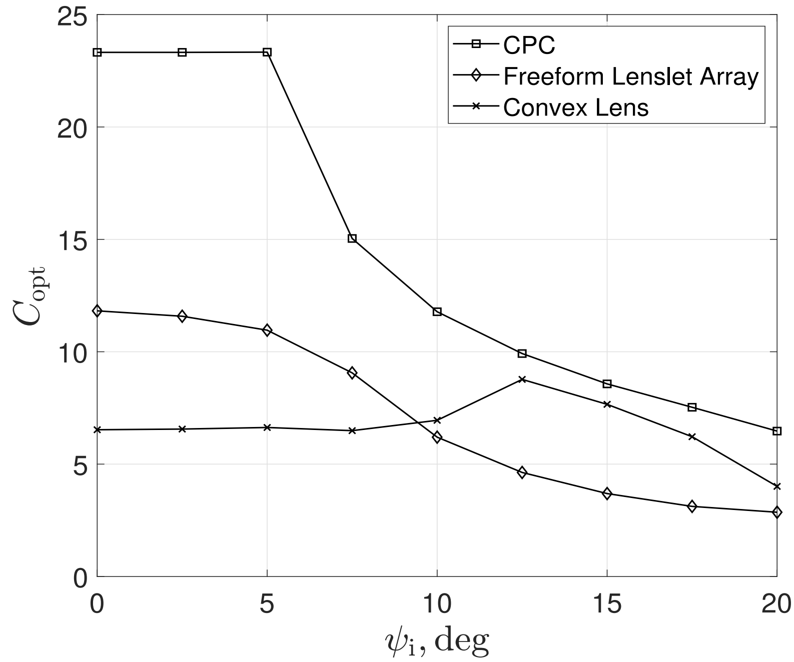

Figure 6.21: Gain comparison between different receiver optics (not corrected for $\bar{\psi}_{\mathrm{r}}$) [370].

As shown in the figure, the optical concentration gain of the CPC significantly decreases due to the substantial loss from Fresnel reflections, whereas the performance of the freeform array remains relatively consistent. The relative optical concentration gain of the CPC, compared to the freeform lenslet array, has reduced from 1.97 to just 1.11. Conversely, the gain of the freeform lenslet array compared to the defocused convex lens has slightly increased from 1.81 to 2.22.

While the performance of the CPC can be significantly enhanced through the use of index-matching materials, the complexity of the design makes such an approach challenging to implement in real-life, limited form-factor devices.

Here, the advantage of the freeform lenslet array becomes evident. It offers a simpler design that can be more easily implemented providing a comparable optical concentration gain to a CPC photodiode optical system, and outperforming a convex lens.

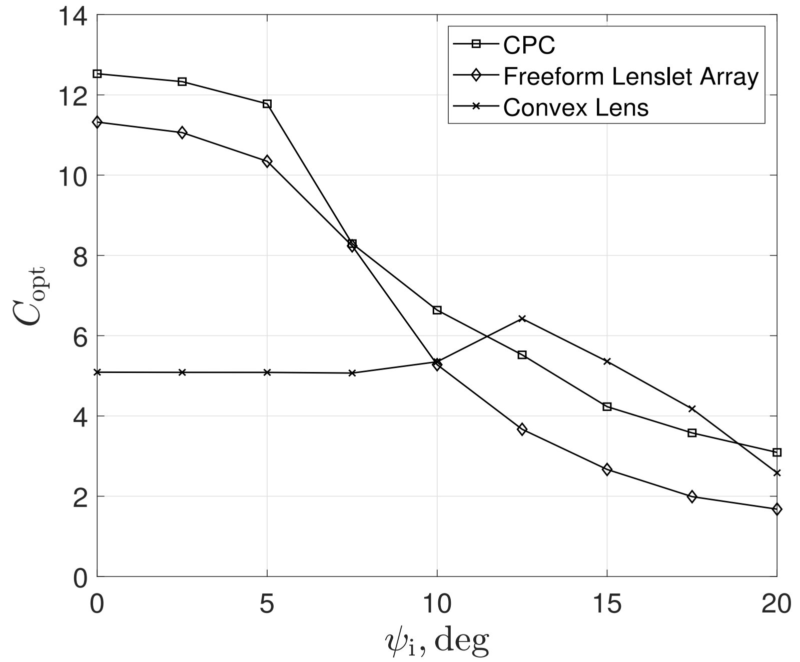

Figure 6.22: Gain comparison between different receiver optics (corrected for $\bar{\psi}_{\rm r}$.)

6.6 Performance of Receiver Optical Elements in Photodiode Arrays

We will now expand our analysis to include photodiode arrays. The electrical circuit diagram for the PD array is given in [374]. Specifically, we will consider $M_{\rm PD} \times M_{\rm PD}$ photodiode arrays with various photodiode sizes. For all these arrays, we will keep the geometrical fill factor of the photodiode array, denoted as FF, fixed and defined as [155]:

$$\mathrm{FF} = \frac{A_{\rm array}}{A_t} = \frac{M_{\rm PD}^2 A_{\rm PD}}{A_t}, \tag{6.17}$$

here, $A_{\rm Array}$ represents the total photoactive area of the entire array, $A_{\rm PD}$ stands for the photoactive area of a single photodiode, and $A_{\rm t}$ denotes the receiver target area where the photodiode array is integrated and light is focused. For our analysis, we maintain a fixed fill factor of FF $= 0.5$.

An example of arrays with different photodiode sizes ($d_{\rm PD} = 250\,\mu$m and $d_{\rm PD} = 10\,\mu$m) but the same FF is superimposed on the irradiance distribution generated by a freeform lenslet array, as shown in Figure 6.23.

The photocurrent produced by an array of $M_{\mathrm{PD}} \times M_{\mathrm{PD}}$ photodiodes can be expressed as per [146]:

$$I_{\mathrm{Array}} = \bar{\alpha}_{mk} M_{\mathrm{PD}} P_{\mathrm{opt}} R_{\mathrm{PD}}, \tag{6.18}$$

here, R_{PD} denotes the photodiode's responsivity, and $\bar{\alpha}_{mk}$ represents the mean fraction of optical power received by a photodiode in the array, which can be calculated using incident irradiance W_{phot} on the array as follows:

$$\bar{\alpha}_{mk} = \frac{1}{M_{\mathrm{PD}}^2} \sum_m \sum_k \int_{A_{\mathrm{PD}_{mk}}} W_{\mathrm{phot}}(x, y) dx dy. \tag{6.19}$$

In our simulations, we assume that the photodiodes have a responsivity of $R_{\mathrm{PD}} = 52\,\mathrm{A/W}$ at $\lambda = 850\,\mathrm{nm}$, which aligns with the specifications of the Hamamtsu SI2023-02 Si APD [375]. To simplify our modeling, we assume that the responsivity is independent of photodiode size and remains constant. Additionally, in our simulations, we disregard reflection losses.

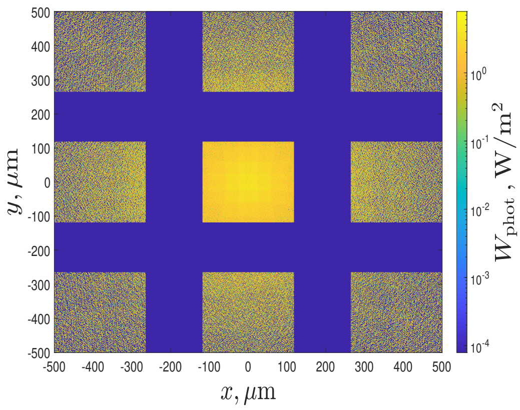

(a)

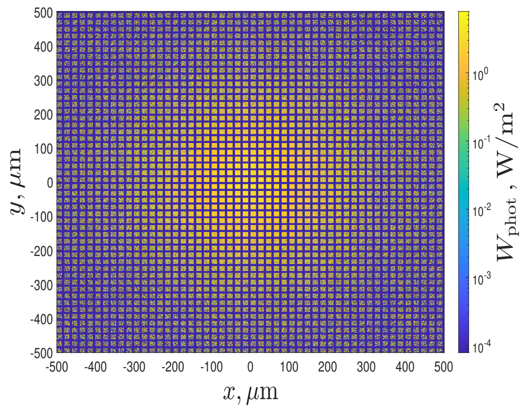

(b)

Figure 6.23: Irradiance distribution superimposed with the PD array at the receiver plane for (a) $d_{\mathrm{PD}} = 250\,\mu$m and (b) $d_{\mathrm{PD}} = 10\,\mu$m sized photodiodes.

Photocurrent Dependency on Incidence Angle in the Photodiode Array

Figure 6.24 illustrates the normalized photocurrent generated by the photodiode array, which depends on the incidence angle components ψ_x and ψ_y at the input aperture of the concentrating optics.

In Figure 6.24, we observe a dependency of the array photocurrent on the incidence angle within the FoV of the receiver. Notably, for the CPC, when compared to Figure 6.21, the optical concentration gain significantly decreases within the FoV. In both cases of a large photodiode array ($d_{\mathrm{PD}} = 250\,\mu\mathrm{m}$) and a small photodiode array ($d_{\mathrm{PD}} = 10\,\mu\mathrm{m}$), the FoV for the CPC has been reduced by approximately 50%.

We observe similar alterations in optical concentration for the freeform lenslet array concentrator and the defocused convex lens. However, in both cases, the effect is significantly less pronounced compared to the CPC, and it diminishes further with the decreasing size of the photodiode.

Furthermore, we notice that for large photodiode arrays relative to the irradiance pattern feature size, the effect is anisotropic, with the optical concentration decreasing more rapidly in certain incidence angle directions. This observation demonstrates that optical concentration depends not only on the incident angle but also on the direction of the incident light. However, it's worth noting that this anisotropic effect diminishes for smaller photodiodes.

The origin of this anisotropy can be intuitively understood by analysing Figure 6.23. When the photodiode size is relatively large compared to the target area and irradiance distribution feature sizes, as shown in Figure 6.23a, the amount of incident flux on the photoactive area can significantly vary depending on the incident angle. For instance, when the incident angle components are $\psi_x = \pm 3$ deg and $\psi_y = \pm 3$ deg, the centre spot will be offset towards the centre of the crosses outside the photoactive area. In such cases, the photocurrent reduces significantly more than when compared to scenarios where $\psi_x = \pm 4.24$ deg and $\psi_y = \pm 0$ deg, or $\psi_x = \pm 0$ deg and $\psi_y = \pm 4.24$ deg, where the spot is simply offset towards a different photoactive area.

In contrast, as shown in Figure 6.23b, regardless of the beam offset, there will always be photodiodes to capture the shifted beam as long as it remains within the target area.

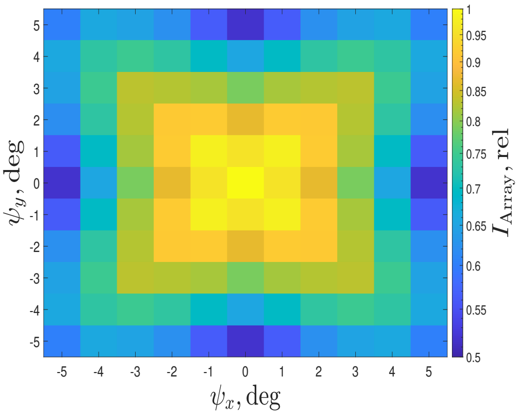

(a) CPC, $d_{\text{PD}} = 250\,\mu$m

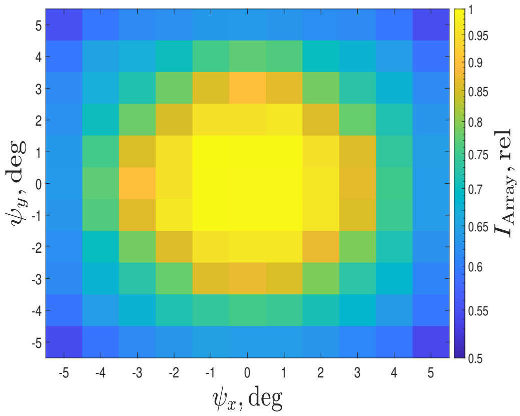

(b) CPC, $d_{\text{PD}} = 10\,\mu$m

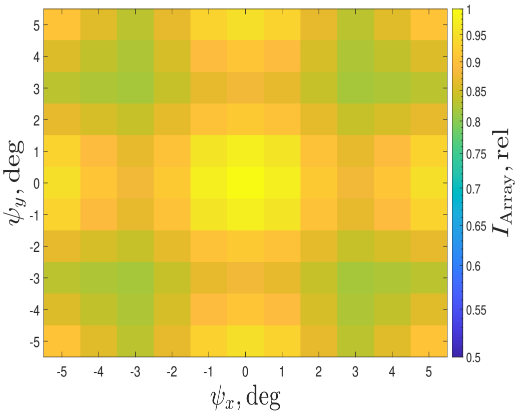

(c) Freeform Concentrator, $d_{\text{PD}} = 250\,\mu$m

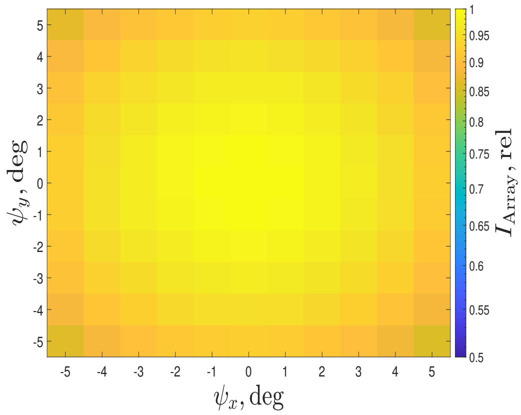

(d) Freeform Concentrator, $d_{\text{PD}} = 10\,\mu$m

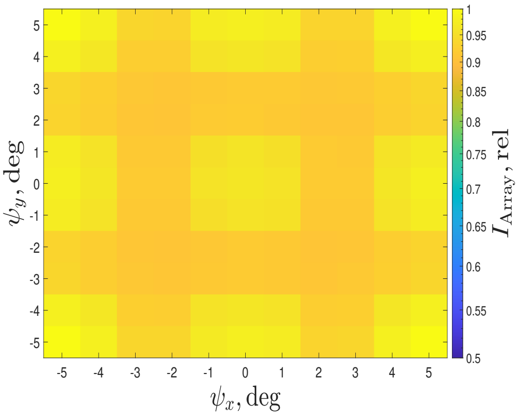

(e) Convex Lens $d_{\text{PD}} = 250\,\mu$m

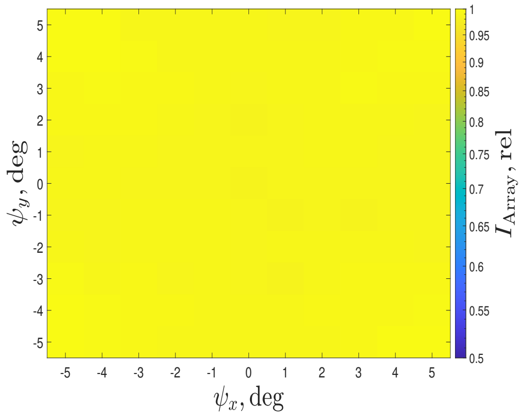

(f) Convex Lens $d_{\text{PD}} = 10\,\mu$m

Figure 6.24: Normalised photocurrent dependence on incidence angle components ψ_{x} and ψ_{x} generated by a PD array for different concentrating optics and two different photodiode sizes.

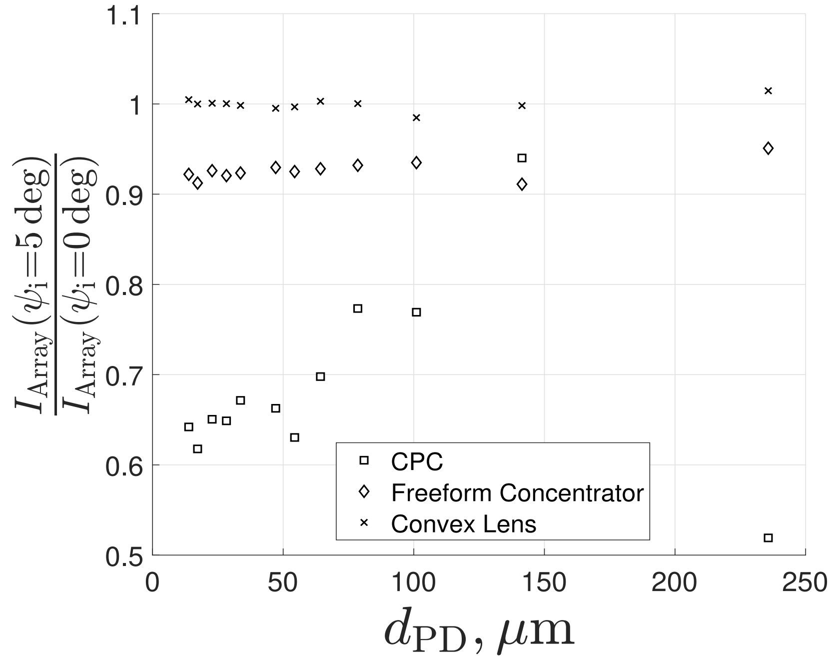

Figure 6.25: Relative photocurrent at FoV compared to normal incidence for different d_{PD}.

To further illustrate the effect of FoV shrinkage in the arrays, depending on the size of photodiodes, we plot the relative photocurrent generated at a $\psi_{\text{i}} = 5$ deg incidence angle versus normal incidence for various photodiode sizes, as depicted in Figure 6.25.

Figure 6.25 shows that the relative photocurrent remains stable within the FoV for the freeform lenslet array concentrator and the convex lens, with only slight deviations. This indicates that the FoV remains stable as determined by the design constraints in these cases.

In contrast, for the CPC, there is a consistent reduction in FoV observed across a wide range of photodiode sizes in the array. The results tend to cluster between 0.6 and 0.7 when photodiode sizes are $d_{\text{PD}} < 75\,\mu$m. This highlights the significance of maintaining uniform irradiance distribution when arrays with FF < 1 are used.

We observe a single outlier point at $d_{\text{PD}} = 148\,\mu$m for the CPC, where it might seem that the optical concentration remains stable within the FoV. However, Figure 6.26 demonstrates that this is not the case. In fact, the photocurrent generated at a

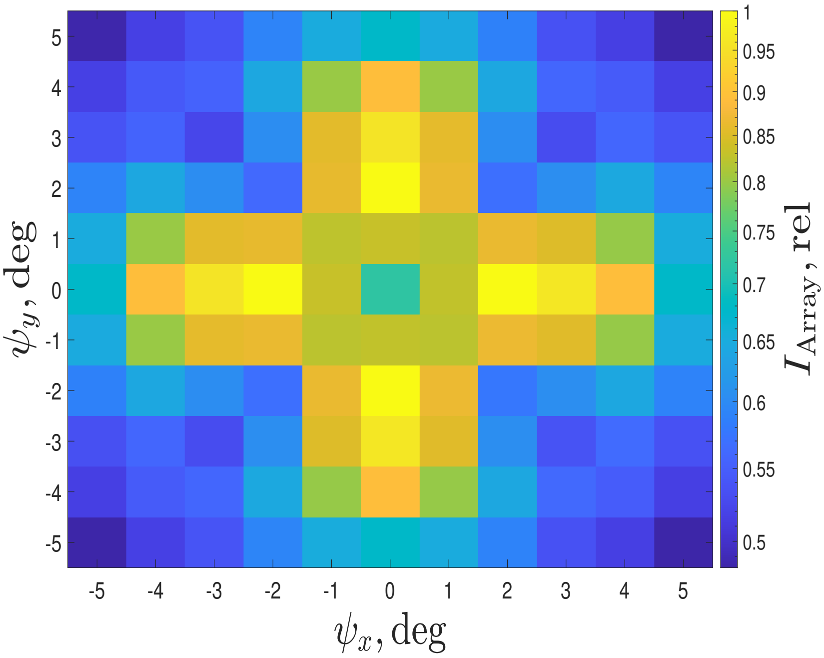

Figure 6.26: Normalised photocurrent dependence on incidence angle components ψ_{x} and ψ_{x} for the CPC outlier measurement.

normal incidence is considerably smaller (by about 25%) than that generated at more oblique angles. Furthermore, there is a strong anisotropy in the incident beam direction dependency.

This behavior illustrates how the non-uniformity of the CPC irradiance distribution significantly affects the performance of optical concentration. Additionally, we notice that, depending on the photodiode size, the photocurrent for a normal incidence can be substantially smaller than for oblique incidence. However, as the photodiodes in the array become smaller and the angular dependency becomes more isotropic, the relative photocurrent for the CPC clusters within the interval of 0.6 to 0.7.

Figure 6.27 provides additional insight into how the effect of non-uniformity contributes to this particular outlier case and its impact on optical concentration. By comparing Figure 6.27b to Figure 6.27a, it becomes evident that at oblique incidences, the photodiode array captures more light than at normal incidences, primarily due to the distribution of irradiance over the superimposed array.

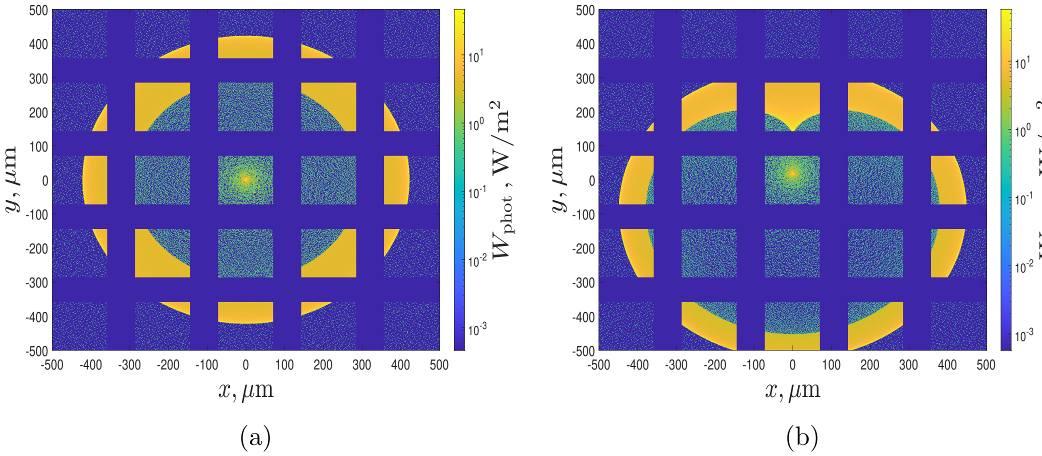

Figure 6.27: Irradiance distribution superimposed with the CPC outlier measurement PD array at the receiver plane for (a) normal incidence and (b) $\psi_{\mathrm{i}} = 5$ deg.

While we have focused on the CPC for non-imaging optics, it's reasonable to anticipate a similar behavior for any non-uniform irradiance-generating optics, which are likely to experience similar limitations. It's important to note that this analysis does not include the impact of the mean refracted incidence angle, as discussed in Section 6.5, which could further influence the total photocurrent generated by the array if index matching materials are not incorporated into the optical design.

When designing an optical concentrator or estimating a link channel budget based on the chosen optical front-end elements, it is essential to take into account the impact of non-uniformity in irradiance and radiance of refracted rays incident at the array. With imaging optics and the presented freeform lenslet array, which offer a more uniform beam distribution, these considerations are less stringent. However, when dealing with non-imaging optics, like the CPC, which create non-uniform irradiance, one must exercise caution in addressing the discussed effects.

Photocurrent Dependency on the Photodiode Size in the Array

Up to this point, we have discussed the effects of decreasing photodiode array size in the context of the relative photocurrent's performance at normal incidence and at the FoV limit. However, it is equally important to determine how the photodiode size affects the photocurrent generated by the array when the same geometrical fill factor is assumed.

At first glance, one might expect that if FF remains constant for two different photodiode size arrays, both would generate the same photocurrent due to the same total photoactive area. However, based on our study [374] we can demonstrate that this is not the case.

First, let us focus on our target area A_{t}, where we embed the photodiode array. This area receives a total optical power P_{opt} as the total flux of photons is incident upon it. Up to this point, we have primarily discussed the effects of irradiance non-uniformity on photocurrent generation. However, for the sake of simplifying the derivation, we can assume a fully uniform irradiance distribution W_{phot} incident on the photodiode array.

Consider a photodiode, denoted as "D", with a width of $d_{\mathrm{PD}} = d_{\mathrm{D}}$, and an area of $A_{\mathrm{PD_D}} = d_{\mathrm{D}}^2$. The fraction of the incident optical power at the photodiode is denoted as α. The photocurrent generated by this photodiode can be expressed as per [146]:

$$I_{\mathrm{PD}} = \alpha_{\mathrm{PD}} P_{\mathrm{opt}} R_{\mathrm{PD}}. \tag{6.20}$$

Since we are assuming uniform irradiance, the fraction of the incident optical power at the photodiode can be expressed as [374]:

$$\alpha_{\mathrm{PD}} = \frac{A_{\mathrm{PD}}}{A_t} = \frac{d_{\mathrm{PD}}^2}{A_t}. \tag{6.21}$$

Now, if we consider an array of photodiodes, we can set $\bar{\alpha}_{mk} = \alpha_{\mathrm{PD}}$ again, thanks to the assumption of uniform irradiance. When we compare the photocurrent of a single photodiode as described in (6.20) to that of the array described by (6.18), we can calculate the array gain [374]:

$$G_{\mathrm{Array}} = \frac{I_{\mathrm{Array}}}{I_{\mathrm{PD}}} = M_{\mathrm{PD}},$$

which due to the square matrix arrangement conserves bandwidth [146].

To compare the impact of size on the generated photocurrent, we introduce another photodiode labeled as "E". The size of this photodiode "E" is denoted as $d = d_{\mathrm{E}}$, with an area of $A_{\mathrm{PD_E}} = d_{\mathrm{E}}^2$. We choose the size of "E" such that it is a factor of $N = d_{\mathrm{D}}/d_{\mathrm{E}}$ smaller compared to photodiode "D". Both photodiodes share the same responsivity, denoted as R_{PD}. Now, we can compare the photocurrent of a single photodiode "E" to that of "D", which can be expressed as [374]:

$$\frac{I_{\mathrm{PD_E}}}{I_{\mathrm{PD_D}}} = \frac{\alpha_{\mathrm{E}}}{\alpha_{\mathrm{D}}} = \frac{d_{\mathrm{E}}^2}{d_{\mathrm{D}}^2} = \frac{1}{N^2}. \tag{6.22}$$

When we extend the analysis to arrays of photodiodes, it becomes evident that a larger number of photodiodes "E" will occupy the array compared to "D". For a fair comparison, we set $\mathrm{FF_D} = \mathrm{FF_E}$. Applying this equality to (6.17), we can derive the following equation [374]:

$$M_{\mathrm{D}}^2 A_{\mathrm{PD_D}} = M_{\mathrm{E}}^2 A_{\mathrm{PD_E}}, \tag{6.23}$$

from which M_{E} can be expressed [374]:

$$M_{\mathrm{E}} = \sqrt{\frac{M_{\mathrm{D}}^2 A_{\mathrm{PD_D}}}{A_{\mathrm{PD_E}}}} = M_{\mathrm{D}} N. \tag{6.24}$$

If the geometrical fill factor of the array of photodiodes "E" is equal to that of the array of photodiodes "D", the comparison of both array photocurrents leads to the following result [374]:

$$\frac{I_{\mathrm{Array_E}}}{I_{\mathrm{Array_D}}} = \frac{\alpha_{\mathrm{E}} M_{\mathrm{E}}}{\alpha_{\mathrm{D}} M_{\mathrm{D}}} = \frac{M_{\mathrm{D}} N}{M_{\mathrm{D}} N^2} = \frac{1}{N}. \tag{6.25}$$

From (6.25), it becomes evident that while the number of parallel series connections of photodiodes "E" in the array has increased by a factor of N, the photocurrent, on the contrary, has decreased by a factor of $1/N$. To compensate for this decrease, one would need to increase the geometrical fill factor for the "E" photodiode array by a factor of N^2, meaning that the number of photodiodes in the E array must increase by a factor of N^2 compared to the "D" array [374].

It is evident that as photodiode size decreases, and if the geometrical fill factor remains constant, more photodiodes must be placed to capture the same amount of light. However, expanding the array of smaller-sized photodiodes not only increases the number of photodiodes in parallel series but also photodiodes connected in-series together. It is intuitively clear that photodiodes in-series may not efficiently contribute to the photocurrent.

This can also be demonstrated using the following energy conservation (thermodynamic) argument. Consider a photodiode array as an energy source connected to a load resistance, which can be thought of as an energy (heat) sink. A photodiode array is essentially an energy converter that transforms photon energy and amplification energy into electrical energy at a specific interval t. We can express the conservation of energy law as follows [374]:

$$I_{\mathrm{Array}} V_{\mathrm{Array}} t = \alpha_{\mathrm{PD}} M_{\mathrm{PD}}^2 (E_{\hbar\omega} + E_{\mathrm{amp}}), \tag{6.26}$$

here, $E_{\hbar\omega}$ represents the energy provided by the incident photon flux to the array, and E_{amp} denotes the external energy supplied by the power source to amplify the generated carrier photocurrent.

Both term contributions are directly proportional to the total number of charges generated by the array. The number of charges depends on the mean number of photons generating electron-hole pairs due to the photoelectric effect and the amplification energy provided to separate charges, facilitate multiplication of charges (in the case of APDs), and transport them away from the depletion layer. It is evident that both energy contributions are contingent on the number of photodiodes present. Therefore, we can incorporate E_{amp} and $E_{\hbar\omega}$ inside the brackets in (6.26) [374].

The energy received by both arrays from incident photons should be equal since the photoactive area of both arrays is the same. This leads to the following equation [374]:

$$I_{\mathrm{Array_E}} V_{\mathrm{Array_E}} t - \alpha_{\mathrm{E}} M_{\mathrm{E}}^2 E_{\mathrm{amp}} = I_{\mathrm{Array_D}} V_{\mathrm{Array_D}} t - \alpha_{\mathrm{D}} M_{\mathrm{D}}^2 E_{\mathrm{amp}}, \tag{6.27}$$

here V_{Array} is the voltage applied across the photodiode array. By inserting (6.22) and (6.24) into (6.27), we get following [374]:

$$\frac{I_{\mathrm{Array_E}}}{I_{\mathrm{Array_D}}} = \frac{V_{\mathrm{D}}}{V_{\mathrm{E}}} = \frac{V_{\mathrm{D}}}{V_{\mathrm{D}}} \frac{1}{\frac{M_{\mathrm{E}}}{M_{\mathrm{D}}}} = \frac{1}{N}, \tag{6.28}$$

which achieves the same result as (6.25).

From (6.28), we can conclude that to overcome the increased series resistance of the array, one must increase the voltage across it to drive the current. However, since there is no additional energy available from the photons and amplification, and without changing the responsivity or geometrical fill factor, a decrease in photocurrent is an inevitable consequence. Otherwise, the photodiode array would output more electrical energy than it received as input, violating the conservation of energy and, by extension, the second law of thermodynamics.

The results of the simulations support this discussion. Firstly, Figure 6.28 illustrates the dependency of $\bar{\alpha}_{mk}$ on d_{PD}. As observed in the figure, the simulation results closely align with the theoretical expression (6.21). Notably, the only significant exception is the outlier case of the CPC, which highlights that the approximation $\bar{\alpha}_{mk} = \alpha_{\text{PD}} = \frac{d_{\text{PD}}^2}{A_t}$ remains applicable even in situations of non-uniform irradiance. In the cases of the freeform lenslet array and defocused lens, nearly perfect fits are achieved.

The dependency of the array photocurrent I_{array} on d_{PD} is depicted in Figure 6.29.

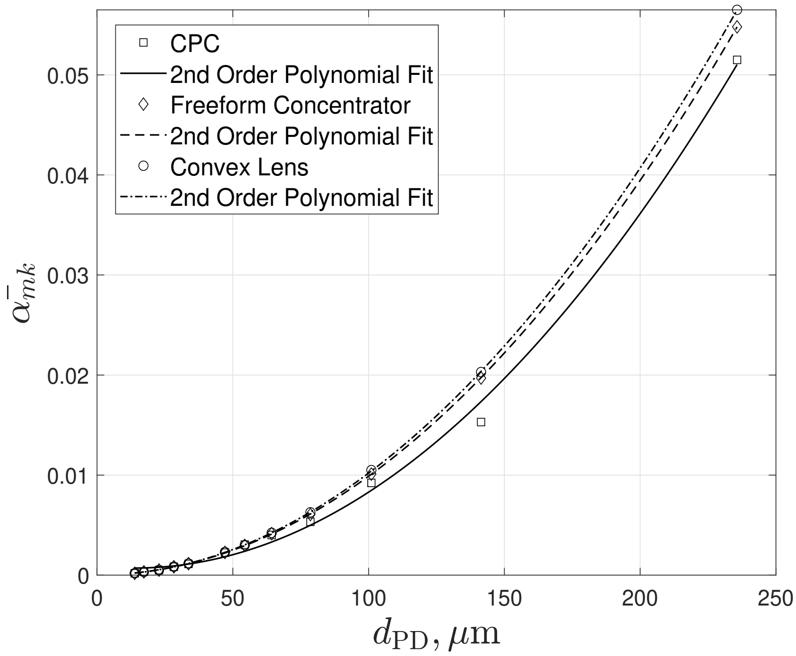

Figure 6.28: $\bar{\alpha}_{mk}$ dependency on d_{PD}. Figure from [374].

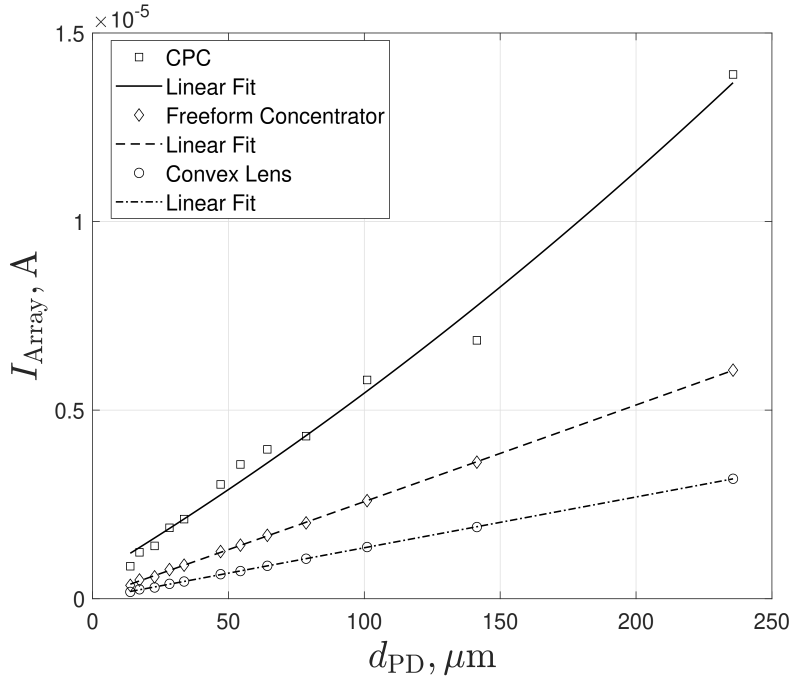

Figure 6.29: I_{array} dependency on d_{PD}. Figure from [374].

As observed in the figure, the simulation results closely align with (6.25). Therefore, it can be concluded that by decreasing the photodiode size while maintaining the same photoactive area, the photocurrent will proportionally decrease with the reduction in size. This establishes a trade-off relation between array photocurrent and photodiode size [374]:

$$\frac{I_{\mathrm{Array_E}}}{d_{\mathrm{E}}} = \frac{I_{\mathrm{Array_D}}}{d_{\mathrm{D}}}. \tag{6.29}$$

Photocurrent Dependency on the Photodiode Bandwidth in the Array

Lastly, we can establish the relationship between the photocurrent generated by the array and its photodiode bandwidth.

It has been demonstrated that the bandwidth B dependency on the photodiode size d_{PD} can be approximated based on the trade-off between photoactive area and bandwidth [155, 307]:

$$B = \frac{1}{C_t d_{\mathrm{PD}}}, \tag{6.30}$$

where the total photodiode capacitance C_t is given by [155, 307]:

$$C_t = \sqrt{\frac{4\pi R_{\mathrm{s}}\epsilon_0\epsilon_{\mathrm{r}}}{0.44 v_s}}, \tag{6.31}$$

here, R_{s} represents the junction series resistance of the photodiode, ϵ_0 is the permittivity of vacuum, v_s is the carrier saturation velocity, and ϵ_{r} represents the relative permittivity of the semiconductor.

By inserting d expression from (6.30) into (6.22) we can express $\alpha_{\mathrm{E}}/\alpha_{\mathrm{D}}$ as [374]:

$$\frac{\alpha_{\mathrm{E}}}{\alpha_{\mathrm{D}}} = (\frac{B_{\mathrm{D}}}{B_{\mathrm{E}}})^2, \tag{6.32}$$

which we insert into (6.25) resulting in [374]:

$$\frac{I_{\mathrm{Array}_{\mathrm{E}}}}{I_{\mathrm{Array}_{\mathrm{D}}}} = (\frac{B_{\mathrm{D}}}{B_{\mathrm{E}}})^2 \frac{M_{\mathrm{E}}}{M_{\mathrm{D}}} = (\frac{B_{\mathrm{D}}}{B_{\mathrm{E}}})^2 \frac{B_{\mathrm{E}}}{B_{\mathrm{D}}}, \tag{6.33}$$

by simplifying and re-arranging the equation, we obtain the trade-off relation between array photocurrent and bandwidth [374]:

$$I_{\mathrm{Array}_{\mathrm{E}}} B_{\mathrm{E}} = I_{\mathrm{Array}_{\mathrm{D}}} B_{\mathrm{D}}, \tag{6.34}$$

if we compare (6.34) to (6.29), we observe an inverted relationship, where the array photocurrent decreases with increasing bandwidth. Analysing (6.34), we notice that the conserved quantity of the photocurrent-bandwidth product on both sides has units of A/s. These units represent the first derivative of current, $\mathrm{d}I/\mathrm{d}t$, or the rate of current change.

In the context of OWC or VLC, the rate of current change can be interpreted as follows. Suppose we modulate a signal at a frequency $f = B$. For illustrative simplicity, let's assume that the signal is modulated as a NRZ-OOK, where the '0' symbol photocurrent level corresponds to $I_{\text{symb}} = 0$ and the logical '1' corresponds to a photocurrent level of $I_{\text{symb}} = I_{\text{Array}}$. Furthermore, without a loss of generality, we can assume that the transmitter bandwidth is much larger than the receiver's, and that the signal bandwidth is limited only by the receiver.

The conserved quantity in (6.34) in this context represents the photodiode array's ability to increase the photocurrent from 0 to I_{Array} within a time interval of $1/B$. However, it's important to note that this value is constrained by the amount of energy available for generating charge carriers. In other words, a photodiode array cannot generate photocurrent faster than the combined energy of the photon flux and amplification allows within a time interval of $1/B$. Violating this constraint would go against the conservation of energy [374].

To illustrate the photocurrent bandwidth trade-off in the simulations, we calculate B using (6.30), and for C_t, we use the parameters provided in [155]. In these calculations, we assume that the material used in the photodiodes is silicon with a relative permittivity of $\epsilon_{\text{r}} = 11.68$.

The array photocurrent dependency I_{array} on B is shown in Figure 6.34. As can be seen from it, the simulation results closely align with (6.34).

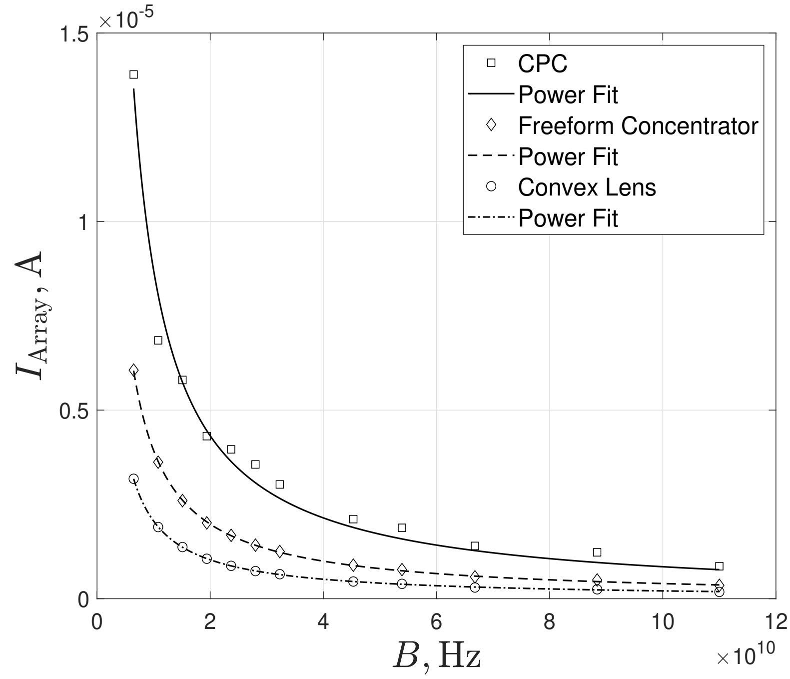

Figure 6.30: I_{array} dependency on B. Figure from [374].

6.7 Combined Model

Incorporating the results from previous chapters, we can formulate a unified photocurrent model expression for integration into the link-budget modeling.

We begin with a basic expression that assumes no reflectance or transmissivity losses, a single photodiode, and FF < 1. In this scenario, when the incidence is within the FoV of the receiver, the photocurrent follows the well-known simple expression:

$$I_0(\psi_{\mathrm{in}}) = P_{\mathrm{ref}} C_{\mathrm{opt}}(\psi_{\mathrm{in}}) R_{\mathrm{PD}} \mathrm{FF}, \tag{6.35}$$

when we consider losses resulting from Fresnel reflection at the photodiode surface and the transmissivity loss of the optical material in the concentrating optics, the equation is modified to:

$$\begin{aligned} I_0(\psi_{\mathrm{in}}) =& P_{\mathrm{ref}} C_{\mathrm{opt}}(\psi_{\mathrm{in}}) R_{\mathrm{PD}} \mathrm{FF} R_{\mathrm{Rel,PD}}(\psi_{\mathrm{r}}) T_{\mathrm{optic}} \\ =& P_{\mathrm{ref}} C_{\mathrm{opt}}(\psi_{\mathrm{in}}) R_{\mathrm{PD}} \mathrm{FF} \cos\psi_{\mathrm{r}} T_{\mathrm{optic}}, \end{aligned} \tag{6.36}$$

where $\psi_{\mathrm{r}} = f(\psi_{\mathrm{in}})$ and T_{optic} is transmissivity of the optical element. If we organize the same photoactive area into an array of smaller photodiodes, following is obtained:

$$I_{\mathrm{Array}}(\psi_x, \psi_y) = I_0(\psi_{\mathrm{in}})\Gamma(\psi_x, \psi_y, d_{\mathrm{PD},1}, \mathrm{FF}, A_t)\frac{d_{\mathrm{PD},1}}{d_{\mathrm{PD},0}}, \tag{6.37}$$

here, $\psi_{\mathrm{in}} = \sqrt{\psi_x^2 + \psi_y^2}$. d_1 represents the size of individual photodiodes in the smaller array, and d_0 is the size of a single larger photodiode. The term $\Gamma(\psi_x, \psi_y, d_1, \mathrm{FF}, A_t)$ denotes the correction factor accounting for the non-uniformity of the irradiance distribution on the photodiode array. This factor generally depends on various factors, including the incidence angle, direction of incident light, the shape of the photodiode array, and the geometrical fill factor. Based on our previous results, we can approximate Γ within the FoV.

At the FoV limit for our freeform lenslet array concentrator, $\Gamma \approx 0.92$ for a wide range of photodiode sizes. In the case of the convex lens, $\Gamma \approx 1$. However, providing an accurate approximation for the CPC is more challenging, as our results have shown significant variation with some outliers. Nonetheless, for photodiode sizes of less than $75\,\mu$m, $\Gamma \approx 0.65$ in the case of the CPC. It's important to note that these values are specific to a FoV of 10 deg and design parameters, which may vary based on the application. A more comprehensive investigation of Γ is required for the future work.

We can also express (6.37) in terms of bandwidth B as:

$$I_{\mathrm{Array}}(\psi_x, \psi_y) = I_0(\psi_{\mathrm{in}})\Gamma(\psi_x, \psi_y, d_{\mathrm{PD},1}, \mathrm{FF}, A_t)\frac{B_0}{B_1}, \tag{6.38}$$

here, B_1 is the bandwidth of the smaller array photodiodes, and B_0 is the bandwidth of the larger single photodiode.

It is essential to apply this model when evaluating the energy efficiency of custom-designed photodiode arrays and optics tailored to specific use-case scenarios such as high data throughput links. The efficiency of array photocurrent generation significantly influences the SNR, impacting transmitter optical power requirements and overall electrical power consumption. This discussion highlights that traditional OWC and VLC receiver solutions, such as non-imaging optics, might not be suitable for high-data-throughput and energy-efficient link designs. Instead, when designing such links, custom optics like our freeform lenslet array or other freeform optical concentrators should be considered.

6.8 Summary

An optical concentrator design methodology based on freeform optics is presented. This design incorporates multiple small lenslets organized in an array, with their surfaces shaped in a freeform manner to achieve the desired irradiance distribution at the receiver plane. The methodology employs the LAP method to calculate the optical surface profiles of various lenslets required to produce the target irradiance at the receiver plane, given the incidence irradiance at the input aperture.

For the methodology validation a proof-of-concept for a simple paraxial imaging concentrator design, resembling a thin Fresnel lens. This method allows for the design of a significantly thinner lenslet array when compared to a conventional plano-convex lens.

Furthermore, using this methodology, we designed a freeform lenslet array concentrator for a compact receiver with a 10 deg FoV and compared its optical concentration gain to conventional imaging optics (a convex lens) and non-imaging optics (a CPC) of the same size. The freeform lenslet array achieved approximately a $2-$fold improvement in concentration compared to the convex lens and half the concentration gain compared to the CPC.

Nevertheless, the freeform lenslet array redirects incident rays toward the receiver plane at shallower angles in comparison to the CPC and convex lens. When accounting for incident ray radiance and the photodiode's relative responsivity, the relative difference in optical concentration between the CPC and the freeform lenslet array reduces to just 1/1.11. This reduction is primarily attributed to the high angle of incidence in the CPC, leading to significant Fresnel reflection losses. While it is possible to mitigate these reflections, it necessitates the addition of an index-matching material at the interface between the CPC and the photodiode, increasing both the cost and complexity of the receiver's optical design.

Furthermore, the irradiance distribution at the receiver plane is notably more uniform for the freeform lenslet array and convex lens when compared to the CPC. While this uniformity may not be critical for a single photodiode, it becomes significant when considering an array of photodiodes. In such cases, we observe a substantial variation in photocurrent generated across the receiver's FoV for the CPC, often effectively reducing the FoV by half.

This effect is much less pronounced in the case of the freeform lenslet array and convex lens, which provide a more uniform photocurrent response based on the incident angle within the FoV. Moreover, this effect diminishes further when employing smaller photodiode arrays, which is not the case with the CPC inidcating importance of uniformity of irradiance distribution in the case of photodiode arrays. This can be extended to a different type of target irradiance distributions, which could benefit LiFi systems utilising GSSK as a transmission protocol.

Additionally, the dependency of photocurrent on incidence angle and the direction of incident light can be anisotropic. This anisotropy is more pronounced when the photodiode array is large compared to the spatial variation and non-uniformity of the irradiance distribution. However, it strongly diminishes when smaller photodiode arrays are used.

The introduction of an array not only affects the relative but also the absolute value of the generated photocurrent when compared to a single photodiode with the same total photoactive area. This relationship between array photocurrent and array photodiode size can be described by a trade-off principle. For two square arrays with the same total photoactive area, the ratio of their photocurrent to their individual photodiode size remains constant. In other words, reducing the photodiode size in a square array while keeping the total photoactive area constant results in a proportional decrease in photocurrent. This principle aligns with the conservation of energy.

An analogous trade-off relation can be demonstrated for the array photocurrent and array photodiode bandwidth. For two square arrays with the same total photoactive area, their photocurrent-bandwidth product remains constant. In other words, increasing the photodiode bandwidth in a square array while maintaining the total photoactive area constant results in a proportional decrease in photocurrent.

While it is true that the proposed concentrator has a slightly decreased overall system gain when compared to a CPC by a factor $1/1.11$ leading to equivalently reduced

SNR. Nevertheless, when photodiode arrays for enhanced bandwidth or collection area are considered, the overall system performance can significantly drop depending by the incidence angle by up to about 35 %. Therefore, within the specified FoV, the freeform concentrator can outperform CPC considerably at different angles compared to the normal incidence, leading to up to about 1.4/1 overall system gain improvement compared to the CPC.

In the adaptive GSSK system utilising array for increased bandwidth and collection area, the overall performance dependence on the incidence angle can affect the beam selection performance, as the beams at the edge of FoV (high incidence angles) will be significantly more attenuated compared to the normal incidence case. Generally, to effectively utilise as many beams as possible within the FoV of the receiver, it is desirable for the relative photocurrent and overall system gain to vary little within the FoV compared to the normal incidence angle. The use of freeform concentrator brings a significant benefit when considered in GSSK LiFi systems offering significantly smaller attenuation of edge FoV beams, as well as increasing the available beams for improved beam selection. However, for full analysis of impact of freeform concentrator on adaptive GSSK, a new set of simulations utilising freeform concentrator in similar scenarios as described in Chapter 4.

The effects of irradiance non-uniformity, Fresnel reflections due to oblique incidence, and the trade-off between array photocurrent size and bandwidth can be incorporated into a unified model. This model takes into account the array dimensions and concentrating optics parameters to estimate the generated photocurrent relative to a single photodiode with the same total photoactive area.

This study underscores the significance of concentrating optics in the context of photodiode arrays, particularly when aiming for high data throughput and energy-efficient OWC or VLC links. Considering the various factors involved in light concentration on the photodiode array, it becomes evident that a simple assumption of classical non-imaging or imaging optics may be inadequate. Designing an OWC link with a photodiode array photodetector necessitates a custom, adaptable, and innovative optics approach. We have demonstrated one such approach using the freeform optics methodology, exemplified by our freeform lenslet array concentrator for the receiver.

Chapter 7

Conclusions, Limitations and Future Research

7.1 Summary and Conclusions

LiFi (short for light fidelity), envisaged as a complementary and viable technology to existing radio frequency (RF) telecommunication systems, requires the development of a physical layer that supports high data throughput (at least 10 Gbit/s) and energy-efficient transmission (less than 1 nJ/bit). However, to design such a physical layer for high speed power efficient LiFi transceiver, a holistic approach is necessary, one that encompasses both the modulation scheme and the opto-electronic front-end. There exists a wide array of research and development avenues to achieve this objective, each with its own set of advantages and limitations.

In this thesis, we explore an approach based on utilising Generalised Space Shift Keying (GSSK) as a digital baseband modulation for the link. The preference for this digital modulation scheme is due to its transmitter design's simplicity, which results in lower implementation complexity. This, in turn, leads to reduced power consumption in the link and provides immunity to the non-linearity of optical sources.

To evaluate whether a GSSK based link can serve as the foundation for a high data throughput and energy-efficient communication system, two common scenarios are considered. In the first scenario, an indoor VLC link is analysed, featuring hemispherical access points (APs) and user equipment (UE). This scenario simulates an environment where a user can move freely across a room with a single AP fixed to the ceiling. The second scenario considers a more directional device-to-device OWC link over a distance of 1 metre, emulating mobile-to-mobile or mobile-to-display communication links.

A well-known property of GSSK is its dependence on the distinguishability of mutual beam channel gains at the receiver. This characteristic makes the modulation scheme sensitive to the time-dependent relative position and orientation of the user device in relation to the transmitter. To compensate for such changes in channel conditions, an adaptive algorithm is required. These adaptive features must include beam selection and spectral efficiency (codebook) adjustment based on the instantaneous channel conditions at any given time.

An adaptive algorithm is proposed for various beam set selection criteria. The performance of these different criteria is evaluated in terms of computational complexity, mean peak data throughput, data throughput uniformity, and energy efficiency.

To facilitate the implementability of such an adaptive GSSK algorithm for a practical LiFi system, a Hardware Description Language (HDL) synthesisable implementation of the algorithm is proposed in this thesis using Mathworks Simulink, including the necessary digital signal processing (DSP) modules.

While the first two contributions address the design of a high data throughput and energy-efficient adaptive GSSK based link, the limitations imposed by off-the-shelf opto-electronic front-end elements on achievable performance become evident. This necessitates an investigation into novel receiver optics suitable for high-speed photodiode (PD) arrays to further enhance energy efficiency and data throughput. In this context, a novel optical concentrator design based on freeform optics is developed, and its performance is compared to that of common imaging and non-imaging solutions. To evaluate the performance of such freeform-based concentrators and existing optical concentrators in the context of PD arrays, a model is proposed that accounts for the irradiance and radiance distribution at the PD array.

Chapter 2 provides relevant background information and a review of the state-of-the-art, setting the context for our investigation into high data throughput and energy-efficient link design. It presents the fundamentals and history of OWC and VLC. The chapter describes a typical OWC and VLC link, covering aspects such as the opto-electronic front-end, modulation schemes, the transmission channel, and noise sources that affect link performance. Finally, a power consumption model is introduced, which is essential for the energy efficiency analysis presented in Chapter 4.

Chapter 3 delves into the performance analysis of the adaptive GSSK link within two use case scenarios. Initially, a general theoretical framework for the adaptive GSSK algorithm is introduced, which encompasses beam selection and spectral efficiency adjustment. The chapter formulates the general problem for beam and receiver set selection aimed at maximising channel capacity. Building on this, a pseudocode for an adaptive GSSK algorithm is proposed, based on three different beam set selection criteria. Two of these criteria, namely the maximal minimal Euclidean distance and the maximal Signal-to-Noise Ratio (SNR), are well-established in the literature. Additionally, a third selection criterion, based on the optimal GSSK channel ratio, is introduced in this thesis.

The algorithms are compared in terms of computational complexity. The maximal minimal Euclidean distance criterion exhibits the highest computational complexity, which increases exponentially with the number of engaged beams in the link. This leads to approximately 10^{10} operations required to select 5 beams for the GSSK link. In contrast, the maximal SNR criterion has the lowest complexity, growing linearly with the number of engaged beams and requiring about 10^4 operations to select 5 beams. The optimal GSSK channel ratio algorithm demonstrates a computational complexity similar to that of the maximal SNR criterion, needing approximately 10^4 to 10^5 operations to select 5 beams.

In Chapter 4 all three adaptive algorithms are evaluated in the Visible Light Communication (VLC) scenario. However, even with an emitted optical power of 1W, none of the adaptive Generalised Space Shift Keying (GSSK) links can achieve a mean data throughput of 10 Gbit/s. The best performance in terms of data throughput and data throughput uniformity is achieved by the maximal minimal Euclidean distance set selector. This link achieves an average of 6.98 Gbit/s with the lowest data throughput distribution entropy of 0.76 nat. The poorest performance is exhibited by the maximal SNR criterion, achieving 5.46 Gbit/s with a high data throughput distribution entropy of 1.13 nat. The optimal GSSK channel ratio criterion provides intermediate results, with 6.04 Gbit/s and an entropy of 0.83 nat.

The results indicate that to achieve high data throughput with low spatial variance in the VLC scenario, the maximal minimal Euclidean distance selection would be preferable. However, the latency incurred by this beam selection algorithm could lead to unacceptably high delays. In contrast, the maximal SNR criterion can facilitate rapid beam selection, but the achievable average data throughput is lower and the spatial variance is significantly higher, resulting in an uneven communication link. The optimal GSSK channel ratio offers an improvement over the maximal SNR criterion, but its performance still considerably lags behind that of the Euclidean selector. Moreover, a pronounced trade-off between mean data throughput and spatial distribution uniformity is evident in this case.

While the results in the VLC scenario fall short of the required data throughput, the energy efficiency is even more concerning, reaching 64.77 nJ/bit in the best case. This figure far exceeds the acceptable threshold value of 1 nJ/bit. The primary reason for this inefficiency is the very high optical power required to provide a sufficient GSSK signal at very high bandwidths, combined with the low electrical-to-optical power conversion efficiency of microLEDs.

The results demonstrate that while high data throughput can be achieved in an indoor VLC scenario using adaptive GSSK, the resulting energy efficiency is notably low. A more suitable approach would be to employ modulation schemes that reduce bandwidth requirements, such as Direct Current Biased Optical OFDM (DCO-OFDM) with adaptive bit loading. This approach would enable the use of microLEDs or LEDs with considerably lower bandwidth and higher emission power, enhancing overall efficiency.

In the OWC scenario, only the optimal GSSK channel ratio beam selection criterion is considered for adaptive GSSK. In this context, significantly better performance can be achieved with off-the-shelf opto-electronic components than in the VLC scenario, both in terms of achievable mean data throughput and energy efficiency. Energy efficiencies of 378.12 pJ/bit and 413.17 pJ/bit, with mean data throughputs of 19.85 Gbit/s and 22.6 Gbit/s, respectively, can be attained for close spacing (emulating mobile-to-mobile) and sparse spacing (emulating mobile-to-display) scenarios using 2x2 Avalanche Photodiode (APD) receivers. The performance of the adaptive GSSK link in this scenario is compared to 64-QAM (Quadrature Amplitude Modulation) and DCO-OFDM, with adaptive GSSK outperforming both modulation schemes in terms of energy efficiency at equivalent data throughput levels.

The primary conclusion of the chapter is that for high data throughput applications in indoor VLC scenarios, adaptive GSSK is not ideally suited, and other modulation schemes should be considered. However, in OWC device-to-device scenarios, adaptive GSSK shows promising performance in terms of both data throughput and energy efficiency. This advantage is particularly notable when combined with the benefits of low computational complexity and straightforward implementation.

Chapter 5 presents a HDL synthesisable implementation of the adaptive GSSK algorithm, demonstrating the feasibility of its implementation. The beam selection algorithm is based on the maximal minimal Euclidean distance criterion and is designed for 4 transmitter beams. With this number of transmitters available for selection, the latency is estimated at 70 ns. For spectral efficiency adjustment until a satisfactory Bit Error Ratio (BER) is achieved per data packet, the time can vary between 2 µs to 9.2 µs. The minimum required electrical SNR, considering noisy channel state information for beam selection, is determined to be 21.99 dB. However, this minimum required electrical SNR can be further decreased by increasing the length of training sequences. For a larger number of available transmitter beams, other beam selection criteria, such as the optimal GSSK channel ratio, should be considered.

Chapter 6 concentrates on the design of optical concentrators for OWC links. It presents a design methodology for a freeform lenslet array with multiple potential functionalities. This methodology is rooted in the linear assignment problem (LAP), a technique used for designing freeform optics. Based on this approach, a lenslet array concentrator with a 10 deg Field of View (FoV) is designed. Such concentrator could be considered in a scenario of 1 m diameter link coverage at 3 m distance from the AP.

This lenslet array concentrator is then compared to a non-imaging compound parabolic concentrator (CPC) and an imaging convex lens of equivalent dimensions. The lenslet array demonstrates nearly double the performance of the convex lens and achieves nearly the same optical concentration as a CPC, assuming no index matching material is used in the CPC case.

The comparison is further extended to scenarios involving an array of photodiodes, highlighting the limitations of non-imaging optics, such as CPCs, for optical concentration on an array of PDs. With CPCs, the optical concentration becomes non-uniform within the FoV depending on the incidence angle, and for certain array sizes, it can even become anisotropic (dependent on the direction of incident light). These issues are much less pronounced in the case of the lenslet array and the convex lens. Furthermore, the control target irradiance prescription at the receiver can allow for a design, which can benefit the performance of LiFi system utilising GSSK.

Further analysis is conducted for an array of photodetectors, each having the same area as a single reference photodiode. A model is proposed that can be used to estimate the generated photocurrent, taking into account the concentrating optics and the PD array configuration. Such model can be used to more accurately model the performance of a receiver utilising an array of PDs.

7.2 Limitations and Future Research

One of the primary objectives of this thesis was to assess whether an adaptive GSSK system can deliver both high data throughput and enhanced energy efficiency in a communication link. Nevertheless, there exist specific limitations and opportunities for future enhancements.

The primary limitation lies in the fact that, for power consumption estimation, only the physical layer has been analysed. It is evident that the DSP and networking layers can contribute to additional power consumption. To accurately model the performance of an adaptive GSSK algorithm in the DSP layer, a fully implemented design with the estimation of the number of operations is required. This calls for a comprehensive experimental demonstration of such an adaptive GSSK link. A demonstration achieving at least a 10 Gbit/s link, emulating a device-to-device scenario, is warranted as a conclusive proof-of-concept for high data throughput and energy efficiency adaptive GSSK.

Chapters 3 and 4 examine two significantly different scenarios, making a direct comparison between them challenging. An analysis of an indoor OWC link, with same dimensions as in the VLC scenario, would offer deeper insights into whether an adaptive OWC GSSK link could better achieve the required mean peak data throughput and energy efficiency. However, it is expected that the high SNR requirements might render such an implementation unfeasible due to laser eye safety regulations. Therefore, an investigation into link performance using other off-the-shelf VCSELs (Vertical-Cavity Surface-Emitting Lasers) with more lenient eye safety constraints, such as a higher wavelength like 1310 nm, should be conducted. The main difficulty of such VCSELs, however, is poor thermal conductivity of such materials as InP [79], which can lead to increasing thermal droop challenges that increase with increasing emission optical power requirements.

One can explore methods to enhance the maximal minimum Euclidean distance beam selection criterion by utilising search algorithms aimed at reducing computational complexity. An open question persists regarding whether, in cases involving a large number of available transmitter beams, improved search algorithms can effectively steer optimal beam selection to be within acceptable latency limits.

In Chapter 6, while the freeform lenslet array concentrator demonstrates optical concentration similar to that of a CPC of the same size and outperforms a convex lens, it is important to note that these results are derived from ray tracing and simulations. Therefore, it is crucial to validate the design experimentally, initially for a single photodiode and subsequently for an array of photodiodes. Furthermore, the model presented at the end of Chapter 6 should also undergo experimental validation.

The optical concentration of the freeform lenslet array concentrator was compared to a limited number of optical concentrating elements. For future research, a more comprehensive comparative study should be conducted, including an evaluation against various optical elements such as other freeform concentrators and lenses, aspherical lenses, and other non-imaging concentrators. Furthermore, a freeform lenslet array design with prescribed target irradiance optimised for GSSK transmission protocol remains to be demonstrated.

Finally, the authors encourage a development of a practical LiFi transceiver utilising the discussed adaptive GSSK algorithms and freeform optical concentrator with or without photodiode arrays.

Appendix A

Derivation of number of operations of the channel capacity maximisation

To derive the number of operations to maximise channel capacity, we first consider the channel capacity expression (3.8):

$$C_{\mathrm{MIMO}}^{N_{\mathrm{t}}^{\mathrm{e}}\times N_{\mathrm{r}}^{\mathrm{e}}} = \mathrm{E}_{\mathbf{H}}\{\log_2(\det(\mathbf{I}_{N_{\mathrm{r}}^{\mathrm{e}}} + \frac{1}{N_{\mathrm{t}}^{\mathrm{e}}}\mathrm{SNR}\times\mathbf{H}\mathbf{H}^T))\}. \tag{A.1}$$

Firstly, assuming the channel state is known, which implies knowledge of both SNR term and $N_{\mathrm{r}}^{\mathrm{e}} \times N_{\mathrm{t}}^{\mathrm{e}}$ channel matrix $\mathbf{H}$, we begin by calculating the transpose of H. The transpose operation necessitates $\frac{N_{\mathrm{r}}^{\mathrm{e}}\times(N_{\mathrm{t}}^{\mathrm{e}}-1)}{2}$ floating-point operations [376]. Next, the channel matrix is multiplied by its transpose, which requires $(N_{\mathrm{r}}^{\mathrm{e}})^2 \times N_{\mathrm{t}}^{\mathrm{e}}$ multiplications using the schoolbook matrix multiplication [377]. Each matrix term is represented by an N_{bit} long binary integer.

Next, employing the schoolbook long multiplication algorithm entails N_{bit}^2 number of operations required to multiply two terms [378]. Therefore, the number of operations required to multiply the elements of two matrices is $(N_{\mathrm{r}}^{\mathrm{e}})^2 \times N_{\mathrm{t}}^{\mathrm{e}} \times N_{\mathrm{bit}}^2$. Furthermore, matrix multiplication results in $(N_{\mathrm{r}}^{\mathrm{e}})^2$ summations of multiplied matrix elements. For each summation N_{bit} operations are required [378]. The total number of operations to sum the multiplied matrix elements is $(N_{\mathrm{r}}^{\mathrm{e}})^2 \times N_{\mathrm{bit}}$.

The resulting $N_{\mathrm{r}}^{\mathrm{e}} \times N_{\mathrm{r}}^{\mathrm{e}}$ square matrix elements are multiplied with the scalar term requiring, which requires $(N_{\mathrm{r}}^{\mathrm{e}})^2 \times N_{\mathrm{bit}}^2$ operations. To sum up the resulting matrix with the identity matrix, only diagonal elements need to be considered. This entails $N_{\mathrm{r}}^{\mathrm{e}}$ summations with the number of operations required being $N_{\mathrm{r}}^{\mathrm{e}} \times N_{\mathrm{bit}}$.

The determinant can be evaluated using LU decomposition, which requires $(N_{\mathrm{r}}^{\mathrm{e}})^3 \times N_{\mathrm{bit}}^2$ operations [379].

Therefore, to evaluate (A.1) the number of operations is:

$$N_{\mathrm{cap}}^{\mathrm{ops}} = (N_{\mathrm{r}}^{\mathrm{e}})^3 N_{\mathrm{bit}}^2 + N_{\mathrm{r}}^{\mathrm{e}} N_{\mathrm{bit}} + (N_{\mathrm{r}}^{\mathrm{e}})^2 N_{\mathrm{bit}}^2 + (N_{\mathrm{r}}^{\mathrm{e}})^2 N_{\mathrm{t}}^{\mathrm{e}} N_{\mathrm{bit}}^2 + (N_{\mathrm{r}}^{\mathrm{e}})^2 N_{\mathrm{bit}} + \frac{\mathrm{N}_{\mathrm{r}}^{\mathrm{e}}(\mathrm{N}_{\mathrm{t}}^{\mathrm{e}} - 1)}{2}. \quad \text{(A.2)}$$

The channel capacity estimation is to be performed for each combination of varying numbers of engaged transmitter beams and receivers. This necessitates summing over the entire search space of different engaged receiver and transmitter beam numbers.

Lastly, once all the channel capacities of all engaged beam and receiver combinations have been estimated, they should be sorted. In total there are $2^{N_{\mathrm{r}}^{\mathrm{a}} + N_{\mathrm{t}}^{\mathrm{a}}}$ combinations. In our analysis, we assume the bubble sort algorithm as it is a fairly common sorting algorithm, which for n number of elements requires n^2 number of operations [380]. Therefore, in addition to estimating $2^{N_{\mathrm{r}}^{\mathrm{a}} + N_{\mathrm{t}}^{\mathrm{a}}}$ channel capacities additional $2^{2(N_{\mathrm{r}}^{\mathrm{a}} + N_{\mathrm{t}}^{\mathrm{a}})}$ sorting operations are required.

Appendix B

Derivation of number of operations of the set selectors

We commence with the maximal minimum Euclidean distance set selector. The algorithm's objective is to identify a beam and receiver set where the minimal Euclidean distance between different symbols is maximised. The Euclidean distance between two symbols k and k' is defined from (3.15) as:

$$d_{\mathbf{x}_k,\mathbf{x}_{k'}} = |\mathbf{H}\Delta_{\mathbf{X}_k,\mathbf{X}_{k'}}|_{\mathrm{F}}. \tag{B.1}$$

Here $\mathbf{H}$ is a $N_{\mathrm{r}}^{\mathrm{a}} \times |\mathbb{E}_{\mathrm{t},\kappa}|$ dimensional channel matrix, while $\Delta_{\mathbf{X}_k,\mathbf{X}_{k'}}$ is a $|\mathbb{E}_{\mathrm{t},\kappa}| \times 1$ dimensional column vector. Evaluating $\Delta_{\mathbf{X}_k,\mathbf{X}_{k'}}$ necessitates the subtraction of two symbol column vectors. In total, there are $|\mathbb{E}_{\mathrm{t},\kappa}|$. Each vector term is represented by a N_{bit} long binary integer. For each subtraction, N_{bit} operations are required [378]. Hence, $\Delta_{\mathbf{X}_k,\mathbf{X}_{k'}}$ necessitates $|\mathbb{E}_{\mathrm{t},\kappa}| \times N_{\mathrm{bit}}$ operations.

Next, one needs to multiply the matrix with the vector. By employing simple schoolbook matrix multiplication, this task necessitates $N_{\mathrm{r}}^{\mathrm{a}} \times |\mathbb{E}_{\mathrm{t},\kappa}|$ matrix term multiplications [377]. Using the schoolbook long multiplication algorithm leads to N_{bit}^2 number of operations required to multiply two terms [378]. Therefore, the number of operations required to multiply the two matrices in (B.1) is $N_{\mathrm{r}}^{\mathrm{a}} \times |\mathbb{E}_{\mathrm{t},\kappa}| \times N_{\mathrm{bit}}^2$.

Next, to evaluate (B.1), the Frobenius norm of the resulting vector is calculated.

Initially, $N_{\mathrm{r}}^{\mathrm{a}}$ vector terms are squared, necessitating $N_{\mathrm{r}}^{\mathrm{a}} N_{\mathrm{bit}}^{2}$operations for multiplication, as squaring terms involves multiplying them with themselves. Subsequently, the $N_{\mathrm{r}}^{\mathrm{a}}$ terms are summed together, requiring $N_{\mathrm{r}}^{\mathrm{a}} N_{\mathrm{bit}}$ operations. If the square root is not explicitly calculated, summing up all the contributions to evaluate (B.1) results in:

$$\begin{aligned} N_{d_{\mathbf{x}_k,\mathbf{x}_{k'}}}^{\mathrm{ops}} &= |\mathbb{E}_{\mathrm{t},\kappa}| N_{\mathrm{bit}} + N_{\mathrm{r}}^{\mathrm{a}} |\mathbb{E}_{\mathrm{t},\kappa}| N_{\mathrm{bit}}^{2} + N_{\mathrm{r}}^{\mathrm{a}} N_{\mathrm{bit}}^{2} + N_{\mathrm{r}}^{\mathrm{a}} N_{\mathrm{bit}} \\ &= |\mathbb{E}_{\mathrm{t},\kappa}| N_{\mathrm{bit}} + N_{\mathrm{r}}^{\mathrm{a}} N_{\mathrm{bit}} (|\mathbb{E}_{\mathrm{t},\kappa}| N_{\mathrm{bit}} + N_{\mathrm{bit}} + 1), \end{aligned} \tag{B.2}$$

which matches expression in (3.25).

For each set $\mathbb{E}_{\mathrm{t},\kappa}$, there are given $\binom{2^{|\mathbb{E}_{\mathrm{t},\kappa}|}}{2}$ symbol pairs for which Euclidean distances can be calculated leading to:

$$N_{\mathbb{E}_{\mathrm{t},\kappa}}^{\mathrm{ops}} = N_{d_{\mathbf{x}_k,\mathbf{x}_{k'}}}^{\mathrm{ops}} (\mathbb{E}_{\mathrm{t},\kappa}) \binom{2^{|\mathbb{E}_{\mathrm{t},\kappa}|}}{2} + (\binom{2^{|\mathbb{E}_{\mathrm{t},\kappa}|}}{2})^2, \tag{B.3}$$

here, the second term accounts for the complexity of the sorting algorithm used to select the minimum Euclidean distance. Various sorting algorithms can be employed for this purpose. In our example, we use Bubble sort, which has a computational time complexity of n^2 for n elements [380].

The total number of operations to select $\mathbb{E}_{\mathrm{t,r}}(\boldsymbol{\Theta}(t))$ up to the number of engaged transmitter beams $|\mathbb{E}_{\mathrm{t}}(\boldsymbol{\Theta}(t))| = G$ can be calculated as follows:

$$N_{\mathrm{tot}}^{\mathrm{ops}}(|\mathbb{E}_{\mathrm{t}}| = G) = \sum_{g=1}^{g=G} \sum_{\substack{\mathbb{E}_{\mathrm{t},\kappa} \\ \in \mathcal{E}_{\mathrm{t}}^{g}}} (N_{\mathbb{E}_{\mathrm{t},\kappa}}^{\mathrm{ops}} + |\mathcal{E}_{\mathrm{t}}^{g}|^2), \tag{B.4}$$

here the second term in the sum represents the number of operations required to select the set that maximises the minimum Euclidean distance in the set $\mathcal{E}_{\mathrm{t}}^{g}$) based on Bubble sort. The number of summations for $g = G$ is $\binom{N_{\mathrm{t}}^{\mathrm{a}}}{G}$.

For the maximal SNR set selector, one firstly needs to successively select columns of H, with each iteration satisfying the following conditions:

$$k_l = \underset{k \neq k_{(l-1)}}{\operatorname{argmax}} \sum_{i=1}^{N_{\mathrm{r}}^{\mathrm{a}}} h_{ik}^2. \tag{B.5}$$

Firstly, all $N_{\mathrm{r}}^{\mathrm{a}} \times N_{\mathrm{t}}^{\mathrm{a}}$ matrix terms should be squared, which, assuming the schoolbook algorithm, requires N_{bit}^2 number of operations [378], leading to a total of $N_{\mathrm{r}}^{\mathrm{a}} \times N_{\mathrm{t}}^{\mathrm{a}} \times N_{\mathrm{bit}}^2$ number of operations. Next, each column's terms should be summed together, which again necessitates a summation of $N_{\mathrm{r}}^{\mathrm{a}} \times N_{\mathrm{t}}^{\mathrm{a}}$ terms, where each summation requires N_{bit} number of integer operations [378]. This results in a total number of operations for summation of $N_{\mathrm{r}}^{\mathrm{a}} \times N_{\mathrm{t}}^{\mathrm{a}} \times N_{\mathrm{bit}}$.

Finally, each matrix channel gain sum should be sorted in descending order using bubble sort, which requires sorting of $N_{\mathrm{t}}^{\mathrm{a}}$ column sum values, resulting in a complexity of $(N_{\mathrm{t}}^{\mathrm{a}})^2$ [380]. Combining contributions from matrix element squaring, summing, and sorting, we get:

$$N_{\mathrm{SNR}}^{\mathrm{ops}} = N_{\mathrm{t}}^{\mathrm{a}} N_{\mathrm{r}}^{\mathrm{a}} N_{\mathrm{bit}}^2 + N_{\mathrm{r}}^{\mathrm{a}} N_{\mathrm{t}}^{\mathrm{a}} N_{\mathrm{bit}} + (N_{\mathrm{t}}^{\mathrm{a}})^2. \tag{B.6}$$

For the optimal GSSK channel ratio set selector, we consider that in each iteration, a matrix H column should be selected such that it satisfies:

$$k_l = \underset{k}{\operatorname{argmin}} \sum_{i=1}^{|\mathbb{A}_{\mathrm{r}}(\boldsymbol{\Theta}(t))|} |\frac{h_{ik_{(l-1)}}^2}{h_{ik}^2} - a|^2. \tag{B.7}$$

Firstly, we perform the same matrix element squaring, summing, and sorting as in the maximal SNR set selector. The first selected matrix column will always maximise the SNR. In each subsequent iteration, the matrix columns are compared to the selected column in the previous iteration.

The elements of each remaining matrix column during the iteration are compared to the selected column elements, which requires taking divisions of $(N_{\mathrm{t}}^{\mathrm{a}} - i) \times N_{\mathrm{r}}^{\mathrm{a}}$ matrix column elements during the i^{th} iteration. The number of operations for integer division is the same as for integer multiplication N_{bit}^2 [378]. Therefore, within each iteration $(N_{\mathrm{t}}^{\mathrm{a}} - i) \times N_{\mathrm{r}}^{\mathrm{a}} \times N_{\mathrm{bit}}^2$ division operations are required. Furthermore, all of the ratios need to be summed again, requiring $(N_{\mathrm{t}}^{\mathrm{a}} - i) \times N_{\mathrm{r}}^{\mathrm{a}}$ summations, with the total number of operations for summation during the iteration being $(N_{\mathrm{t}}^{\mathrm{a}} - i) \times N_{\mathrm{r}}^{\mathrm{a}} \times N_{\mathrm{bit}}$. Finally, a bubble sort is performed during each iteration over $N_{\mathrm{t}}^{\mathrm{a}} - i$ column values. The following operations during i^{th} iteration can be summarised as:

$$N_{\text{iter}}^{\text{ops}} = (N_{\text{t}}^{\text{a}} - i)N_{\text{r}}^{\text{a}}N_{\text{bit}}^{2} + (N_{\text{t}}^{\text{a}} - i)N_{\text{r}}^{\text{a}}N_{\text{bit}} + (N_{\text{t}}^{\text{a}} - i)^{2}. \tag{B.8}$$

Performing selection up to the j^{th} iteration requires summing the number of operations contributed by each iteration, resulting in

$$N_{\text{iters}}^{\text{ops}} = \sum_{i=1}^{\text{j}}((N_{\text{t}}^{\text{a}} - i)N_{\text{r}}^{\text{a}}N_{\text{bit}}^{2} + (N_{\text{t}}^{\text{a}} - i)N_{\text{r}}^{\text{a}}N_{\text{bit}} + (N_{\text{t}}^{\text{a}} - i)^{2}). \tag{B.9}$$

Finally, combining the number of operations from j algorithm iterations with the number of operations from the initial maximal SNR-based set selection, we get:

$$\begin{aligned} N_{\text{alg3}}^{\text{ops}} = N_{\text{t}}^{\text{a}}N_{\text{r}}^{\text{a}}N_{\text{bit}}^{2} + N_{\text{r}}^{\text{a}}N_{\text{t}}^{\text{a}}N_{\text{bit}} + (N_{\text{t}}^{\text{a}})^{2} + \\ \sum_{i=1}^{\text{j}}((N_{\text{t}}^{\text{a}} - i)N_{\text{r}}^{\text{a}}N_{\text{bit}}^{2} + (N_{\text{t}}^{\text{a}} - i)N_{\text{r}}^{\text{a}}N_{\text{bit}} + (N_{\text{t}}^{\text{a}} - i)^{2}). \end{aligned} \tag{B.10}$$

Appendix C

64-QAM BER Evaluation

To evaluate BER of M-QAM modulation for a given SNR $\gamma_{\mathrm{b(elec)}}$ per bit given as [295]:

$$P_{\mathrm{bit,QAM}} = \frac{4(\sqrt{M}-1)}{\sqrt{M}\log_2(M)} Q(\sqrt{\frac{3\log_2(M)}{M-1}\gamma_{\mathrm{b(elec)}}}) + \frac{4(\sqrt{M}-2)}{\sqrt{M}\log_2(M)} Q(3\sqrt{\frac{3\log_2(M)}{M-1}\gamma_{\mathrm{b(elec)}}}), \tag{C.1}$$

one needs to estimate $\gamma_{\mathrm{b(elec)}}$. The SNR per bit is given as [125]:

$$\gamma_{\mathrm{b(elec)}} = \frac{\bar{E}_{\mathrm{bit}}}{N_0} \tag{C.2}$$

where $\bar{E}_{\mathrm{bit}}$ - average energy per bit, which can be calculated from [251]:

$$E_{\mathrm{bit}} = \frac{\bar{E}_{\mathrm{symb}}}{\log_2 M} \tag{C.3}$$

where $\bar{E}_{\mathrm{symb}}$ is average symbol electrical energy. The noise spectral density can be calculated using expressions described in subsection 3.4.1. By definition, the symbol energy E_{symb}, in turn, can be calculated from the rms symbol electrical power P_{rms} as:

$$E_{\mathrm{symb}} = P_{\mathrm{rms}} T_{\mathrm{symb}}, \tag{C.4}$$

where T_{symb} is symbol duration. The rms symbol electrical power is within the range of P_{min} and P_{max}, where P_{min} corresponds to the QAM symbol with the lowest electrical energy, while P_{max} corresponds to the symbol with the highest electrical energy.

For 64-QAM, we assume the use of repetition coding, with all transmitters emitting the same QAM symbol. In evaluating the root mean square (rms) QAM electrical power, it is important to note that both the I (in-phase) and Q (quadrature) components are represented by sine waveforms. The relationship between the peak-to-peak and rms voltage for sine waveforms is well established and is given as follows

$$V_{\mathrm{rms}} = \frac{V_{\mathrm{pp}}}{2\sqrt{2}}, \tag{C.5}$$

while the relation between rms electrical power and rms voltage is given by:

$$P_{\mathrm{rms}} = \frac{V_{\mathrm{rms}}^2}{R} \tag{C.6}$$

Assuming for simplicity load resistance of $R = 1\,\Omega$, the rms signal electrical power is given as:

$$P_{\mathrm{rms}} = \frac{V_{\mathrm{pp}}^2}{8}. \tag{C.7}$$

The maximum rms electrical power that a transmitter beam can supply to the receiver, given the channel conditions, is denoted as P_{max}. Consequently, when both the I (in-phase) and Q (quadrature) components are at their maximum, the maximum rms power for each component's sine wave can be expressed as $0.5P_{\mathrm{max}}$. Therefore, the maximum rms power of either the I or Q component's sine wave, in terms of peak-to-peak voltage, can be expressed as follows:

$$P_{\mathrm{max}_{\mathrm{I,Q}}} = \frac{1}{2}P_{\mathrm{max}} = \frac{1}{2}V_{\mathrm{rms,max}}^2 = \frac{1}{2}\frac{V_{\mathrm{pp,max}}^2}{8}. \tag{C.8}$$

we can determine the value of $V_{\mathrm{pp,max}}^2$ from the peak received optical power following the steps described in 3.4.1 subsection. The $P_{\mathrm{min}_{\mathrm{I,Q}}}$ assuming extinction ratio of 10 is given as:

$$P_{\mathrm{min}_{\mathrm{I,Q}}} = 0.1P_{\mathrm{max}_{\mathrm{I,Q}}}. \tag{C.9}$$

We assume that the transmitters are located at a considerable distance from the receiver, such that the electrical power generated at the receiver by each transmitter beam is approximately equal. The maximum electrical signal power received therefore is $N_{\text{beams}} P_{\text{max}_{\text{I,Q}}}$.

In a 64-QAM square lattice the lattice constant (spacing) between constellation points is:

$$\Delta P_{\text{symb}} = \frac{P_{\text{max}_{\text{I,Q}}} - P_{\text{min}_{\text{I,Q}}}}{7}, \tag{C.10}$$

based on the expressions above, all of the QAM symbol electrical powers and energies can be calculated. The number of transmitter beams required can be determined to achieve the desired BER for the targeted data throughput. Once the number of beams has been established, the energy consumption can be evaluated.

Appendix D

Prober Module Implementation in Simulink

The overview of the prober module implementation, along with related modules, is illustrated in Figure D.1. The prober is a module that "probes" i.e, determines the signal strength of each transmitter at the receiver to determine the number of avilable transmitters for the beam selection algorithm, as well as to estimate the channel gain of each transmitter beam at the receiver.

The module comprises the following main subsystems: PROBE, TX_ALG_BODY, and TGR_PRB_RX1. Its two principal outputs are READ_SEL (serving as an input to the beam selector module BEAM_SLC) and CH_CTRL_OUT, a control signal that indicates whether the algorithm is in the probing stage or data transmission phase.

The PROBE subsystem comprises a simple HDL counter that operates with a sample time of 2 ns. This counter initiates counting from an initial value of 1, incrementing by a step value of 1 until it reaches 10. It inputs values ranging from 1 to 10 into a 1-D lookup table. Depending on the input from the HDL counter, the lookup table's data outputs are 1, 2, 4, 8, 15, or 0. The probe module is enabled by default at the beginning of algorithm execution. This activation is ensured by the switch block above, which, at the start of the algorithm execution, receives a control input of 0, thereby triggering the PROBE subsystem. The lookup data outputs are selected to ensure that the integers, when represented in binary, correspond to 0000, 0001, 0010, 0100, and

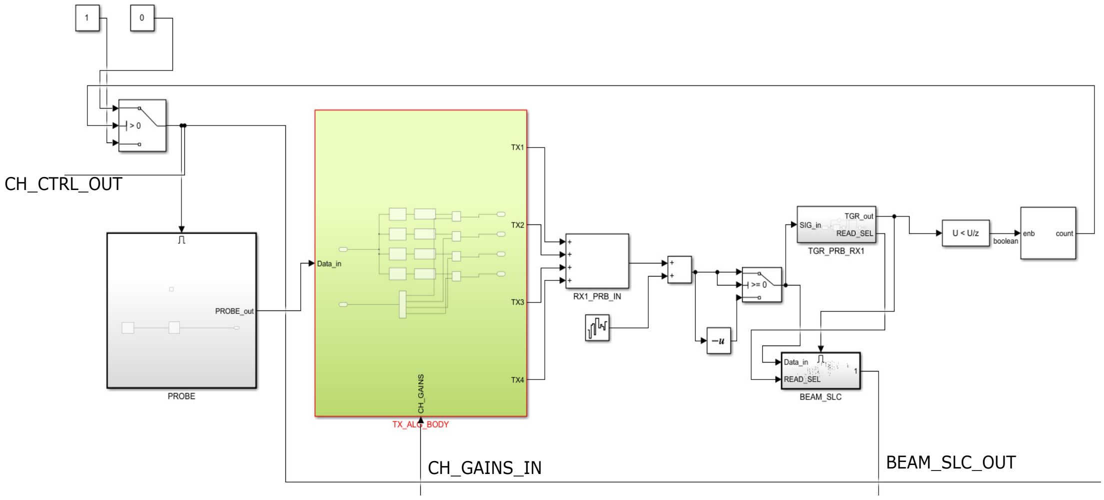

Figure D.1: Prober module implementation in Simulink overview.

1000 values, with each binary position indicating a transmitter beam to be activated.

The PROBE_OUT signal subsequently serves as an input to TX_ALG_BODY, an overview of which is depicted in Figure D.2. In this stage, the signal, represented by binary vectors, is divided into four parallel paths. These paths are then converted into 16-bit binary vectors for channel amplitude representation. In a real system, the outputs from the slicing blocks would act as inputs to the transmitter beam's analogue front-end. Following this, the CH_GAINS input, which models the optical wireless channel and the analogue front-end of the receiver and is represented as a 4-D 16-bit vector, is demultiplexed and each component is multiplied with the corresponding transmitter beam output to simulate signal transmission. Outputs from TX1 to TX4 represent the transmitted electrical power from each beam. These outputs are then aggregated by a sum block, RX_PRB_IN, which simulates the combination of beams at the receiver. Finally, AWG noise is added to the output of RX_PRB_IN.

To ensure the signal maintains a unipolar format in 16-bit representation, a unary minus block, in conjunction with a switch, is employed to convert negative samples into positive values.

The output from the switch divides into two paths: one leading to the subsystem TGR_PRB_RX, and the other to BEAM_SLC (beam selector module). At the beginning of the algorithm's execution, the beam selector module is not in an activated state. The

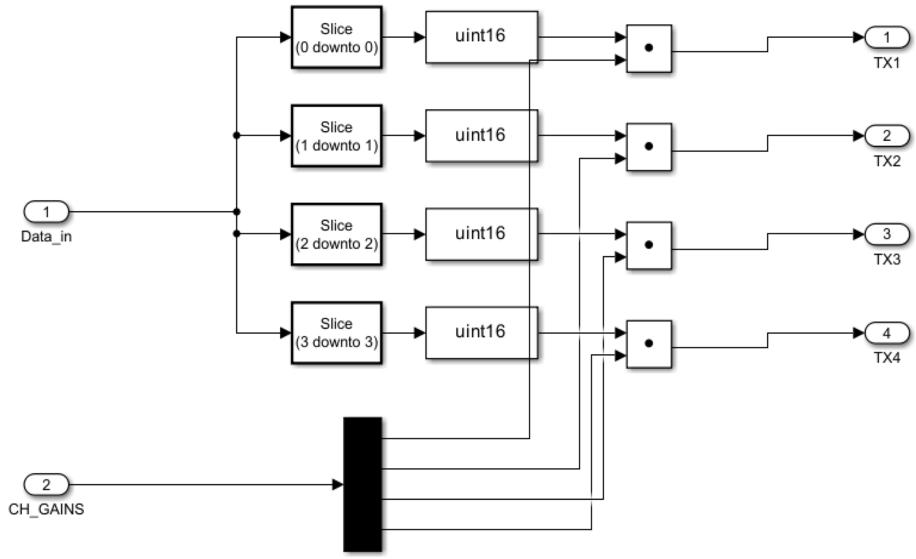

Figure D.2: TX_ALG_BODY subsystem overview.

trigger signal is provided by the subsystem TGR_PRB_RX1, an overview of which is illustrated in Figure D.3.

Within the subsystem, the received electrical signal is directed to the interval test block, where it is compared against a lower limit threshold. The upper limit is set at $2^{16}-1$, representing the maximum amplitude signal of 16 '1's, while the minimum value is established at 2^12. This minimum threshold is chosen to ensure that noise alone does not activate the probing trigger. Following the interval test, the detection of a rising edge causes the boolean output of the 'detect increase' function to activate the HDL counter. This counter is equipped with input, output, and reset ports, starting at an initial value of 0, with a step increment of one. It operates in a free-running mode, where each 'true' boolean signal prompts it to count during a sample period.

Should the HDL counter output a value greater than 0, it activates another HDL counter block, which is designed with a count limit. This second counter also starts with an initial value of 0 and a step value of 1 but has a maximum count of 31. Its output is then routed to a TGR_OUT port, the READ_SEL port, and back into a

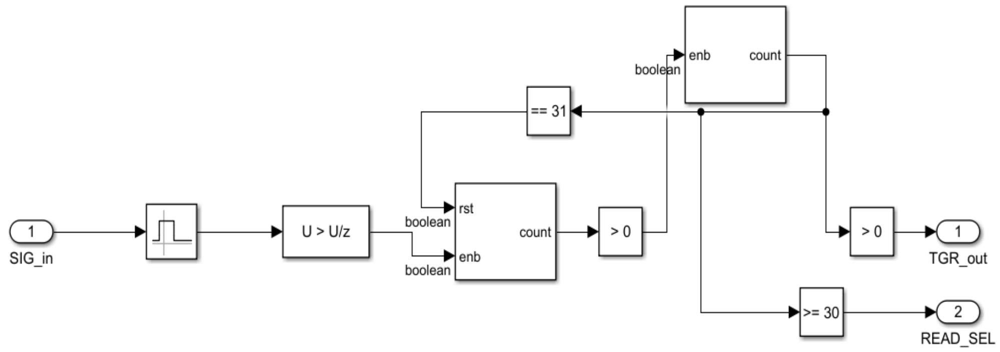

Figure D.3: TGR_PBR subsystem overview.

feedback reset port of the initial counter.

The READ_SEL port triggers the readout of the beam selector module. The TGR_OUT value is directed to both a falling edge detector (detect decrease block) and the BEAM_SLC subsystem. When TGR_OUT is in a high state ("1"), the beam selector module is active and performs beam selection. It can be observed that the read-out of beam selection occurs one sample before transitioning to the data transmission stage.

The transition occurs once a count of 31 is reached within the TGR_PRB_RX1 subsystem. At this point, the count on the first HDL counter is reset, and the second counter is deactivated and reset to 0. Subsequently, the falling edge detector activates the final HDL counter, which operates in free-running mode with an initial value of 0 and a step value of 1. The output from this HDL counter is directed to the switch, which then deactivates the prober module, signalling the commencement of the data transmission stage.

Appendix E

Encoder Module Implementation in Simulink

The overview of the encoder module implementation and its associated modules is depicted in Figure E.1. The module possesses three inputs: enable (ENBL), feedback (FDBCK), and beam selector input (BEAM_SLC_IN).

After the probing stage is completed, the enable signal activates the HDL counter, which counts from 1 to 1151 with a step value of 1. The value of 1151 sets the length of the test data packet. In this model, the test data is predetermined and encoded in codebook blocks, represented by 1D lookup table blocks. For random data bits, an additional input data port would be necessary, which would program the codebooks in real time to output the GSSK symbol corresponding to the random data bit.

Based on the BEAM_SLC_IN input, the encoder determines whether the test data packet should be encoded using 4, 3, 2-beam GSSK encoding or as an OOK one. Each codebook block generates a binary vector, the content of which varies depending on the GSSK encoding scheme employed. For instance, with 4-beam GSSK encoding, the binary vector can assume any value from 0000 to 1111, with each vector representing a distinct GSSK symbol. It is important to note that the BEAM_SLC_IN input comprises a 16-bit vector, where each quarter of the bits represents the beam selection for the corresponding number of active beams.

To select the suitable GSSK codebook block output based on the beam selector

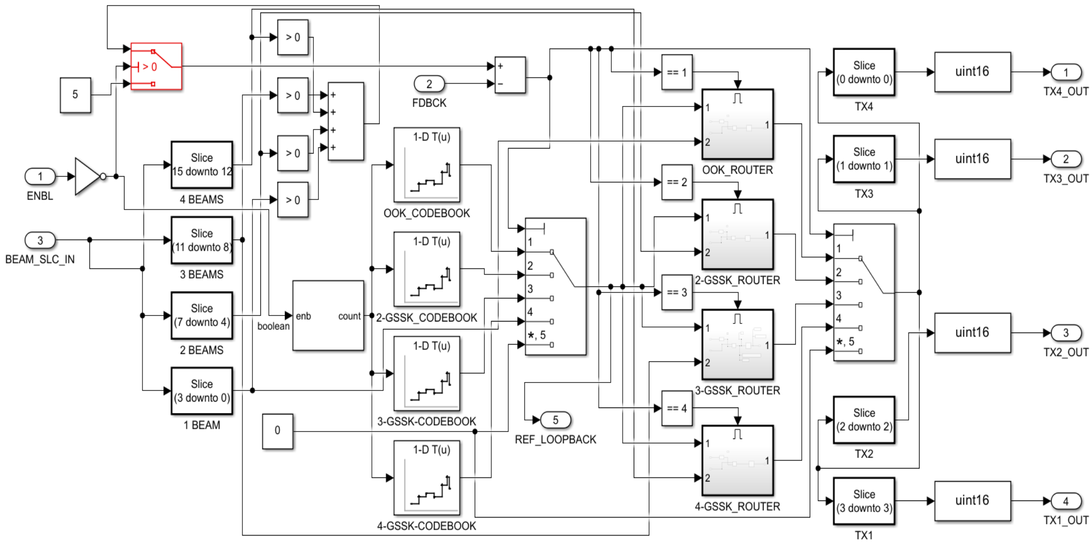

Figure E.1: Encoder module implementation in Simulink overview.

input, a switch block is utilised subsequent to the codebook blocks. The control input (labelled as number 1) relies on the signal derived from the sum of slice blocks, indicating the number of engaged beams. During the transmission of the first test data packet, the encoder lacks feedback on the Bit Error Ratio (BER) and thus bases its encoding decision solely on the selection made during the probing stage. At the conclusion of the first data packet transmission, a memory reset (MEM_RST) and read signal is activated at the receiver. In the course of the memory read, the packet analyser assesses the BER; should the BER of the data packet surpass the maximum threshold, the analyser emits a signal of one, which is then sent through the feedback channel to the encoder while simultaneously storing this value in the receiver's memory.

The feedback signal is integrated with the sum from the beam slice block for the subsequent packet transmission, indicating a reduction in the number of beams engaged in the link. The combined output of the feedback (FDBCK) signal and the sum from the beam slice blocks is utilised to activate the corresponding GSSK_ROUTER subsystem. This subsystem then maps the GSSK symbol to the specific combination of engaged beams.

The implementation of the subsystem is illustrated in Figure E.2. This subsystem straightforwardly concatenates the GSSK symbol with the chosen combination

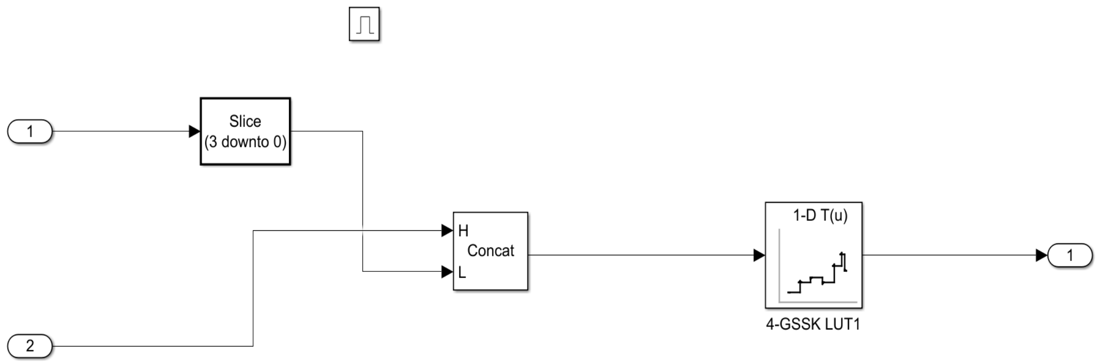

Figure E.2: GSSK_ROUTER subsystem overview.

of engaged beams. Subsequently, the concatenated binary vector is mapped to a specific beam activation pattern using a lookup table block. The output from the GSSK_ROUTER subsystem is a 4-bit binary vector.

The output from the GSSK_ROUTER is subsequently selected by a switch block, which employs the difference between the beam selection and feedback signal to choose the appropriate signal. The 4-bit binary vector is then demultiplexed to the TX outputs, which are designed to drive the analogueue transmitter beams.

Appendix F

Beam Selector Module Implementation in Simulink

The overview of the beam selection module implementation and its associated subsystems is depicted in Figure F.1. The module features two inputs: Data_in and READ_SEL, and one output: BEAM_SLC_OUT. Data_in represents the probing data from the probing stage, which is utilised to assess the signal strength from each transmitter beam at the receiver. To avoid capturing the noise floor, a dot product of Data_in with the output from its interval test block is computed. This process determines whether the signal exceeds the threshold of 2^{12} bits.

The module is activated when it receives a signal marking the start of the probing phase, thereby triggering the module. It employs HDL counter blocks to simulate an internal clock mechanism. The leftmost HDL counter block has a count range limited from 0 to 1, with an increment step of 1. When its output reaches the high state of binary '1', it activates two other HDL counter blocks by splitting its output into two separate paths.

The lower HDL counter block is configured to count from 0 to 14, with an increment step of 1. Its output is fed into a 1-D lookup table block, which, based on the input from the HDL counter block, generates an output of either 0 or 1. When the state is "1", the output from the lookup table block instructs the Euclidean beam selection subsystems to analyse the Data_in signal level.

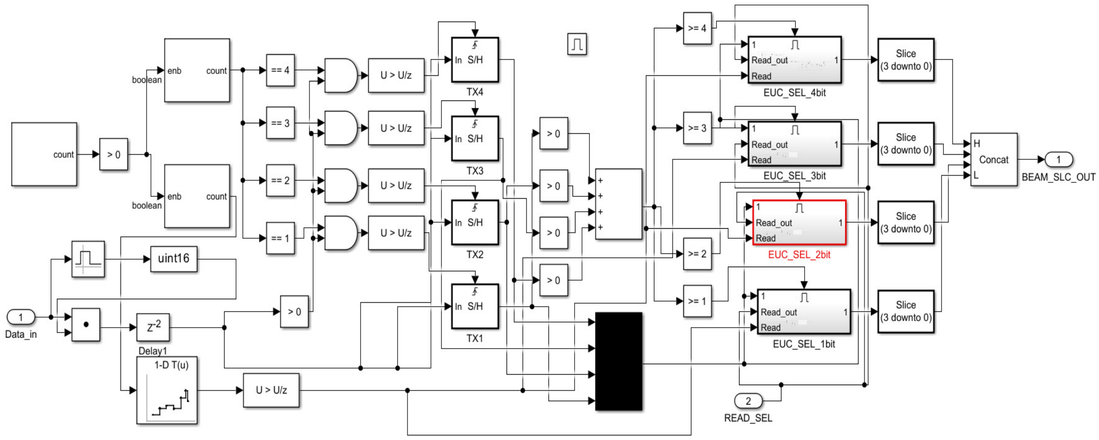

Figure F.1: Beam selection module implementation in Simulink overview.

The upper HDL counter is configured to count from 0 to 4, with an increment step of 1. Its output is compared against four distinct constants, with values ranging from 1 to 4, each corresponding to a probed transmitter beam. The boolean outputs from this comparison block are then directed to AND blocks. The second input to these AND blocks is derived from comparing the Data_in signal to a constant value of 0. Essentially, the AND blocks serve to identify whether a TX beam of a specific index has been detected.

This identification is crucial for reading the signal level of the TX beam, which is necessary for the Euclidean beam selection process. Upon detection of a rising edge in the AND block's output, the Data_in signal level at that instant is captured and stored using sample and hold blocks. This mechanism effectively assigns the measured Data_in signal level to a specific transmitter beam index.

The output of sample-and-hold blocks is directed into two primary branches. In the upper branch, the outputs are aggregated. Depending on the aggregate value, one out of four Euclidean selection blocks will be activated for beam selection, contingent upon the number of available beams in the link.

The lower branch processes the outputs by multiplexing them using a multiplexing block. The output of this block determines which transmitter beams participate in the beam selection process.

The Euclidean selection subsystem utilises the Data_in signal, the trigger from the

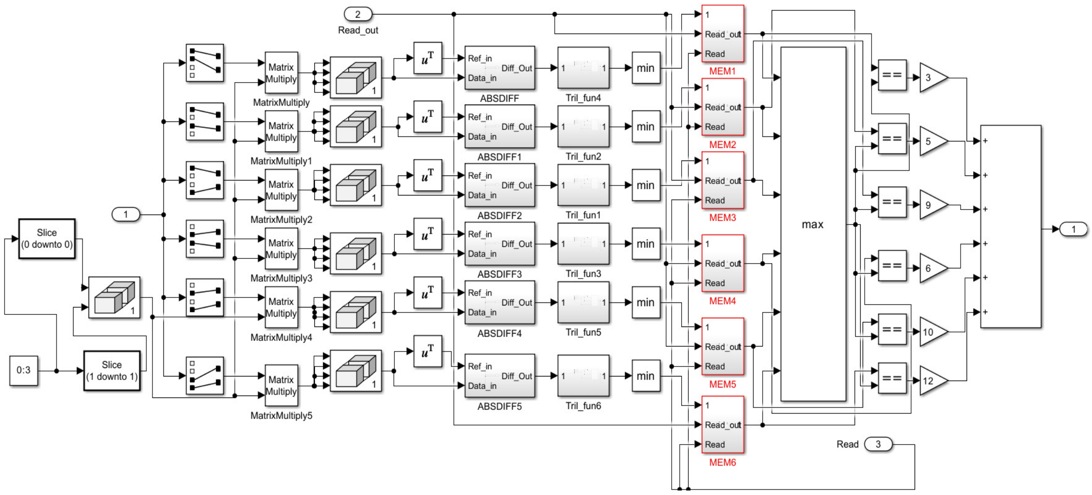

Figure F.2: Euclidean beam selection subsystem overview.

upper branch of the sample-and-hold block outputs, and the multiplexed signal of corresponding transmitter beam indices as inputs. Additionally, the READ_SEL signal is employed to control the read out of the signal levels.

The Euclidean beam selection subsystem employs the maximal minimum Euclidean distance selection criterion as described in this thesis. An example overview of a Euclidean beam selection subsystem, which selects 2 beams out of a maximum of 4, is illustrated in Figure F.2.

The module utilises the Data_in signal (input port 1), which is directed to multiple selector blocks. Each block represents a combination of engaged transmitter beams (e.g., 1,4). The output of the selector block is an index vector, which selects 2 multiplexed values out of 4, such as the 1st and 4th values of the multiplexed signal vector. In this specific example, the output pair forms a 1×2 vector. This vector undergoes matrix multiplication with a 2×4 matrix, where each element of the matrix represents a possible symbol of 2-beam GSSK encoding (totaling 4 symbols). The result of the matrix multiplication is a 1×4 vector, with each element corresponding to the signal level of a specific symbol.

To compute all possible pairwise Euclidean distances between the GSSK symbols, the 1×4 vector must first be transformed into a 4×4 matrix. This is achieved by concatenating the same vector 4 times. One of the outputs of the concatenation block is then transposed, while the other remains unchanged. Both blocks are directed into the ABSDIFF subsystem, where the absolute difference is calculated for each symbol pair. The computation of absolute differences for beam combinations is conducted in parallel. The output of the ABSDIFF subsystem is a 4×4 matrix, from which only the upper triangular part needs to be retained due to its symmetry.

Finally, the elements of the upper triangular matrix are fed into a minimum block, which identifies the minimum Euclidean pairwise symbol distance. It is noteworthy that the same procedure applies to the 1, 3, and 4 beam GSSK beam selector subsystems.

To enhance beam selection precision and diminish error probability, the probing sequences are repeated three times, resulting in three beam selection attempts. The mean value of the three minimum Euclidean distances for each beam combination is computed. This is achieved through MEM subsystems, each allocated to the corresponding beam combination. Within these subsystems, the minimum pairwise Euclidean distances of each repeated probing sequence are stored in memory, summed up, and then divided by three. Subsequently, the output of each memory subsystem is directed to the max block, which selects the beam combination with the maximum minimum Euclidean pairwise distance.

Each Euclidean beam selector subsystem facilitates the selection of combinations of engaged beams within the link. The outputs of all beam selector subsystems are concatenated into a single 16-bit vector, which is subsequently routed to the encoder. In instances where the available beam number is insufficient for the selection required by a particular beam selector subsystem, the subsystem outputs a string of four zeros.

Appendix G

Decoder Module Implementation in Simulink

The overview of the decoder module implementation and its related subsystems is depicted in Figure G.1. The module comprises a single port for three inputs and a trigger, along with 10 output ports.

As depicted in the Figure, the module comprises 5 subsystems: 4 for respective GSSK modulation decoding and one for modulation scheme identification (ID subsystem). Upon receiving Data_in transmitted over the channel from the transmitter, the module outputs, based on the identified modulation scheme, all the Euclidean distances between the received symbol and reference symbols obtained during training and stored in memory for the codebook.

These Euclidean distances are then directed to the maximum likelihood algorithm module, responsible for symbol selection and decoding into bits. In addition to the Euclidean distance outputs, there are DCD_ON outputs used to signal which decoder subsystem is active. Furthermore, the MEM_RST_OUT port indicates the end of the data packet for readout and reset purposes. An additional RX_CTR_OUT port, in conjunction with DCD_ON, controls the maximum likelihood algorithm block.

The received data, represented by the Data_in signal, is routed to the GSSK-DECODER subsystems. The selection and triggering of the subsystem processing the input data are determined by the output of the ID subsystem.

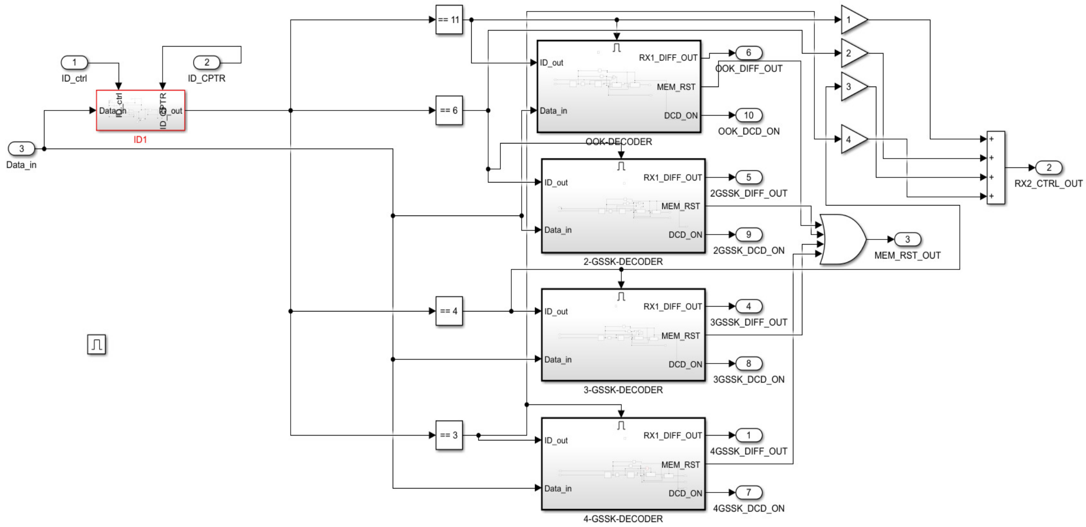

Figure G.1: Decoder module implementation in Simulink overview.

The overview of the ID subsystem is presented in Figure G.2. This subsystem comprises a single output port, which provides the count of rectangular pulses captured during the ID stage. This count is subsequently utilised to trigger the appropriate modulation decoder.

Furthermore, the subsystem consists of the following three inputs: Data_in, ID_ctrl, and ID_CPTR. The latter two inputs delineate the start and readout of the ID frame. The rising edge block triggers and counts the number of rectangular pulses by providing input to the HDL counter block. Additionally, the ID_ctrl input resets the pulse count-

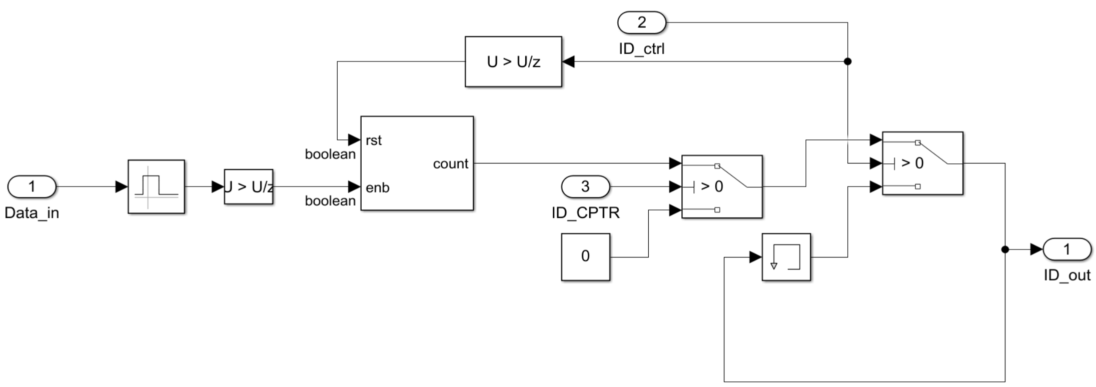

Figure G.2: ID subsystem overview.

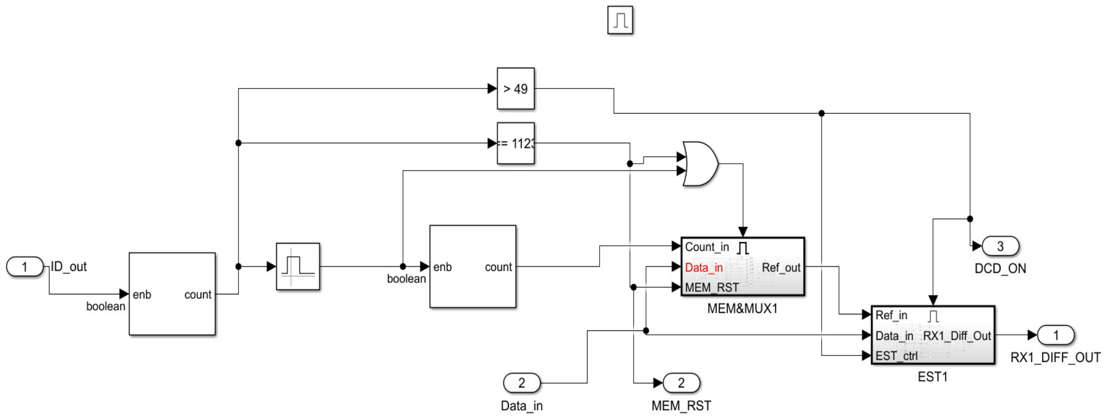

Figure G.3: GSSK-DECODER subsystem overview.

ing, essential for modulation identification during subsequent package transmissions. The subsystem also incorporates a memory block to store information on the identified GSSK modulation.

The Data_in signal is subsequently processed by the activated GSSK-DECODER. The overview of the GSSK-DECODER is depicted in Figure G.3. In this subsystem, the ID_out signal is input into the HDL counter block, which counts from 1 to the end of the packet. The output of the counter block is then directed to two components: firstly, to the interval test block, which outputs "1" if the count is between 2 and the end of the training frame, and secondly, to two constant comparison blocks.

The top comparison block serves to trigger the symbol distance estimation subsystem upon completion of the training frame. Conversely, the bottom comparison block, alongside the interval test block, is directed into a logical OR block. This OR block is responsible for triggering the memory and multiplexing subsystem, which is utilised for training data acquisition and storage. Additionally, the interval test block is routed to another HDL counter block, which functions as a clock counting from 0 to 1 with a count step of 1.

Once triggered, the MEM&MUX subsystem, as depicted in Figure G.4, receives input data from the Data_in port. It utilises SYMB subsystems to sample and store the symbol levels. Additionally, the SYMB subsystems accumulate the respective symbol levels until three values are stored, and their mean value is utilised as the reference level.

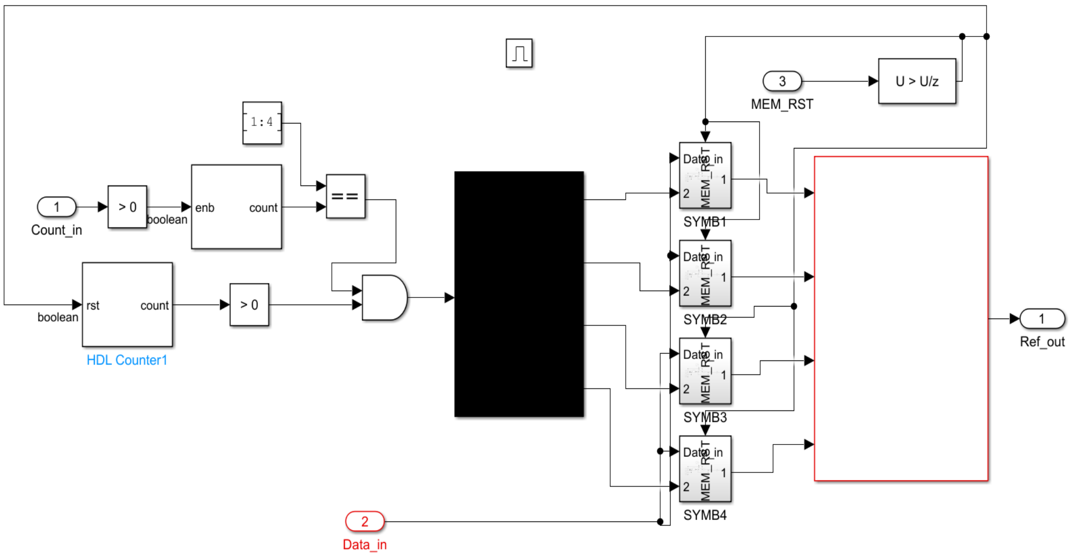

Figure G.4: MEM&MUX subsystem overview.

This process aims to enhance the precision of the symbol reference level determination.

The reference levels are then multiplexed and directed to the EST subsystem, as depicted in Figure G.5. This subsystem comprises three inputs: Ref_in, Data_in, and EST_ctrl. The Ref_in input is demultiplexed and routed to the difference subsystem, where the absolute difference between the received symbol in Data_in and the reference level is computed. Once the differences have been calculated, they are multiplexed and forwarded to the maximum likelihood algorithm module.

The overview of the maximum likelihood algorithm module is illustrated in Figure G.6. This module comprises eight input ports. Four of these ports receive Euclidean distance inputs from different receiver decoders. The GSSK_CTRL port triggers the GSSK_ML_ALG subsystem, responsible for selecting and decoding the received symbol into bits. The MEM_RST_IN block resets the packet analyser subsystem (CMP_GSSK) at the end of the packet. REF_LOOPBACK provides the packet analyser with the reference packet data necessary for bit error rate (BER) estimation. DCD_ON, in conjunction with the GSSK_CTRL signal, triggers the maximum likelihood subsystem.

The Frobenius norm is computed for the Euclidean distance inputs from multiple receivers, which are then directed to the GSSK_ML_ALG subsystem illustrated in

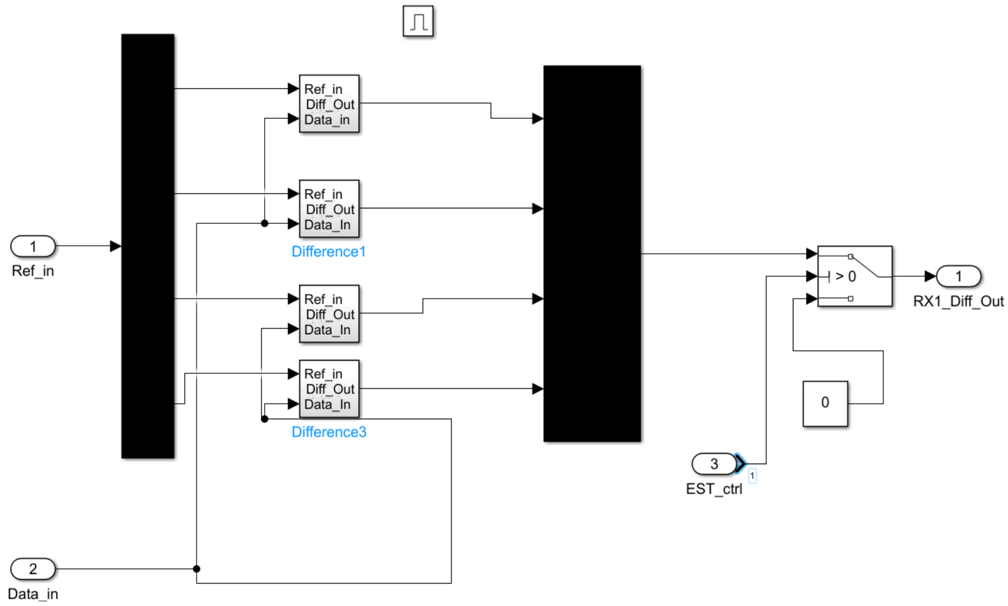

Figure G.5: EST subsystem overview.

Figure G.7. Within this subsystem, the Data_in signal of the Euclidean distances is compared to its minimum value to ascertain which reference symbol, during sampling, exhibits the least difference to the received symbol. Subsequently, the output of the equal block comprises a multiplexed signal consisting of a multiple 0 binary word and a single non-zero binary word vector.

These multiplexed vectors are ordered and then multiplied with another multiplexed signal of vectors, where each vector represents the binary string corresponding to the selected symbol. A dot product is performed, and all the multiplexed vectors are summed into a single vector, yielding the binary decoded output of the received symbol.

Finally, the decoded symbol is transmitted to the packet analyser subsystem labeled as CMP_GSSK, where it undergoes comparison with the reference data to estimate the BER. The analyser outputs the number of erroneous bits in the packet. Should the packet surpass the permissible number of erroneous bits (e.g., 4 bits), the FDBCK signal becomes 1, indicating that the signal is sent to the encoder module via the feedback channel to adjust the modulation scheme. Conversely, if the number of erroneous bits does not exceed the threshold, the modulation scheme remains unchanged.

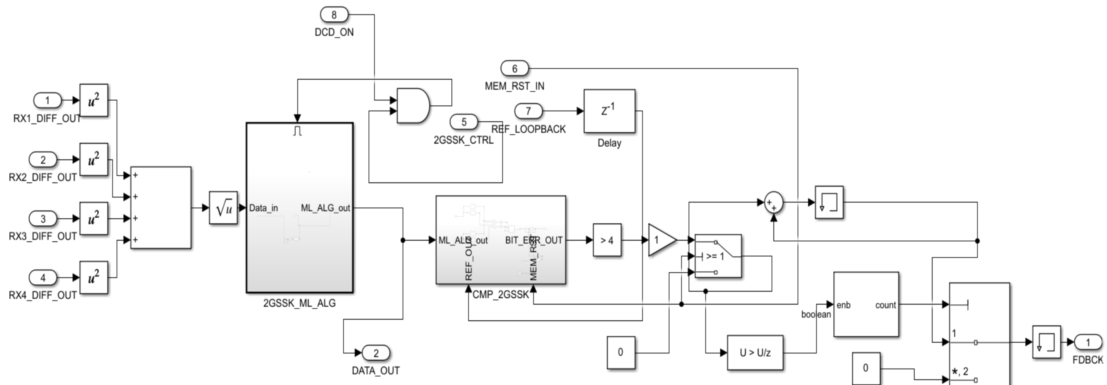

Figure G.6: Maximum likelihood module overview.

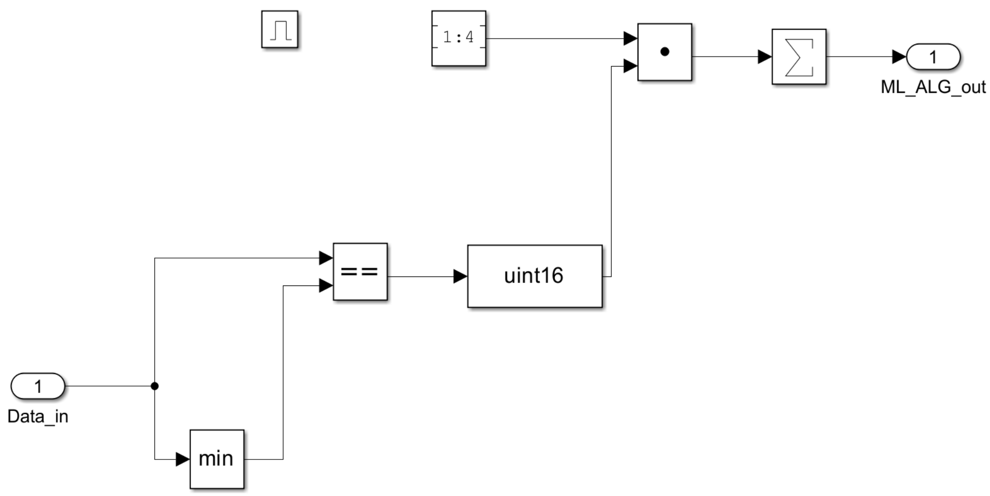

Figure G.7: GSSK_ML_ALG subsystem overview.

Appendix H

List of Publications

Patents:

- Haas, Harald Ulrich, and Janis Sperga. Freeform optics for optical wireless communications, issued November 16, 2023.

Conference publications:

- J. Sperga, M. S. Islim, R. Bian, G. L. Martena, and H. Haas, "Photodiode Arrays Do Not Violate the Second Law of Thermodynamics: Photocurrent Bandwidth Trade-Off," ICC 2024 - IEEE International Conference on Communications, Denver, CO, USA, 2024, pp. 2414-2419, doi: 10.1109/ICC51166.2024.10622212.
- J. Sperga et al., "Thin Receiver Freeform Lenslet Concentrator Array for LiFi," 2023 IEEE International Conference on Communications Workshops (ICC Workshops), Rome, Italy, 2023, pp. 92-97, doi: 10.1109/ICCWorkshops57953.2023.10283779.
- G. L. Martena et al., "A Simulation Tool for Interference Analysis in MIMO Wavelength Division LiFi Indoor Networks," 2023 IEEE International Conference on Communications Workshops (ICC Workshops), Rome, Italy, 2023, pp. 86-91, doi: 10.1109/ICCWorkshops57953.2023.10283751.
- J. Sperga, R. Bian and H. Haas, "Beam Selection in Angle Diversity MIMO Systems for Optical Wireless Systems," 2022 IEEE International Conference on

Communications Workshops (ICC Workshops), Seoul, Korea, Republic of, 2022, pp. 445-450, doi: 10.1109/ICCWorkshops53468.2022.9814683.

Bibliography

[1] "Mobile data traffic forecast – mobility report - ericsson," 2023. [Online]. Available: https://www.ericsson.com/en/reports-and-papers/mobility-report/dataforecasts/mobile-traffic-forecast

[2] Sandvine, "The global internet phenomena report: Covid-19 spotlight," *Sandvine*, 2020. [Online]. Available: https://www.sandvine.com/covid-internet-spotlight-report

[3] "Enerdata, 2020. between 10 and 20% of electricity consumption from the ict* sector in 2030?" Aug 2018. [Online]. Available: https://www.enerdata.net/publications/executive-briefing/between-10-and-20-electricity-consumption-ict-sector-2030.html

[4] N. Jones, "How to stop data centres from gobbling up the world's electricity," *Nature*, vol. 561, no. 7722, p. 163–166, 2018. [Online]. Available: https://doi.org/10.1038/d41586-018-06610-y

[5] E. Masanet, A. Shehabi, N. Lei, S. Smith, and J. Koomey, "Recalibrating global data center energy-use estimates," *Science*, vol. 367, no. 6481, pp. 984–986, 2020. [Online]. Available: https://doi.org/10.1126/science.aba3758

[6] S. Al-Sarawi, M. Anbar, R. Abdullah, and A. B. Al Hawari, "Internet of things market analysis forecasts, 2020–2030," in *2020 Fourth World Conference on Smart Trends in Systems, Security and Sustainability (WorldS4)*, 2020, pp. 449–453. [Online]. Available: https://doi.org/10.1109/WorldS450073.2020.9210375

[7] M. Khan and J. Chakareski, “Visible light communication for next generation untethered virtual reality systems,” in *2019 IEEE International Conference on Communications Workshops (ICC Workshops)*, 2019, pp. 1–6. [Online]. Available: https://doi.org/10.1109/ICCW.2019.8757099

[8] M. Hu, X. Luo, J. Chen, Y. C. Lee, Y. Zhou, and D. Wu, “Virtual reality: A survey of enabling technologies and its applications in iot,” *Journal of Network and Computer Applications*, vol. 178, p. 102970, 2021. [Online]. Available: https://doi.org/10.1016/j.jnca.2020.102970

[9] “2023 mobile industry impact report summary,” Sep 2023. [Online]. Available: https://www.gsma.com/betterfuture/resources/2023-mobile-industry-impact-report-summary

[10] J. S. Jones, “5g 90% more energy efficient than 4g, nokia and telefónica find,” May 2021. [Online]. Available: https://www.smart-energy.com/digitalisation/5g-90-more-energy-efficient-than-4g-nokia-and-telefonica-find/

[11] S. Sen, J. Koo, and S. Bagchi, “Trifecta: Security, energy efficiency, and communication capacity comparison for wireless iot devices,” *IEEE Internet Computing*, vol. 22, no. 1, pp. 74–81, 2018. [Online]. Available: https://doi.org/10.1109/MIC.2018.011581520

[12] G. Aceto, V. Persico, and A. Pescapé, “A survey on information and communication technologies for industry 4.0: State-of-the-art, taxonomies, perspectives, and challenges,” *IEEE Communications Surveys & Tutorials*, vol. 21, no. 4, pp. 3467–3501, 2019. [Online]. Available: https://doi.org/10.1109/COMST.2019.2938259

[13] J. Laitner and M. Berners-Lee, “Smarter2030 ict solutions for 21st century challenges,” 2015. [Online]. Available: https://smarter2030.gesi.org/downloads/Full_report.pdf

[14] C. Gabriel, Hansang, and A. Chern, “Green 5g: Building a sustainable world,” August 2020. [Online]. Avail-

able: https://www-file.huawei.com/-/media/corp2020/pdf/public-policy/green_5g_building_a_sustainable_world_v1.pdf?la=en

[15] A. Abrol and R. K. Jha, “Power optimization in 5g networks: A step towards green communication,” *IEEE Access*, vol. 4, pp. 1355–1374, 2016. [Online]. Available: https://doi.org/10.1109/ACCESS.2016.2549641

[16] R. Dangi, P. Lalwani, G. Choudhary, I. You, and G. Pau, “Study and investigation on 5g technology: A systematic review,” *Sensors*, vol. 22, no. 1, 2022. [Online]. Available: https://doi.org/10.3390/s22010026

[17] T. L. Marzetta, “Noncooperative cellular wireless with unlimited numbers of base station antennas,” *IEEE Transactions on Wireless Communications*, vol. 9, no. 11, pp. 3590–3600, 2010. [Online]. Available: https://doi.org/10.1109/TWC.2010.092810.091092

[18] E. Björnson, J. Hoydis, and L. Sanguinetti, “Massive mimo networks: Spectral, energy, and hardware efficiency,” *Foundations and Trends® in Signal Processing*, vol. 11, no. 3-4, pp. 154–655, 2017. [Online]. Available: http://dx.doi.org/10.1561/2000000093

[19] Özlem Tugfe Demir, E. Björnson, and L. Sanguinetti, “Foundations of user-centric cell-free massive mimo,” *Foundations and Trends® in Signal Processing*, vol. 14, no. 3-4, pp. 162–472, 2021. [Online]. Available: http://dx.doi.org/10.1561/2000000109

[20] X. Lin, J. Li, R. Baldemair, J.-F. T. Cheng, S. Parkvall, D. C. Larsson, H. Koorapaty, M. Frenne, S. Falahati, A. Grovlen, and K. Werner, “5g new radio: Unveiling the essentials of the next generation wireless access technology,” *IEEE Communications Standards Magazine*, vol. 3, no. 3, pp. 30–37, 2019. [Online]. Available: https://doi.org/10.1109/MCOMSTD.001.1800036

[21] D. López-Pérez, A. De Domenico, N. Piovesan, G. Xinli, H. Bao, S. Qitao, and M. Debbah, “A survey on 5g radio access network energy efficiency:

Massive mimo, lean carrier design, sleep modes, and machine learning," *IEEE Communications Surveys & Tutorials*, vol. 24, no. 1, pp. 653–697, 2022. [Online]. Available: https://doi.org/10.1109/COMST.2022.3142532

[22] O. Blume, D. Zeller, and U. Barth, "Approaches to energy efficient wireless access networks," in *2010 4th International Symposium on Communications, Control and Signal Processing (ISCCSP)*, 2010, pp. 1–5. [Online]. Available: https://doi.org/10.1109/ISCCSP.2010.5463328

[23] N. C. Luong, D. T. Hoang, S. Gong, D. Niyato, P. Wang, Y.-C. Liang, and D. I. Kim, "Applications of deep reinforcement learning in communications and networking: A survey," *IEEE Communications Surveys & Tutorials*, vol. 21, no. 4, pp. 3133–3174, 2019. [Online]. Available: https://doi.org/10.1109/COMST.2019.2916583

[24] Y. Xiao, G. Shi, Y. Li, W. Saad, and H. V. Poor, "Toward self-learning edge intelligence in 6g," *IEEE Communications Magazine*, vol. 58, no. 12, pp. 34–40, 2020. [Online]. Available: https://doi.org/10.1109/MCOM.001.2000388

[25] W. Saad, M. Bennis, and M. Chen, "A vision of 6g wireless systems: Applications, trends, technologies, and open research problems," *IEEE Network*, vol. 34, no. 3, pp. 134–142, 2020. [Online]. Available: https://doi.org/10.1109/MNET.001.1900287

[26] I. F. Akyildiz, C. Han, Z. Hu, S. Nie, and J. M. Jornet, "Terahertz band communication: An old problem revisited and research directions for the next decade," *IEEE Transactions on Communications*, vol. 70, no. 6, pp. 4250–4285, 2022. [Online]. Available: https://doi.org/10.1109/TCOMM.2022.31718007

[27] Y. Liu, S. Zhang, X. Mu, Z. Ding, R. Schober, N. Al-Dhahir, E. Hossain, and X. Shen, "Evolution of noma toward next generation multiple access (ngma) for 6g," *IEEE Journal on Selected Areas in Communications*, vol. 40, no. 4, pp. 1037–1071, 2022. [Online]. Available: https://doi.org/10.1109/JSAC.2022.3145234

[28] F. Fang, Y. Xu, Q.-V. Pham, and Z. Ding, "Energy-efficient design of irs-noma networks," *IEEE Transactions on Vehicular Technology*, vol. 69, no. 11, pp. 14 088–14 092, 2020. [Online]. Available: https://doi.org/10.1109/TVT.2020.3024005

[29] R. Alghamdi, R. Alhadrami, D. Alhothali, H. Almorad, A. Faisal, S. Helal, R. Shalabi, R. Asfour, N. Hammad, A. Shams, N. Saeed, H. Dahrouj, T. Y. Al-Naffouri, and M.-S. Alouini, "Intelligent surfaces for 6g wireless networks: A survey of optimization and performance analysis techniques," *IEEE Access*, vol. 8, pp. 202 795–202 818, 2020. [Online]. Available: https://doi.org/10.1109/ACCESS.2020.3031959

[30] B. Zheng, C. You, W. Mei, and R. Zhang, "A survey on channel estimation and practical passive beamforming design for intelligent reflecting surface aided wireless communications," *IEEE Communications Surveys & Tutorials*, vol. 24, no. 2, pp. 1035–1071, 2022. [Online]. Available: https://doi.org/10.1109/COMST.2022.3155305

[31] Q.-V. Pham, D. C. Nguyen, S. Mirjalili, D. T. Hoang, D. N. Nguyen, P. N. Pathirana, and W.-J. Hwang, "Swarm intelligence for next-generation networks: Recent advances and applications," *Journal of Network and Computer Applications*, vol. 191, p. 103141, 2021. [Online]. Available: https://doi.org/10.1016/j.jnca.2021.103141

[32] J. Mei, X. Wang, and K. Zheng, "An intelligent self-sustained ran slicing framework for diverse service provisioning in 5g-beyond and 6g networks," *Intelligent and Converged Networks*, vol. 1, no. 3, pp. 281–294, 2020. [Online]. Available: https://doi.org/10.23919/ICN.2020.0019

[33] C. D. Alwis, A. Kalla, Q.-V. Pham, P. Kumar, K. Dev, W.-J. Hwang, and M. Liyanage, "Survey on 6g frontiers: Trends, applications, requirements, technologies and future research," *IEEE Open Journal of the*

Communications Society, vol. 2, pp. 836–886, 2021. [Online]. Available: https://doi.org/10.1109/OJCOMS.2021.3071496

[34] T. S. Rappaport, Y. Xing, O. Kanhere, S. Ju, A. Madanayake, S. Mandal, A. Alkhateeb, and G. C. Trichopoulos, "Wireless communications and applications above 100 ghz: Opportunities and challenges for 6g and beyond," *IEEE Access*, vol. 7, pp. 78 729–78 757, 2019. [Online]. Available: https://doi.org/10.1109/ACCESS.2019.2921522

[35] M. Polese, J. M. Jornet, T. Melodia, and M. Zorzi, "Toward end-to-end, full-stack 6g terahertz networks," *IEEE Communications Magazine*, vol. 58, no. 11, pp. 48–54, 2020. [Online]. Available: https://doi.org/10.1109/MCOM.001.2000224

[36] I. F. Akyildiz and J. M. Jornet, "Realizing ultra-massive mimo (1024×1024) communication in the (0.06–10) terahertz band," *Nano Communication Networks*, vol. 8, pp. 46–54, 2016, electromagnetic Communication in Nano-scale. [Online]. Available: https://doi.org/10.1016/j.nancom.2016.02.001

[37] H. Elgala, R. Mesleh, and H. Haas, "Indoor optical wireless communication: potential and state-of-the-art," *IEEE Communications Magazine*, vol. 49, no. 9, pp. 56–62, 2011. [Online]. Available: https://doi.org/10.1109/MCOM.2011.6011734

[38] H. Haas, J. Elmirghani, and I. White, "Optical wireless communication," *Philosophical Transactions of the Royal Society A: Mathematical, Physical and Engineering Sciences*, vol. 378, no. 2169, p. 20200051, 2020. [Online]. Available: https://doi.org/10.1098/rsta.2020.0051

[39] P. H. Pathak, X. Feng, P. Hu, and P. Mohapatra, "Visible light communication, networking, and sensing: A survey, potential and challenges," *IEEE Communications Surveys & Tutorials*, vol. 17, no. 4, pp. 2047–2077, 2015. [Online]. Available: https://doi.org/10.1109/COMST.2015.2476474

[40] L. E. M. Matheus, A. B. Vieira, L. F. M. Vieira, M. A. M. Vieira, and O. Gnawali, "Visible light communication: Concepts, applications and challenges," *IEEE*

Communications Surveys & Tutorials, vol. 21, no. 4, pp. 3204–3237, 2019. [Online]. Available: https://doi.org/10.1109/COMST.2019.2913348

[41] L. U. Khan, "Visible light communication: Applications, architecture, standardization and research challenges," *Digital Communications and Networks*, vol. 3, no. 2, pp. 78–88, 2017. [Online]. Available: https://doi.org/10.1016/j.dcan.2016.07.004

[42] D. A. Rockwell and G. S. Mecherle, "Wavelength selection for optical wireless communications systems," in *Optical Wireless Communications IV*, E. J. Korevaar, Ed., vol. 4530, International Society for Optics and Photonics. SPIE, 2001, pp. 27 – 35. [Online]. Available: https://doi.org/10.1117/12.449812

[43] E. Ramadhani and G. P. Mahardika, "The technology of lifi: A brief introduction," *IOP Conference Series: Materials Science and Engineering*, vol. 325, no. 1, p. 012013, mar 2018. [Online]. Available: https://dx.doi.org/10.1088/1757-899X/325/1/012013

[44] W. Ali, G. Cossu, L. Gilli, E. Ertunc, A. Messa, A. Sturniolo, and E. Ciaramella, "10 gbit/s owc system for intra-data centers links," *IEEE Photonics Technology Letters*, vol. 31, no. 11, pp. 805–808, 2019. [Online]. Available: https://doi.org/10.1109/LPT.2019.2905647

[45] R. Bian, I. Tavakkolnia, and H. Haas, "15.73 gb/s visible light communication with off-the-shelf leds," *Journal of Lightwave Technology*, vol. 37, no. 10, pp. 2418–2424, 2019. [Online]. Available: https://doi.org/10.1109/JLT.2019.2906464

[46] H. Haas. (2011, August) Wireless data from every light bulb. TED. [Online]. Available: https://www.youtube.com/watch?v=NaoSp4NpkGg

[47] H. Haas, L. Yin, Y. Wang, and C. Chen, "What is lifi?" *Journal of Lightwave Technology*, vol. 34, no. 6, pp. 1533–1544, 2016. [Online]. Available: https://doi.org/10.1109/JLT.2015.2510021

[48] "Lifi companies," May 2023. [Online]. Available: https://lifi.co/lifi-companies/

[49] M. Jackson, "802.11bb standard released for wifi style visible light lifi networks," Jul 2023. [Online]. Available: https://www.ispreview.co.uk/index.php/2023/07/802-11bb-standard-released-for-wifi-style-visible-light-lifi-networks.html

[50] C. Jenila and R. Jeyachitra, "Green indoor optical wireless communication systems: Pathway towards pervasive deployment," *Digital Communications and Networks*, vol. 7, no. 3, pp. 410–444, 2021. [Online]. Available: https://doi.org/10.1016/j.dcan.2020.09.004

[51] E. Khorov, A. Kiryanov, A. Lyakhov, and G. Bianchi, "A tutorial on ieee 802.11ax high efficiency wlans," *IEEE Communications Surveys & Tutorials*, vol. 21, no. 1, pp. 197–216, 2019. [Online]. Available: https://doi.org/10.1109/COMST.2018.2871099

[52] A. Wooden, "5g advanced trial clocks 10 gbps in uae," Aug 2023. [Online]. Available: https://telecoms.com/523017/5g-advanced-trial-clocks-10-gbps-in-uae/

[53] Z. Ghassemlooy, W. Popoola, and S. Rajbhandari, *Optical wireless communications: system and channel modelling with Matlab®*. CRC press, 2019.

[54] A. B. Raj and A. K. Majumder, "Historical perspective of free space optical communications: from the early dates to today's developments," *IET Communications*, vol. 13, no. 16, pp. 2405–2419, 2019. [Online]. Available: https://doi.org/10.1049/iet-com.2019.0051

[55] J. Senior, *Optical Fiber Communications: Principles and practice*. Prentice-Hall, 2013.

[56] "1.53 petabit per second transmission in 55-mode fiber with standard cladding diameter," 2022. [Online]. Available: https://www.nict.go.jp/en/press/2022/11/10-1.html

[57] G. P. Agrawal, "Optical communication: its history and recent progress," *Optics in our time*, pp. 177–199, 2016.

[58] J. Cho, J. H. Park, J. K. Kim, and E. F. Schubert, "White light-emitting diodes: History, progress, and future," *Laser & Photonics Reviews*, vol. 11, no. 2, p. 1600147, 2017. [Online]. Available: https://doi.org/10.1002/lpor.201600147

[59] J. Y. Lin and H. X. Jiang, "Development of microLED," *Applied Physics Letters*, vol. 116, no. 10, p. 100502, 03 2020. [Online]. Available: https://doi.org/10.1063/1.5145201

[60] M. Uysal and H. Nouri, "Optical wireless communications — an emerging technology," in *2014 16th International Conference on Transparent Optical Networks (ICTON)*, 2014, pp. 1–7. [Online]. Available: https://doi.org/10.1109/ICTON.2014.6876267

[61] F. Goodwin, "A review of operational laser communication systems," *Proceedings of the IEEE*, vol. 58, no. 10, pp. 1746–1752, 1970. [Online]. Available: https://doi.org/10.1109/PROC.1970.7998

[62] M. R. Hogan and Hank, "A history of the laser: 1960 - 2019," Jun 2019. [Online]. Available: https://www.photonics.com/Articles/A_History_of_the_Laser_1960_-_2019/a42279

[63] F. Zafar, M. Bakaul, and R. Parthiban, "Laser-diode-based visible light communication: Toward gigabit class communication," *IEEE Communications Magazine*, vol. 55, no. 2, pp. 144–151, 2017. [Online]. Available: https://doi.org/10.1109/MCOM.2017.1500672CM

[64] K. James Singh, Y.-M. Huang, T. Ahmed, A.-C. Liu, S.-W. Huang Chen, F.-J. Liou, T. Wu, C.-C. Lin, C.-W. Chow, G.-R. Lin, and H.-C. Kuo, "Micro-led as a promising candidate for high-speed visible light communication," *Applied Sciences*, vol. 10, no. 20, 2020. [Online]. Available: https://doi.org/10.3390/app10207384

[65] S. Dimitrov and H. Haas, *Principles of LED light communications: Towards networked li-fi.* Cambridge University Press, 2015.

[66] S. Ishimura, R. Morita, T. Inoue, K. Nishimura, H. Takahashi, T. Tsuritani, M. De Zoysa, K. Ishizaki, M. Suzuki, and S. Noda, "Proposal and demonstration of free-space optical communication using photonic crystal surface-emitting lasers," *Journal of Lightwave Technology*, vol. 41, no. 12, pp. 3688–3694, 2023. [Online]. Available: https://doi.org/10.1109/JLT.2023.3273563

[67] T. Koonen, K. A. Mekonnen, Z. Cao, F. Huijskens, N. Q. Pham, and E. Tangdiongga, "Beam-steered optical wireless communication for industry 4.0," *IEEE Journal of Selected Topics in Quantum Electronics*, vol. 27, no. 6, pp. 1–10, 2021. [Online]. Available: https://doi.org/10.1109/JSTQE.2021.3092837

[68] T. Umezawa, T. Sakamoto, A. Kanno, A. Matsumoto, K. Akahane, N. Yamamoto, and T. Kawanishi, "25-gbaud 4-wdm free-space optical communication using high-speed 2-d photodetector array," *Journal of Lightwave Technology*, vol. 37, no. 2, pp. 612–618, 2019. [Online]. Available: https://doi.org/10.1109/JLT.2018.2881979

[69] P. Brandl, S. Schidl, and H. Zimmermann, "Pin photodiode optoelectronic integrated receiver used for 3-gb/s free-space optical communication," *IEEE Journal of Selected Topics in Quantum Electronics*, vol. 20, no. 6, pp. 391–400, 2014. [Online]. Available: https://doi.org/10.1109/JSTQE.2014.2336539

[70] H. Zimmermann, "Apd and spad receivers : Invited paper," in *2019 15th International Conference on Telecommunications (ConTEL)*, 2019, pp. 1–5. [Online]. Available: https://doi.org/10.1109/ConTEL.2019.8848547

[71] W. Gao, S. Zhang, F. Zhang, P. Wen, L. Zhang, Y. Sun, H. Chen, Z. Zheng, M. Yang, D. Luo, N. Huo, and J. Li, "2d ws2 based asymmetric schottky photodetector with high performance," *Advanced Electronic Materials*, vol. 7, no. 7, p. 2000964, 2021. [Online]. Available: https://doi.org/10.1002/aelm.202000964

[72] B. Fahs, J. Chellis, M. J. Senneca, A. Chowdhury, S. Ray, A. Mirvakili, B. Mazzara, Y. Zhang, J. Ghasemi, Y. Miao, P. Zarkesh-Ha, V. J. Koomson,

and M. M. Hella, "A 6-m ook vlc link using cmos-compatible p-n photodiode and red led," *IEEE Photonics Technology Letters*, vol. 28, no. 24, pp. 2846–2849, 2016. [Online]. Available: https://doi.org/10.1109/LPT.2016.2623558

[73] J. Kahn and J. Barry, "Wireless infrared communications," *Proceedings of the IEEE*, vol. 85, no. 2, pp. 265–298, 1997. [Online]. Available: https://doi.org/10.1109/5.554222

[74] H. Kazemi, E. Sarbazi, M. D. Soltani, M. Safari, and H. Haas, "A tb/s indoor optical wireless backhaul system using vcsel arrays," in *2020 IEEE 31st Annual International Symposium on Personal, Indoor and Mobile Radio Communications*, 2020, pp. 1–6. [Online]. Available: https://doi.org/10.1109/PIMRC48278.2020.9217368

[75] J. B. Carruthers, "Wireless infrared communications," 2002.

[76] M. Grabherr, D. Wiedenmann, R. Jaeger, and R. King, "Fabrication and performance of tuneable single-mode VCSELs emitting in the 750- to 1000-nm range," in *Vertical-Cavity Surface-Emitting Lasers IX*, C. Lei and K. D. Choquette, Eds., vol. 5737, International Society for Optics and Photonics. SPIE, 2005, pp. 120 – 128. [Online]. Available: https://doi.org/10.1117/12.590178

[77] D. M. Kuchta, A. V. Rylyakov, F. E. Doany, C. L. Schow, J. E. Proesel, C. W. Baks, P. Westbergh, J. S. Gustavsson, and A. Larsson, "A 71-gb/s nrz modulated 850-nm vcsel-based optical link," *IEEE Photonics Technology Letters*, vol. 27, no. 6, pp. 577–580, 2015. [Online]. Available: https://doi.org/10.1109/LPT.2014.2385671

[78] Z. Khan, N. Ledentsov, L. Chorchos, J.-C. Shih, Y.-H. Chang, N. N. Ledentsov, and J.-W. Shi, "Single-mode 940 nm vcsels with narrow divergence angles and high-power performances for fiber and free-space optical communications," *IEEE Access*, vol. 8, pp. 72 095–72 101, 2020. [Online]. Available: https://doi.org/10.1109/ACCESS.2020.2987818

[79] A. Babichev, S. Blokhin, E. Kolodeznyi, L. Karachinsky, I. Novikov, A. Egorov, S.-C. Tian, and D. Bimberg, "Long-wavelength vcsels: Status and prospects," *Photonics*, vol. 10, no. 3, 2023. [Online]. Available: https://doi.org/10.3390/photonics10030268

[80] C.-Y. Peng, H.-T. Cheng, Y.-H. Hong, W.-C. Hsu, F.-H. Hsiao, T.-C. Lu, S.-W. Chang, S.-C. Chen, C.-H. Wu, and H.-C. Kuo, "Performance analyses of photonic-crystal surface-emitting laser: Toward high-speed optical communication," *Nanoscale Research Letters*, vol. 17, no. 1, 2022. [Online]. Available: https://doi.org/10.1186/s11671-022-03728-x

[81] F. Capasso, R. Paiella, R. Martini, R. Colombelli, C. Gmachl, T. Myers, M. Taubman, R. Williams, C. Bethea, K. Unterrainer, H. Hwang, D. Sivco, A. Cho, A. Sergent, H. Liu, and E. Whittaker, "Quantum cascade lasers: ultrahigh-speed operation, optical wireless communication, narrow linewidth, and far-infrared emission," *IEEE Journal of Quantum Electronics*, vol. 38, no. 6, pp. 511–532, 2002. [Online]. Available: https://doi.org/10.1109/JQE.2002.1005403

[82] R. Michalzik, *VCSEL Fundamentals.* Berlin, Heidelberg: Springer Berlin Heidelberg, 2013, pp. 19–75. [Online]. Available: https://doi.org/10.1007/978-3-642-24986-0_2

[83] M. Jetter, R. Roßbach, and P. Michler, *Red Emitting VCSEL.* Berlin, Heidelberg: Springer Berlin Heidelberg, 2013, pp. 379–401. [Online]. Available: https://doi.org/10.1007/978-3-642-24986-0_12

[84] M. Kanskar, T. Earles, T. Goodnough, E. Stiers, D. Botez, and L. Mawst, "73% cw power conversion efficiency at 50 w from 970 nm diode laser bars," *Electronics Letters*, vol. 41, pp. 245–247(2), March 2005. [Online]. Available: https://doi.org/10.1049/el:20058260

[85] P. Crump, G. Erbert, H. Wenzel, C. Frevert, C. M. Schultz, K.-H. Hasler, R. Staske, B. Sumpf, A. Maaßdorf, F. Bugge, S. Knigge, and G. Tränkle, "Efficient high-power laser diodes," *IEEE Journal of Selected Topics in Quantum*

Electronics, vol. 19, no. 4, pp. 1 501 211–1 501 211, 2013. [Online]. Available: https://doi.org/10.1109/JSTQE.2013.2239961

[86] S. Kumari, J. Gustavsson, E. P. Haglund, J. Bengtsson, A. Larsson, G. Roelkens, and R. Baets, "Design of an 845-nm gaas vertical-cavity silicon-integrated laser with an intracavity grating for coupling to a sin waveguide circuit," *IEEE Photonics Journal*, vol. 9, no. 4, p. 1–9, Aug 2017. [Online]. Available: https://doi.org/10.1109/jphot.2017.2717380

[87] G. Overton, "Vcsels boast 63.4

[88] M. D. Soltani, E. Sarbazi, N. Bamiedakis, P. de Souza, H. Kazemi, R. V. Penty, H. Haas, and M. Safari, "Safety analysis for laser-based optical wireless communications: A tutorial," *CoRR*, vol. abs/2102.08707, 2021. [Online]. Available: https://doi.org/10.48550/arXiv.2102.08707

[89] J. Rodríguez, D. G. Lamar, P. F. Miaja, D. G. Aller, and J. Sebastián, "Power-efficient vlc transmitter based on pulse-width modulated dc–dc converters and the split of the power," *IEEE Transactions on Power Electronics*, vol. 34, no. 2, pp. 1726–1743, 2019. [Online]. Available: https://doi.org/10.1109/TPEL.2018.2830881

[90] C. Desset, B. Debaillie, V. Giannini, A. Fehske, G. Auer, H. Holtkamp, W. Wajda, D. Sabella, F. Richter, M. J. Gonzalez, H. Klessig, I. Gódor, M. Olsson, M. A. Imran, A. Ambrosy, and O. Blume, "Flexible power modeling of lte base stations," in *2012 IEEE Wireless Communications and Networking Conference (WCNC)*, 2012, pp. 2858–2862. [Online]. Available: https://doi.org/10.1109/WCNC.2012.6214289

[91] M. S. Islim, R. X. Ferreira, X. He, E. Xie, S. Videv, S. Viola, S. Watson, N. Bamiedakis, R. V. Penty, I. H. White, A. E. Kelly, E. Gu, H. Haas, and M. D. Dawson, "Towards 10 gb/s orthogonal frequency division multiplexing-based visible light communication using a gan violet micro-led,"

Photon. Res., vol. 5, no. 2, pp. A35–A43, Apr 2017. [Online]. Available: https://doi.org/10.1364/PRJ.5.000A35

[92] D. M. Maclure, J. J. D. McKendry, M. S. Islim, E. Xie, C. Chen, X. Sun, X. Liang, X. Huang, H. Abumarshoud, J. Herrnsdorf, E. Gu, H. Haas, and M. D. Dawson, "10 gbps wavelength division multiplexing using uv-a, uv-b, and uv-c micro-leds," *Photon. Res.*, vol. 10, no. 2, pp. 516–523, Feb 2022. [Online]. Available: https://doi.org/10.1364/PRJ.445984

[93] B. Saleh and M. Teich, *Fundamentals of Photonics*, ser. Wiley Series in Pure and Applied Optics. Wiley, 2019. [Online]. Available: https://books.google.co.uk/books?id=rcqKDwAAQBAJ

[94] E. Haglund, P. Westbergh, J. Gustavsson, E. Haglund, A. Larsson, M. Geen, and A. Joel, "30 ghz bandwidth 850 nm vcsel with sub-100 fj/bit energy dissipation at 25–50 gbit/s," *Electronics Letters*, vol. 51, no. 14, pp. 1096–1098, 2015. [Online]. Available: https://doi.org/10.1049/el.2015.0785

[95] C.-H. Cheng, W.-C. Lo, B. Su, C.-H. Wu, and G.-R. Lin, "Review of vcsels for complex data-format transmission beyond 100-gbit/s," *IEEE Photonics Journal*, vol. 13, no. 5, pp. 1–13, 2021. [Online]. Available: https://doi.org/10.1109/JPHOT.2021.3104647

[96] A. Krishnamoorthy, K. Goossen, L. Chirovsky, R. Rozier, P. Chandramani, S. Hui, J. Lopata, J. Walker, and L. D'Asaro, "16 x 16 vcsel array flip-chip bonded to cmos vlsi circuit," *IEEE Photonics Technology Letters*, vol. 12, no. 8, pp. 1073–1075, 2000. [Online]. Available: https://doi.org/10.1109/68.868012

[97] H. Lu, J. S. Lee, Y. Zhao, C. Scarcella, P. Cardile, A. Daly, M. Ortsiefer, L. Carroll, and P. O'Brien, "Flip-chip integration of tilted vcsels onto a silicon photonic integrated circuit," *Opt. Express*, vol. 24, no. 15, pp. 16 258–16 266, Jul 2016. [Online]. Available: https://doi.org/10.1364/OE.24.016258

[98] S. Mowlavi, S. Giannakopoulos, and L. Svensson, "Vcsel integrated circuit drivers: A review," in *2022 IEEE Nordic Circuits and Systems Conference*

(NorCAS), 2022, pp. 1–7. [Online]. Available: https://doi.org/10.1109/NorCAS57515.2022.9934536

[99] M. Yoshikawa, A. Murakami, J. Sakurai, H. Nakayama, and T. Nakamura, “High power vcsel devices for free space optical communications,” in *Proceedings Electronic Components and Technology, 2005. ECTC ’05.*, 2005, pp. 1353–1358 Vol. 2. [Online]. Available: https://doi.org/10.1109/ECTC.2005.1441445

[100] M.-R. Park, O.-K. Kwon, W.-S. Han, K.-H. Lee, S.-J. Park, and B.-S. Yoo, “All-epitaxial inalgaas-inp vcsels in the 1.3-1.6-µm wavelength range for cwdm band applications,” *IEEE Photonics Technology Letters*, vol. 18, no. 16, pp. 1717–1719, 2006. [Online]. Available: https://doi.org/10.1109/LPT.2006.879940

[101] S. A. Blokhin, A. V. Babichev, A. G. Gladyshev, I. I. Novikov, A. A. Blokhin, M. A. Bobrov, N. A. Maleev, V. V. Andryushkin, D. V. Denisov, K. O. Voropaev, V. M. Ustinov, V. E. Bougrov, A. Y. Egorov, and L. Y. Karachinsky, “20-Gbps 1300-nm range wafer-fused vertical-cavity surface-emitting lasers with InGaAs/InAlGaAs superlattice-based active region,” *Optical Engineering*, vol. 61, no. 9, p. 096109, 2022. [Online]. Available: https://doi.org/10.1117/1.OE.61.9.096109

[102] D. R. Paschotta, “Laser diode collimators,” Nov 2023. [Online]. Available: https://www.rp-photonics.com/laser_diode_collimators.html

[103] A. M. Alatwi, A. N. Z. Rashed, and E. M. El-Gammal, “Wavelength division multiplexing techniques based on multi transceiver in low earth orbit intersatellite systems,” *Journal of Optical Communications*, p. 000010151520190171, 2020. [Online]. Available: https://doi.org/10.1515/joc-2019-0171

[104] I. S. Amiri, A. N. Z. Rashed, A. E. A. Mohammed, E. S. El-Din, and P. Yupapin, “Spatial continuous wave laser and spatiotemporal vcsel for high-speed long haul optical wireless communication channels,” *Journal of Optical Communications*, vol. 44, no. 1, pp. 43–51, 2023. [Online]. Available: https://doi.org/10.1515/joc-2019-0061

[105] U. Kaufmann, M. Kunzer, K. Köhler, H. Obloh, W. Pletschen, P. Schlotter, J. Wagner, A. Ellens, W. Rossner, and M. Kobusch, "Single chip white leds," *physica status solidi (a)*, vol. 192, no. 2, pp. 246–253, 2002. [Online]. Available: https://doi.org/10.1002/1521-396X(200208)192:2⟨246::AID-PSSA246⟩3.0.CO;2-I

[106] E. Schubert, *Light-Emitting Diodes (3rd Edition, 2018)*. E. Fred Schubert, 2018. [Online]. Available: https://books.google.co.uk/books?id=GEFKDwAAQBAJ

[107] S. Rajbhandari, J. J. D. McKendry, J. Herrnsdorf, H. Chun, G. Faulkner, H. Haas, I. M. Watson, D. O'Brien, and M. D. Dawson, "A review of gallium nitride leds for multi-gigabit-per-second visible light data communications," *Semiconductor Science and Technology*, vol. 32, no. 2, p. 023001, jan 2017. [Online]. Available: https://dx.doi.org/10.1088/1361-6641/32/2/023001

[108] J. M. Smith, R. Ley, M. S. Wong, Y. H. Baek, J. H. Kang, C. H. Kim, M. J. Gordon, S. Nakamura, J. S. Speck, and S. P. DenBaars, "Comparison of size-dependent characteristics of blue and green InGaN microLEDs down to 1 µm in diameter," *Applied Physics Letters*, vol. 116, no. 7, p. 071102, 02 2020. [Online]. Available: https://doi.org/10.1063/1.5144819

[109] E. Xie, R. Bian, X. He, M. S. Islim, C. Chen, J. J. D. McKendry, E. Gu, H. Haas, and M. D. Dawson, "Over 10 gbps vlc for long-distance applications using a gan-based series-biased micro-led array," *IEEE Photonics Technology Letters*, vol. 32, no. 9, pp. 499–502, 2020. [Online]. Available: https://doi.org/10.1109/LPT.2020.2981827

[110] Z. Li, X. Zhang, Z. Hao, Y. Luo, C. Sun, B. Xiong, Y. Han, J. Wang, H. Li, L. Gan, and L. Wang, "Bandwidth analysis of high-speed ingan micro-leds by an equivalent circuit model," *IEEE Electron Device Letters*, vol. 44, no. 5, pp. 785–788, 2023. [Online]. Available: https://doi.org/10.1109/LED.2023.3256422

[111] J. F. C. Carreira, E. Xie, R. Bian, J. Herrnsdorf, H. Haas, E. Gu, M. J. Strain, and M. D. Dawson, "Gigabit per second visible light communication

based on algainp red micro-led micro-transfer printed onto diamond and glass," *Opt. Express*, vol. 28, no. 8, pp. 12 149–12 156, Apr 2020. [Online]. Available: https://doi.org/10.1364/OE.391488

[112] J. Bai, Y. Cai, P. Feng, P. Fletcher, X. Zhao, C. Zhu, and T. Wang, "A direct epitaxial approach to achieving ultrasmall and ultrabright ingan micro light-emitting diodes (µleds)," *ACS Photonics*, vol. 7, no. 2, pp. 411–415, 2020, pMID: 32296730. [Online]. Available: https://doi.org/10.1021/acsphotonics.9b01351

[113] H. Elgala, R. Mesleh, and H. Haas, "Non-linearity effects and predistortion in optical ofdm wireless transmission using leds," *International Journal of Ultra Wideband Communications and Systems*, vol. 1, no. 2, pp. 143–150, 2009. [Online]. Available: https://www.inderscienceonline.com/doi/abs/10.1504/IJUWBCS.2009.029003

[114] M. E. Belkin, L. Belkin, A. Loparev, A. S. Sigov, and V. Iakovlev, "Long wavelength vcsels and vcsel-based processing of microwave signals," in *Optoelectronics*, S. L. Pyshkin and J. Ballato, Eds. Rijeka: IntechOpen, 2015, ch. 6. [Online]. Available: https://doi.org/10.5772/60480

[115] H. Fu and Y. Zhao, "9 - efficiency droop in gainn/gan leds," in *Nitride Semiconductor Light-Emitting Diodes (LEDs) (Second Edition)*, 2nd ed., ser. Woodhead Publishing Series in Electronic and Optical Materials, J. Huang, H.-C. Kuo, and S.-C. Shen, Eds. Woodhead Publishing, 2018, pp. 299–325. [Online]. Available: https://www.sciencedirect.com/science/article/pii/B9780081019429000095

[116] M. Meneghini, C. De Santi, A. Tibaldi, M. Vallone, F. Bertazzi, G. Meneghesso, E. Zanoni, and M. Goano, "Thermal droop in III-nitride based light-emitting diodes: Physical origin and perspectives," *Journal of Applied Physics*, vol. 127, no. 21, p. 211102, 06 2020. [Online]. Available: https://doi.org/10.1063/5.0005874

[117] X. Deng, S. Mardanikorani, Y. Wu, K. Arulandu, B. Chen, A. M. Khalid, and J.-P. M. G. Linnartz, "Mitigating led nonlinearity to enhance visible light communications," *IEEE Transactions on Communications*, vol. 66, no. 11, pp. 5593–5607, 2018. [Online]. Available: https://doi.org/10.1109/TCOMM.2018.2858239

[118] X. Li, Q. Gao, C. Gong, and Z. Xu, "Nonlinearity mitigation for vlc with an artificial neural network based equalizer," in *2018 IEEE Globecom Workshops (GC Wkshps)*, 2018, pp. 1–6. [Online]. Available: https://doi.org/10.1109/GLOCOMW.2018.8644499

[119] Y. Zhou, Y. Wei, F. Hu, J. Hu, Y. Zhao, J. Zhang, F. Jiang, and N. Chi, "Comparison of nonlinear equalizers for high-speed visible light communication utilizing silicon substrate phosphorescent white led," *Opt. Express*, vol. 28, no. 2, pp. 2302–2316, Jan 2020. [Online]. Available: https://doi.org/10.1364/OE.383775

[120] E. Monteiro and S. Hranilovic, "Design and implementation of color-shift keying for visible light communications," *Journal of Lightwave Technology*, vol. 32, no. 10, pp. 2053–2060, 2014. [Online]. Available: https://doi.org/10.1109/JLT.2014.2314358

[121] X. Tang, Z. Ghassemlooy, S. Rajbhandari, W. O. Popoola, M. Uysal, and D. Wu, "Experimental demonstration of polarisation shift keying in the free space optical turbulence channel," in *2012 1st IEEE International Conference on Communications in China Workshops (ICCC)*, 2012, pp. 31–36. [Online]. Available: https://doi.org/10.1109/ICCCW.2012.6316470

[122] "Dac39rf10 data sheet, product information and support — ti.com." [Online]. Available: https://www.ti.com/product/DAC39RF10

[123] D. PDF, "Direct-sampling dacs in theory and application," Nov 2022. [Online]. Available: https://www.analog.com/en/technical-articles/directsampling-dacs-in-theory-and-application.html

[124] F. A. Dahri, F. A. Umrani, A. Baqai, and H. B. Mangrio, "Design and implementation of led–led indoor visible light communication system," *Physical Communication*, vol. 38, p. 100981, 2020. [Online]. Available: https://doi.org/10.1016/j.phycom.2019.100981

[125] S. Dimitrov and H. Haas, "Information rate of ofdm-based optical wireless communication systems with nonlinear distortion," *Journal of Lightwave Technology*, vol. 31, no. 6, pp. 918–929, 2013. [Online]. Available: https://doi.org/10.1109/JLT.2012.2236642

[126] X. Ling, J. Wang, X. Liang, Z. Ding, and C. Zhao, "Offset and power optimization for dco-ofdm in visible light communication systems," *IEEE Transactions on Signal Processing*, vol. 64, no. 2, pp. 349–363, 2016. [Online]. Available: https://doi.org/10.1109/TSP.2015.2477799

[127] J. Sebastián, D. G. Lamar, D. G. Aller, J. Rodríguez, and P. F. Miaja, "On the role of power electronics in visible light communication," *IEEE Journal of Emerging and Selected Topics in Power Electronics*, vol. 6, no. 3, pp. 1210–1223, 2018. [Online]. Available: https://doi.org/10.1109/JESTPE.2018.2830878

[128] K. Arulandu, J.-P. Linnartz, and X. Deng, "Efficient amplitude modulator and ripple canceller for visible light communication," in *2018 IEEE Globecom Workshops (GC Wkshps)*, 2018, pp. 1–6. [Online]. Available: https://doi.org/10.1109/GLOCOMW.2018.8644210

[129] D. G. Aller, D. G. Lamar, P. F. Miaja, J. Rodríguez, and J. Sebastián, "Taking advantage of the sum of the light in outphasing technique for visible light communication transmitter," *IEEE Journal of Emerging and Selected Topics in Power Electronics*, vol. 9, no. 1, pp. 138–145, 2021. [Online]. Available: https://doi.org/10.1109/JESTPE.2020.2965774

[130] C. Yu, X. Chen, Z. Zhang, G. Song, J. Lin, and J. Xu, "Experimental verification of diffused laser beam-based optical wireless communication through

air and water channels," *Optics Communications*, vol. 495, p. 127079, 2021. [Online]. Available: https://doi.org/10.1016/j.optcom.2021.127079

[131] P. Delaporte, D. Karnakis, and I. Zergioti, "12 - laser processing of flexible organic electronic materials," in *Handbook of Flexible Organic Electronics*, S. Logothetidis, Ed. Oxford: Woodhead Publishing, 2015, pp. 285–313. [Online]. Available: https://doi.org/10.1016/B978-1-78242-035-4.00012-9

[132] S. Katz, N. Kaplan, and I. Grossinger, "Using diffractive optical elements," *Optik & Photonik*, vol. 13, no. 4, pp. 83–86, 2018. [Online]. Available: https://doi.org/10.1002/opph.201870416

[133] D. Tsonev, S. Videv, and H. Haas, "Towards a 100 gb/s visible light wireless access network," *Opt. Express*, vol. 23, no. 2, pp. 1627–1637, Jan 2015. [Online]. Available: https://doi.org/10.1364/OE.23.001627

[134] K. M. Thu and T. Maruyama, "Stabilization of optical wireless power transmission system using spatial light modulator," in *Laser Beam Shaping XXIII*, A. Dudley and A. V. Laskin, Eds., vol. 12667, International Society for Optics and Photonics. SPIE, 2023, p. 126670A. [Online]. Available: https://doi.org/10.1117/12.2676582

[135] P.-C. Kuo, S.-I. Kuo, J.-W. Wang, Y.-H. Jian, Z. Ahmad, P.-H. Fu, Y.-C. Chang, J.-W. Shi, D.-W. Huang, Y. Liu, C.-H. Yeh, and C.-W. Chow, "Actively steerable integrated optical phased array (opa) for optical wireless communication (owc)," in *Optical Fiber Communication Conference (OFC) 2022*. Optica Publishing Group, 2022, p. M1C.7. [Online]. Available: https://doi.org/10.1364/OFC.2022.M1C.7

[136] V. Ghaffari and L. Yousefi, "Integrated optical beam steering device using switchable nanoantennas and a reflective metalens," *Scientific Reports*, vol. 13, no. 1, 2023. [Online]. Available: https://doi.org/10.1038/s41598-023-33939-w

[137] P. Berini, “Optical beam steering using tunable metasurfaces,” *ACS Photonics*, vol. 9, no. 7, pp. 2204–2218, 2022. [Online]. Available: https://doi.org/10.1021/acsphotonics.2c00439

[138] L. Yang, F. Shen, Z. Ding, X. Tao, Z. Zheng, F. Wu, Y. Li, and R. Wu, “Freeform optical design of beam shaping systems with variable illumination properties,” *Opt. Express*, vol. 29, no. 20, pp. 31 993–32 005, Sep 2021. [Online]. Available: https://doi.org/10.1364/OE.436340

[139] P. Benitez, J. C. Minano, F. J. Lopez, D. Biosca, R. Mohedano, M. Labrador, F. Munoz, K. Hirohashi, and M. Sakai, “Eye-safe collimated laser emitter for optical wireless communications,” in *Optical Wireless Communications V*, E. J. Korevaar, Ed., vol. 4873, International Society for Optics and Photonics. SPIE, 2002, pp. 30 – 40. [Online]. Available: https://doi.org/10.1117/12.455517

[140] A. M. Abdelhady, O. Amin, M.-S. Alouini, and B. Shihada, “Revolutionizing optical wireless communications via smart optics,” *IEEE Open Journal of the Communications Society*, vol. 3, pp. 654–669, 2022. [Online]. Available: https://doi.org/10.1109/OJCOMS.2022.3164790

[141] P. F. McManamon, P. J. Bos, M. J. Escuti, J. Heikenfeld, S. Serati, H. Xie, and E. A. Watson, “A review of phased array steering for narrow-band electrooptical systems,” *Proceedings of the IEEE*, vol. 97, no. 6, pp. 1078–1096, 2009. [Online]. Available: https://doi.org/10.1109/JPROC.2009.2017218

[142] M. Ostaszewski, S. Harford, N. Doughty, C. Hoffman, M. Sanchez, D. Gutow, and R. Pierce, “Risley prism beam pointer,” in *Free-Space Laser Communications VI*, A. K. Majumdar and C. C. Davis, Eds., vol. 6304, International Society for Optics and Photonics. SPIE, 2006, p. 630406. [Online]. Available: https://doi.org/10.1117/12.679097

[143] Q. Zhou, P. Ben-Tzvi, D. Fan, and A. A. Goldenberg, “Design of fast steering mirror systems for precision laser beams steering,” in *2008 International*

Workshop on Robotic and Sensors Environments, 2008, pp. 144–149. [Online]. Available: https://doi.org/10.1109/ROSE.2008.4669196

[144] V. Aksyuk, F. Pardo, D. Carr, D. Greywall, H. Chan, M. Simon, A. Gasparyan, H. Shea, V. Lifton, C. Bolle, S. Arney, R. Frahm, M. Paczkowski, M. Haueis, R. Ryf, D. Neilson, J. Kim, C. Giles, and D. Bishop, "Beam-steering micromirrors for large optical cross-connects," *Journal of Lightwave Technology*, vol. 21, no. 3, pp. 634–642, 2003. [Online]. Available: https://doi.org/10.1109/JLT.2003.811792

[145] K. Johnson, D. McKnight, and I. Underwood, "Smart spatial light modulators using liquid crystals on silicon," *IEEE Journal of Quantum Electronics*, vol. 29, no. 2, pp. 699–714, 1993. [Online]. Available: https://doi.org/10.1109/3.199323

[146] T. Koonen, K. Mekonnen, F. Huijskens, Z. Cao, and E. Tangdiongga, "Novel broadband owc receiver with large aperture and wide field-of-view," in *2020 European Conference on Optical Communications (ECOC)*, 2020, pp. 1–4. [Online]. Available: https://doi.org/10.1109/ECOC48923.2020.9333278

[147] "Si apd s16453-02k." [Online]. Available: https://www.hamamatsu.com/us/en/product/optical-sensors/apd/si-apd/S16453-02K.html

[148] I. Takai, H. Matsubara, M. Soga, M. Ohta, M. Ogawa, and T. Yamashita, "Single-photon avalanche diode with enhanced nir-sensitivity for automotive lidar systems," *Sensors*, vol. 16, no. 4, 2016. [Online]. Available: https://doi.org/10.3390/s16040459

[149] E. Sarbazi, M. Safari, and H. Haas, "On the information transfer rate of spad receivers for optical wireless communications," in *2016 IEEE Global Communications Conference (GLOBECOM)*, 2016, pp. 1–6. [Online]. Available: https://doi.org/10.1109/GLOCOM.2016.7842057

[150] B. Razavi, "The transimpedance amplifier [a circuit for all seasons]," *IEEE Solid-State Circuits Magazine*, vol. 11, no. 1, pp. 10–97, 2019. [Online]. Available: https://doi.org/10.1109/MSSC.2018.2881860

[151] "Adc12dj5200rf data sheet, product information and support — ti.com." [Online]. Available: https://www.ti.com/product/ADC12DJ5200RF

[152] "Thorlabs, bandpass filter tutorial." [Online]. Available: https://www.thorlabs.com/newgrouppage9.cfm?objectgroup_id=10772

[153] J. R. Barry and J. M. Kahn, "Link design for nondirected wireless infrared communications," *Appl. Opt.*, vol. 34, no. 19, pp. 3764–3776, Jul 1995. [Online]. Available: https://doi.org/10.1364/AO.34.003764

[154] R. Mulyawan, A. Gomez, H. Chun, S. Rajbhandari, P. P. Manousiadis, D. A. Vithanage, G. Faulkner, G. A. Turnbull, I. D. W. Samuel, S. Collins, and D. O'Brien, "A comparative study of optical concentrators for visible light communications," in *Broadband Access Communication Technologies XI*, B. B. Dingel, K. Tsukamoto, and S. Mikroulis, Eds., vol. 10128, International Society for Optics and Photonics. SPIE, 2017, p. 101280L. [Online]. Available: https://doi.org/10.1117/12.2252355

[155] M. Dehghani Soltani, H. Kazemi, E. Sarbazi, T. E. H. El-Gorashi, J. M. H. Elmirghani, R. V. Penty, I. H. White, H. Haas, and M. Safari, "High-speed imaging receiver design for 6g optical wireless communications: A rate-fov trade-off," *IEEE Transactions on Communications*, vol. 71, no. 2, pp. 1024–1043, 2023. [Online]. Available: https://doi.org/10.1109/TCOMM.2022.3230954

[156] A. Rabl, "Optical and thermal properties of compound parabolic concentrators," *Solar Energy*, vol. 18, no. 6, pp. 497–511, 1976. [Online]. Available: https://doi.org/10.1016/0038-092X(76)90069-4

[157] X. Ning, R. Winston, and J. O'Gallagher, "Dielectric totally internally reflecting concentrators," *Appl. Opt.*, vol. 26, no. 2, pp. 300–305, Jan 1987. [Online]. Available: https://doi.org/10.1364/AO.26.000300

[158] R. Kirrbach, M. Faulwaßer, and B. Jakob, "Non-rotationally symmetric freeform fresnel-lenses for arbitrary shaped li-fi communication channels,"

in *2019 Global LIFI Congress (GLC)*, 2019, pp. 1–6. [Online]. Available: https://doi.org/10.1109/GLC.2019.8864138

[159] M. Hernández, A. Cvetkovic, P. Benítez, and J. C. Miñano, "High-performance Köhler concentrators with uniform irradiance on solar cell," in *Nonimaging Optics and Efficient Illumination Systems V*, R. Winston and R. J. Koshel, Eds., vol. 7059, International Society for Optics and Photonics. SPIE, 2008, p. 705908. [Online]. Available: https://doi.org/10.1117/12.794927

[160] C. E. Shannon, "A mathematical theory of communication," *The Bell System Technical Journal*, vol. 27, no. 3, pp. 379–423, 1948. [Online]. Available: https://doi.org/10.1002/j.1538-7305.1948.tb01338.x

[161] S. Benson and J. M. Madey, "Shot and quantum noise in free electron lasers," *Nuclear Instruments and Methods in Physics Research Section A: Accelerators, Spectrometers, Detectors and Associated Equipment*, vol. 237, no. 1, pp. 55–60, 1985. [Online]. Available: https://doi.org/10.1016/0168-9002(85)90329-8

[162] "Transimpedance amplifier noise considerations," Mar 2018. [Online]. Available: https://www.analog.com/en/technical-articles/transimpedance-amplifier-noise-considerations.html

[163] J. Rutenbeck, *Tech Terms: What Every Telecommunications and Digital Media Professional Should Know.* Taylor & Francis, 2012. [Online]. Available: https://books.google.co.uk/books?id=dfFsAAAAQBAJ

[164] Y. Wang, X. Huang, L. Tao, J. Shi, and N. Chi, "4.5-gb/s rgb-led based wdm visible light communication system employing cap modulation and rls based adaptive equalization," *Opt. Express*, vol. 23, no. 10, pp. 13 626–13 633, May 2015. [Online]. Available: https://doi.org/10.1364/OE.23.013626

[165] A. Pradana, N. Ahmadi, and T. Adionos, "Design and implementation of visible light communication system using pulse width modulation," in *2015 International Conference on Electrical Engineering and Informatics (ICEEI)*, 2015, pp. 25–30. [Online]. Available: https://doi.org/10.1109/ICEEI.2015.7352464

[166] Y. Fan and R. J. Green, “Comparison of pulse position modulation and pulse width modulation for application in optical communications,” *Optical Engineering*, vol. 46, no. 6, p. 065001, 2007. [Online]. Available: https://doi.org/10.1117/1.2746010

[167] D.-S. Ly-Gagnon, S. Tsukamoto, K. Katoh, and K. Kikuchi, “Coherent detection of optical quadrature phase-shift keying signals with carrier phase estimation,” *J. Lightwave Technol.*, vol. 24, no. 1, p. 12, Jan 2006. [Online]. Available: https://opg.optica.org/jlt/abstract.cfm?URI=jlt-24-1-12

[168] M. Nakazawa, S. Okamoto, T. Omiya, K. Kasai, and M. Yoshida, “256 qam (64 gbit/s) coherent optical transmission over 160 km with an optical bandwidth of 5.4 ghz,” in *Optical Fiber Communication Conference.* Optica Publishing Group, 2010, p. OMJ5. [Online]. Available: https://doi.org/10.1364/OFC.2010.OMJ5

[169] G. A. Mahdiraji and E. Zahedi, “Comparison of selected digital modulation schemes (ook, ppm and dpim) for wireless optical communications,” in *2006 4th Student Conference on Research and Development*, 2006, pp. 5–10. [Online]. Available: https://doi.org/10.1109/SCORED.2006.4339297

[170] J. R. García-Meré, J. Rodríguez, D. G. Lamar, and J. Sebastián, “On the use of class d switching-mode power amplifiers in visible light communication transmitters,” *Sensors*, vol. 22, no. 13, 2022. [Online]. Available: https://doi.org/10.3390/s22134858

[171] R. V. L. Hartley, “Transmission of information1,” *Bell System Technical Journal*, vol. 7, no. 3, pp. 535–563, 1928. [Online]. Available: https://doi.org/10.1002/j.1538-7305.1928.tb01236.x

[172] L. Hanzo, W. Webb, and T. Keller, *Single- and Multi-carrier Quadrature Amplitude Modulation: Principles and Applications for Personal Communications, WATM and Broadcasting: 2nd.* IEEE Press - John Wiley, April 2000. [Online]. Available: https://eprints.soton.ac.uk/253429/

[173] B. Lankl and G. Sebald, "Jitter-reduced digital timing recovery for multilevel pam and qam systems," in *Proceedings of ICC '93 - IEEE International Conference on Communications*, vol. 2, 1993, pp. 804–810 vol.2. [Online]. Available: https://doi.org/10.1109/ICC.1993.397384

[174] C. Rivera and J. Ritcey, "Error probabilities for qam systems on partially coherent channels with intersymbol interference and crosstalk," *IEEE Transactions on Communications*, vol. 46, no. 6, pp. 775–783, 1998. [Online]. Available: https://doi.org/10.1109/26.681414

[175] J. Terry and J. Heiskala, *OFDM Wireless LANs: A Theoretical and Practical Guide*, ser. Kaleidoscope Series. Sams, 2002. [Online]. Available: https://books.google.co.uk/books?id=p_rMm2l237gC

[176] J. Armstrong, "Ofdm for optical communications," *Journal of Lightwave Technology*, vol. 27, no. 3, pp. 189–204, 2009. [Online]. Available: https://doi.org/10.1109/JLT.2008.2010061

[177] Y. Li and G. Stuber, *Orthogonal Frequency Division Multiplexing for Wireless Communications*, ser. Signals and Communication Technology. Springer US, 2006. [Online]. Available: https://books.google.co.uk/books?id=xrCkZXN1rEMC

[178] H. Levin, "A complete and optimal data allocation method for practical discrete multitone systems," in *GLOBECOM'01. IEEE Global Telecommunications Conference (Cat. No.01CH37270)*, vol. 1, 2001, pp. 369–374 vol.1. [Online]. Available: https://doi.org/10.1109/GLOCOM.2001.965141

[179] J. Armstrong and B. J. Schmidt, "Comparison of asymmetrically clipped optical ofdm and dc-biased optical ofdm in awgn," *IEEE Communications Letters*, vol. 12, no. 5, pp. 343–345, 2008. [Online]. Available: https://doi.org/10.1109/LCOMM.2008.080193

[180] D. Tsonev, S. Sinanovic, and H. Haas, "Novel unipolar orthogonal frequency division multiplexing (u-ofdm) for optical wireless," in *2012 IEEE 75th Vehicular*

Technology Conference (VTC Spring), 2012, pp. 1–5. [Online]. Available: https://doi.org/10.1109/VETECS.2012.6240060

[181] D. Tsonev and H. Haas, "Avoiding spectral efficiency loss in unipolar ofdm for optical wireless communication," in *2014 IEEE International Conference on Communications (ICC)*, 2014, pp. 3336–3341. [Online]. Available: https://doi.org/10.1109/ICC.2014.6883836

[182] M. S. Islim, D. Tsonev, and H. Haas, "A generalized solution to the spectral efficiency loss in unipolar optical ofdm-based systems," in *2015 IEEE International Conference on Communications (ICC)*, 2015, pp. 5126–5131. [Online]. Available: https://doi.org/10.1109/ICC.2015.7249137

[183] R. Singh, T. O'Farrell, M. Biagi, R. V. Penty, and J. P. R. David, "Vector coding optical wireless links," *Journal of Lightwave Technology*, vol. 41, no. 17, pp. 5577–5587, 2023. [Online]. Available: https://doi.org/10.1109/JLT.2023.3265628

[184] E. Telatar, "Capacity of multi-antenna gaussian channels," *European Transactions on Telecommunications*, vol. 10, no. 6, pp. 585–595, 1999. [Online]. Available: https://doi.org/10.1002/ett.4460100604

[185] J. Laneman, D. Tse, and G. Wornell, "Cooperative diversity in wireless networks: Efficient protocols and outage behavior," *IEEE Transactions on Information Theory*, vol. 50, no. 12, pp. 3062–3080, 2004. [Online]. Available: https://doi.org/10.1109/TIT.2004.838089

[186] S. M. Navidpour, M. Uysal, and M. Kavehrad, "Ber performance of free-space optical transmission with spatial diversity," *IEEE Transactions on Wireless Communications*, vol. 6, no. 8, pp. 2813–2819, 2007. [Online]. Available: https://doi.org/10.1109/TWC.2007.06109

[187] A. J. Paulraj and T. Kailath, "Increasing capacity in wireless broadcast systems using distributed transmission/directional reception (dtdr)," Sep 1994.

[188] R. Y. Mesleh, H. Haas, S. Sinanovic, C. W. Ahn, and S. Yun, "Spatial modulation," *IEEE Transactions on Vehicular Technology*, vol. 57, no. 4, pp. 2228–2241, 2008. [Online]. Available: https://doi.org/10.1109/TVT.2007.912136

[189] A. Younis, N. Serafimovski, R. Mesleh, and H. Haas, "Generalised spatial modulation," in *2010 Conference Record of the Forty Fourth Asilomar Conference on Signals, Systems and Computers*, 2010, pp. 1498–1502. [Online]. Available: https://doi.org/10.1109/ACSSC.2010.5757786

[190] J. Jeganathan, A. Ghrayeb, and L. Szczecinski, "Generalized space shift keying modulation for mimo channels," in *2008 IEEE 19th International Symposium on Personal, Indoor and Mobile Radio Communications*, 2008, pp. 1–5. [Online]. Available: https://doi.org/10.1109/PIMRC.2008.4699782

[191] H. Holtkamp, G. Auer, V. Giannini, and H. Haas, "A parameterized base station power model," *IEEE Communications Letters*, vol. 17, no. 11, pp. 2033–2035, 2013. [Online]. Available: https://doi.org/10.1109/LCOMM.2013.091213.131042

[192] A. Zappone and E. Jorswieck, "Energy efficiency in wireless networks via fractional programming theory," *Foundations and Trends® in Communications and Information Theory*, vol. 11, no. 3-4, pp. 185–396, 2015. [Online]. Available: http://dx.doi.org/10.1561/0100000088

[193] L. Kong, C. Chen, Y. Wang, and H. Haas, "Power consumption evaluation in high speed visible light communication systems," in *2018 IEEE Global Communications Conference (GLOBECOM)*, 2018, pp. 1–6. [Online]. Available: https://doi.org/10.1109/GLOCOM.2018.8647711

[194] S. Dimitrov and H. Haas, *Principles of LED Light Communications: Towards Networked Li-Fi*. Cambridge University Press, 2015.

[195] A. D. Griffiths, J. Herrnsdorf, J. J. D. McKendry, M. J. Strain, and M. D. Dawson, "Gallium nitride micro-light-emitting diode structured light sources for multi-modal optical wireless communications systems," *Philosophical*

Transactions of the Royal Society A: Mathematical, Physical and Engineering Sciences, vol. 378, no. 2169, p. 20190185, Mar. 2020. [Online]. Available: https://doi.org/10.1098/rsta.2019.0185

[196] F. Xu, Z. Jin, T. Tao, P. Tian, G. Wang, X. Liu, T. Zhi, Q.-a. Yan, D. Pan, Z. Xie, K. Xu, B. Liu, and R. Zhang, “C-plane blue micro-led with 1.53 ghz bandwidth for high-speed visible light communication,” *IEEE Electron Device Letters*, vol. 43, no. 6, pp. 910–913, 2022. [Online]. Available: https://doi.org/10.1109/LED.2022.3168314

[197] H. Kazemi, E. Sarbazi, M. D. Soltani, T. E. H. El-Gorashi, J. M. H. Elmirghani, R. V. Penty, I. H. White, M. Safari, and H. Haas, “A tb/s indoor mimo optical wireless backhaul system using vcsel arrays,” *IEEE Transactions on Communications*, vol. 70, no. 6, pp. 3995–4012, 2022. [Online]. Available: https://doi.org/10.1109/TCOMM.2022.3165187

[198] W. Niu, Z. Xu, Y. Liu, X. Lin, J. Cai, J. Shi, X. Wang, G. Wang, J. Zhang, F. Jiang, Z. He, S. Yu, C. Shen, J. Zhang, and N. Chi, “Key technologies for high-speed si-substrate led based visible light communication,” *Journal of Lightwave Technology*, vol. 41, no. 11, pp. 3316–3331, 2023. [Online]. Available: https://doi.org/10.1109/JLT.2023.3252005

[199] A. Gomez, K. Shi, C. Quintana, M. Sato, G. Faulkner, B. C. Thomsen, and D. O’Brien, “Beyond 100-gb/s indoor wide field-of-view optical wireless communications,” *IEEE Photonics Technology Letters*, vol. 27, no. 4, pp. 367–370, 2015. [Online]. Available: https://doi.org/10.1109/LPT.2014.2374995

[200] A. Gomez, K. Shi, C. Quintana, R. Maher, G. Faulkner, P. Bayvel, B. C. Thomsen, and D. O’Brien, “Design and demonstration of a 400 gb/s indoor optical wireless communications link,” *Journal of Lightwave Technology*, vol. 34, no. 22, pp. 5332–5339, 2016. [Online]. Available: https://doi.org/10.1109/JLT.2016.2616844

[201] Y. Hong, F. Feng, K. R. H. Bottrill, N. Taengnoi, R. Singh, G. Faulkner, D. C. O'Brien, and P. Petropoulos, "Demonstration of >1tbit/s wdm owc with wavelength-transparent beam tracking-and-steering capability," *Opt. Express*, vol. 29, no. 21, pp. 33 694–33 702, Oct 2021. [Online]. Available: https://doi.org/10.1364/OE.436239

[202] R. S. Tucker, "Green optical communications—part i: Energy limitations in transport," *IEEE Journal of Selected Topics in Quantum Electronics*, vol. 17, no. 2, pp. 245–260, 2011. [Online]. Available: https://doi.org/10.1109/JSTQE.2010.2051216

[203] ——, "Green optical communications—part ii: Energy limitations in networks," *IEEE Journal of Selected Topics in Quantum Electronics*, vol. 17, no. 2, pp. 261–274, 2011. [Online]. Available: https://doi.org/10.1109/JSTQE.2010.2051217

[204] M. Z. Chowdhury, M. Shahjalal, M. K. Hasan, and Y. M. Jang, "The role of optical wireless communication technologies in 5g/6g and iot solutions: Prospects, directions, and challenges," *Applied Sciences*, vol. 9, no. 20, 2019. [Online]. Available: https://doi.org/10.3390/app9204367

[205] Y. Zhang, R. Xu, Q. Kang, X. Zhang, and Z.-h. Zhang, "Recent advances on gan-based micro-leds," *Micromachines*, vol. 14, no. 5, 2023. [Online]. Available: https://doi.org/10.3390/mi14050991

[206] M. A. Dastgheib, E. Zolala, H. Beyranvand, and J. A. Salehi, "On fundamental limits of energy efficient signaling in visible light communication systems," *IEEE Wireless Communications Letters*, pp. 1–1, 2023. [Online]. Available: https://doi.org/10.1109/LWC.2023.3290206

[207] T. Koonen, F. Gomez-Agis, F. Huijskens, K. A. Mekonnen, Z. Cao, and E. Tangdiongga, "High-capacity optical wireless communication using two-dimensional ir beam steering," *Journal of Lightwave Technology*, vol. 36, no. 19, pp. 4486–4493, 2018. [Online]. Available: https://doi.org/10.1109/JLT.2018.2834374

[208] Y. Ma, B. Dong, J. Wei, Y. Chang, L. Huang, K.-W. Ang, and C. Lee, "High-responsivity mid-infrared black phosphorus slow light waveguide photodetector," *Advanced Optical Materials*, vol. 8, no. 13, p. 2000337, 2020. [Online]. Available: https://doi.org/10.1002/adom.202000337

[209] N. T. H. Nguyen, I. A. Ukaegbu, J. Sangirov, and M. Hashmi, "Ultra-low power tia with variable bandwidth in 0.13 µm cmos for short-range optical interconnects," *The Journal of Engineering*, vol. 2021, no. 5, pp. 295–300, 2021. [Online]. Available: https://doi.org/10.1049/tje2.12034

[210] Y. Song, M. Wolny, C. Li, K. A. Mekonnen, C. R. B. Correa, M. Spiegelberg, E. Tangdiongga, and O. Raz, "Compact owc receiver: Micro-lens and pd array on glass interposer," *Journal of Lightwave Technology*, pp. 1–8, 2023. [Online]. Available: https://doi.org/10.1109/JLT.2023.3285154

[211] C. T. Manimegalai, S. Gauni, N. Raghavan, and T. R. Rao, "Investigations on suitable modulation techniques for visible light communications," in *2017 International Conference on Wireless Communications, Signal Processing and Networking (WiSPNET)*, 2017, pp. 1818–1822. [Online]. Available: https://doi.org/10.1109/WiSPNET.2017.8300075

[212] P. Dwivedy, V. Dixit, and A. Kumar, "A survey on visible light communication for 6g: Architecture, application and challenges," in *2023 International Conference on Computer, Electronics & Electrical Engineering & their Applications (IC2E3)*, 2023, pp. 1–6. [Online]. Available: https://doi.org/10.1109/IC2E357697.2023.10262462

[213] M. S. Islim, "Spectrum and energy efficient digital modulation techniques for practical visible light communication systems," Ph.D. dissertation, The University of Edinburgh, 2019.

[214] X. Zhang, Z. Babar, P. Petropoulos, H. Haas, and L. Hanzo, "The evolution of optical ofdm," *IEEE Communications Surveys & Tutorials*, vol. 23, no. 3, pp.

1430–1457, 2021. [Online]. Available: https://doi.org/10.1109/COMST.2021.3065907

[215] J. Carruthers and J. Kahn, "Multiple-subcarrier modulation for nondirected wireless infrared communication," *IEEE Journal on Selected Areas in Communications*, vol. 14, no. 3, pp. 538–546, 1996. [Online]. Available: https://doi.org/10.1109/49.490239

[216] J. Armstrong and A. Lowery, "Power efficient optical OFDM," *Electronics Letters*, vol. 42, no. 6, p. 370, 2006. [Online]. Available: https://doi.org/10.1049/el:20063636

[217] N. Fernando, Y. Hong, and E. Viterbo, "Flip-ofdm for optical wireless communications," in *2011 IEEE Information Theory Workshop*, 2011, pp. 5–9. [Online]. Available: https://doi.org/10.1109/ITW.2011.6089566

[218] S. C. J. Lee, S. Randel, F. Breyer, and A. M. J. Koonen, "Pam-dmt for intensity-modulated and direct-detection optical communication systems," *IEEE Photonics Technology Letters*, vol. 21, no. 23, pp. 1749–1751, 2009. [Online]. Available: https://doi.org/10.1109/LPT.2009.2032663

[219] T. Fath and H. Haas, "Performance comparison of mimo techniques for optical wireless communications in indoor environments," *IEEE Transactions on Communications*, vol. 61, no. 2, pp. 733–742, 2013. [Online]. Available: https://doi.org/10.1109/TCOMM.2012.120512.110578

[220] J. Jeganathan, A. Ghrayeb, L. Szczecinski, and A. Ceron, "Space shift keying modulation for mimo channels," *IEEE Transactions on Wireless Communications*, vol. 8, no. 7, pp. 3692–3703, 2009. [Online]. Available: https://doi.org/10.1109/TWC.2009.080910

[221] R. Bian, S. Videv, A. D. Griffiths, J. J. D. McKendry, E. Xie, E. Gu, M. D. Dawson, and H. Haas, "Experimental demonstration of generalised space shift keying for visible light communication," in *2017 IEEE International Black Sea*

Conference on Communications and Networking (BlackSeaCom), 2017, pp. 1–5. [Online]. Available: https://doi.org/10.1109/BlackSeaCom.2017.8277716

[222] R. Bian, "Practical implementation of multiple-input multiple-output visible light communication systems," Ph.D. dissertation, The University of Edinburgh, 2019.

[223] W. O. Popoola, E. Poves, and H. Haas, "Error performance of generalised space shift keying for indoor visible light communications," *IEEE Transactions on Communications*, vol. 61, no. 5, pp. 1968–1976, 2013. [Online]. Available: https://doi.org/10.1109/TCOMM.2013.022713.120501

[224] W. O. Popoola and H. Haas, "Demonstration of the merit and limitation of generalised space shift keying for indoor visible light communications," *Journal of Lightwave Technology*, vol. 32, no. 10, pp. 1960–1965, 2014. [Online]. Available: https://doi.org/10.1109/JLT.2014.2310499

[225] Y. Sun, D. K. Borah, and E. Curry, "Optimal symbol set selection in gssk visible light wireless communication systems," *IEEE Photonics Technology Letters*, vol. 28, no. 3, pp. 303–306, 2016. [Online]. Available: https://doi.org/10.1109/LPT.2015.2495235

[226] K. Ntontin, M. D. Renzo, A. Perez-Neira, and C. Verikoukis, "Adaptive generalized space shift keying," *EURASIP Journal on Wireless Communications and Networking*, vol. 2013, no. 1, Feb. 2013. [Online]. Available: https://doi.org/10.1186/1687-1499-2013-43

[227] E. Panayirci, A. Yesilkaya, T. Cogalan, H. V. Poor, and H. Haas, "Physical-layer security with optical generalized space shift keying," *IEEE Transactions on Communications*, vol. 68, no. 5, pp. 3042–3056, 2020. [Online]. Available: https://doi.org/10.1109/TCOMM.2020.2969867

[228] A. Yesilkaya, A. A. Purwita, E. Panayirci, H. V. Poor, and H. Haas, "Flexible led index modulation for mimo optical wireless communications," in *GLOBECOM 2020 - 2020 IEEE Global Communications Conference*, 2020, pp. 1–7. [Online]. Available: https://doi.org/10.1109/GLOBECOM42002.2020.9322528

[229] A. Nuwanpriya, S.-W. Ho, and C. S. Chen, "Indoor mimo visible light communications: Novel angle diversity receivers for mobile users," *IEEE Journal on Selected Areas in Communications*, vol. 33, no. 9, pp. 1780–1792, 2015. [Online]. Available: https://doi.org/10.1109/JSAC.2015.2432514

[230] S. Catreux, V. Erceg, D. Gesbert, and R. Heath, "Adaptive modulation and mimo coding for broadband wireless data networks," *IEEE Communications Magazine*, vol. 40, no. 6, pp. 108–115, 2002. [Online]. Available: https://doi.org/10.1109/MCOM.2002.1007416

[231] A. Forenza, A. Pandharipande, H. Kim, and R. Heath, "Adaptive mimo transmission scheme: exploiting the spatial selectivity of wireless channels," in *2005 IEEE 61st Vehicular Technology Conference*, vol. 5, 2005, pp. 3188–3192 Vol. 5. [Online]. Available: https://doi.org/10.1109/VETECS.2005.1543936

[232] P. Yang, M. Di Renzo, Y. Xiao, S. Li, and L. Hanzo, "Design guidelines for spatial modulation," *IEEE Communications Surveys & Tutorials*, vol. 17, no. 1, pp. 6–26, 2015. [Online]. Available: https://doi.org/10.1109/COMST.2014.2327066

[233] Q. Li, G. Li, W. Lee, M.-i. Lee, D. Mazzarese, B. Clerckx, and Z. Li, "Mimo techniques in wimax and lte: a feature overview," *IEEE Communications Magazine*, vol. 48, no. 5, pp. 86–92, 2010. [Online]. Available: https://doi.org/10.1109/MCOM.2010.5458368

[234] R. Rajashekar, K. Hari, and L. Hanzo, "Antenna selection in spatial modulation systems," *IEEE Communications Letters*, vol. 17, no. 3, pp. 521–524, 2013. [Online]. Available: https://doi.org/10.1109/LCOMM.2013.012213.122650

[235] P. Yang, Y. Xiao, Y. Yu, and S. Li, "Adaptive spatial modulation for wireless mimo transmission systems," *IEEE Communications Letters*, vol. 15, no. 6, pp. 602–604, 2011. [Online]. Available: https://doi.org/10.1109/LCOMM.2011.040711.110014

[236] P. Yang, Y. Xiao, L. Li, Q. Tang, Y. Yu, and S. Li, "Link adaptation for spatial modulation with limited feedback," *IEEE Transactions on Vehicular*

Technology, vol. 61, no. 8, pp. 3808–3813, 2012. [Online]. Available: https://doi.org/10.1109/TVT.2012.2207973

[237] A. Garcia-Rodriguez, C. Masouros, and L. Hanzo, "Pre-scaling optimization for space shift keying based on semidefinite relaxation," *IEEE Transactions on Communications*, vol. 63, no. 11, pp. 4231–4243, 2015. [Online]. Available: https://doi.org/10.1109/TCOMM.2015.2470656

[238] C. Masouros and L. Hanzo, "Constellation randomization achieves transmit diversity for single-rf spatial modulation," *IEEE Transactions on Vehicular Technology*, vol. 65, no. 10, pp. 8101–8111, 2016. [Online]. Available: https://doi.org/10.1109/TVT.2015.2513380

[239] P. Yang, Y. Xiao, B. Zhang, S. Li, M. El-Hajjar, and L. Hanzo, "Power allocation-aided spatial modulation for limited-feedback mimo systems," *IEEE Transactions on Vehicular Technology*, vol. 64, no. 5, pp. 2198–2204, 2015. [Online]. Available: https://doi.org/10.1109/TVT.2014.2339297

[240] W.-H. Chung and C.-Y. Hung, "Multi-antenna selection using space shift keying in mimo systems," in *2012 IEEE 75th Vehicular Technology Conference (VTC Spring)*, 2012, pp. 1–5. [Online]. Available: https://doi.org/10.1109/VETECS.2012.6240337

[241] A. Molisch, M. Win, and J. Winters, "Reduced-complexity transmit/receive-diversity systems," *IEEE Transactions on Signal Processing*, vol. 51, no. 11, pp. 2729–2738, 2003. [Online]. Available: https://doi.org/10.1109/TSP.2003.818211

[242] K. Xu, H. Yu, and Y.-J. Zhu, "Channel-adapted spatial modulation for massive mimo visible light communications," *IEEE Photonics Technology Letters*, vol. 28, no. 23, pp. 2693–2696, 2016. [Online]. Available: https://doi.org/10.1109/LPT.2016.2615128

[243] J.-Y. Wang, H. Ge, J.-X. Zhu, J.-B. Wang, J. Dai, and M. Lin, "Adaptive spatial modulation for visible light communications with an arbitrary number of

transmitters," *IEEE Access*, vol. 6, pp. 37 108–37 123, 2018. [Online]. Available: https://doi.org/10.1109/ACCESS.2018.2851280

[244] I. Tavakkolnia, C. Chen, R. Bian, and H. Haas, "Energy-efficient adaptive mimo-vlc technique for indoor lifi applications," in *2018 25th International Conference on Telecommunications (ICT)*, 2018, pp. 331–335. [Online]. Available: https://doi.org/10.1109/ICT.2018.8464933

[245] J. W. Kim, S. Y. Shin, and V. C. M. Leung, "Performance enhancement of downlink noma by combination with gssk," *IEEE Wireless Communications Letters*, vol. 7, no. 5, pp. 860–863, 2018. [Online]. Available: https://doi.org/10.1109/LWC.2018.2833469

[246] F. Wang, T. Leng, and Y. Zhang, "Naive bayesian aided antenna selection for indoor noma gssk vlc network," *Digital Signal Processing*, vol. 130, p. 103706, 2022. [Online]. Available: https://doi.org/10.1016/j.dsp.2022.103706

[247] J. Wu, F. Wang, P. Sun, Y. Zhang, and R. Li, "Machine learning assisted leds combination selection and user matching of riss enabled gssk-vlc system," *Optik*, vol. 276, p. 170640, 2023. [Online]. Available: https://doi.org/10.1016/j.ijleo.2023.170640

[248] J. B. Kuipers, *Quaternions and Rotation Sequences.* Princeton University Press, Jan. 1999. [Online]. Available: https://doi.org/10.1515/9780691211701

[249] A. Younis, D. A. Basnayaka, and H. Haas, "Performance analysis for generalised spatial modulation," in *European Wireless 2014; 20th European Wireless Conference*, 2014, pp. 1–6. [Online]. Available: https://ieeexplore.ieee.org/abstract/document/6843125

[250] T. Lakshmi Narasimhan and A. Chockalingam, "On the capacity and performance of generalized spatial modulation," *IEEE Communications Letters*, vol. 20, no. 2, pp. 252–255, 2016. [Online]. Available: https://doi.org/10.1109/LCOMM.2015.2497255

[251] J. G. Proakis, *Digital Communications.* McGraw Hill, 2001.

[252] A. Goldsmith, *Wireless Communications.* Cambridge University Press, 2005.

[253] M. D. Soltani, A. A. Purwita, Z. Zeng, H. Haas, and M. Safari, "Modeling the random orientation of mobile devices: Measurement, analysis and lifi use case," *IEEE Transactions on Communications*, vol. 67, no. 3, pp. 2157–2172, 2019. [Online]. Available: https://doi.org/10.1109/TCOMM.2018.2882213

[254] S. Parkvall, E. Dahlman, A. Furuskar, and M. Frenne, "Nr: The new 5g radio access technology," *IEEE Communications Standards Magazine*, vol. 1, no. 4, pp. 24–30, 2017. [Online]. Available: https://doi.org/10.1109/MCOMSTD.2017.1700042

[255] J. Sachs, G. Wikstrom, T. Dudda, R. Baldemair, and K. Kittichokechai, "5g radio network design for ultra-reliable low-latency communication," *IEEE Network*, vol. 32, no. 2, pp. 24–31, 2018. [Online]. Available: https://doi.org/10.1109/MNET.2018.1700232

[256] Metaswitch, "What is 5g ultra reliable low latency communications (urllc)?" [Online]. Available: https://www.metaswitch.com/knowledge-center/reference/what-is-5g-ultra-reliable-low-latency-communications-urllc

[257] S. Kim, J. Lee, and C.-H. Cho, "Extremely low latency interactive streaming over an 802.11 wireless link," in *2023 IEEE 97th Vehicular Technology Conference (VTC2023-Spring)*, 2023, pp. 1–6. [Online]. Available: https://doi.org/10.1109/VTC2023-Spring57618.2023.10199675

[258] P. Lin, Q. Song, F. R. Yu, D. Wang, A. Jamalipour, and L. Guo, "Wireless virtual reality in beyond 5g systems with the internet of intelligence," *IEEE Wireless Communications*, vol. 28, no. 2, pp. 70–77, 2021. [Online]. Available: https://doi.org/10.1109/MWC.001.2000303

[259] "Qualcomm snapdragon 8 gen 2." [Online]. Available: https://nanoreview.net/en/soc/qualcomm-snapdragon-8-gen-2

[260] D. K. Borah, A. C. Boucouvalas, C. C. Davis, S. Hranilovic, and K. Yiannopoulos, "A review of communication-oriented optical wireless systems," *EURASIP Journal on Wireless Communications and Networking*, vol. 2012, no. 1, Mar. 2012. [Online]. Available: https://doi.org/10.1186/1687-1499-2012-91

[261] Tsbmail, "G.975.1 : forward error correction for high bit-rate dwdm submarine systems." [Online]. Available: https://www.itu.int/rec/T-REC-G.975.1-200402-I/en

[262] W. S. Ciciora, *Modern cable television technology: Video, voice and Data Communications.* Elsevier/Morgan Kaufmann Publishers, 2004.

[263] J. Sperga, R. Bian, and H. Haas, "Beam selection in angle diversity mimo systems for optical wireless systems," in *2022 IEEE International Conference on Communications Workshops (ICC Workshops)*, 2022, pp. 445–450. [Online]. Available: https://doi.org/10.1109/ICCWorkshops53468.2022.9814683

[264] J. Fakidis, M. Ijaz, S. Kucera, H. Claussen, and H. Haas, "On the design of an optical wireless link for small cell backhaul communication and energy harvesting," in *2014 IEEE 25th Annual International Symposium on Personal, Indoor, and Mobile Radio Communication (PIMRC)*, 2014, pp. 58–62. [Online]. Available: https://doi.org/10.1109/PIMRC.2014.7136132

[265] "450nm cwl, 25mm dia. hard coated od 4.0 50nm bandpass filter." [Online]. Available: https://www.edmundoptics.eu/p/450nm-cwl-25mm-dia-hard-coated-od-4-50nm-bandpass-filter/27851/

[266] "Nt25l51 — 2.5gbps tia/gpon(apd)/oc-48." [Online]. Available: https://www.semtech.com/products/signal-integrity/transimpedance-amplifiers/nt25l51

[267] Apr 2023. [Online]. Available: https://www.onsemi.com/pdf/datasheet/arrayc-series-d.pdf

[268] "Si apd s12023-10 — hamamatsu photonics." [Online]. Available: https://www.hamamatsu.com/jp/en/product/optical-sensors/apd/si-apd/S12023-10.html

[269] "25° 4.34mm output dia., compound parabolic concentrator - no longer available at edmund optics®." [Online]. Available: https://www.edmundoptics.com/p/25deg-434mm-output-dia-compound-parabolic-concentrator/17843/

[270] "Lamp spectral power distribution database, led ge a19 domestic, october 2012." [Online]. Available: https://lspdd.org/app/en/lamps/2595

[271] HSE, *Lighting at work.* HSE, 2005.

[272] X. Huang, Z. Wang, J. Shi, Y. Wang, and N. Chi, "1.6 gbit/s phosphorescent white led based vlc transmission using a cascaded pre-equalization circuit and a differential outputs pin receiver," *Opt. Express*, vol. 23, no. 17, pp. 22 034–22 042, Aug 2015. [Online]. Available: https://doi.org/10.1364/OE.23.022034

[273] Y. Wang, L. Tao, X. Huang, J. Shi, and N. Chi, "8-gb/s rgby led-based wdm vlc system employing high-order cap modulation and hybrid post equalizer," *IEEE Photonics Journal*, vol. 7, no. 6, pp. 1–7, 2015. [Online]. Available: https://doi.org/10.1109/JPHOT.2015.2489927

[274] K. Tyszka, M. Dobosz, and T. Bilaszewski, "Double wedge prism based beam deflector for precise laser beam steering," *Review of Scientific Instruments*, vol. 89, no. 2, p. 025113, 02 2018. [Online]. Available: https://doi.org/10.1063/1.5011979

[275] "Sm85-1ah001 — optowell co., ltd." [Online]. Available: http://www.optowell.com/download/01/SM85-1AH001_rev_2.0.pdf

[276] "Thorlabs, inc. - your source for fiber optics, laser diodes, optical instrumentation and polarization measurement & control." [Online]. Available: https://www.thorlabs.com/thorproduct.cfm?partnumber=ACL108U-B

[277] "Gaussian models." [Online]. Available: https://uk.mathworks.com/help/curvefit/gaussian.html

[278] "Si apd s14643-02." [Online]. Available: https://www.hamamatsu.com/us/en/product/optical-sensors/distance-position-sensor/lidar-sensor/si-apd-for-lidar/S14643-02.html

[279] "Thorlabs, inc. - your source for fiber optics, laser diodes, optical instrumentation and polarization measurement & control." [Online]. Available: https://www.thorlabs.com/thorproduct.cfm?partnumber=354140-B

[280] J. A. Duffie and W. A. Beckman, *Concentrating Collectors.* John Wiley & Sons, Ltd, 2013, ch. 7, pp. 322–372. [Online]. Available: https://onlinelibrary.wiley.com/doi/abs/10.1002/9781118671603.ch7

[281] R. B. Johnson and R. Kingslake, *Lens design fundamentals by Rudolf Kingslake, R. Barry Johnson.* Academic Press, 2010. [Online]. Available: https://doi.org/10.1016/C2009-0-22069-1

[282] S. Kim, M. Jahandar, J. H. Jeong, and D. C. Lim, "Recent progress in solar cell technology for low-light indoor applications," *Current Alternative Energy*, vol. 3, no. 1, p. 3–17, Nov 2019. [Online]. Available: https://doi.org/10.2174/1570180816666190112141857

[283] "Adn2880 datasheet and product info — analog devices," Jul 2005. [Online]. Available: https://www.analog.com/en/products/adn2880.html

[284] K. F. Wallis. [Online]. Available: https://warwick.ac.uk/fac/soc/economics/staff/academic/wallis/publications/entropy.pdf

[285] M. Dehghani Soltani, A. A. Purwita, Z. Zeng, C. Chen, H. Haas, and M. Safari, "An orientation-based random waypoint model for user mobility in wireless networks," in *2020 IEEE International Conference on Communications Workshops (ICC Workshops)*, 2020, pp. 1–6. [Online]. Available: https://doi.org/10.1109/ICCWorkshops49005.2020.9145333

[286] M. D. Soltani, A. A. Purwita, Z. Zeng, H. Haas, and M. Safari, "Modeling the random orientation of mobile devices: Measurement, analysis and lifi use case,"

IEEE Transactions on Communications, vol. 67, no. 3, pp. 2157–2172, 2019. [Online]. Available: https://doi.org/10.1109/TCOMM.2018.2882213

[287] K. Modepalli and L. Parsa, "Dual-purpose offline led driver for illumination and visible light communication," *IEEE Transactions on Industry Applications*, vol. 51, no. 1, pp. 406–419, 2015. [Online]. Available: https://doi.org/10.1109/TIA.2014.2330066

[288] S. Haese, L. Mtimet, and M. Hélard, "Led driver performance analysis for joint visible light communication and illumination," in *2016 IEEE 59th International Midwest Symposium on Circuits and Systems (MWSCAS)*, 2016, pp. 1–4. [Online]. Available: https://doi.org/10.1109/MWSCAS.2016.7870038

[289] C. Pfistner, "Avicena demonstrates first microled based transceiver ic in 16nm finfet cmos for chip-to-chip communications at ecoc 2023," Oct 2023. [Online]. Available: https://avicena.tech/avicena-demonstrates-first-microled-based-transceiver-ic-in-16nm-finfet-cmos-for-chip-to-chip-c

[290] "Npn bipolar transistor pro 2n5179-nrc." [Online]. Available: https://www.farnell.com/datasheets/2899729.pdf

[291] Z. Khan, J.-C. Shih, R.-L. Chao, T.-L. Tsai, H.-C. Wang, G.-W. Fan, Y.-C. Lin, and J.-W. Shi, "High-brightness and high-speed vertical-cavity surface-emitting laser arrays," *Optica*, vol. 7, no. 4, p. 267, Mar 2020. [Online]. Available: https://doi.org/10.1364/optica.383406

[292] "Rohm semiconductor 2sc5662." [Online]. Available: https://eu.mouser.com/datasheet/2/348/ROHM_S_A0001071611_1-2561382.pdf

[293] "Data sheet ad9209 - analog devices." [Online]. Available: https://www.analog.com/media/en/technical-documentation/data-sheets/ad9209.pdf

[294] "Adc12j4000 12-bit, 4-gsps adc with integrated ddc datasheet (rev. d)." [Online]. Available: https://www.ti.com/lit/ds/symlink/adc12j4000.pdf

[295] J. Li, X.-D. Zhang, Q. Gao, Y. Luo, and D. Gu, "Exact bep analysis for coherent m-ary pam and qam over awgn and rayleigh fading channels," in *VTC Spring 2008 - IEEE Vehicular Technology Conference*, 2008, pp. 390–394. [Online]. Available: https://doi.org/10.1109/VETECS.2008.93

[296] "Max19692/max19693 evaluation kit user's guide - analog devices." [Online]. Available: https://www.analog.com/media/en/technical-documentation/data-sheets/MAX19692EVKIT-MAX19693EVKIT.pdf

[297] "Lmh6401 dc to 4.5 ghz, fully-differential, digital variable-gain." [Online]. Available: https://www.ti.com/lit/ds/symlink/lmh6401.pdf

[298] R. Rodriguez-Gomez, E. J. Fernandez-Sanchez, J. Diaz, and E. Ros, "Codebook hardware implementation on fpga for background subtraction," *Journal of Real-Time Image Processing*, vol. 10, no. 1, p. 43–57, 2012. [Online]. Available: https://doi.org/10.1007/s11554-012-0249-6

[299] W. Nurmi and S. Nooshabadi, "An adaptive space-time coding / spatial multiplexing detector on fpga," in *Proceedings of 2010 IEEE International Symposium on Circuits and Systems*, 2010, pp. 4169–4172. [Online]. Available: https://doi.org/10.1109/ISCAS.2010.5537594

[300] A. Ramirez-Agundis, R. Gadea-Girones, and R. Colom-Palero, "A hardware design of a massive-parallel, modular nn-based vector quantizer for real-time video coding," *Microprocessors and Microsystems*, vol. 32, no. 1, pp. 33–44, 2008. [Online]. Available: https://doi.org/10.1016/j.micpro.2007.06.004

[301] J. Kim, S. Hosseinalipour, A. C. Marcum, T. Kim, D. J. Love, and C. G. Brinton, "Learning-based adaptive irs control with limited feedback codebooks," *IEEE Transactions on Wireless Communications*, vol. 21, no. 11, pp. 9566–9581, 2022. [Online]. Available: https://doi.org/10.1109/TWC.2022.3178055

[302] H. Kimura, K. Asaka, H. Nakamura, S. Kimura, and N. Yoshimoto, "Energy efficient im-dd ofdm-pon using dynamic snr management and adaptive

modulation," *Opt. Express*, vol. 22, no. 2, pp. 1789–1795, Jan 2014. [Online]. Available: https://doi.org/10.1364/OE.22.001789

[303] D. Zou and I. B. Djordjevic, "Fpga-based rate-adaptive ldpc-coded modulation for the next generation of optical communication systems," *Opt. Express*, vol. 24, no. 18, pp. 21 159–21 166, Sep 2016. [Online]. Available: https://doi.org/10.1364/OE.24.021159

[304] J. Krivochiza, J. Merlano Duncan, S. Andrenacci, S. Chatzinotas, and B. Ottersten, "Fpga acceleration for computationally efficient symbol-level precoding in multi-user multi-antenna communication systems," *IEEE Access*, vol. 7, pp. 15 509–15 520, 2019. [Online]. Available: https://doi.org/10.1109/ACCESS.2019.2894181

[305] J.-L. Fournier, D. Titz, F. Ferrero, C. Luxey, E. Dekneuvel, and G. Jacquemod, "Phased array antenna controlled by neural network fpga," in *2011 Loughborough Antennas & Propagation Conference*, 2011, pp. 1–5. [Online]. Available: https://doi.org/10.1109/LAPC.2011.6114104

[306] T. Onizawa, A. Ohta, and Y. Asai, "Experiments on fpga-implemented eigenbeam mimo-ofdm with transmit antenna selection," *IEEE Transactions on Vehicular Technology*, vol. 58, no. 3, pp. 1281–1291, 2009. [Online]. Available: https://doi.org/10.1109/TVT.2008.928900

[307] E. Sarbazi, H. Kazemi, M. D. Soltani, M. Safari, and H. Haas, "Design tradeoffs of non-imaging angle diversity receivers for 6g optical wireless access networks," in *GLOBECOM 2022 - 2022 IEEE Global Communications Conference*, 2022, pp. 419–424. [Online]. Available: https://doi.org/10.1109/GLOBECOM48099.2022.10000825

[308] R. Winston, "Light collection within the framework of geometrical optics∗," *J. Opt. Soc. Am.*, vol. 60, no. 2, pp. 245–247, Feb 1970. [Online]. Available: https://doi.org/10.1364/JOSA.60.000245

[309] A. Rabl, N. Goodman, and R. Winston, "Practical design considerations for cpc solar collectors," *Solar Energy*, vol. 22, no. 4, pp. 373–381, 1979. [Online]. Available: https://doi.org/10.1016/0038-092X(79)90192-0

[310] J. Chaves, *Introduction to nonimaging optics.* Taylor & Francis, 2017.

[311] H.-J. Choi, C. Cho, S. Woo, J.-Y. Lee, Y.-E. Yoo, M. Jeon, G.-H. Kim, T.-J. Je, and E.-c. Jeon, "Manufacturing of compound parabolic concentrator devices using an ultra-fine planing method for enhancing efficiency of a solar cell," *International Journal of Precision Engineering and Manufacturing-Green Technology*, vol. 8, no. 5, p. 1405–1414, 2020. [Online]. Available: https://doi.org/10.1007/s40684-020-00287-3

[312] D. A. Bykov, L. L. Doskolovich, A. A. Mingazov, E. A. Bezus, and N. L. Kazanskiy, "Linear assignment problem in the design of freeform refractive optical elements generating prescribed irradiance distributions," *Opt. Express*, vol. 26, no. 21, pp. 27 812–27 825, Oct 2018. [Online]. Available: https://doi.org/10.1364/OE.26.027812

[313] J. P. Rolland, M. A. Davies, T. J. Suleski, C. Evans, A. Bauer, J. C. Lambropoulos, and K. Falaggis, "Freeform optics for imaging," *Optica*, vol. 8, no. 2, pp. 161–176, Feb 2021. [Online]. Available: https://doi.org/10.1364/OPTICA.413762

[314] J. M. Rodgers and K. P. Thompson, "Benefits of freeform mirror surfaces in optical design," in *Proceedings of the American Society of Precision Engineering 2004 Winter Topical Meeting on Freeform Optics*, vol. 31, 2004, pp. 73–78.

[315] H. Chretien, "Anamorphotic lens system and method of making the same," Jun. 12 1934, U.S Patent 1,962,892.

[316] L. W. Alvarez and W. E. Humphrey, "Variable-power lens and system," Apr. 21 1970, U.S Patent 3,507,565.

[317] W. T. Plummer, "Unusual optics of the polaroid sx-70 land camera," *Appl. Opt.*, vol. 21, no. 2, pp. 196–202, Jan 1982. [Online]. Available: https://doi.org/10.1364/AO.21.000196

[318] P. Jester, C. Menke, and K. Urban, "B-spline representation of optical surfaces and its accuracy in a ray trace algorithm," *Appl. Opt.*, vol. 50, no. 6, pp. 822–828, Feb 2011. [Online]. Available: https://doi.org/10.1364/AO.50.000822

[319] O. Cakmakci, B. Moore, H. Foroosh, and J. P. Rolland, "Optimal local shape description for rotationally non-symmetric optical surface design and analysis," *Opt. Express*, vol. 16, no. 3, pp. 1583–1589, Feb 2008. [Online]. Available: https://doi.org/10.1364/OE.16.001583

[320] P. Jester, C. Menke, and K. Urban, "Wavelet methods for the representation, analysis and simulation of optical surfaces," *IMA Journal of Applied Mathematics*, vol. 77, no. 4, pp. 495–515, 07 2011. [Online]. Available: https://doi.org/10.1093/imamat/hxr030

[321] von F. Zernike, "Beugungstheorie des schneidenver-fahrens und seiner verbesserten form, der phasenkontrastmethode," *Physica*, vol. 1, no. 7, pp. 689–704, 1934. [Online]. Available: https://doi.org/10.1016/S0031-8914(34)80259-5

[322] G. W. Forbes, "Characterizing the shape of freeform optics," *Opt. Express*, vol. 20, no. 3, pp. 2483–2499, Jan 2012. [Online]. Available: https://doi.org/10.1364/OE.20.002483

[323] N. Takaki, A. Bauer, and J. P. Rolland, "On-the-fly surface manufacturability constraints for freeform optical design enabled by orthogonal polynomials," *Opt. Express*, vol. 27, no. 5, pp. 6129–6146, Mar 2019. [Online]. Available: https://doi.org/10.1364/OE.27.006129

[324] D. Ochse, K. Uhlendorf, and L. Reichmann, "Describing freeform surfaces with orthogonal functions," in *Imaging and Applied Optics 2015.* Optica Publishing Group, 2015, p. FT2B.4. [Online]. Available: https://doi.org/10.1364/FREEFORM.2015.FT2B.4

[325] H. Gross, A. Brömel, M. Beier, R. Steinkopf, J. Hartung, Y. Zhong, M. Oleszko, and D. Ochse, "Overview on surface representations for freeform surfaces," in *Optical Systems Design 2015: Optical Design and Engineering VI*, L. Mazuray, R. Wartmann, and A. P. Wood, Eds., vol. 9626, International Society for Optics and Photonics. SPIE, 2015, p. 96260U. [Online]. Available: https://doi.org/10.1117/12.2191255

[326] G. W. Forbes, "Fitting freeform shapes with orthogonal bases," *Opt. Express*, vol. 21, no. 16, pp. 19 061–19 081, Aug 2013. [Online]. Available: https://doi.org/10.1364/OE.21.019061

[327] F. Liu, B. M. Robinson, P. Reardon, and J. M. Geary, "Analyzing optics test data on rectangular apertures using 2-D Chebyshev polynomials," *Optical Engineering*, vol. 50, no. 4, p. 043609, 2011. [Online]. Available: https://doi.org/10.1117/1.3569692

[328] J. Ye, L. Chen, X. Li, Q. Yuan, and Z. Gao, "Review of optical freeform surface representation technique and its application," *Optical Engineering*, vol. 56, no. 11, p. 110901, 2017. [Online]. Available: https://doi.org/10.1117/1.OE.56.11.110901

[329] R. Wu, L. Xu, P. Liu, Y. Zhang, Z. Zheng, H. Li, and X. Liu, "Freeform illumination design: a nonlinear boundary problem for the elliptic monge–ampére equation," *Opt. Lett.*, vol. 38, no. 2, pp. 229–231, Jan 2013. [Online]. Available: https://doi.org/10.1364/OL.38.000229

[330] R. Wu, Y. Zhang, M. M. Sulman, Z. Zheng, P. Benítez, and J. C. Minano, "Initial design with l2 monge-kantorovich theory for the monge–ampère equation method in freeform surface illumination design," *Opt. Express*, vol. 22, no. 13, pp. 16 161–16 177, Jun 2014. [Online]. Available: https://doi.org/10.1364/OE.22.016161

[331] C. R. Prins, J. H. M. Ten Thije Boonkkamp, J. van Roosmalen, W. L. Jzerman, and T. W. Tukker, "A monge–ampère-solver for free-form reflector design,"

SIAM Journal on Scientific Computing, vol. 36, no. 3, pp. B640–B660, 2014. [Online]. Available: https://doi.org/10.1137/130938876

[332] Y. Zhang, R. Wu, P. Liu, Z. Zheng, H. Li, and X. Liu, "Double freeform surfaces design for laser beam shaping with monge–ampère equation method," *Optics Communications*, vol. 331, pp. 297–305, 2014. [Online]. Available: https://doi.org/10.1016/j.optcom.2014.06.043

[333] V. Oliker, "Mathematical aspects of design of beam shaping surfaces in geometrical optics," in *Trends in Nonlinear Analysis*, M. Kirkilionis, S. Krömker, R. Rannacher, and F. Tomi, Eds. Berlin, Heidelberg: Springer Berlin Heidelberg, 2003, pp. 193–224. [Online]. Available: https://doi.org/10.1007/978-3-662-05281-5_4

[334] C. Bösel and H. Gross, "Ray mapping approach for the efficient design of continuous freeform surfaces," *Opt. Express*, vol. 24, no. 13, pp. 14 271–14 282, Jun 2016. [Online]. Available: https://doi.org/10.1364/OE.24.014271

[335] C. Bösel, N. G. Worku, and H. Gross, "Ray-mapping approach in double freeform surface design for collimated beam shaping beyond the paraxial approximation," *Appl. Opt.*, vol. 56, no. 13, pp. 3679–3688, May 2017. [Online]. Available: https://doi.org/10.1364/AO.56.003679

[336] L. L. Doskolovich, A. A. Mingazov, D. A. Bykov, E. S. Andreev, and E. A. Bezus, "Variational approach to calculation of light field eikonal function for illuminating a prescribed region," *Opt. Express*, vol. 25, no. 22, pp. 26 378–26 392, Oct 2017. [Online]. Available: https://doi.org/10.1364/OE.25.026378

[337] K. Desnijder, P. Hanselaer, and Y. Meuret, "Ray mapping method for off-axis and non-paraxial freeform illumination lens design," *Opt. Lett.*, vol. 44, no. 4, pp. 771–774, Feb 2019. [Online]. Available: https://opg.optica.org/ol/abstract.cfm?URI=ol-44-4-771

[338] S. Wei, Z. Zhu, Z. Fan, and D. Ma, “Least-squares ray mapping method for freeform illumination optics design,” *Opt. Express*, vol. 28, no. 3, pp. 3811–3822, Feb 2020. [Online]. Available: https://doi.org/10.1364/OE.385254

[339] P. Benitez, R. M. Arroyo, and J. C. Minano, “Design in 3D geometry with the simultaneous multiple surface design method of nonimaging optics,” in *Nonimaging Optics: Maximum Efficiency Light Transfer V*, R. Winston, Ed., vol. 3781, International Society for Optics and Photonics. SPIE, 1999, pp. 12 – 21. [Online]. Available: https://doi.org/10.1117/12.368248

[340] P. Gimenez-Benitez, J. C. Miñano, J. Blen, R. M. Arroyo, J. Chaves, O. Dross, M. Hernandez, and W. Falicoff, “Simultaneous multiple surface optical design method in three dimensions,” *Optical Engineering*, vol. 43, no. 7, pp. 1489 – 1502, 2004. [Online]. Available: https://doi.org/10.1117/1.1752918

[341] Y. Nie, D. R. Shafer, H. Ottevaere, H. Thienpont, and F. Duerr, “Automated freeform imaging system design with generalized ray tracing and simultaneous multi-surface analytic calculation,” *Opt. Express*, vol. 29, no. 11, pp. 17 227–17 245, May 2021. [Online]. Available: https://doi.org/10.1364/OE.426207

[342] J. C. Miñano, P. Benítez, and A. Santamaría, “Free-form optics for illumination,” *Optical Review*, vol. 16, no. 2, p. 99–102, 2009. [Online]. Available: https://doi.org/10.1007/s10043-009-0017-4

[343] Y. Chen and A. Y. Yi, “Design and fabrication of freeform glass concentrating mirrors using a high volume thermal slumping process,” *Solar Energy Materials and Solar Cells*, vol. 95, no. 7, pp. 1654–1664, 2011. [Online]. Available: https://doi.org/10.1016/j.solmat.2011.01.024

[344] J. C. M. nano, P. Benítez, P. Zamora, M. Buljan, R. Mohedano, and A. Santamaría, “Free-form optics for fresnel-lens-based photovoltaic concentrators,” *Opt. Express*, vol. 21, no. S3, pp. A494–A502, May 2013. [Online]. Available: https://doi.org/10.1364/OE.21.00A494

[345] F. Duerr, Y. Meuret, and H. Thienpont, "Tailored free-form optics with movement to integrate tracking in concentrating photovoltaics," *Opt. Express*, vol. 21, no. S3, pp. A401–A411, May 2013. [Online]. Available: https://doi.org/10.1364/OE.21.00A401

[346] P. Benítez, J. C. Miñano, P. Zamora, M. Buljan, A. Cvetković, M. Hernandez, R. Mohedano, J. Chaves, and O. Dross, "Free-form Köhler nonimaging optics for photovoltaic concentration," in *Optical Design and Testing IV*, Y. Wang, J. Bentley, C. Du, K. Tatsuno, and H. P. Urbach, Eds., vol. 7849, International Society for Optics and Photonics. SPIE, 2010, p. 78490K. [Online]. Available: https://doi.org/10.1117/12.873884

[347] P. Zamora, P. Benítez, R. M. Arroyo, A. Cvetkovic, J. F. Vilaplana, Y. Li, M. Hernández, J. C. Chaves, and J. C. Miñano, "Experimental characterization of Fresnel-Köhler concentrators," *Journal of Photonics for Energy*, vol. 2, no. 1, p. 021806, 2012. [Online]. Available: https://doi.org/10.1117/1.JPE.2.021806

[348] M. Buljan, J. Mendes-Lopes, P. Benítez, and J. C. Miñano, "Recent trends in concentrated photovoltaics concentrators' architecture," *Journal of Photonics for Energy*, vol. 4, no. 1, p. 040995, 2014. [Online]. Available: https://doi.org/10.1117/1.JPE.4.040995

[349] A. Plesniak, R. Jones, J. Schwartz, G. Martins, J. Hall, A. Narayanan, D. Whelan, P. Benítez, J. C. Miñano, A. Cvetkovíc, M. Hernandez, O. Dross, and R. Alvarez, "High performance concentrating photovoltaic module designs for utility scale power generation," in *2009 34th IEEE Photovoltaic Specialists Conference (PVSC)*, 2009, pp. 002 231–002 236. [Online]. Available: https://doi.org/10.1109/PVSC.2009.5411374

[350] S. Kumar, Z. Tong, and X. Jiang, "Advances in the design and manufacturing of novel freeform optics," *International Journal of Extreme Manufacturing*, vol. 4, no. 3, p. 032004, jul 2022. [Online]. Available: https://dx.doi.org/10.1088/2631-7990/ac7617

[351] C.-Y. Tsai, "Optimized solar thermal concentrator system based on free-form trough reflector," *Solar Energy*, vol. 125, pp. 146–160, 2016. [Online]. Available: https://doi.org/10.1016/j.solener.2015.12.011

[352] X.-l. Meng, F.-P. Ren, P. Zhang, and Z.-x. Tang, "Trough-type free-form secondary solar concentrator for cpv/t application," *Energies*, vol. 15, no. 21, 2022. [Online]. Available: https://doi.org/10.3390/en15218023

[353] B. Narasimhan, P. Benitez, J. C. Miñano, J. Chaves, D. Grabovickic, M. Nikolic, and J. Infante, "Freeform aplanatic concentrators," in *Nonimaging Optics: Efficient Design for Illumination and Solar Concentration XII*, R. Winston and J. M. Gordon, Eds., vol. 9572, International Society for Optics and Photonics. SPIE, 2015, p. 95720M. [Online]. Available: https://doi.org/10.1117/12.2189092

[354] X. long Meng, X. lin Xia, C. Sun, Y. Li, and X. lei Li, "A novel free-form cassegrain concentrator for pv/t combining utilization," *Solar Energy*, vol. 135, pp. 864–873, 2016. [Online]. Available: https://doi.org/10.1016/j.solener.2016.06.034

[355] P. Berto, L. Philippet, J. Osmond, C. F. Liu, A. Afridi, M. Montagut Marques, B. Molero Agudo, G. Tessier, and R. Quidant, "Tunable and free-form planar optics," *Nature Photonics*, vol. 13, no. 9, p. 649–656, 2019. [Online]. Available: https://doi.org/10.1038/s41566-019-0486-3

[356] C.-Y. Tsai, "Improved irradiance distribution on high concentration solar cell using free-form concentrator," *Solar Energy*, vol. 115, pp. 694–707, 2015. [Online]. Available: https://doi.org/10.1016/j.solener.2015.03.032

[357] J. C. Valencia-Estrada, J. García-Márquez, X. Zhang, and L. Shi, "Free-form compound concentrators for optical wireless communications," in *2019 Global LIFI Congress (GLC)*, 2019, pp. 1–6. [Online]. Available: https://doi.org/10.1109/GLC.2019.8864132

[358] D. Sabui, S. Chatterjee, V. Mishra, B. Roy, and G. S. Khan, "Compact monolithic freeform Fresnel receiver front-end for Li-Fi application: a step

forward," in *International Optical Design Conference 2023*, D. M. Aikens, H. Rehn, S. Thibault, and K. Uhlendorf, Eds., vol. 12798, International Society for Optics and Photonics. SPIE, 2023, p. 1279809. [Online]. Available: https://doi.org/10.1117/12.2691611

[359] R. Kirrbach, T. Schneider, M. Faulwaßer, and K. Zielant, "Multipath lens for eye-safe optical wireless communications," *Opt. Express*, vol. 29, no. 19, pp. 30 208–30 222, Sep 2021. [Online]. Available: https://doi.org/10.1364/OE.435890

[360] R. Kirrbach, M. Faulwaßer, M. Stephan, T. Schneider, and F. Deicke, "High power eye-safe optical wireless gigabit link employing a freeform multipath lens," *IEEE Communications Letters*, vol. 26, no. 6, pp. 1343–1347, 2022. [Online]. Available: https://doi.org/10.1109/LCOMM.2022.3162642

[361] R. Kirrbach, T. Schneider, M. Stephan, A. Noack, M. Faulwaßer, and F. Deicke, "Total internal reflection lens for optical wireless receivers," *Photonics*, vol. 9, no. 5, 2022. [Online]. Available: https://doi.org/10.3390/photonics9050276

[362] D. Sabui, S. Chatterjee, A. Prakash, B. Roy, and G. S. Khan, "Design of an off-axis freeform diversity receiver to improve sinr performance of a multi-cell vlc system," *Optics Communications*, vol. 510, p. 127937, 2022. [Online]. Available: https://doi.org/10.1016/j.optcom.2022.127937

[363] D. Sabui, V. Mishra, S. Chatterjee, B. Roy, and G. S. Khan, "Freeform based compact receiver front-end for indoor multi-cell vlc system: Fabrication, optical characterization and associated challenges," *Optik*, vol. 274, p. 170539, 2023. [Online]. Available: https://doi.org/10.1016/j.ijleo.2023.170539

[364] R. Wu, P. Liu, Y. Zhang, Z. Zheng, H. Li, and X. Liu, "A mathematical model of the single freeform surface design for collimated beam shaping," *Opt. Express*, vol. 21, no. 18, pp. 20 974–20 989, Sep 2013. [Online]. Available: https://doi.org/10.1364/OE.21.020974

[365] C. Bösel and H. Gross, "Single freeform surface design for prescribed input wavefront and target irradiance," *J. Opt. Soc. Am. A*, vol. 34, no. 9, pp. 1490–1499, Sep 2017. [Online]. Available: https://doi.org/10.1364/JOSAA.34.001490

[366] C. R. Prins, R. Beltman, J. H. M. ten Thije Boonkkamp, W. L. IJzerman, and T. W. Tukker, "A least-squares method for optimal transport using the monge–ampère equation," *SIAM Journal on Scientific Computing*, vol. 37, no. 6, pp. B937–B961, 2015. [Online]. Available: https://doi.org/10.1137/140986414

[367] G. Beadie, M. Brindza, R. A. Flynn, A. Rosenberg, and J. S. Shirk, "Refractive index measurements of poly(methyl methacrylate) (pmma) from 0.4–1.6 μm," *Appl. Opt.*, vol. 54, no. 31, pp. F139–F143, Nov 2015. [Online]. Available: https://doi.org/10.1364/AO.54.00F139

[368] F. A. Jenkins and H. E. White, *Fundamentals of optics. 4.Ed.* McGraw-Hill, 1976.

[369] L. N. Andreev, V. V. Ezhova, E. A. Tsyganok, and A. D. Kozhina, "Compensators of petzval field curvature and astigmatism," *J. Opt. Technol.*, vol. 88, no. 4, pp. 175–177, Apr 2021. [Online]. Available: https://doi.org/10.1364/JOT.88.000175

[370] J. Sperga, R. Bian, M. S. Islim, J. Kosman, G. L. Martena, E. Murphy, and H. Haas, "Thin receiver freeform lenslet concentrator array for lifi," in *2023 IEEE International Conference on Communications Workshops (ICC Workshops), Rome, Italy*, 2023.

[371] N. Sultanova, S. Kasarova, and I. Nikolov, "Dispersion properties of optical polymers," *Acta Physica Polonica A*, vol. 116, no. 4, pp. 585–587, 2009.

[372] T. Saito, "Spectral properties of semiconductor photodiodes," *Advances in photodiodes*, pp. 3–24, 2011.

[373] T. Saito, M. Yuri, and H. Onuki, "Polarization characteristics of semiconductor photodiodes," *Metrologia*, vol. 32, no. 6, p. 485, dec 1995. [Online]. Available: https://dx.doi.org/10.1088/0026-1394/32/6/16

[374] J. Sperga, M. S. Islim, R. Bian, G. L. Martena, and H. Haas, "Photodiode arrays do not violate the second law of thermodynamics: Photocurrent bandwidth trade-off," in *ICC 2024 - IEEE International Conference on Communications*, 2024, pp. 2414–2419. [Online]. Available: https://doi.org/10.1109/ICC51166.2024.10622212

[375] "Si apd s12023-02 — hamamatsu photonics." [Online]. Available: https://www.hamamatsu.com/us/en/product/optical-sensors/apd/si-apd/S12023-02.html

[376] S. Chatterjee and S. Sen, "Cache-efficient matrix transposition," in *Proceedings Sixth International Symposium on High-Performance Computer Architecture. HPCA-6 (Cat. No.PR00550)*, 2000, pp. 195–205. [Online]. Available: https://doi.org/10.1109/HPCA.2000.824350

[377] V. Strassen, "Gaussian elimination is not optimal," *Numerische Mathematik*, vol. 13, no. 4, p. 354–356, Aug 1969. [Online]. Available: https://doi.org/10.1007/bf02165411

[378] R. P. Brent and P. Zimmermann, *Modern Computer Arithmetic.* Cambridge University Press, Nov. 2010, p. ix–x. [Online]. Available: http://dx.doi.org/10.1017/cbo9780511921698.001

[379] G. Rote, *Division-Free Algorithms for the Determinant and the Pfaffian: Algebraic and Combinatorial Approaches", bookTitle="Computational Discrete Mathematics: Advanced Lectures.* Berlin, Heidelberg: Springer Berlin Heidelberg, 2001, pp. 119–135. [Online]. Available: https://doi.org/10.1007/3-540-45506-X_9

[380] W. Min, "Analysis on bubble sort algorithm optimization," in *2010 International Forum on Information Technology and Applications*, vol. 1, 2010, pp. 208–211.